

# Thermo-Mechanical Behavior of High-Strength Concrete with Nylon Granule Aggregates: Experimental Evaluation and Predictive Analysis

Fariborz Sasania <sup>a</sup>, Mahdi Nematzadeh <sup>a\*</sup>, Maryam Asadi <sup>a</sup>, Arman Aminian <sup>a</sup>

<sup>a</sup> Department of Civil Engineering, Faculty of Engineering and Technology, University of Mazandaran, Babolsar, Iran

## ARTICLE INFO

### Keywords:

High-strength concrete  
Recycled nylon granules  
Elevated temperatures  
Mechanical properties  
Microstructure  
Compressive stress-strain behavior

### Article history:

Received 09 May 2025  
Accepted 14 May 2025  
Available online 21 May 2025

## ABSTRACT

In recent years, incorporating polymer trash as a substitute for natural aggregates in cementitious material has emerged as a sustainable approach to minimize environmental impact. Despite growing interest, limited studies have addressed the mechanical and microstructural performance of high-strength concrete (HSC) incorporating polymer waste under elevated temperature conditions. This research investigates the residual stress-strain response of HSC incorporating nylon granules (NG) as a partial substitute for natural sand at proportions of 0, 10, and 20%. Specimens were subjected to axial compressive loading after exposure to high temperatures of 20, 300, and 600°C. The analysis covered several physical and mechanical characteristics such as loss of weight, compressive strength, splitting tensile strength, elastic modulus, strain at peak stress, ultimate strain, toughness, stress-strain model, visual changes, and microstructure. The experimental findings were benchmarked against established codes and standards, including ACI 216, ASCE, EN 1994-1-2, EN 1992-1-2, and CEB-FIP. Results demonstrated that higher temperatures substantially impaired concrete performance, with compressive strength and modulus of elasticity declining by approximately 59% and 75%, respectively, at 600°C. Furthermore, the inclusion of NG led to additional reductions in mechanical performance. Based on the experimental observations, predictive models were formulated for mechanical properties, and a stress-strain model for NG-modified concrete was developed, which correlated well with the experimental results.

## 1. Introduction

Nowadays, with the growing global population, the consumption of both natural and non-natural resources is increasing significantly. As a result, human societies and the environment are facing the challenge of massive waste accumulation, which can lead to irreversible damage. Many researchers are striving to find effective ways to reduce the impact of these destructive activities or to identify suitable substitutes that cause less harm to the environment. In this context, polymer waste, particularly nylon bags, is considered one of the most damaging materials worldwide. A promising method for tackling environmental concerns involves repurposing waste materials by converting them into nylon granules (NG) through recycling processes, which can then serve as a partial substitute for natural aggregates in concrete [1]. Incorporating recycled NG into concrete not only reduces the reliance on natural resources but also results in a lighter composite material. This practice contributes to lowering the environmental footprint associated with excessive aggregate consumption. Additionally, the integration of recycled nylon materials into concrete can help alleviate pollution problems linked to discarded nylon products, such as bags [2]. Given the limited number of studies focusing on the application of recycled NG in concrete, this section reviews prior research on the behavior of concrete incorporating polymer-based waste. Tayebi and Nematzadeh [3], by examining the mechanical performance of concrete containing nylon granules at

\* Corresponding author.

E-mail addresses: [m.nematzadeh@umz.ac.ir](mailto:m.nematzadeh@umz.ac.ir) (M. Nematzadeh).

<https://doi.org/10.22080/ceas.2025.29200.1011>

ISSN: 3092-7749/© 2025 The Author(s). Published by University of Mazandaran.

This article is an open access article distributed under the terms and conditions of the Creative Commons Attribution (CC-BY) license (<https://creativecommons.org/licenses/by/4.0/deed.en>)

How to cite this article: Sasania, F., Nematzadeh, M., Asadi, M., Aminian, A. Thermo-mechanical behavior of high-strength concrete with nylon granule aggregates: experimental evaluation and predictive analysis. Civil Engineering and Applied Solutions. 2025;1(1): 1–35. doi:10.22080/ceas.2025.29200.1011.



replacement levels of 0, 10, and 20% of natural sand volume and reinforced with steel fibers at 0, 0.75, and 1.25%, under temperatures of 20, 300, and 600°C, demonstrated that increasing temperature results in significant degradation and reduction in the concrete's properties. The greatest decrease in compressive strength occurred after exposure to 600°C, with compressive strength and modulus of elasticity decreasing by 61 and 84%, respectively. In another study, Thomas and Chandra Gupta [4], investigating the performance of high-strength concrete (HSC) containing crumbed rubber for environmental benefits, reported that using crumb rubber (CR) particles as a partial substitute for concrete aggregates at volume fractions ranging from 0 to 20% is capable of producing concrete with compressive strengths of up to 60 MPa. On the other hand, Gupta et al. [5], in their investigation of the mechanical performance of rubber-containing concrete, showed that for 0.35, 0.4, and 0.55 water-to-cement (W/C) ratios, increased flowability of the fresh concrete was associated with improved compressive strength. In a study by Pelisser et al. [6], the effect of substituting 10% recycled rubber particles in HSC was reported, where only a 14% depletion in compressive strength was noticed compared to rubber-free concrete. Additionally, due to the lack of density of rubber aggregates, the specific weight of rubberized concrete decreased by 13% compared to ordinary concrete. Mousavimehr and Nematzadeh [7], through an experimental study on concrete incorporating crumb tire rubber exposed to high temperatures, reported that substituting 15% of natural fine aggregates with CR resulted in a 35% reduction in concrete specimens' compressive strength at ambient temperature compared to the control specimen. The greatest decrease in compressive strength was observed in the specimen with 30% CR content exposed to 400°C. Extensive studies at different replacement levels and particle sizes of crumb rubber have shown that, under a constant water-to-cement (W/C) ratio, increasing the amount of waste rubber particles leads to a drop in concrete specimens' compressive strength [8-10]. In this regard, Yilmaz and Degirmenci [11], investigating the effects of rubber aggregates on concrete, reported that all replacement levels of rubber aggregates used as a percentage of both fine and coarse aggregates leads to a drop in concrete compressive strength. However, increasing the particle size slightly decreased the water absorption of the concrete. Additionally, Nematzadeh and Mousavimehr [12], in their study on concrete containing CR and polyethylene terephthalate (PET) particles, reported that replacing 15% of natural aggregates with PET particles and 15% with CR led to a 40% drop in compressive strength relative to the control concrete specimens.

Nowadays, due to the significance of critical structures such as high-rise buildings, bridges, coastal structures, pavements, and industrial floors, high-strength concrete is widely used. HSC is a high-cement-content concrete with a dense internal structure and fine pores, typically produced using superplasticizers and silica fume powder [13]. The advantages of using HSC include improved compressive strength, reduced dead load, faster construction, and increased service life [14]. Singh et al. [15] conducted a study to evaluate the feasibility of using granite cutting waste (GCW) as a partial replacement for natural sand in HSC. The experimental results showed that replacing 25 to 40% of river sand with GCW positively affected compressive and flexural strength, abrasion resistance, permeability, and other durability indicators. The microstructural analysis confirmed these findings, revealing improvements in morphology and hydration processes within this replacement range. These results suggest that GCW is a sustainable material for partial sand replacement in concrete. In another study, Mohammad and Karim [16] investigated the impacts of using PET fibers on the mechanical behavior, initial crack impact resistance, and ultimate impact load capacity of HSC. PET fibers of varying lengths (10, 20, and 40 mm) and volume fractions (0.5, 0.75, 1.00, 1.25, and 1.5%) were added to the concrete, and 16 mix designs were tested. The findings indicated that using waste PET fibers can improve key properties of HSC and is recommended at up to 1.5% by volume.

Since the fire resistance of structural elements, particularly reinforced concrete (RC) members, is a key consideration in the design, evaluating the mechanical properties of concrete during fire exposure is crucial [17]. Accordingly, much research has been organized on the behavior of concrete and RC members under high temperatures and the detrimental impacts of heat on their structural and mechanical performance [18, 19]. Most of these studies concluded that adding small amounts of rubber or polymer aggregates to concrete mixtures slightly reduces the risk of explosive spalling at elevated temperatures. In one such study, Karimi and Nematzadeh [20] explored how concrete-filled steel tube (CFST) columns behave when incorporating recycled tire rubber, particularly emphasizing their response to thermal exposure. This aspect has received limited attention in previous research, restricting the broader use of rubberized concrete in such structural elements. The study involved high-strength concrete (HSC) cores encased in seamless steel tubes subjected to various temperatures (20, 250, 500, and 750 °C). Key variables included the replacement rate of sand with recycled tire rubber (0, 5, and 10%), steel fiber content (0, 1, and 1.5%), and the diameter-to-thickness (D/t) ratio of the steel tubes (43 and 25.4). The findings indicated that a 10% rubber replacement led to a 12% reduction in the compressive strength of the confined specimens. However, thermal treatment did not significantly influence this strength reduction. Increasing steel fiber content and tube thickness improved the stiffness and enhanced the ductility trend in most specimens. The optimal steel fiber content was identified as 1%, which, while having minimal impact on compressive strength, significantly improved the ductility and energy absorption of the specimens, especially those exposed to elevated temperatures. Strength reduction was minimal up to 250 °C, but greater strength and post-peak stress-strain slope losses were observed at higher temperatures. In another study, Guo et al. [21] investigated the impacts of elevated temperatures on concrete containing crumb tire rubber reinforced with steel fibers. They reported that replacing natural fine aggregates with varying amounts of crumb tire rubber reduced mechanical behaviors such as compressive strength and modulus of elasticity at 200, 400, and 600°C. The average compressive strength reductions were approximately 25, 50, and 84% compared to reference concrete for each temperature, respectively. Nematzadeh et al. [22] investigated the behavior of concrete incorporating steel fibers and PET waste when exposed to high temperatures, reporting a significant drop in compressive strength for the PET-modified concrete relative to the control mix. The inclusion of steel fibers, however, enhanced mechanical performance, partially offsetting the thermal damage. In a separate study, Gupta et al. [23] examined concrete specimens with more than 10% natural aggregates substituted by rubber aggregates. They observed that after being subjected to 750 °C for two hours, the specimens experienced such extensive damage that compressive strength testing could not be

conducted. Marques et al. [24] reported that rubberized concrete with 5, 10, and 15% replacement of natural fine aggregates by recycled rubber particles exhibited compressive strength reductions of 64, 67, and 85%, respectively, after exposure to 400, 600, and 800°C, compared to normal concrete at room temperature. Al-Mutairi et al. [25] studied the effect of microsilica addition on the compressive strength of concrete containing coarse and fine rubber aggregates at elevated temperatures and found that rubberized concrete strength could improve at temperatures above 150°C with the inclusion of up to 5% microsilica. Mousa [26] investigated the impacts of crumb rubber aggregates on the behavior of concrete specimens exposed to 300, 400, 600, and 800°C for 120 minutes. After testing, many visible cracks were observed on the surface of specimens containing 5% rubber aggregates. Furthermore, the loss in compressive strength in rubberized concrete was more pronounced compared to reference concrete specimens. In the study conducted by Nematzadeh et al. [27], the effects of steel fibers and carbon fiber-reinforced polymer (CFRP) sheets on the post-fire bond behavior of steel rebars embedded in HSC containing waste polyethylene terephthalate (WPET) were investigated. The results showed that CFRP sheets positively impacted the rebar pull-out debonding energy, while steel fibers exhibited this positive effect only at 600 °C. On the other hand, steel fibers did not compensate for the negative influence of polymer aggregates and altered the failure mode at different temperatures. These fibers generally reduced bond strength under most conditions, although smaller rebar diameters mitigated this negative effect. In another study, Nematzadeh et al. [28] explored the influence of steel fibers and crumb rubber aggregates on the shear behavior of HSC beams reinforced with glass fiber-reinforced polymer (GFRP) bars aimed at reducing reinforcement congestion in areas with dense bar arrangements. Thirty beam specimens were cast to evaluate the effects of GFRP reinforcement ratio, shear span-to-depth ratio, crumb rubber content, and steel fiber volume fraction on shear performance. Results indicated that increasing fiber content, concrete compressive strength, and GFRP reinforcement ratio improved the beams' shear capacity while increasing the shear span-to-depth ratio and crumb rubber content reduced it. It was also found that steel fibers had a greater influence in enhancing shear performance at higher crumb rubber percentages, shifting from shear to flexural failure mode.

In light of the aforementioned studies, and aiming to better understand and predict the properties of HSC containing NG aggregates, this research investigates the mechanical behavior of HSC with nylon granules after experiencing elevated temperatures. To achieve this, compressive performance parameters such as compressive strength, strain at peak stress, elastic modulus, ultimate strain, and stress-strain curves were analyzed. The main variables include the volumetric replacement ratio of nylon granules for natural fine aggregate (0, 10, and 20%) and the exposure temperature (20, 300, and 600 °C). The obtained compressive strengths were compared with values estimated using design codes, including ACI 216 [29], ASCE [30], EN 1994-1-2 [31], EN 1992-1-2 [32], and CEB-FIP [33].

## 2. Research significance

High-strength concrete is widely used in critical and large-scale structures such as towers, bridges, and tunnels due to its superior mechanical properties. However, exposure to elevated temperatures during fire incidents can significantly reduce its strength and durability. To promote sustainable construction and address durability concerns, this research examines how elevated temperatures influence the mechanical behavior and microstructure of high-strength concrete containing nylon granules, which partially substitute natural fine aggregates. The study involves substituting a portion of natural sand with these granules and assesses their effects on compressive strength, splitting tensile strength, and elastic modulus both at room temperature and after exposure to high temperatures. Beyond mechanical and post-fire performance, the study emphasizes the environmental benefits of using recycled nylon granules, such as reducing dependency on natural aggregates and mitigating environmental degradation caused by excessive natural aggregate extraction. Incorporating plastic waste into concrete promotes sustainable construction practices, reduces environmental pollution, and supports economic principles. This study aims to contribute to the innovation of environmentally friendly and heat-resistant concrete, which can be highly beneficial for modern construction applications. The methodology of this study is illustrated in Fig. 1.

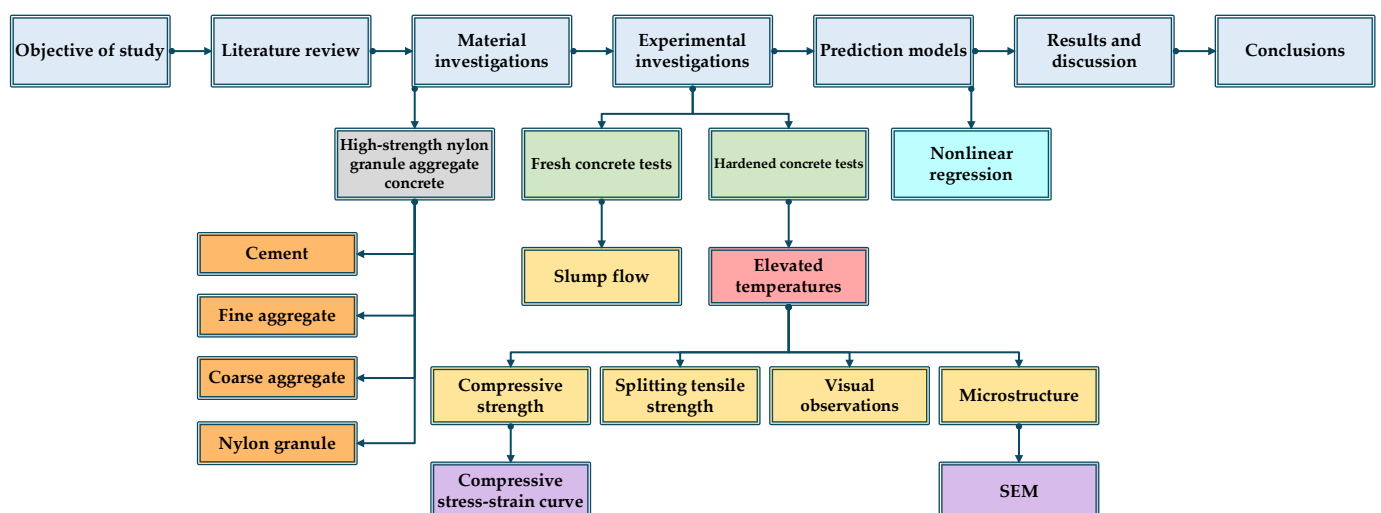


Fig. 1. Research methodology.

### 3. Experimental program

#### 3.1. Material properties

This study used Type II Portland cement (CEM II/A-LL 42.5 N) compliant with ASTM C150 [34]. The physical and chemical properties of the cement composition provided by the manufacturer are presented in Table 1. Crushed dolomitic stone was used as the natural coarse aggregate, with a specific gravity of 2.66 gr/cm<sup>3</sup>, water absorption of 0.7%, and a maximum particle size of 12.5 mm. Additionally, natural fine aggregates with a fineness modulus of 2.77, a specific gravity of 2.63 gr/cm<sup>3</sup>, and a water absorption rate of 1.65% were used. Fig. 2 shows the particle size distribution of natural fine and coarse aggregates based on the requirements of ASTM C33 [35]. The percentage passing of aggregates through different sieves is presented in Table 2.

**Table 1. Chemical, physical, and mechanical properties of Type II portland cement.**

Chemical properties	Type II portland cement (CEM II/A-LL 42.5 N)	
	(wt.%)	
Silicon dioxide (SiO <sub>2</sub> )	20.7	
Aluminium oxide (Al <sub>2</sub> O <sub>3</sub> )	5.2	
Ferric oxide (Fe <sub>2</sub> O <sub>3</sub> )	4.6	
Calcium oxide (CaO)	65	
Magnesium oxide (MgO)	1.8	
Sulfur trioxide (SO <sub>3</sub> )	2.2	
	0.5	
Sodium oxide (Na <sub>2</sub> O)	0.15	
Free calcium oxide (Free CaO)	1.3	
Loss on ignition (L.O.I)	1	
Insoluble residue (In.R)	0.4	
Tricalcium silicate (C <sub>3</sub> S)	59.47	
Dicalcium silicate (C <sub>2</sub> S)	14.48	
Tricalcium aluminate (C <sub>3</sub> A)	6	
Tetracalcium aluminoferrite (C <sub>4</sub> AF)	14	
Physical properties	Type II portland cement (CEM II/A-LL 42.5 N)	
	Autoclave expansion (%)	
	0.08	
	Specific surface (cm <sup>2</sup> /gr)	
	32	
Mechanical properties	Type II portland cement (CEM II/A-LL 42.5 N)	
	3 days	
	26.47	
Compressive strength (MPa)	7 days	
	43.14	
	28 days	
	51.97	

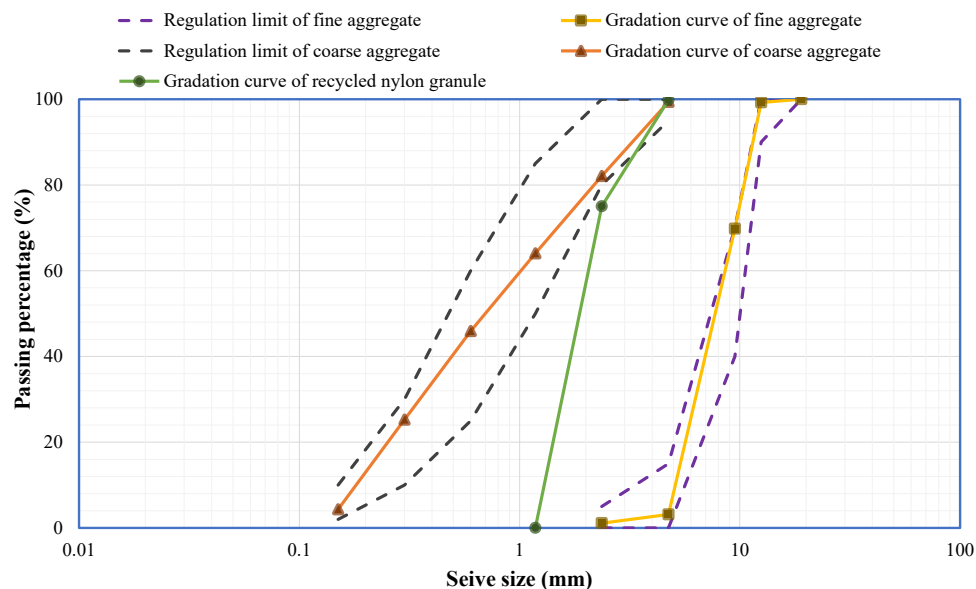


**Fig. 2. Particle size distributions of fine and coarse aggregates according to ASTM C33 [35].**



**Table 2. Classification of aggregates.**

Sieve size	Coarse aggregate		Sand aggregate		Nylon granule
	ASTM C33 [35] Min-Max	Passing percentage (%)	ASTM C33 [35] Min-Max	Passing percentage (%)	Passing percentage (%)
¾ inch (19 mm)	100	100	100	100	100
½ inch (12.5 mm)	90-100	99	100	100	100
3/8 inch (9.5 mm)	40-70	69	100	100	100
No. 4 (4.75 mm)	0-15	3	95-100	99	99
No. 8 (2.36 mm)	0-5	1	80-100	82	75
No. 16 (1.18 mm)	-	-	50-85	64	-
No. 30 (0.6 mm)	-	-	25-60	45	-
No. 50 (0.3 mm)	-	-	5-30	25	-
No. 100 (0.15 mm)	-	-	0-10	4	-

In this study, granulated nylon particles were produced by recycling plastic nylon bags and subsequently used as a partial replacement for natural fine aggregates in the concrete mix. The size and shape of the NGs are shown in Fig. 3. The specific gravity of the NGs, determined according to ASTM C128 [36], was found to be 0.84. The thermal gravimetric analysis (TGA) curve for the NGs is presented in Fig. 4, which shows that the material loses approximately 90% of its mass at 600°C. It is also observed that the degradation temperature is 447.8°C. However, as a thermoplastic, the melting point of the nylon granules is significantly lower than their decomposition temperature. The silica fume powder used in this study was of type MK.A102 in powdered form. It was added to the concrete mix at 10% of the cement weight. Table 3 provides the chemical composition and physical properties of the micro-silica powder.

**Fig. 3. Shape and dimensions of recycled nylon granules.****Table 3. Chemical and physical properties of silica fume.**

Chemical properties	Silica fume (MK.A102)
	(wt.%)
Silicon dioxide (SiO <sub>2</sub> )	≤ 95
Aluminium oxide (Al <sub>2</sub> O <sub>3</sub> )	0.6
Ferric oxide (Fe <sub>2</sub> O <sub>3</sub> )	1.2
Calcium oxide (CaO)	0.5
Magnesium oxide (MgO)	0.6
Potassium oxide (K <sub>2</sub> O)	0.4
Sodium oxide (Na <sub>2</sub> O)	0.7
Loss on ignition (L.O.I)	1.5 – 2.5
Moisture	0.4
<b>Physical properties</b>	
Specific gravity (g/cm <sup>3</sup> )	2.2
Specific surface (m <sup>2</sup> /g)	15
Bulk density (kg/m <sup>3</sup> )	350
Mean particle size (mic)	0.6
pH	8

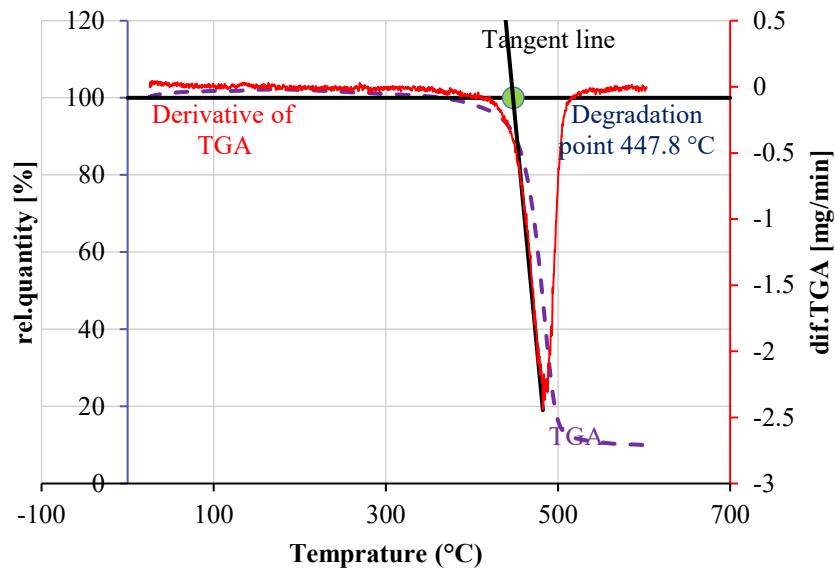


Fig. 4. Thermal gravimetric analysis (TGA).

In this study, a polycarboxylate ether-based superplasticizer (SP), commercially known as PCE-SR5, with a solid content of 42% and a specific gravity of 1.03 gr/cm<sup>3</sup>, was used in all concrete mix designs at 0.8% by mass of cement. The superplasticizer was employed to improve the dispersion of pozzolanic materials throughout the concrete mix, achieve good workability, and enhance both early and final compressive strengths. The properties of the superplasticizer additive are presented in Table 4.

Table 4. Superplasticizer properties.

Name	Appearance	Chemical mixture	Ionic nature	PPM	Density	Freezing temperatures
PCE-SR5	Light brown liquid	Modified polycarboxylic acid copolymers	Anionic	500 MAX	1.03 g/cm <sup>3</sup>	About -2°C

### 3.2. Concrete mix design and specimen preparation

This study developed three mix designs for high-strength concrete HSC incorporating nylon granules, as presented in Table 5. To prepare the concrete, natural coarse and fine aggregates were first mixed in a concrete mixer for 1 minute. Then, cement and silica fume powder were added and mixed for an additional minute. Afterward, a premixed solution of water and superplasticizer was gradually introduced into the mixer and blended with the dry materials for 3 minutes. In the mixes containing nylon granules, these particles were added to the mixer along with the natural aggregates. A total of 54 cylindrical concrete specimens with a diameter of 100 mm and a height of 200 mm were cast to evaluate the compressive behavior of HSC containing NG after exposure to elevated temperatures. To minimize experimental error, three identical specimens were prepared and tested for each group. The three mix designs incorporated nylon granules as a partial volumetric replacement for natural fine aggregates at 0, 10, and 20% replacement levels. A constant water-to-cement ratio (W/C) of 0.31 was used across all mixes. The mix proportions per cubic meter were determined in accordance with ACI 211.1 [37] and are detailed in Table 5.

Table 5. Proportions of mix components.

Mix No.	Mix ID	Coarse agg.	Fine agg.	Nylon granule (kg/m <sup>3</sup> )	Cement	Silica fume	Water	W/C	SP* (%)	Slump (mm)
1	HSC-NG0®	951	437	0	564	63	212	0.31	0.8	80
2	HSC-NG10	951	379	14	564	63	212	0.31	0.8	100
3	HSC-NG20	951	321	28	564	63	212	0.31	0.8	110

\* Percentage of total weight of cementitious material.

In this study, the slump test was conducted to evaluate the workability and flowability of fresh concrete in accordance with ASTM C143 [38]. The procedure involved placing the fresh concrete into a slump cone in three layers. Each layer was compacted with 25 blows using a tamping rod to ensure uniformity and eliminate air voids. Subsequently, the cone was lifted vertically, and the fresh concrete slump was determined by comparing the settled concrete's height to the cone's height. It is important to note that the tamping rod penetrated into the underlying layers during compaction. As mentioned in Table 5, a specific amount of superplasticizer was added to each mix to ensure proper workability. The measured slump values ranged from 80 to 110 mm. It was observed that the workability and flowability of the fresh concrete increased with the NGs addition. This improvement is attributed to the deformability and non-absorbent nature of nylon granules compared to natural sand. After casting, the concrete was compacted using a vibrating table to further reduce air entrapment and enhance homogeneity. All mixing, casting, and testing procedures were performed at a room temperature of 20°C. After 48 hours, the concrete specimens were demolded according to ASTM C192 [39].

The demolded specimens were then cured in a lime-saturated water solution for a minimum of 27 days, also in accordance with ASTM C192 [39].

For identification purposes, codes were assigned to each concrete mix. As shown in Table 5, "NG0" represents the control high-strength concrete with no nylon granules, while the numbers following "NG" indicate the percentage of nylon granules used as a volumetric replacement for natural fine aggregate. For heat-exposed specimens, additional labels such as T20, T300, and T600 were added to the codes, indicating the temperature in °C to which the specimens were subjected. For example, "HSC-NG20-T600" refers to a high-strength concrete specimen containing 20% nylon granules exposed to a high temperature of 600°C. A selection of hardened manufactured concrete cylinder specimens is shown in Fig. 5.



Fig. 5. A view of some hardened concrete specimens.

### 3.3. Thermal exposure

Each concrete mix group was subjected to three temperature levels: 20°C (ambient temperature), 300°C, and 600°C, with the latter two representing elevated temperature conditions. Thermal exposure was carried out using an electric furnace. Prior to exposure, all specimens were pre-heated at 60°C for 24 hours in accordance with ISO 834 [40] to remove surface moisture and ensure uniform initial conditions. Immediately after reaching 60°C, the specimens were heated to the target temperatures of 300°C and 600°C. The specimens were maintained at each target temperature for 1 hour. Following thermal exposure, the furnace vents were partially opened to accelerate cooling, and the specimens were left inside the furnace until they reached ambient temperature. During the heating process, thermocouples installed on the furnace's interior walls recorded the furnace temperature, while additional thermocouples embedded in the center of the specimens measured the concrete's internal temperature. Fig. 6 illustrates the time-temperature curve for both the specimen core and furnace environment at 300 and 600°C.

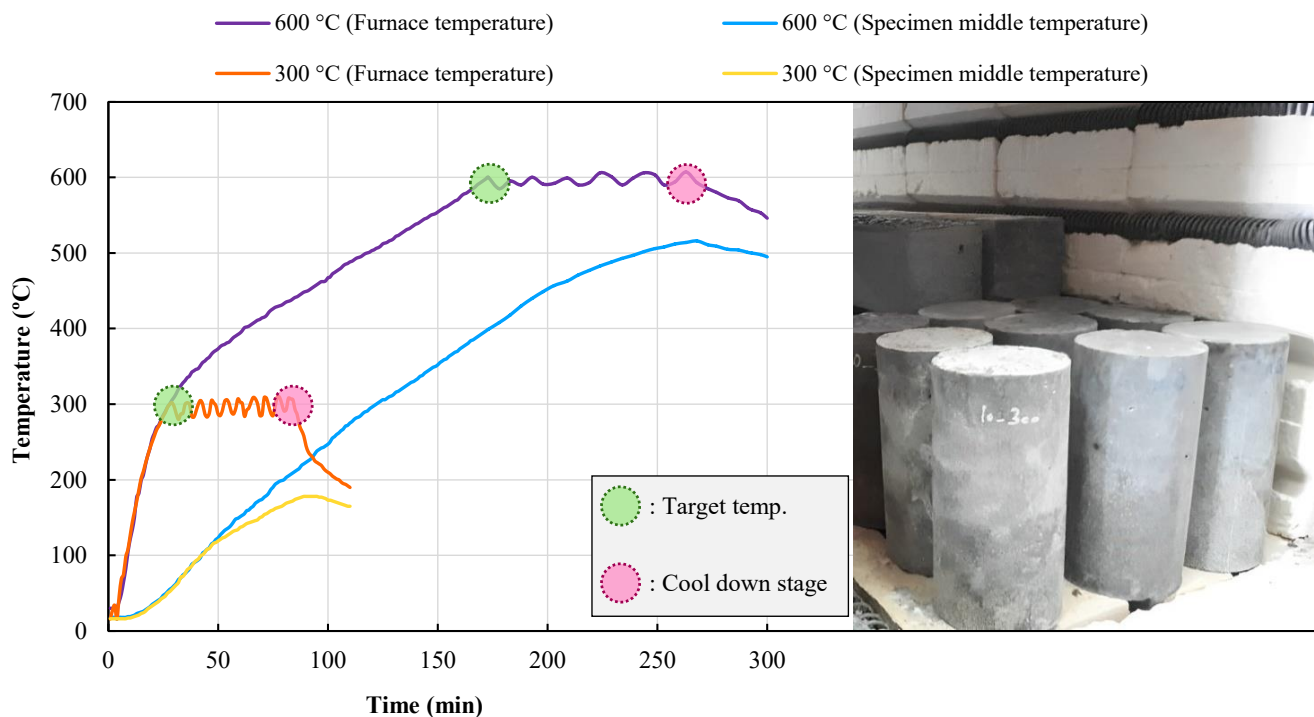


Fig. 6. Temperature variations in and out of concrete specimens.

Due to moisture loss and surface cracking caused by high temperatures, the concrete tends to reabsorb moisture from the environment upon cooling and removal from the furnace. This post-exposure rehydration leads to volumetric expansion and increased crack widths, ultimately reducing the heat-exposed specimens' mechanical strength. According to literature studies [41, 42], the specimens were stored at room temperature for a minimum of 10 days before mechanical testing to stabilize moisture content and microstructure. This procedure aligns with ACI 216 [29], which recommends a minimum post-exposure conditioning period of six days. After this period, compressive and splitting tensile strength tests were conducted under axial loading conditions. The overall procedure for specimen preparation and their exposure to elevated temperatures is illustrated in Fig. 7.



Fig. 7. High-strength nylon granule aggregate concrete manufacturing steps.

### 3.4. Testing Procedure

#### 3.4.1. Compressive strength test

After 28 days of curing, the concrete cylindrical specimens were evaluated for compressive strength according to ASTM C39 [43], following the procedures outlined in ASTM C192 [39]. The testing apparatus used in this experiment, along with the concrete cylindrical specimen (100×200 mm), is shown in Fig. 8. The standard loading rate is within the range of 0.2 MPa/s to 0.3 MPa/s, and in this study, a loading rate of 0.25 MPa/s was used for the cylindrical specimens. Two thin wooden sheets were used to prevent stress concentration caused by the surface roughness of the specimens and achieve better axial compressive load distribution. As illustrated in Fig. 8, the cylindrical specimen's axial deformation was measured using two Linear Variable Differential Transformers (LVDTs), which were symmetrically attached to the specimen using a setup consisting of two steel rings. The final data for axial deformation were obtained by averaging the readings from the two LVDTs. The data related to load and displacement were used to plot the axial compressive stress-strain curve for the HSC cylindrical specimens containing NGs, both before and after exposure to elevated temperatures.

#### 3.4.2. Splitting tensile strength test

After 28 days of curing the concrete cylindrical specimens in accordance with ASTM C192 [39], the splitting tensile strength test was conducted on the concrete cylinders based on ASTM C496 [44]. The standard loading rate ranges from 0.7 MPa/min to 1.4 MPa/min, and in this study, a loading rate of 1.15 MPa/min was used for the concrete cylindrical specimens. Similar to the compressive strength test, a thin wooden sheet was placed at the loading surface to ensure uniform load distribution.

#### 3.4.3. Modulus of elasticity test

The initial elastic modulus of the concrete cylindrical specimens was determined from the slope of the axial compressive stress-strain curve at the beginning of axial compressive loading. Therefore, two LVDTs were used to obtain deformation data alongside the load measurements to plot the stress-strain curve. Additionally, the secant modulus of elasticity was determined according to ASTM C469 [45], using the chord slope drawn on the stress-strain curve between the strain point of 50  $\mu\epsilon$  and the stress level corresponding to 40% of the material's compressive strength.



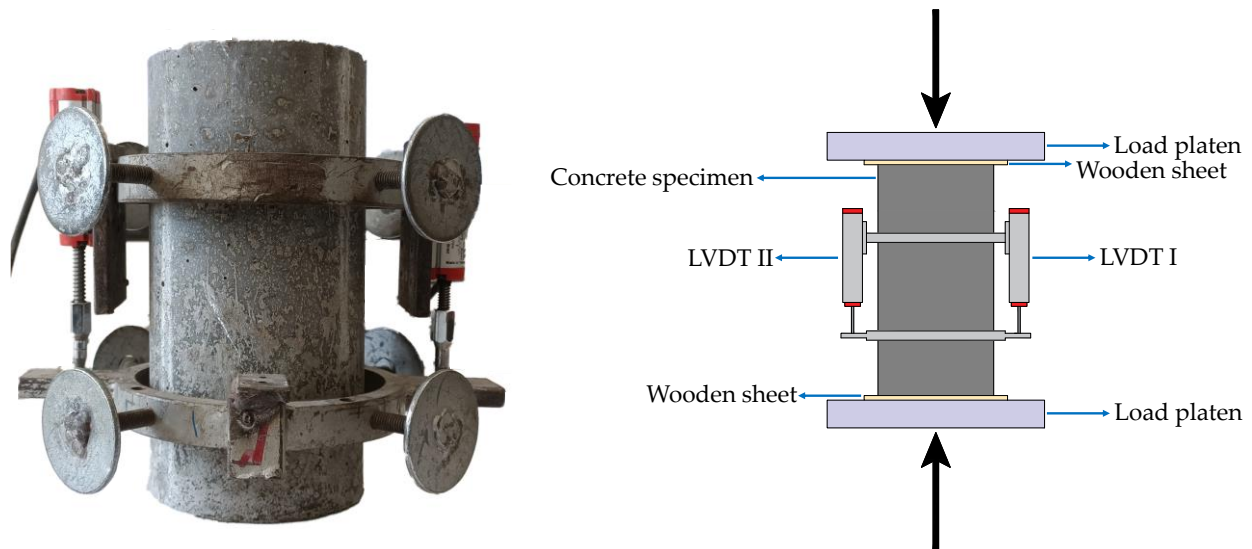


Fig. 8. Axial compressive stress–strain test setup.

## 4. Results and discussion

### 4.1. Loss of weight

High temperatures can have severely detrimental effects on the mechanical properties and durability of concrete specimens. One such effect is the weight loss of concrete specimens after exposure to elevated temperatures. This is particularly significant in the present study, as nylon granules with a decomposition temperature of  $447.8^{\circ}\text{C}$  were used in the specimen preparation. According to the thermal gravimetric analysis curve presented in Fig. 4, nylon granules lose approximately 90% of their mass at  $600^{\circ}\text{C}$ . Therefore, the specimens were weighed before and after the heat treatment and the weight loss percentage was calculated. The percentage of weight loss is presented in Fig. 9, which shows that the weight loss increases with rising temperature. As illustrated in Fig. 9, the specimens exposed to  $300^{\circ}\text{C}$  and  $600^{\circ}\text{C}$  exhibited approximately 2 and 8% weight loss, respectively, compared to the reference specimens (at ambient temperature). The weight loss at  $300^{\circ}\text{C}$  is primarily attributed to the evaporation of surface and physically bound water from the concrete specimens after exposure to high temperatures [46-48]. Additionally, the water within the calcium silicate hydrate (C-S-H) gel begins to be released at around  $150^{\circ}\text{C}$ , marking the initial stage of C-S-H decomposition. As the temperature increases to about  $300^{\circ}\text{C}$ , a significant reduction in specimen weight is observed. This is mainly due to the decomposition of calcium hydroxide (CH) crystals, continued release of water from the C-S-H gel, evaporation of water from capillary pores, partial decomposition of nylon granules, and the release of physically absorbed water. Upon further temperature increase to  $600^{\circ}\text{C}$ , there is a sharp decline in specimen weight. This notable reduction is due to the near-complete decomposition of the nylon granules within this temperature range. Given that the decomposition temperature of nylon granules is approximately  $447.8^{\circ}\text{C}$ , at  $600^{\circ}\text{C}$ , the granules decompose entirely and evaporate through the existing pores and microcracks in the concrete. The weight loss was such that, compared to specimens exposed to  $20^{\circ}\text{C}$ , those with 10% nylon granule replacement experienced approximately 3 and 10% weight loss at  $300^{\circ}\text{C}$  and  $600^{\circ}\text{C}$ , respectively, and specimens with 20% nylon replacement showed approximately 4 and 11% weight loss at the same temperatures. Overall, the specimens without nylon replacement at room temperature and those with 20% nylon replacement at  $600^{\circ}\text{C}$  exhibited the lowest (approximately 2%) and highest (approximately 11%) weight loss, respectively.

### 4.2. Compressive strength

Compressive strength in concrete materials is one of the most critical criteria for evaluating their mechanical performance. The compressive strength results of all high-strength concrete HSC cylindrical specimens containing NG exposed to elevated temperatures are presented in Fig. 10 and Table 6. According to Table 6, the compressive strength of HSC specimens containing NG, before and after exposure to high temperatures, ranged approximately from 21 MPa to 83 MPa. As shown in Fig. 10, the reference specimen without nylon granules at room temperature had the highest compressive strength. On the other hand, the results indicate that replacing 10 and 20% of natural fine aggregate with NG in unheated specimens led to a reduction in compressive strength of 25.2 and 59.2%, respectively. These findings show that including nylon granules reduces compressive strength, with the most significant reduction observed in specimens where 20% of the natural fine aggregate was replaced with NG. This decrease in strength is attributed to the fact that nylon granules are much softer and more flexible than natural fine aggregates when in contact with cement paste. As a result, cracks form more readily around the NG particles under axial compressive loading, weakening the material. Another contributing factor to the reduction in compressive strength could be the insufficient bond between the ductile nylon granules and the cement paste, leading to stress concentrations in the interfacial transition zone (ITZ) [49]. Compared to natural aggregates, nylon granules are more deformable and have smoother surfaces, behaving like voids within the concrete matrix. Additionally, NG has a lower density than natural fine aggregates, which disrupts the overall structure of the concrete aggregates and ultimately contributes to the reduction in compressive strength.

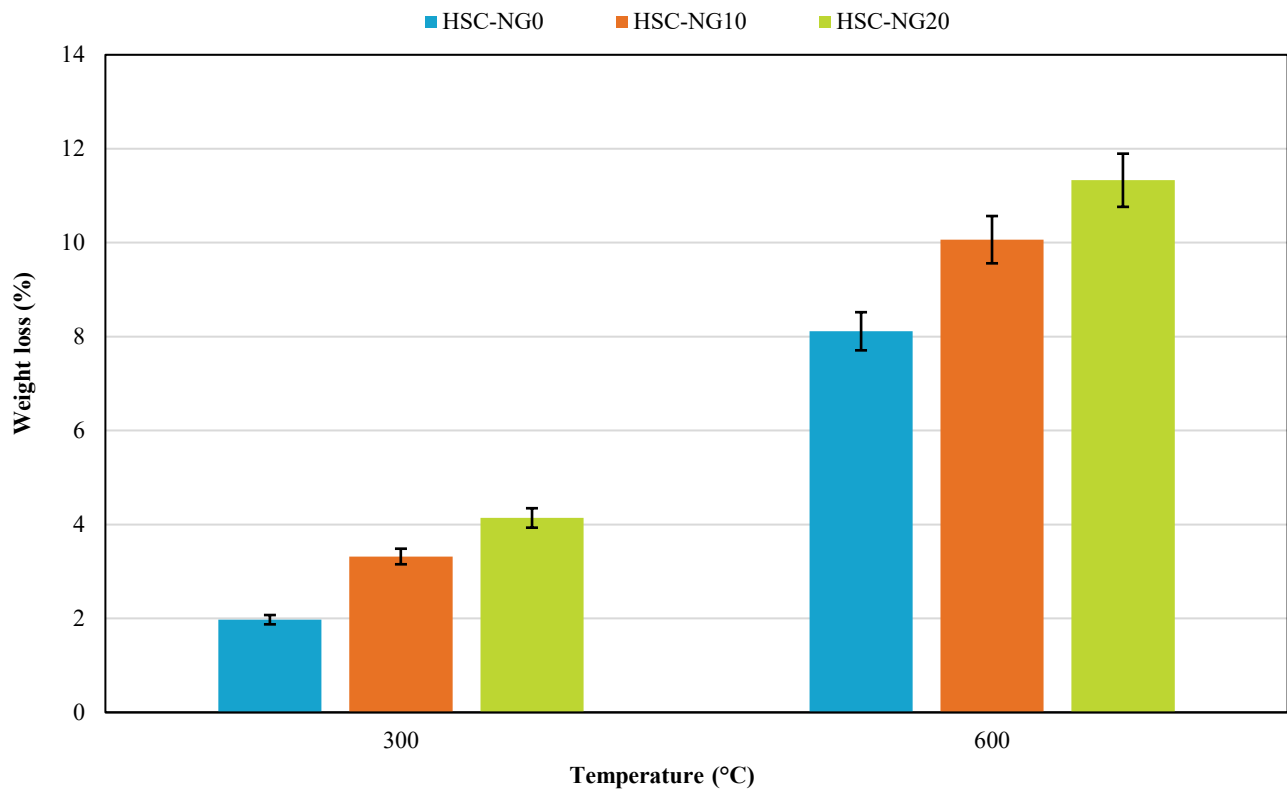


**Fig. 9. Percentage of specimen weight loss in terms of elevated temperatures.**

After exposure to high temperatures, the compressive strength of all groups significantly decreased. For instance, applying a temperature of 300 °C to specimens without NG resulted in a 25.2% reduction in strength compared to the same specimens at 20 °C. This reduction can be attributed to the loss of free and chemically bound water in the C-S-H gel, which leads to internal stresses and surface microcracking [50]. Furthermore, the compressive strength reductions for specimens HSC-NG0, HSC-NG10, and HSC-NG20 after exposure to 300 °C, compared to their counterparts at 20 °C, were 25.2, 12.2, and 11%, respectively. The majority of compressive strength loss occurred between 20 and 300 °C. In contrast, in the temperature range of 300 to 600 °C, the reductions in compressive strength for specimens HSC-NG0, HSC-NG10, and HSC-NG20 were 59.2, 65.2, and 63.6%, respectively, compared to those at 20 °C. Based on these results, specimens with 20% NG replacement exhibited less compressive strength loss at room temperature compared to the other groups. In addition to the aforementioned causes, dehydration (i.e., evaporation of chemically bound water from CH) also plays a significant role in the reduction of strength. At 600 °C, the nylon granules exceed their melting point, causing them to shrink and lose up to 90% of their mass. This results in increased porosity in the concrete matrix and ultimately reduces the strength of heat-exposed concrete specimens [48, 51]. Overall, the results presented in Fig. 10 and Table 6 indicate that using NG reduces concrete compressive strength. Interestingly, this reduction is less severe for the 20% NG replacement than the 10% replacement at high temperatures. However, the compressive strength loss for specimens containing 10% NG appears to stabilize at temperatures above 300 °C. Moreover, using up to 10% NG replacement with natural fine aggregates seems to offer a suitable balance between environmental and structural performance goals.

**Table 6. Mechanical properties experimental results of specimens at elevated temperatures.**

Specimen ID	Temperature (°C)	Compressive strength (MPa)		Splitting tensile strength (MPa)		Initial modulus of elasticity (GPa)		Secant modulus of elasticity (GPa)	
		Mean in MPa	CV (%)	Mean in MPa	CV (%)	Mean in GPa	CV (%)	Mean in GPa	CV (%)
HSC-NG0®	20	83.3 (-)	3.2	6.1 (-)	1.9	48.0 (-)	12.7	39.2 (-)	10.6
	300	62.3 (-)	1.0	5.0 (-)	7.0	44.7 (-)	11.3	34.8 (-)	8.7
	600	33.9 (-)	5.8	2.1 (-)	3.3	12.1 (-)	8.2	9.3 (-)	5.9
HSC-NG10	20	64.0 (-23.2 %)	3.4	4.9 (-19.7 %)	4.5	42.5 (-11.5 %)	9.3	33.5 (-14.5 %)	10.8
	300	56.2 (-9.8 %)	8.5	4.5 (-10 %)	11.4	41.3 (-7.6 %)	8.1	31.2 (-10.3 %)	11.0
	600	22.3 (-34.2 %)	9.4	2.0 (-4.8 %)	8.0	10.3 (-14.9 %)	7.6	8.14 (-12.5 %)	7.1
HSC-NG20	20	57.7 (-30.7 %)	2.3	4.6 (-24.6 %)	7.4	41.1 (-14.4 %)	8.9	31.2 (-20.4 %)	8.4
	300	51.4 (-17.5 %)	8.9	4.2 (-16 %)	7.3	38.1 (-14.8 %)	9.7	27.7 (-20.4 %)	8.8
	600	21.0 (-38 %)	3.0	1.6 (-23.8 %)	7.1	9.6 (-20.7 %)	9.1	7.8 (-16.1 %)	8.9

Note: The numbers in the parentheses show the percentage of increase or decrease in the concrete specimens' mechanical properties compared to the reference specimens (without nylon granule).



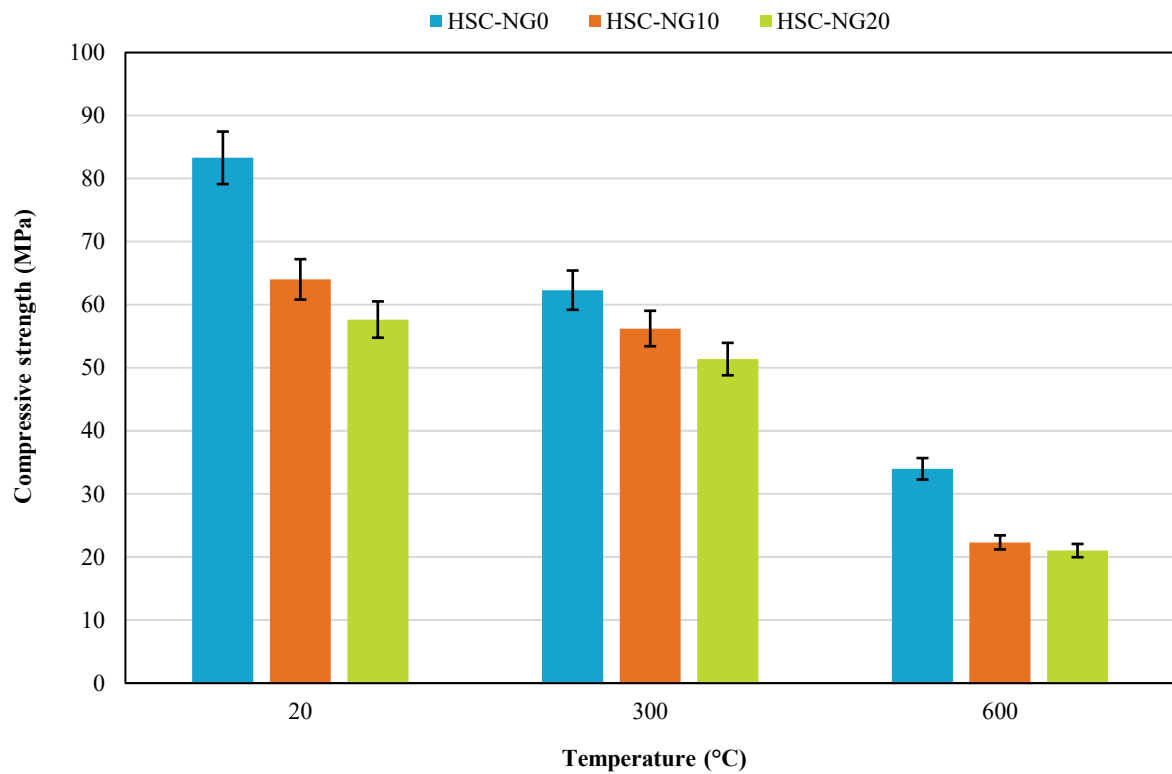


**Fig. 10. Compressive strength of specimens before and after exposure to elevated temperatures.**

The normalized compressive strength is defined as the ratio of the compressive strength of a specimen exposed to a target temperature ( $f_{c(G,T)}$ ) to the compressive strength of the specimen at 20 °C ( $f_{c(0,20)}$ ). Fig. 11 shows the values of normalized compressive strength as a function of temperature based on ACI 216 [29], ASCE [30] and EN 1994-1-2 [31]. This figure generally indicates that these codes provide reasonably accurate estimates of the normalized compressive strength values for the tested specimens. Furthermore, it appears that the presented experimental results closely align with the relationships proposed in the regulations.

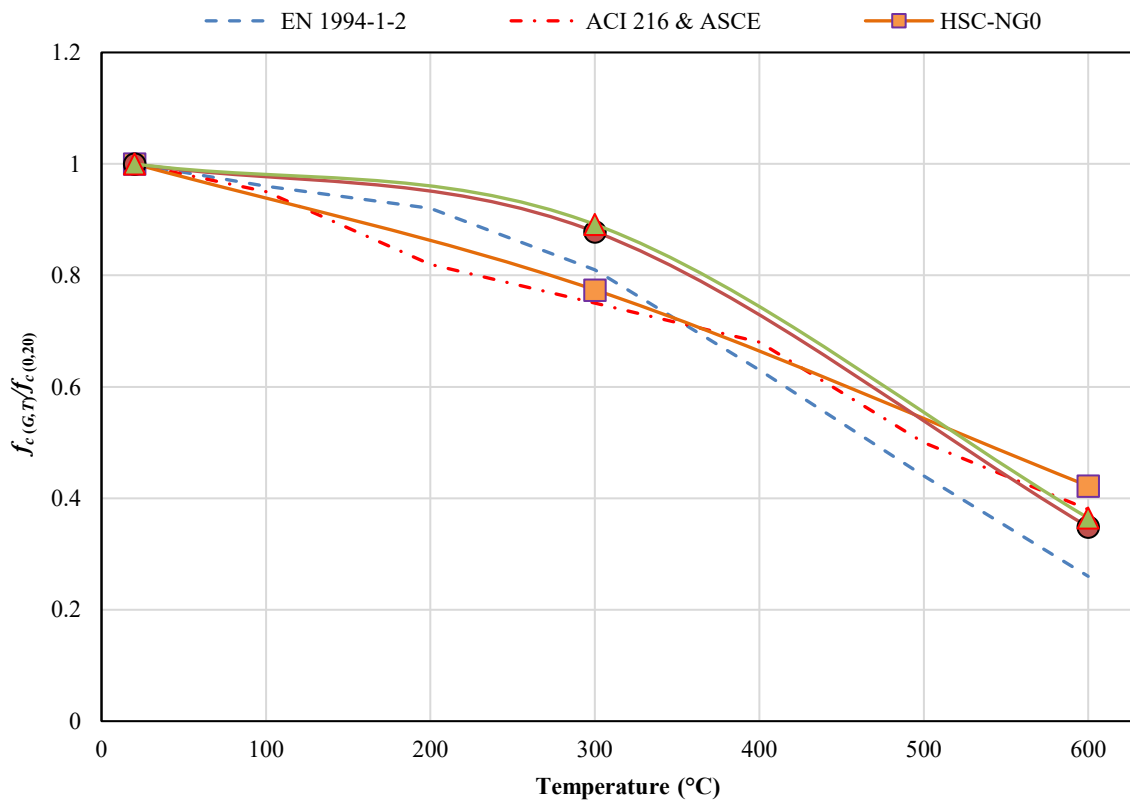


**Fig. 11. Normalized compressive strength of concrete specimens in terms of temperature.**

Using nonlinear regression analysis, Eq. 1 was developed to determine the compressive strength of specimens containing nylon granules exposed to elevated temperatures. In this equation,  $T$  represents the target temperature in degrees Celsius,  $T'$  is the temperature ratio, and  $G$  is the percentage of nylon granule replacement. Fig. 12 illustrates the trend of changes in normalized compressive strength concerning these parameters.

$$\frac{f_{c(G,T)}}{f_{c(0,20)}} = (-0.497T'^2 - 0.769T' + 1) + (-0.0591T'^2 + 0.0469T' - 0.0151)G$$

$$T' = \frac{T-20}{1000}$$
(1)

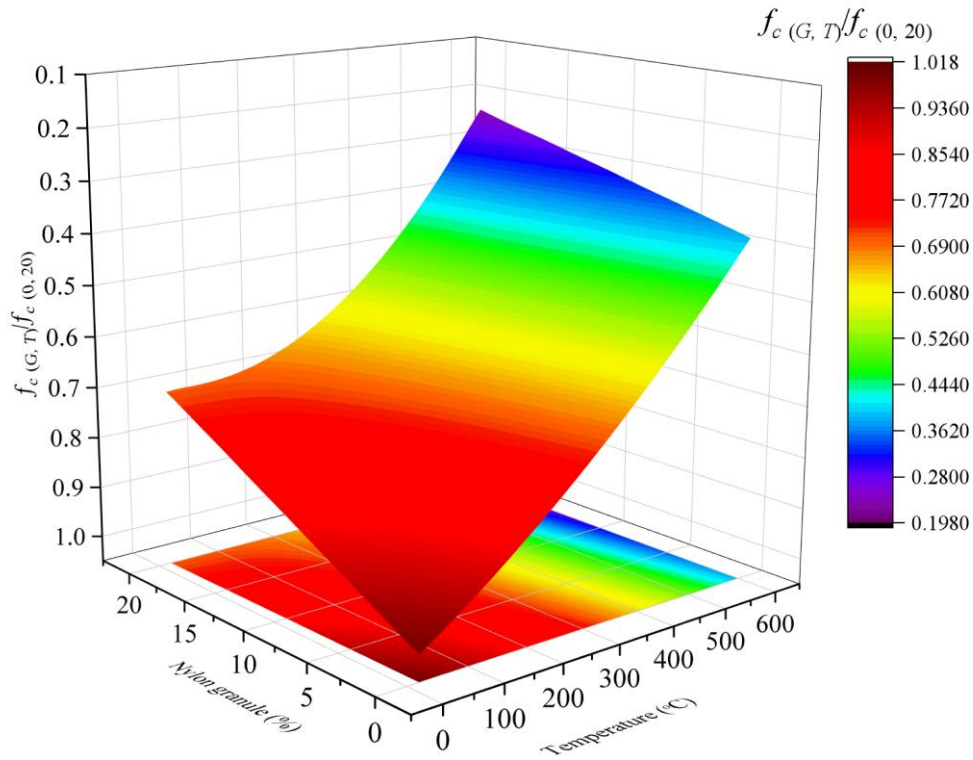


Fig. 12. Normalized compressive strength contour based on Eq. 1.

Based on the developed equation and the experimental data, several statistical performance indicators were used to evaluate the equation's accuracy. These indicators include the coefficient of correlation ( $R$ ), coefficient of determination ( $R^2$ ), mean squared error (MSE), root mean squared error (RMSE), mean absolute error (MAE), and coefficient of variation (CV). The equations for these statistical performance indicators are presented in Eqs. 2 to 6.

$$R = \frac{\sum_{i=1}^n (m_i - \bar{m})(t_i - \bar{t})}{\sqrt{\sum_{i=1}^n (m_i - \bar{m})^2 \sum_{i=1}^n (t_i - \bar{t})^2}}$$
(2)

$$R^2 = \frac{\sum_{i=1}^n (m_i - \bar{m})^2}{\sum_{i=1}^n (t_i - \bar{t})^2}$$
(3)

$$MSE = \frac{\sum_{i=1}^n (m_i - t_i)^2}{n}$$
(4)

$$RMSE = \sqrt{\frac{\sum_{i=1}^n (m_i - t_i)^2}{n}}$$
(5)

$$MAE = \frac{\sum_{i=1}^n |m_i - t_i|}{n}$$
(6)

In these equations,  $n$  represents the number of input specimens used;  $m_i$  and  $t_i$  are the predicted and experimental values for the  $i^{th}$  specimen, respectively. Additionally,  $\bar{m}$  and  $\bar{t}$  represent the mean of the predicted results and the mean of the experimental values, respectively. Table 7 summarizes the statistical performance indicators of Eq. 1 compared to the experimental results. According to the performance indicators listed in Table 7, the proposed Eq. 1 has successfully predicted the normalized compressive strength of the specimens with suitable accuracy.

Table 7. Statistical performance indicators results of Eq. 1.

R	R <sup>2</sup>	MAE	MSE	RMSE	Mean*	CV*(%)
0.997	0.995	0.0122	0.000309	0.0176	0.999	2.715

\* Calculated for the predicted to experimental results ratio

Fig. 13 is presented to better understand the proposed relationship and compare it with the experimental data from this study as well as other studies in the literature (on concrete specimens containing recycled aggregates). The proposed relationship provides a relatively accurate estimation of the experimental results from other researchers [4, 52, 53].

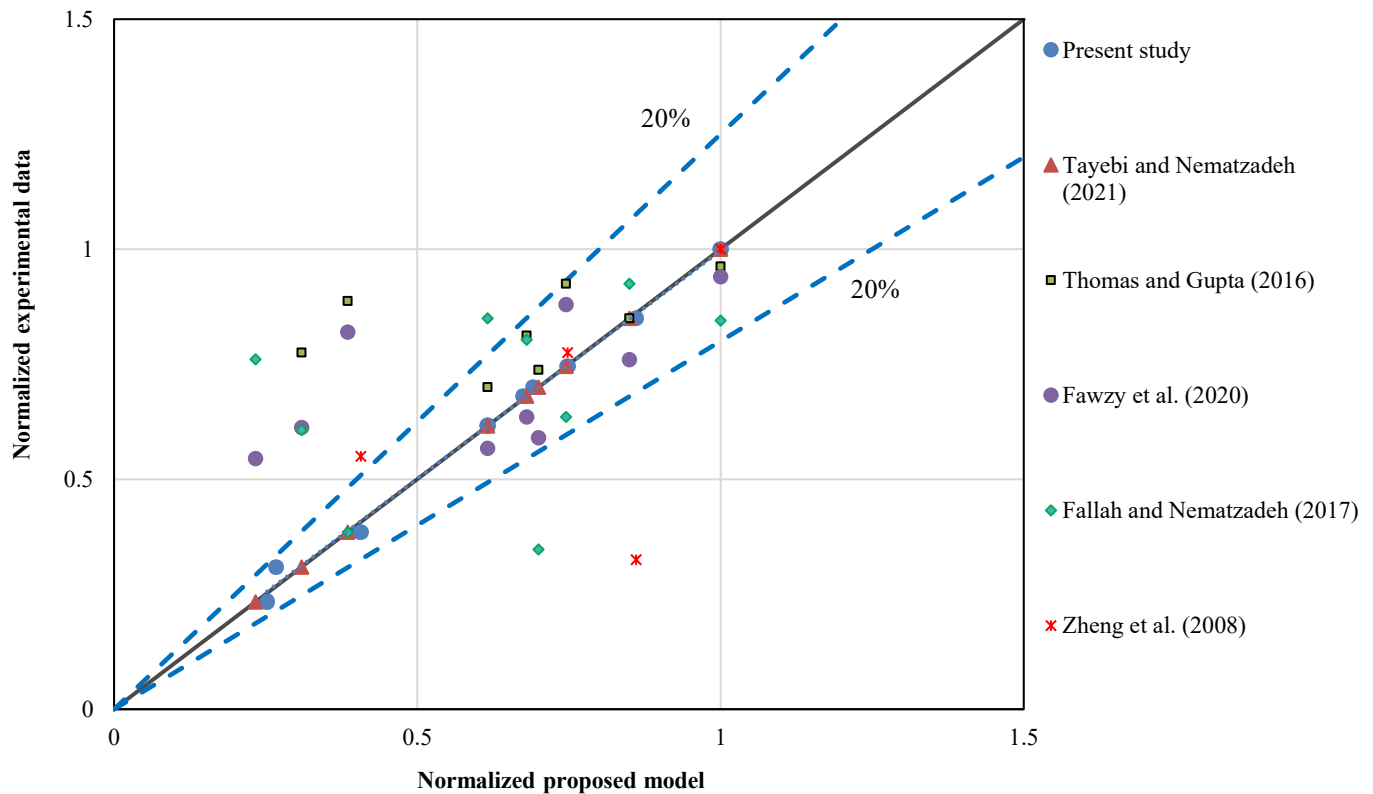


Fig. 13. Comparison of experimental data reported by different researchers with the equation proposed for compressive strength.

#### 4.3. Splitting tensile strength

Splitting tensile strength is one of the most important mechanical properties of concrete, indicating the material's ability to resist indirect tensile forces. The results of the splitting tensile strength tests for all HSC cylindrical specimens containing NGs exposed to elevated temperatures are shown in Fig. 14 and Table 6. According to Table 6, the splitting tensile strength of the HSC specimens containing NG before and after exposure to elevated temperatures ranged from approximately 2 to 6 MPa. Similar to the compressive strength behavior, increasing both the exposure temperature and the nylon granule replacement percentage reduced the splitting tensile strength.

At room temperature, the splitting tensile strength of the HSC-NG10 and HSC-NG20 specimens decreased by 19.7 and 24.6%, respectively, compared to the reference specimen (without nylon granules). One reason for this reduction, similar to the compressive strength drop, is poor bonding between the nylon aggregates and the cement paste. Micro-cracks tend to form at the interface between the nylon granules and the paste, which accelerates the failure of the concrete. For nylon granules to contribute positively to splitting tensile strength, the bonding force between the granules and cement paste must exceed the force required to tear them, which is not the case in practice. Additionally, unlike natural fine aggregates, nylon granules have very smooth and non-porous surfaces, which interferes with aggregate interlocking and ultimately reduces both compressive and splitting tensile strength.

Upon exposure to 300°C, all specimens exhibited reduced splitting tensile strength. Specifically, the HSC-NG0, HSC-NG10, and HSC-NG20 specimens experienced decreases of 18, 8.2, and 8.7%, respectively. This reduction can be attributed to the formation of surface microcracks, internal stresses, and the chemical decomposition of the C-S-H gel at elevated temperatures. At 600°C, the strength loss peaked. The reductions in splitting tensile strength for the HSC-NG0, HSC-NG10, and HSC-NG20 specimens were 65.6, 59.2, and 65.2%, respectively, compared to their counterparts at 20°C. Notably, the 10% NG replacement specimens showed less tensile strength reduction compared to the other groups, suggesting some relative resilience under thermal exposure.

The normalized splitting tensile strength is defined as the ratio of the splitting tensile strength of a specimen exposed to a target temperature ( $f_{t(G,T)}$ ) to the splitting tensile strength of the specimen at 20 °C ( $f_{t(0,20)}$ ). Fig. 15 shows the values of normalized splitting tensile strength as a function of temperature based on EN 1994-1-2 [31]. This figure generally indicates that these codes provide reasonably accurate estimates of the tested specimens' normalized splitting tensile strength values. Furthermore, it appears that the presented experimental results closely align with the relationships proposed in the regulations.

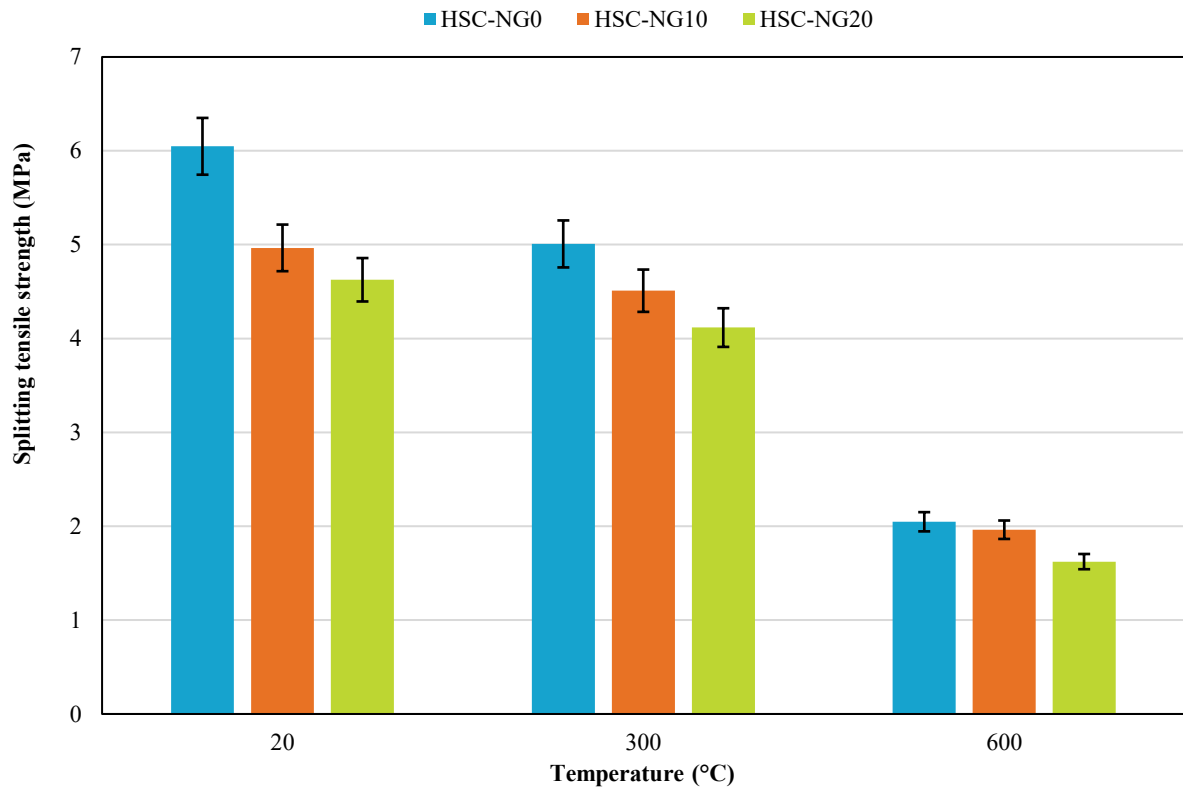


Fig. 14. Splitting tensile strength of specimens before and after exposure to elevated temperatures.

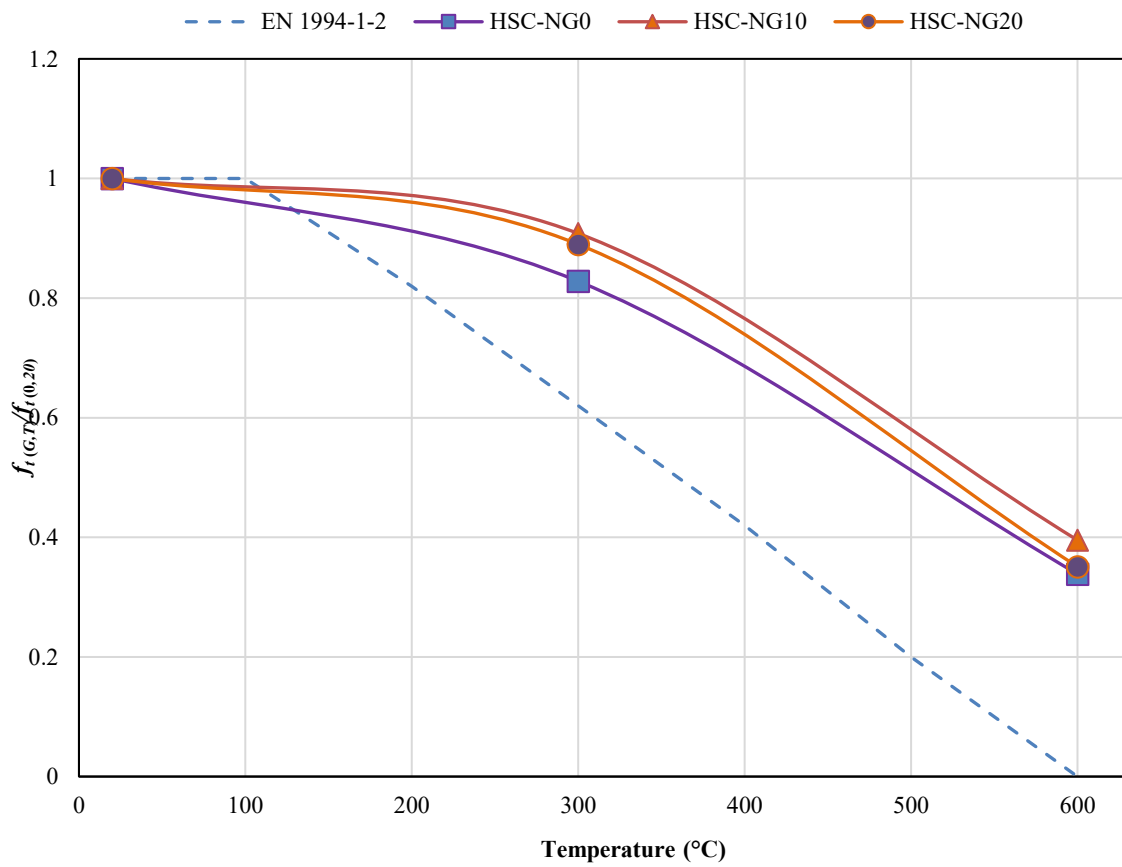


Fig. 15. Normalized splitting tensile strength of concrete specimens in terms of temperature.

Using nonlinear regression analysis, Eq. 7 was developed to determine the splitting tensile strength of specimens containing nylon granules exposed to elevated temperatures. In this equation,  $T$  represents the target temperature in degrees Celsius,  $T'$  is the temperature ratio, and  $G$  is the percentage of nylon granule replacement. Fig. 16 illustrates the trend of normalized splitting tensile

strength changes concerning these parameters.

$$\frac{f_{t(G,T)}}{f_{t(0,20)}} = (1 - 0.0657T' - 0.0136G - 1.834T'^2 + 0.0000321G^2 + 0.0165T'G) \quad (7)$$

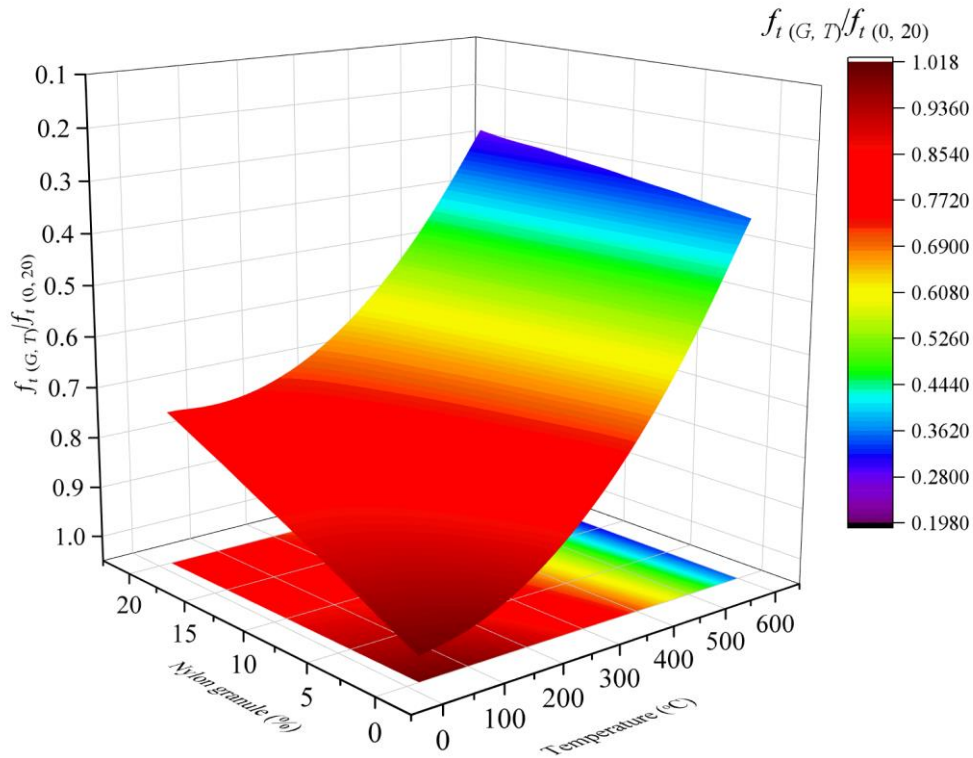


Fig. 16. Normalized initial modulus of elasticity contour based on Eq. 7.

Table 8 summarizes the statistical performance indicators of Eq. 7 compared to the experimental results. According to the performance indicators listed in Table 8, the proposed Eq. 7 has successfully predicted the normalized splitting tensile strength of the specimens with suitable accuracy. Fig. 17 is presented to better understand the proposed relationship and compare it with the experimental data from this study as well as other studies in the literature (on concrete specimens containing recycled aggregates). The proposed relationship provides a relatively accurate estimation of the experimental results from other researchers [7, 25, 54, 55].

Table 8. Statistical performance indicators results of Eq. 7.

R	R <sup>2</sup>	MAE	MSE	RMSE	Mean*	CV*(%)
0.997	0.994	0.0143	0.000371	0.0192	0.996	2.567

\* Calculated for the predicted to experimental results ratio

#### 4.4. Modulus of elasticity

The elastic modulus is a critical mechanical property of concrete that reflects its stiffness against elastic deformations under loading. In simpler terms, this parameter indicates the extent to which concrete deforms under a given stress. The elastic modulus is especially important in designing and analyzing structures where deformation and displacement are significant concerns. The values of the initial elastic modulus (tangent elastic modulus) for all concrete specimens are presented in Table 6 and Fig. 18. Additionally, the results for the secant modulus are shown in Table 6 and Fig. 19. The results reveal that increasing the replacement percentage of NG with natural fine aggregates reduces both the initial and secant elastic moduli across all target temperatures. It should also be noted that the reduction rate in elastic modulus decreases with increasing exposure temperature for all specimens. This reduction is mainly due to the weaker physical structure of nylon granules, especially at elevated temperatures, resulting in lower resistance to deformation compared to natural fine aggregates [7]. The elastic modulus of concrete specimens is significantly influenced by the size, shape, and type of aggregates used [56]. After exposure to 300°C, the initial elastic modulus of HSC-NG0, HSC-NG10, and HSC-NG20 specimens decreased by 6.9, 2.8, and 7.3%, respectively, compared to their corresponding values at 20°C.

Similarly, the secant modulus decreased by 11.2, 6.9, and 11.2%, respectively. The main reasons for these reductions are similar to those observed in the compressive and splitting tensile strength declines. According to the results, at 300°C, the highest reduction in both the initial and secant modulus occurred in specimens with 20% NG replacement, while the lowest reduction was observed in specimens with 10% NG replacement. The temperature of 300°C is close to the melting point of the nylon granules, leading to

weakened cohesion between particles and other concrete components, ultimately reducing deformation resistance [7, 57]. At 600°C, the initial elastic modulus of HSC-NG0, HSC-NG10, and HSC-NG20 specimens dropped by 74.8, 75.8, and 76.6%, respectively, compared to their values at 20°C. The secant modulus decreased by 76.3, 75.7, and 75%, respectively. Based on the results, at 600°C, the highest reduction in initial modulus was observed in the specimens with 20% NG replacement and the lowest in the control specimens without NG. Conversely, for the secant modulus, the greatest reduction occurred in the reference specimens, while the least reduction was seen in specimens with 20% NG replacement.

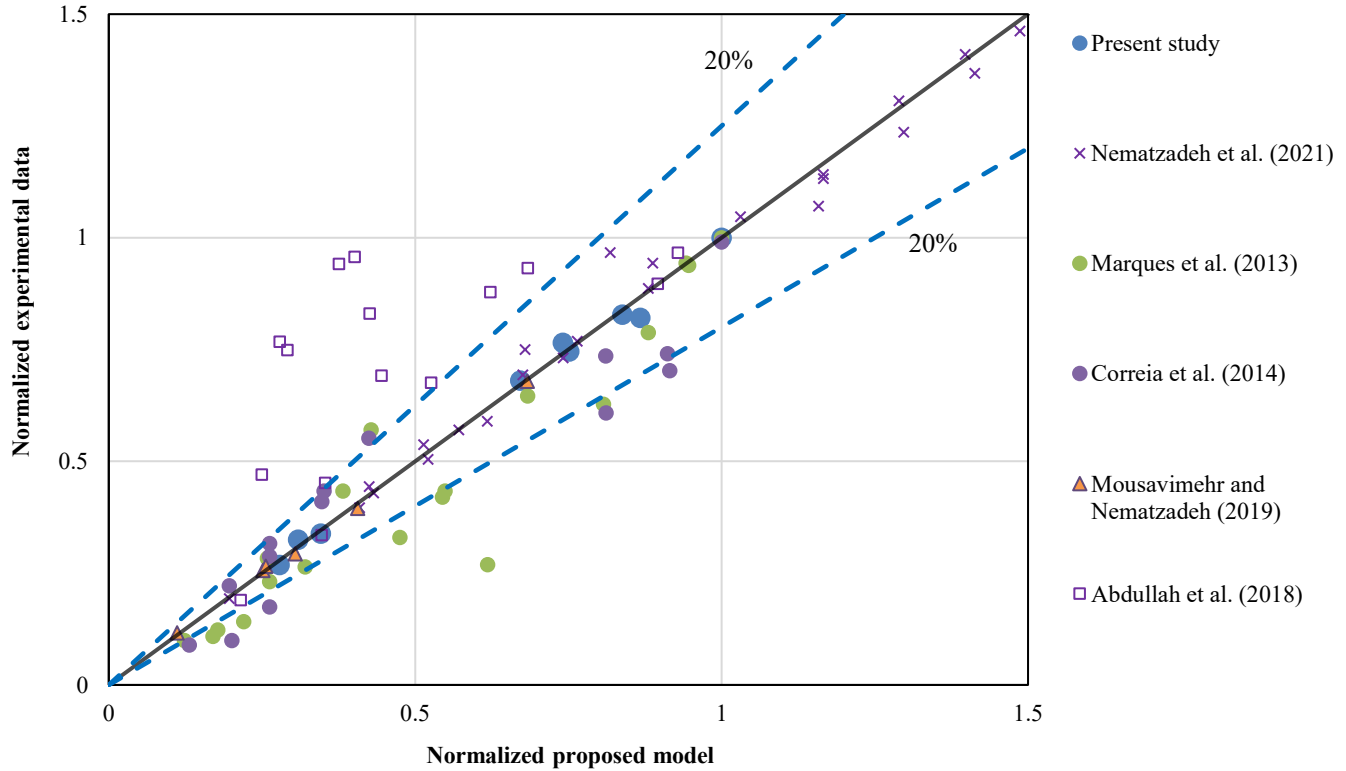


**Fig. 17. Comparison of experimental data reported by different researchers with the equation proposed for splitting tensile strength.**

These trends can be attributed to the decomposition of CH and the degradation of C-S-H gel, which increase the porosity of the cement paste and promote microcracking in the ITZ, ultimately reducing resistance to deformation [57]. Furthermore, heat exposure beyond the melting point of nylon granules and the loss of approximately 90% of their mass leads to void formation within the concrete, further decreasing both the initial and secant elastic moduli. The normalized initial modulus of elasticity is defined as the ratio of the initial modulus of elasticity of a specimen exposed to a target temperature ( $E_{i(G,T)}$ ) to the initial modulus of elasticity of the specimen at 20 °C ( $E_{i(0,20)}$ ).

The values of the normalized initial modulus of elasticity as a function of temperature, based on ASCE [30] and CEB-FIP [33], are shown in Fig. 20. Additionally, the normalized secant modulus of elasticity is defined as the ratio of the secant modulus of elasticity of a specimen exposed to a target temperature ( $E_{s(G,T)}$ ) to the secant modulus of elasticity of the specimen at 20 °C ( $E_{s(0,20)}$ ). The values of normalized secant modulus of elasticity as a function of temperature, based on ACI 216 [29], ASCE [30], and, EN 1994-1-2 [31] are shown in Fig. 21. These figures generally indicate that these codes provide reasonably accurate estimates of the initial and second modulus of elasticity values for the tested specimens. Furthermore, it appears that the presented experimental results closely align with the relationships proposed in the regulations.

Using nonlinear regression analysis, Eq. 8 was developed to determine the initial modulus of elasticity of specimens containing nylon granules exposed to elevated temperatures. In this equation,  $T$  represents the target temperature in degrees Celsius,  $T'$  is the temperature ratio, and  $G$  is the percentage of nylon granule replacement. Fig. 22 is presented to better illustrate the trend of changes in the normalized initial modulus of elasticity concerning these parameters.

$$\frac{E_{i(G,T)}}{E_{i(0,20)}} = (-3.506T'^2 + 0.732T' + 1) + (0.0209T'^2 - 0.003T' - 0.0078)G \quad (8)$$

Table 9 summarizes the statistical performance indicators of Eq. 8 compared to the experimental results. According to the performance indicators listed in Table 9, the proposed Eq. 8 has successfully predicted the normalized initial modulus of elasticity of the specimens with suitable accuracy.



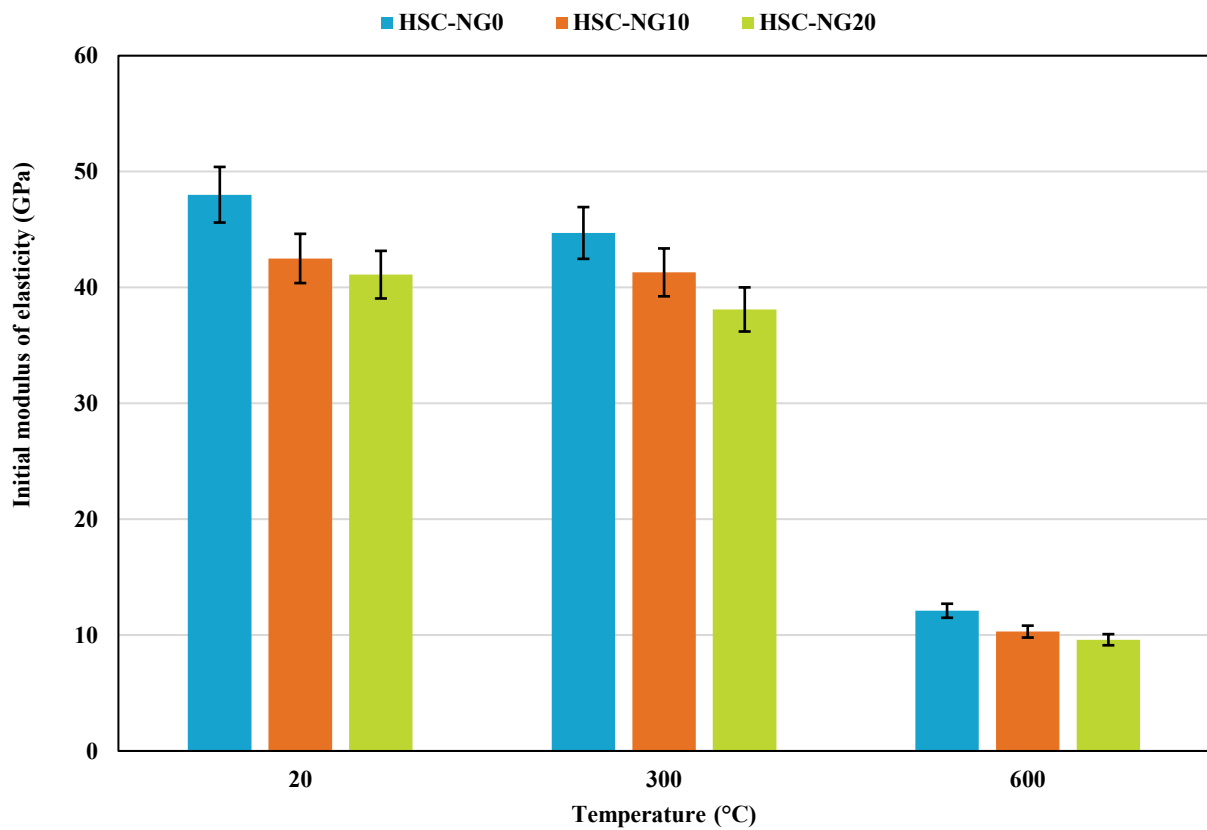


Fig. 18. Initial modulus of elasticity of concrete specimens before and after exposure to elevated temperatures.

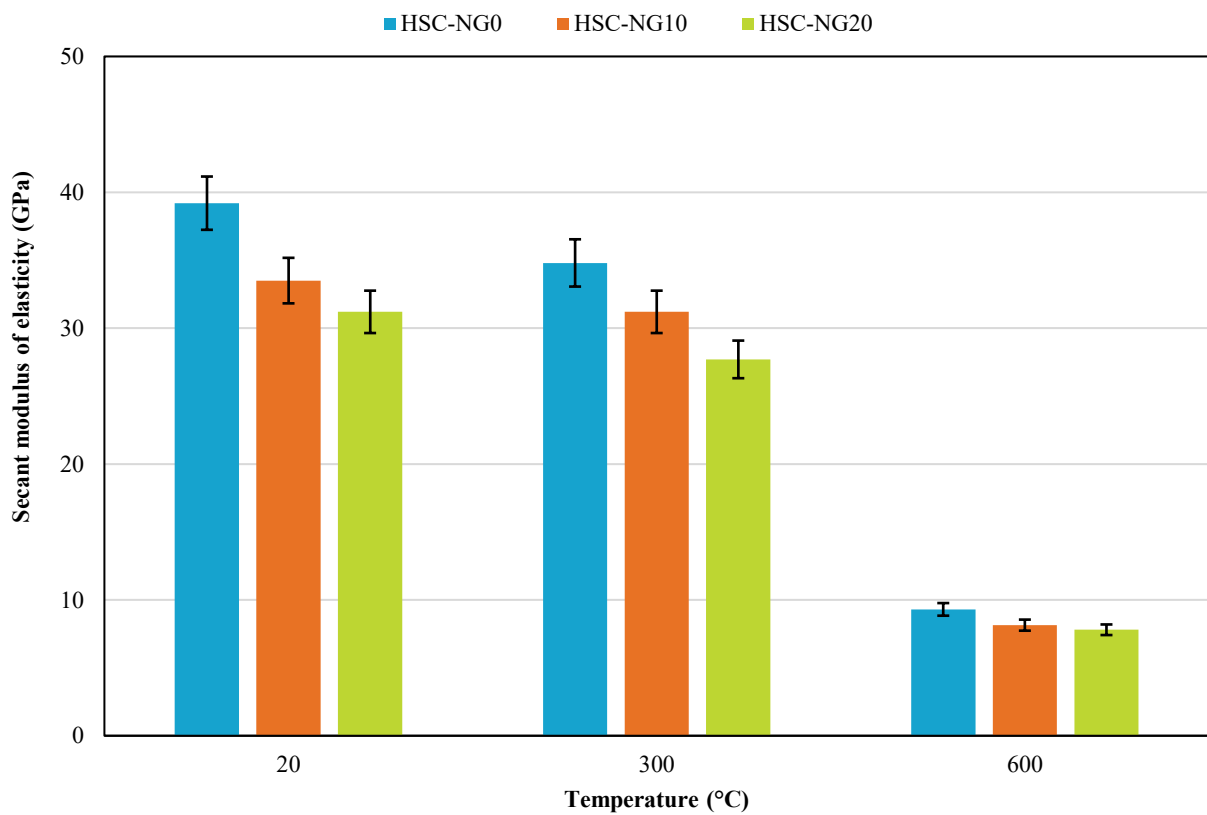


Fig. 19. Secant modulus of elasticity of concrete specimens before and after exposure to elevated temperatures.

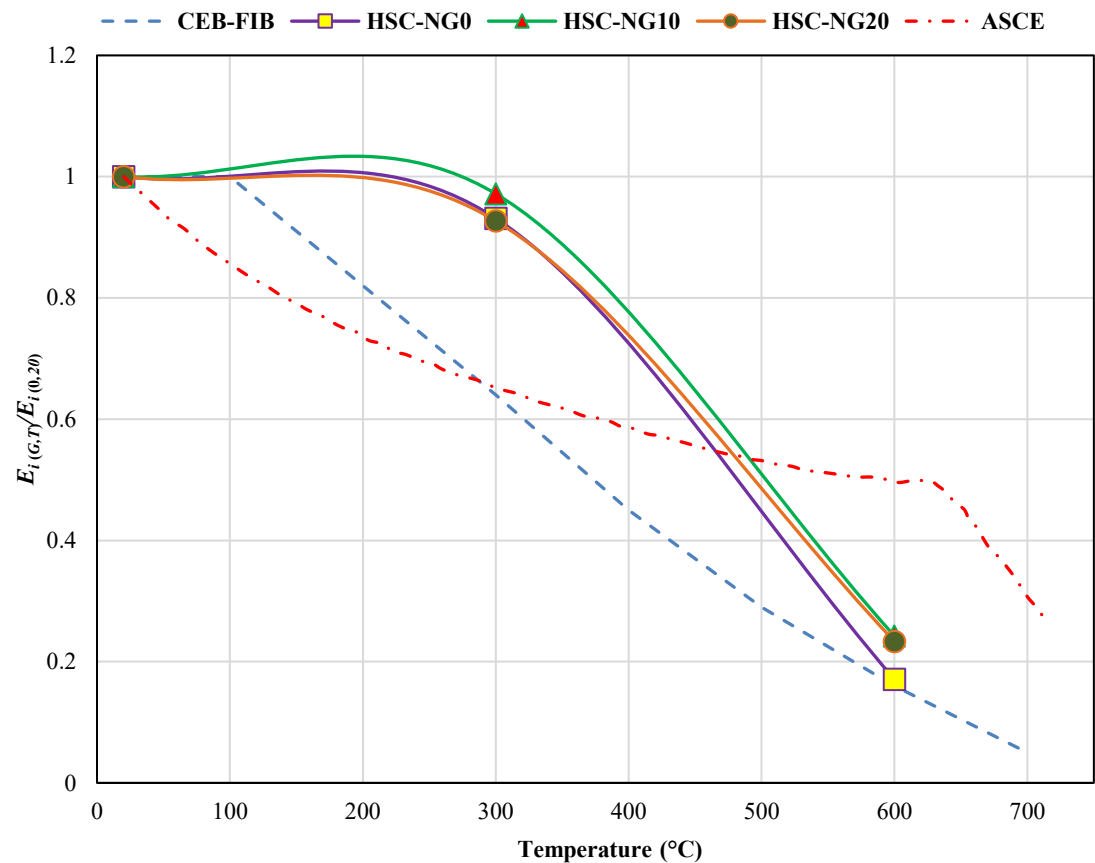


Fig. 20 Normalized initial modulus of elasticity of concrete specimens in terms of temperature.

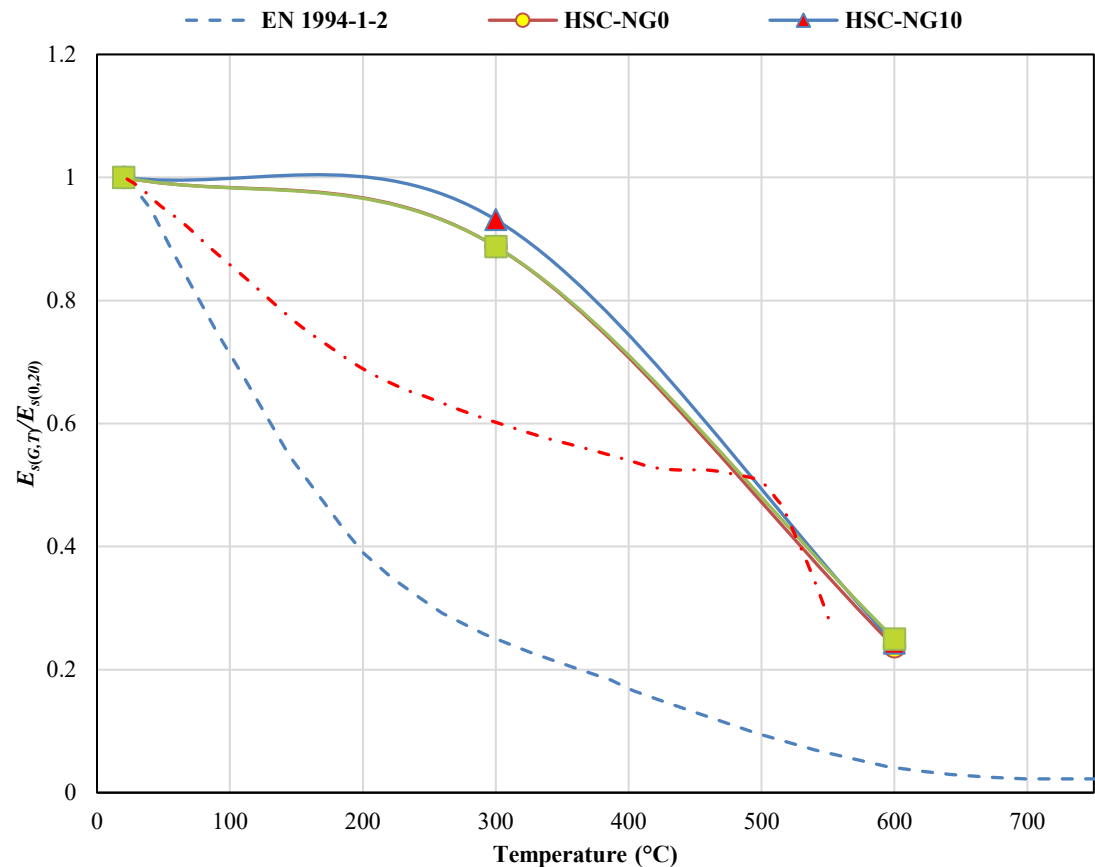


Fig. 21. Normalized secant modulus of elasticity of concrete specimens in terms of temperature.

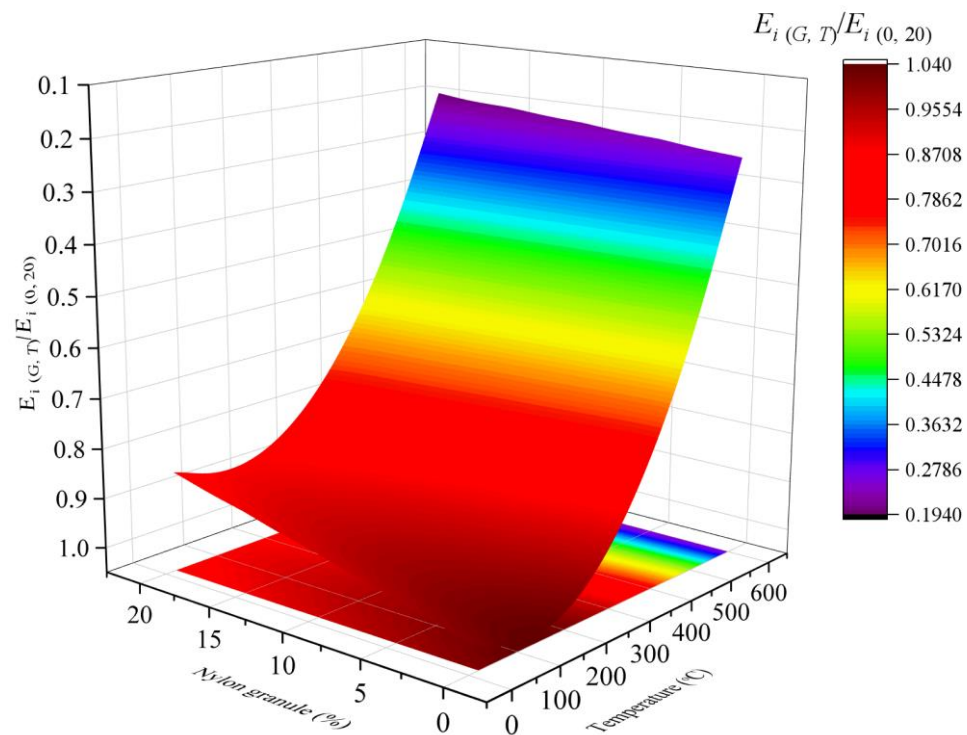


Fig. 22. Normalized initial modulus of elasticity contour based on Eq. 8.

Table 9. Statistical performance indicators results of Eq. 8.

R	R <sup>2</sup>	MAE	MSE	RMSE	Mean*	CV*(%)
0.999	0.998	0.00794	0.000179	0.0134	0.999	2.211

\* Calculated for the predicted to experimental results ratio

Fig. 23 is presented to better understand the proposed relationship and compare it with the experimental data from this study as well as other studies in the literature (on concrete specimens containing recycled aggregates). The proposed relationship provides a relatively accurate estimation of the experimental results from other researchers [4, 22, 52, 53].

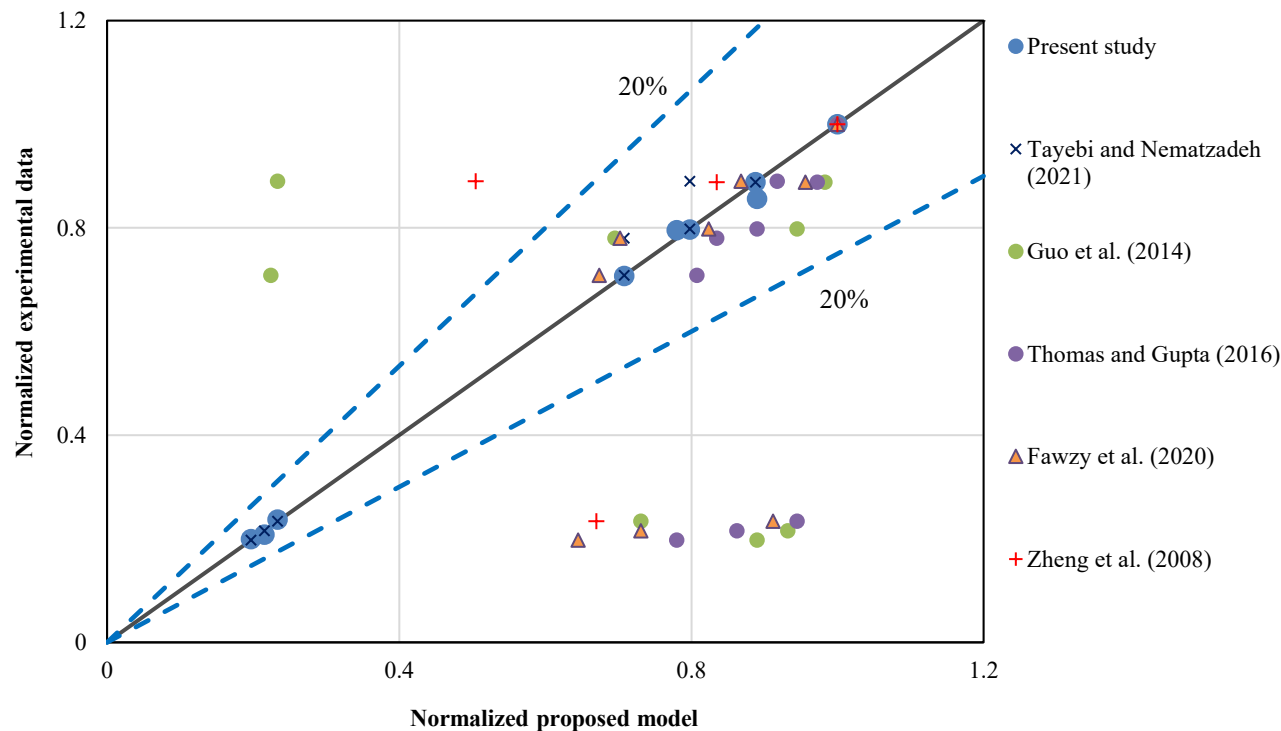


Fig. 23. Comparison of experimental data reported by different researchers with the equation proposed for the initial modulus of elasticity.

Using nonlinear regression analysis, Eq. 9 was developed to determine the secant modulus of elasticity of specimens containing nylon granules exposed to elevated temperatures. In this equation,  $T$  represents the target temperature in degrees Celsius,  $T'$  is the temperature ratio, and  $G$  is the percentage of nylon granule replacement. Fig. 24 is presented to better illustrate the trend of changes in the normalized secant modulus of elasticity concerning these parameters.

$$\frac{E_{s(G,T)}}{E_{s(0,20)}} = (-3.077T'^2 + 0.469T' + 1) + (0.0279T'^2 - 0.00067T' - 0.011)G \quad (9)$$

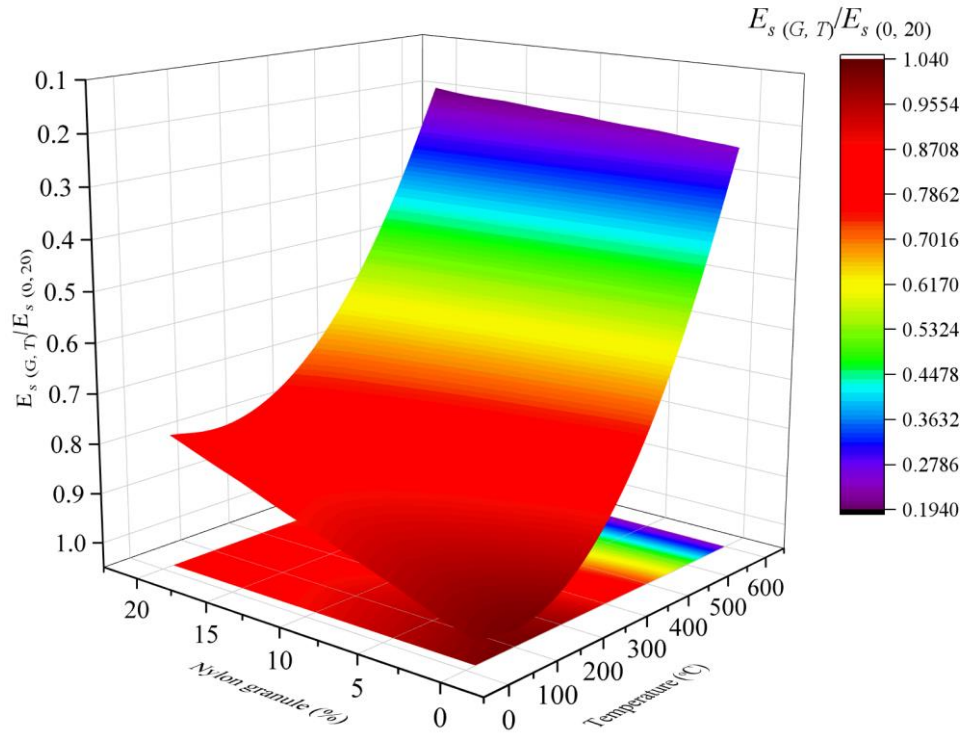


Fig. 24. Normalized secant modulus of elasticity contour based on Eq. 9.

Table 10 summarizes the statistical performance indicators of Eq. 9 compared to the experimental results. According to the performance indicators listed in Table 10, the proposed Eq. 9 has successfully predicted the specimens' normalized secant modulus of elasticity with suitable accuracy.

Table 10. Statistical performance indicators results of Eq. 9.

R	R <sup>2</sup>	MAE	MSE	RMSE	Mean*	CV*(%)
0.999	0.998	0.00814	0.000181	0.0134	0.995	2.356

\* Calculated for the predicted to experimental results ratio

Fig. 25 is presented to better understand the proposed relationship and compare it with the experimental data from this study as well as other studies in the literature (on concrete specimens containing recycled aggregates). The proposed relationship provides a relatively accurate estimation of the experimental results from other researchers [12, 54, 58, 59].

#### 4.5. Strain at peak stress

Table 11 and Fig. 26 present the peak strain (strain at peak stress) values for all specimens. According to the results, the peak strain ranged between 0.002 mm/mm and 0.0056 mm/mm. Notably, the minimum and maximum peak strain values were observed for the HSC-NG20 specimen at room temperature and the HSC-NG0 specimen at 600°C, respectively. At ambient temperature, the HSC-NG10 sample exhibited the highest peak strain. Moreover, the results indicate that the peak strain significantly changed after exposure to 600°C, which is consistent with findings from Akbarzadeh Bengar et al. [60]. Upon heating the specimens to 300°C, the peak strain ranged between 0.0022 mm/mm and 0.0035 mm/mm, which is comparable to the range observed at room temperature. However, after exposure to 600°C, all specimens showed a substantial increase in peak strain. This trend is attributed to the concrete softening due to heat and the loss of cohesion between the cement paste and aggregates at high temperatures [48]. Based on the data in Table 10, it was found that for most specimens except HSC-NG10 at room temperature and 300°C, an increase in the nylon granule replacement ratio reduced peak strain compared to the control specimens without nylon granules. Additionally, peak strain increased with rising exposure temperatures. Specifically, after exposure to 600°C, the peak strain increased by 166.7, 46.9, and 90% for the HSC-NG0, HSC-NG10, and HSC-NG20 specimens, respectively. The normalized strain at peak stress is defined as the ratio of the strain at peak stress of a specimen exposed to a target temperature ( $\varepsilon_{c(G,T)}$ ) to the strain at peak stress of the specimen at 20 °C ( $\varepsilon_{c(0,20)}$ ).

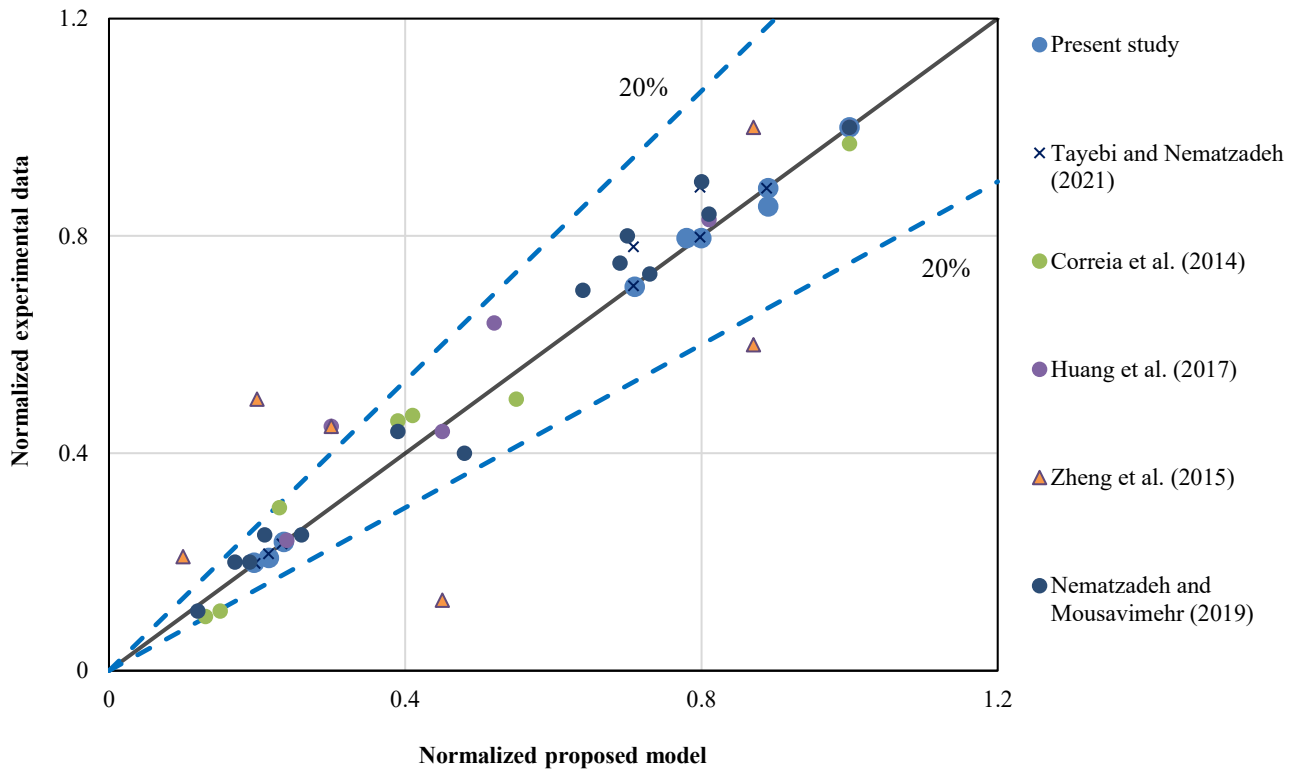


Fig. 25. Comparison of experimental data reported by different researchers with the equation proposed for the secant modulus of elasticity.

Table 11. Axial strain and toughness values of the specimens at elevated temperatures.

Specimen ID	Temperature (°C)	Strain at peak stress (mm/mm)	Ultimate strain (Residual strength of $0.3f'_c$ )	Ultimate strain (Residual strength of $0.85f'_c$ )	Toughness (J/m³)
HSC-NG0	20	0.0021	0.0031	0.0027	0.089
	300	0.0027	0.0037	0.0033	0.083
	600	0.0056	0.0081	0.0072	0.087
HSC-NG10	20	0.0032 (+52.4%)	0.0062	0.0048	0.071
	300	0.0035 (+29.6%)	0.0065	0.005	0.065
	600	0.0047 (-16.0%)	0.0067	0.0061	0.064
HSC-NG20	20	0.002 (-4.8%)	0.0031	0.0031	0.069
	300	0.0022 (-25.9%)	0.0033	0.0035	0.064
	600	0.0038 (-32.1%)	0.0055	0.0065	0.054

Fig. 27 shows the values of normalized strain at peak stress as a function of temperature based on EN 1994-1-2 [31]. This figure generally indicates that these codes provide reasonably accurate estimates of the normalized strain at peak stress values for the tested specimens. Furthermore, it appears that the presented experimental results closely align with the relationships proposed in the regulations.

Using nonlinear regression analysis, Eq. 10 was developed to determine the strain of specimens containing nylon granules exposed to elevated temperatures at peak stress. In this equation,  $T$  represents the target temperature in degrees Celsius,  $T'$  is the temperature ratio, and  $G$  is the percentage of nylon granule replacement. Fig. 28 is presented to better illustrate the trend of changes in the normalized strain at peak stress concerning these parameters.

$$\frac{\epsilon_{c(G,T)}}{\epsilon_{c(0,20)}} = (1 - 0.0855T' + 0.0735G + 4.621T'^2 - 0.00361G^2 - 0.0685T'G) \quad (10)$$

Table 11 summarizes the statistical performance indicators of Eq. 10 compared to the experimental results. According to the performance indicators listed in Table 11, the proposed Eq. 10 has successfully predicted the normalized strain at peak stress of the specimens with suitable accuracy.

Fig. 29 is presented to better understand the proposed relationship and compare it with the experimental data from this study as well as other studies in the literature (on concrete specimens containing recycled aggregates). The proposed relationship provides a relatively accurate estimation of the experimental results from other researchers [4, 52, 61].

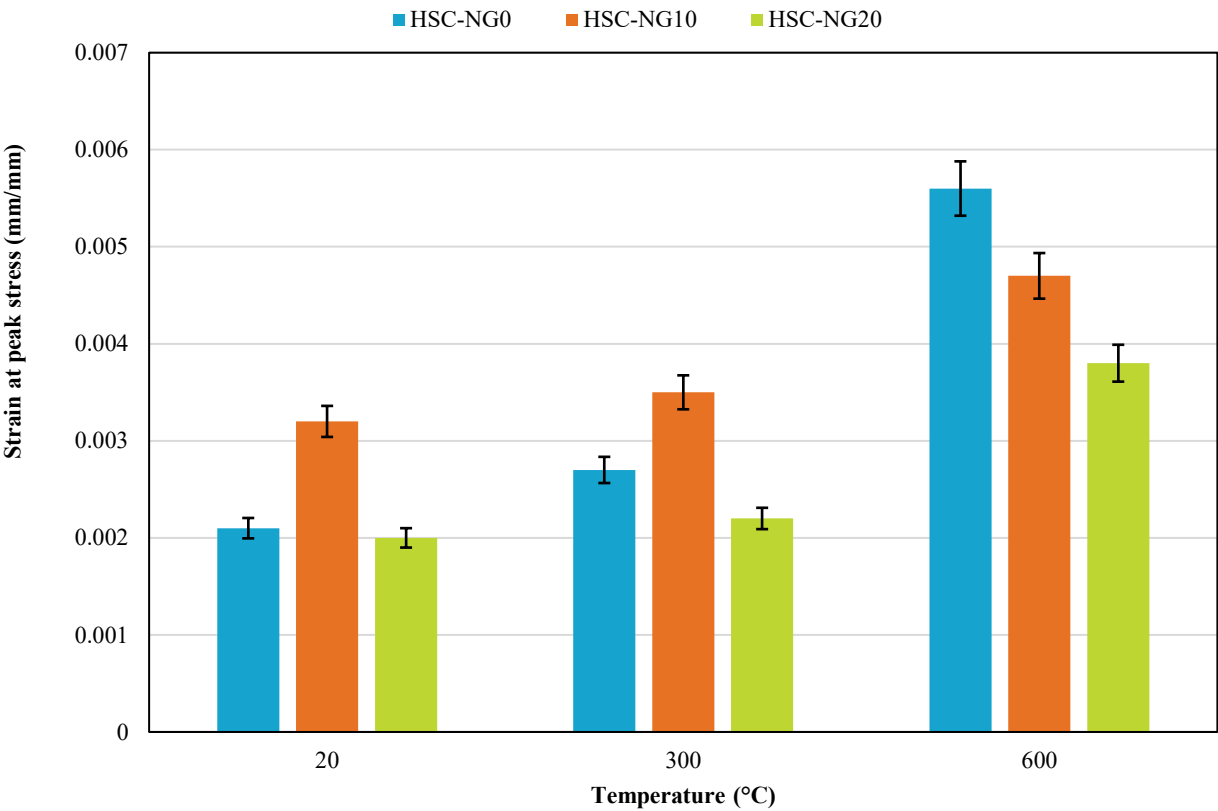


Fig. 26. Strain at peak stress of concrete specimens before and after exposure to elevated temperatures.

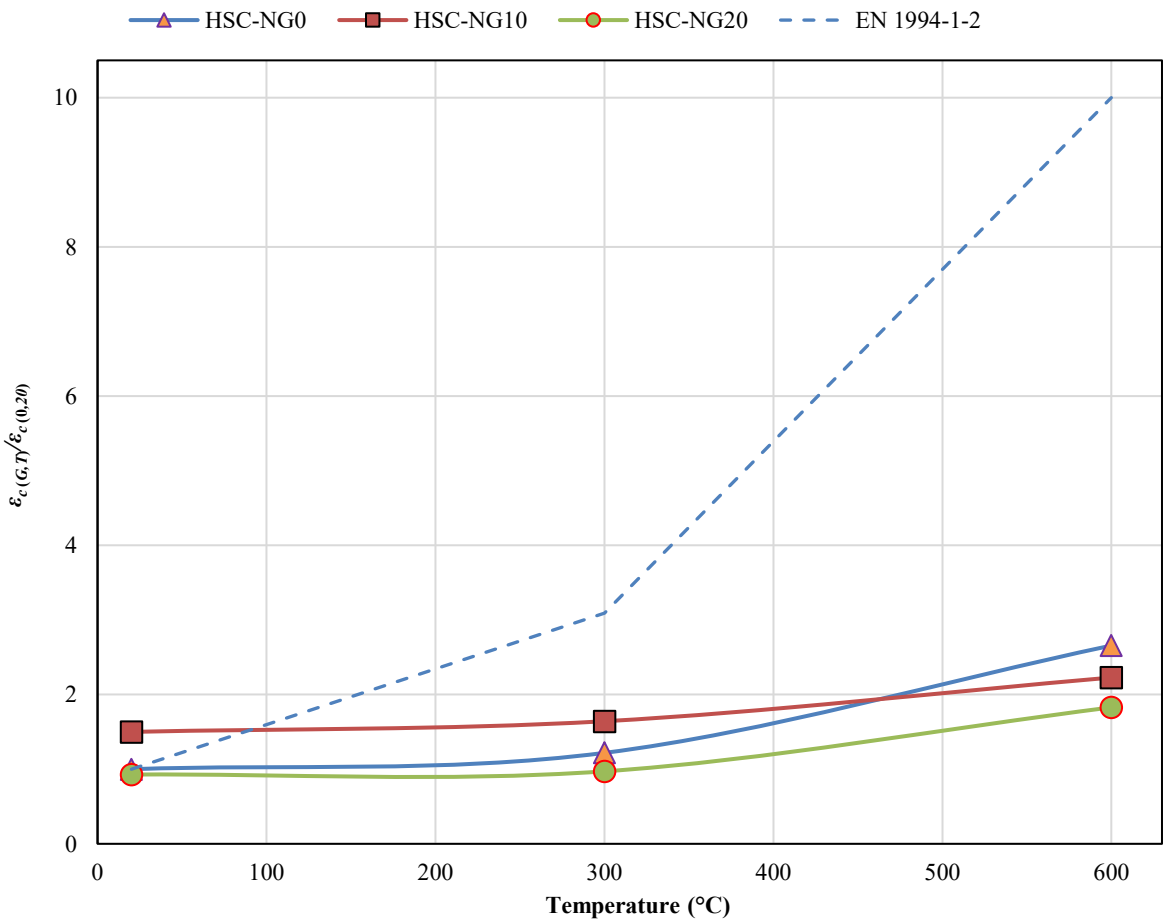


Fig. 27. Normalized strain at peak stress of concrete specimens in terms of temperature.



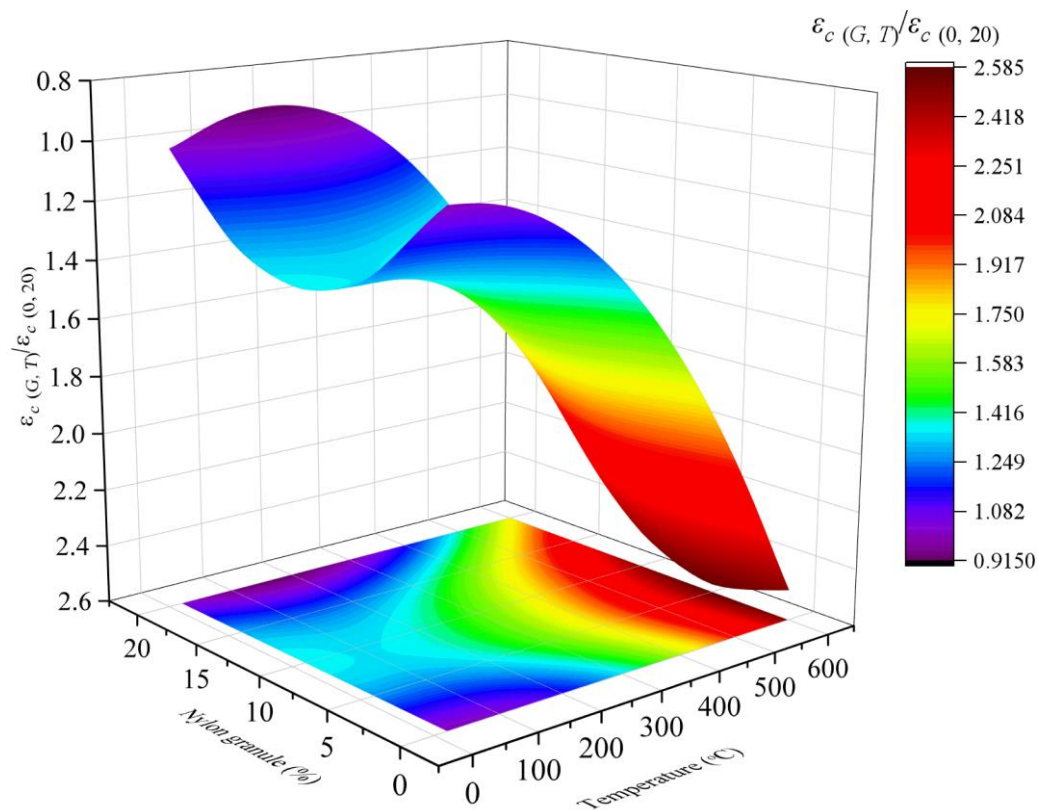


Fig. 28. Normalized strain at peak stress contour based on Eq. 10.

Table 11. Statistical performance indicators results of Eq. 10.

R	R <sup>2</sup>	MAE	MSE	RMSE	Mean*	CV*(%)
0.974	0.948	0.108	0.0167	0.129	1.008	2.972

\* Calculated for the predicted to experimental results ratio

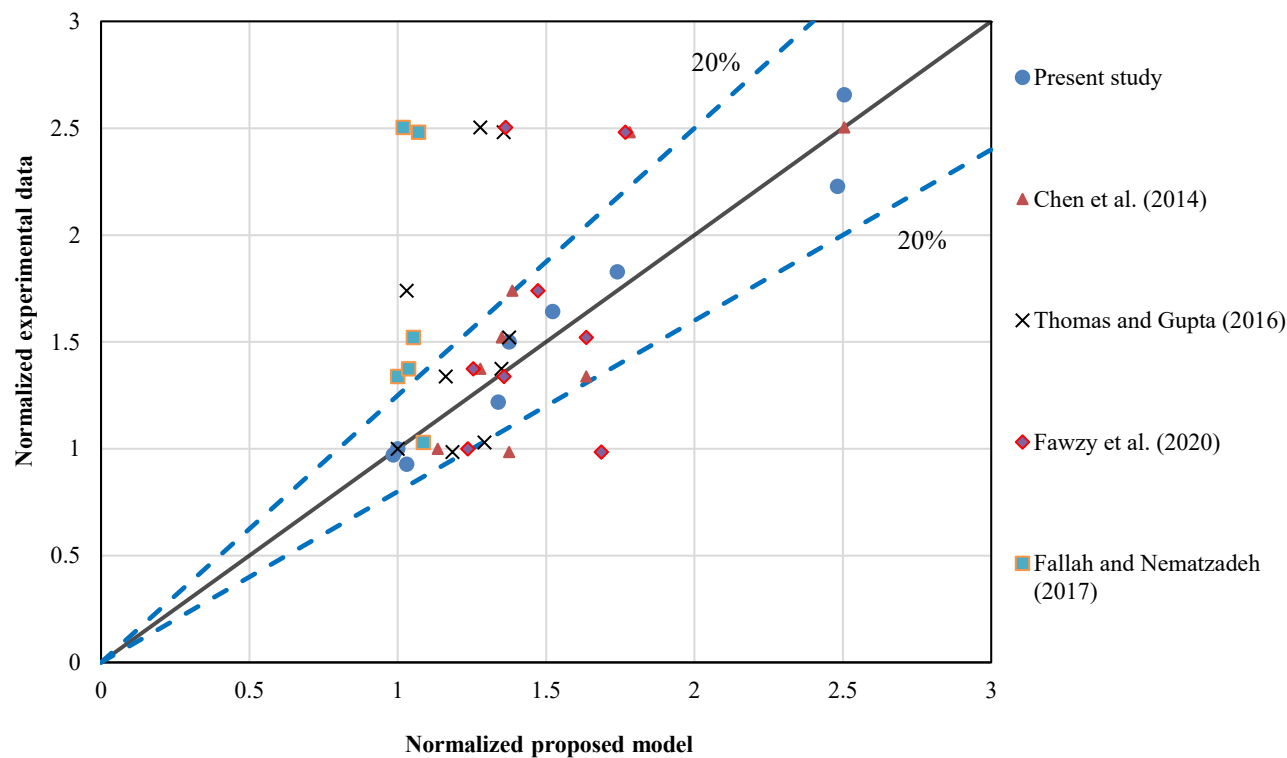


Fig. 29. Comparison of experimental data reported by different researchers with the equation proposed for the strain at peak stress.

#### 4.6. Ultimate strain

To describe the post-peak stress-strain behavior of concrete, several criteria are typically employed to define the descending branch of the stress-strain curve. For example, Sheikh and Uzumeri [62] used the strain corresponding to a 70% drop in compressive strength (i.e., 30% residual compressive strength) as the ultimate strain, while Frangou et al. [63] considered the strain at a 15% strength drop (i.e., 85% residual compressive strength) as the ultimate strain. The corresponding values of ultimate strain based on these two criteria are presented in Figs. 30 and 31, respectively. Additionally, the exact values of the ultimate strain for the concrete specimens are provided in Table 10. According to the results presented in Figs. 30 and 31, at room temperature and 300°C, the highest ultimate strain was observed in the specimens with 10% NG replacement. However, it should also be noted that the maximum ultimate strain at 600°C occurred in the control specimens without NG. After exposure to 300°C, the ultimate strain in all specimens increased compared to those tested at room temperature. This increase is attributed to the softening and ductility of nylon granules near their decomposition temperature, CH dehydration, and the degradation of C-S-H gel. When exposed to 600°C, the decomposition of nylon granules, softening, and dehydration of cement paste further increased the ultimate strain. In the specimens containing NG, significant mass loss was observed at 600°C (see Fig. 9), which resulted in increased porosity. Nevertheless, this increased porosity facilitates the release of trapped gases within concrete voids, thereby reducing internal cracking and, in turn, enhancing the specimens' ultimate strain capacity.

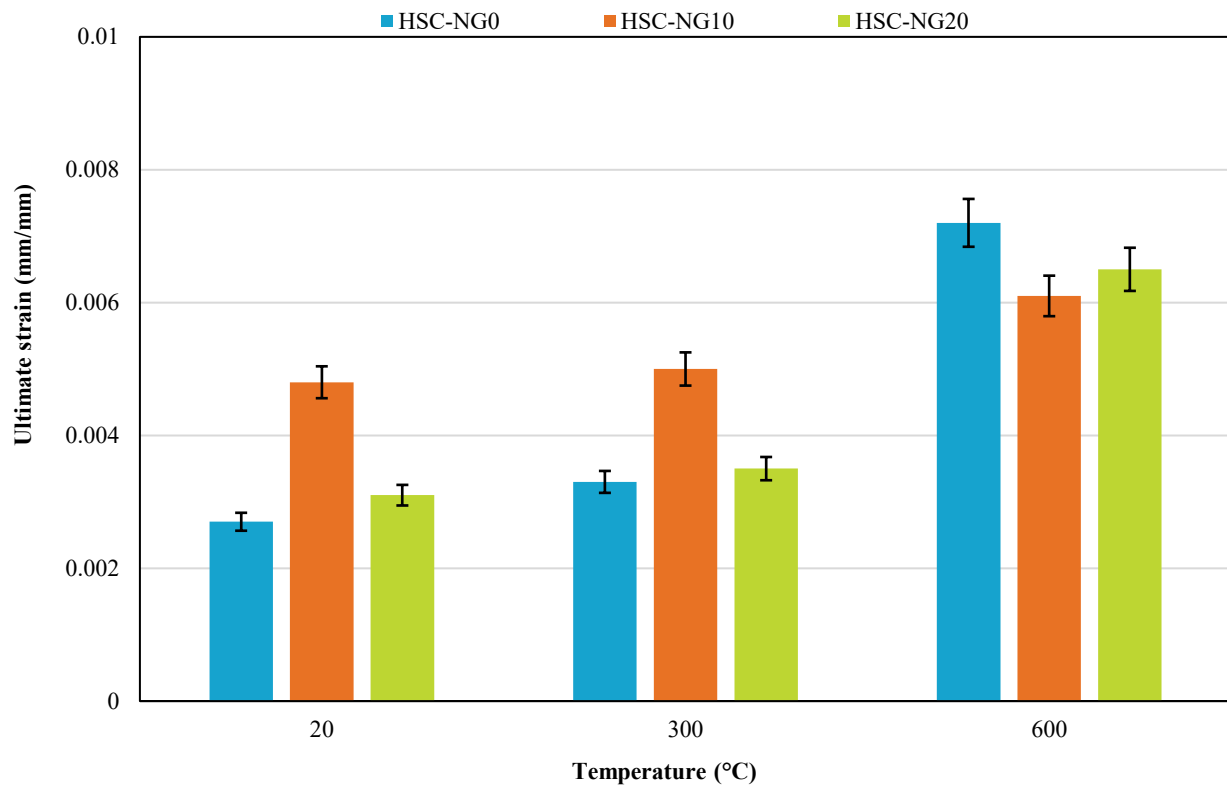


Fig. 30. Ultimate strain corresponding to a 15% reduction in compressive strength.

#### 4.7. Toughness

The toughness of concrete specimens under axial compression is defined as the area under the stress-strain curve up to the peak stress point [64, 65]. The results related to the toughness of all HSC specimens containing NG are presented in Table 10 and Fig. 32. According to the results, the toughness of the reference specimens (without NG replacement) was greater than that of all NG-containing specimens at all tested temperatures. Furthermore, the toughness decreased at all temperature levels with an increase in NG replacement percentage. This reduction is attributed to reference specimens' higher compressive strength than those containing NG. Moreover, the peak strain values for all specimens were relatively close to each other, which resulted in a greater area under the stress-strain curve (i.e., higher toughness) for the control specimens. Additionally, the toughness of all concrete specimens decreased with increasing temperature. This nonlinear trend in toughness reduction with temperature is due to the simultaneous decrease in compressive strength and increase in peak strain with rising temperature, which have opposite effects on the resulting toughness.

#### 4.8. Stress-strain behavior and proposed model

The axial compressive stress-strain curves for all specimens are plotted in separate groups in Fig. 33. These curves allow for the evaluation of changes in compressive strength, elastic modulus, peak strain, and toughness. Based on the stress-strain curves shown in Fig. 33, the ascending branch of NG-containing concrete specimens exhibits a more nonlinear behavior compared to reference specimens (without NG), particularly at 300 and 600°C. This behavior is attributed to the thermal degradation of NG particles at elevated temperatures and the formation of internal voids within the concrete matrix.

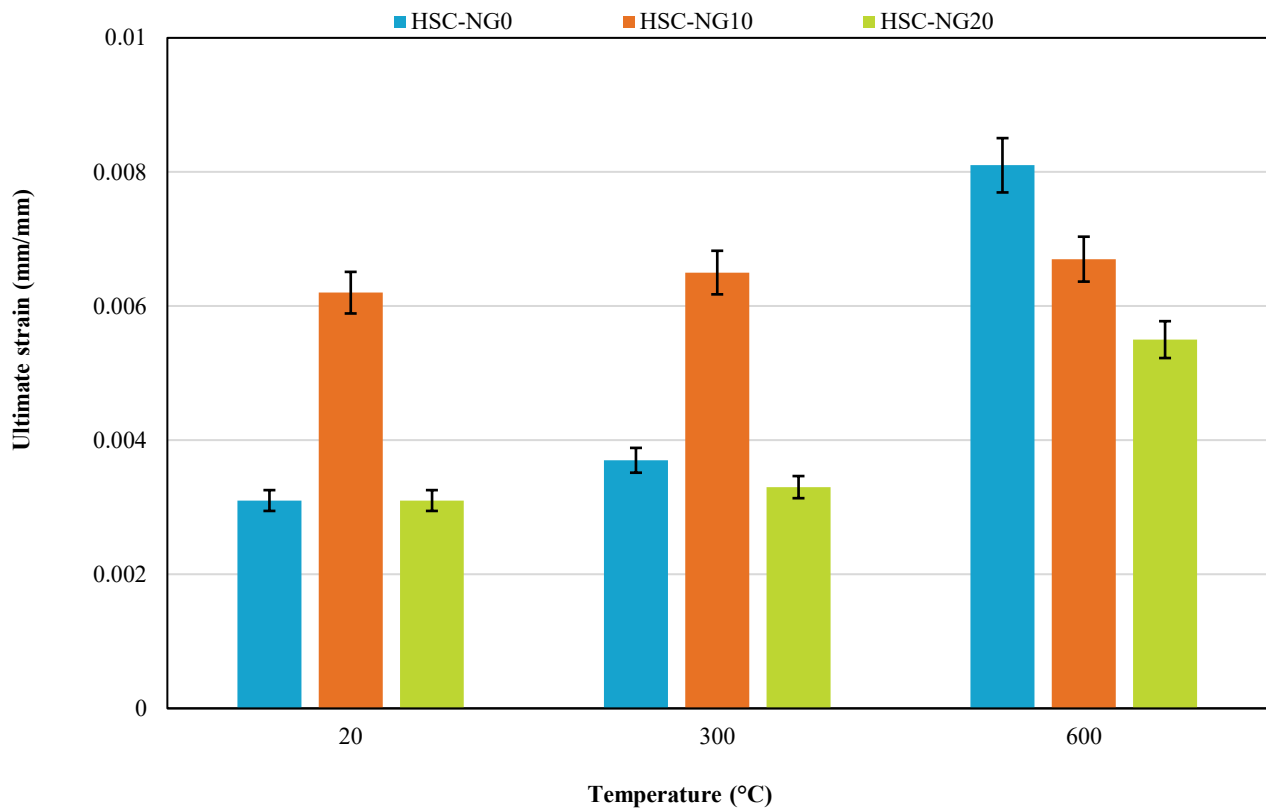


Fig. 31. Ultimate strain corresponding to a 70% reduction in compressive strength.

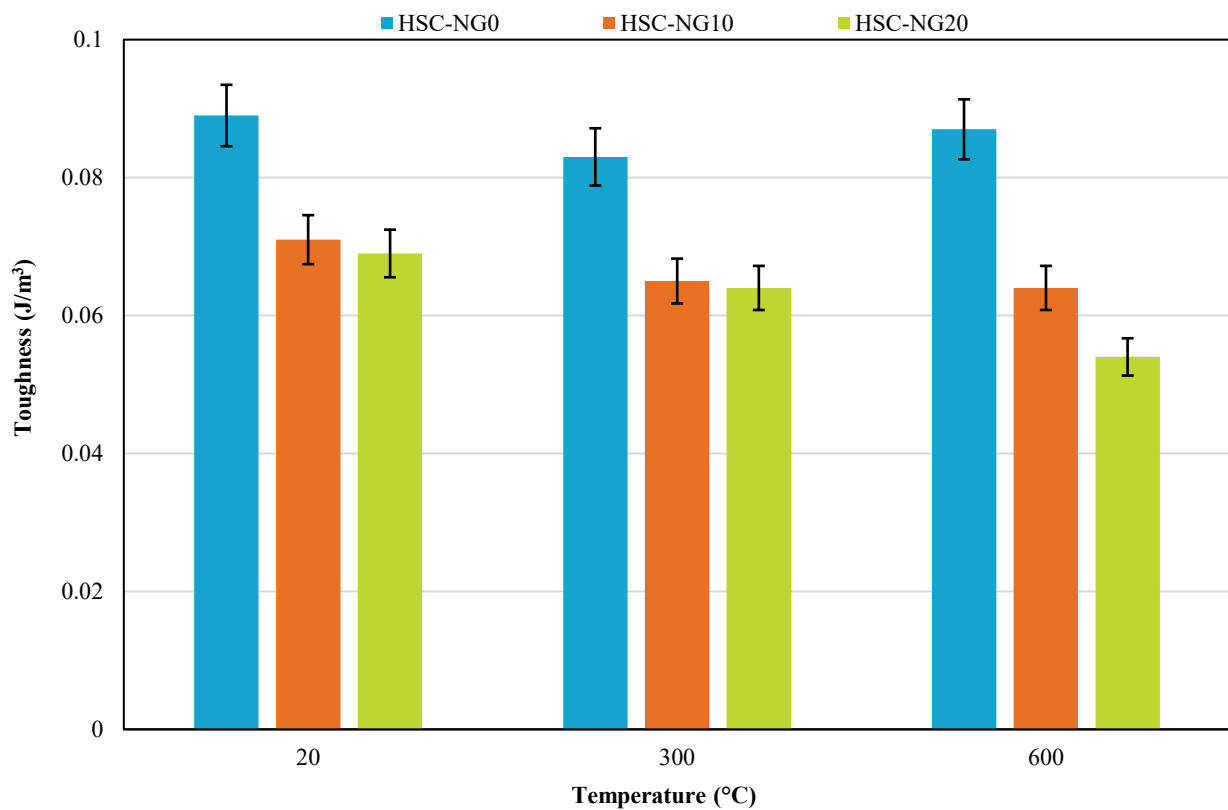


Fig. 32. Toughness of concrete specimens before and after exposure to elevated temperatures.

Additionally, as the exposure temperature increases, the overall shape of the stress-strain curve changes, with a reduction in the slope of both the ascending and descending branches. Notably, an increase in peak strain eventually accompanies the decrease in slope in the descending branch. This study predicted the stress-strain behavior of concrete specimens exposed to elevated temperatures based on the relationships provided in previous sections. To predict the stress-strain response of high-strength concrete specimens containing NG after thermal exposure, the model proposed by Nematzadeh et al. [66] was utilized. Given the noticeable difference in behavior between the pre-peak and post-peak regions, separate equations were employed for the ascending and

descending branches of the stress-strain curve. Specifically, Eqs. 11 and 12 were used to model the ascending branch of the stress–strain behavior.

$$f_c = f_{c(G,T)} \frac{m \left( \frac{\varepsilon}{\varepsilon_{c(G,T)}} \right)}{\left( \frac{\varepsilon}{\varepsilon_{c(G,T)}} \right)^{1/\ln m}} \quad 0 \leq \left( \frac{\varepsilon}{\varepsilon_{c(G,T)}} \right) \leq 1 \quad (11)$$

$$m = \frac{E_{i(G,T)} \varepsilon_{c(G,T)}}{f_{c(G,T)}} \quad (12)$$

where  $\varepsilon$  represents the axial strain of the concrete specimens at any moment, and  $f_{c(G,T)}$ ,  $\varepsilon_{c(G,T)}$ , and  $E_{i(G,T)}$  denote the axial compressive strength, strain at peak stress, and initial elastic modulus of the concrete specimens, respectively. These parameters were calculated based on Eqs. 1, 8, and 10. For the descending branch, Eq. 13 was employed.

$$f_c = f_{c(G,T)} \frac{\alpha \left( \frac{\varepsilon}{\varepsilon_{c(G,T)}} \right)}{(\alpha-1) \left( \frac{\varepsilon}{\varepsilon_{c(G,T)}} \right) + e^{\left[ \frac{\left( \frac{\varepsilon}{\varepsilon_{c(G,T)}} \right)^n - 1}{n} \right]}} \quad (13)$$

where  $\alpha = 1$  and  $n = 0.2(f_{c(G,T)} + 20)^{-0.25}$  are parameters obtained through trial-and-error and by calibrating the proposed model with the experimental results. To validate the proposed stress-strain relationship, the experimental stress-strain behavior of HSC specimens containing NG exposed to temperatures ranging from 20 to 600°C was compared with the predictions of the proposed model, as illustrated in Fig. 33. According to Fig. 33, the proposed model accurately predicted the stress-strain behavior in all cases except for the HSC-NG10 specimen exposed to 20°C, where the model failed to provide a good fit with the experimental data.

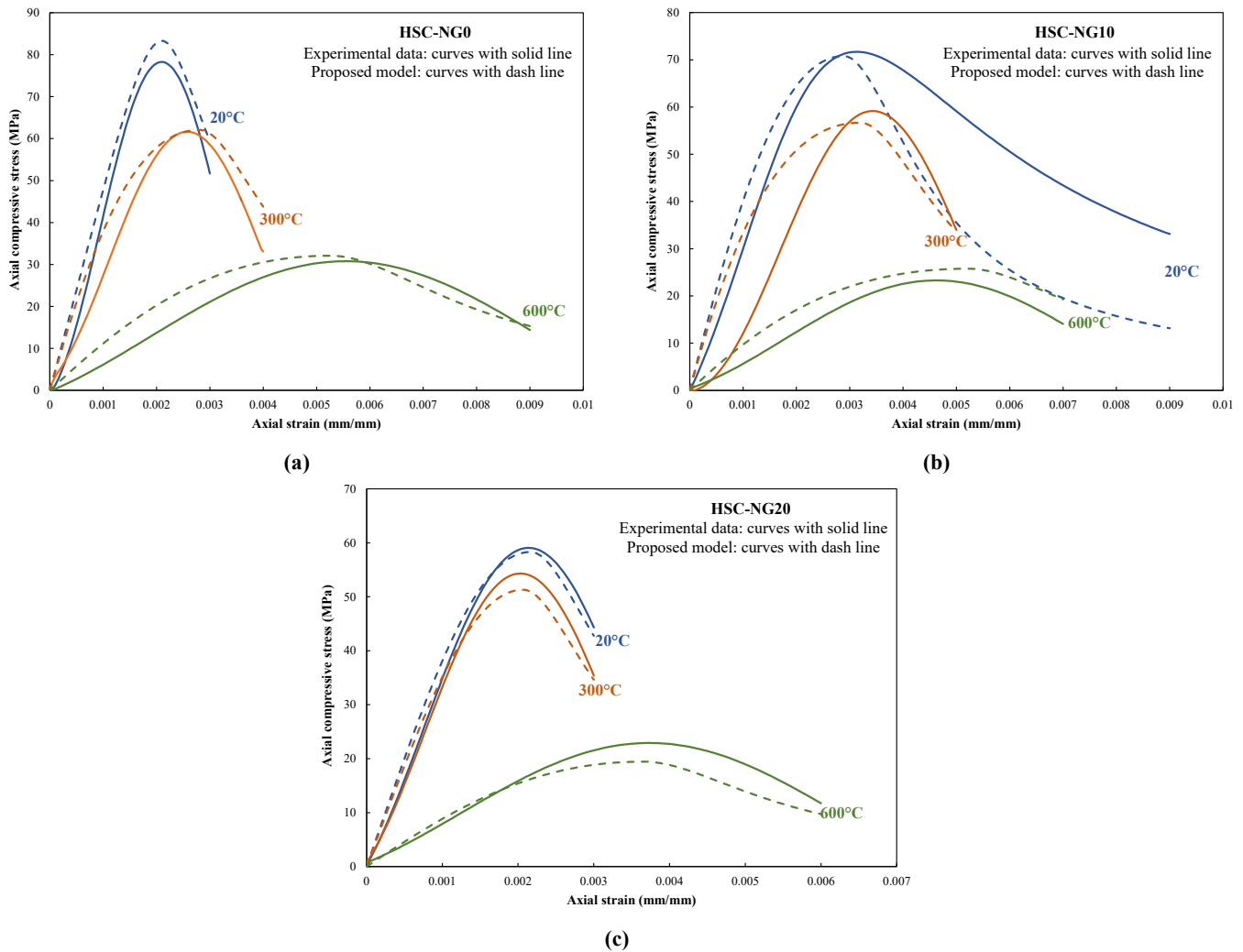


**Fig. 33. Stress-strain curves obtained from the proposed model compared with experimental results of concrete specimens; (a) HSC-NG0, (b) HSC-NG10, and (c) HSC-NG20.**

#### 4.9. Visual observations and failure modes

The damage sustained by concrete due to fire is generally identifiable through visual inspection of its surface. Typical signs on concrete surfaces after fire exposure include color change, cracking, and spalling. This study examined the surfaces of concrete specimens exposed to high temperatures and subsequently removed from the electric furnace for such changes. The condition of



HSC specimens containing NG after exposure to different temperatures is shown in Fig. 34, while Fig. 35 displays the specimens with the highest NG replacement ratio after heating. Based on the images of the specimen surfaces, all specimens' color gradually changed from dark gray to light gray as the exposure temperature increased.










Specimen	20 °C	300 °C	600 °C
HSC-NG0®			
HSC-NG10			
HSC-NG20			

Fig. 34. Surface of HSC specimens containing NG after exposure to elevated temperatures.

HSC-NG20-20	HSC-NG20-300	HSC-NG20-600
		

Fig. 35. Top surface HSC specimens containing NG after exposure to elevated temperatures.

Additionally, after exposure to 300°C, surface cracks appeared on all specimens. When the temperature reached 600°C, the number and width of these cracks increased significantly (Figs. 30 and 32). These effects can be attributed to the evaporation of free and surface moisture, as well as the dehydration of chemically bound water in the C-S-H gel, which leads to internal stresses, microcracking, and color change [52]. In addition to cracking, the number of surface pores on the specimens increased significantly after exposure to high temperatures. In specimens containing NG granules, the increase in temperature and subsequent degradation of these particles led to a substantial rise in internal porosity, ultimately resulting in concrete porosity. Given the melting point of nylon granules, at around 300°C, they begin to soften and migrate toward the internal or surface pores of the concrete (see Figs. 34 and 36). As shown in Fig. 34, at 600°C, the NG particles are completely degraded. Specifically, in the HSC-NG10 specimen, the NG particles are entirely decomposed and evaporated through the cracks and pores formed on the surface after exposure to 600°C. Furthermore, in the HSC-NG20 specimen, due to the higher NG replacement ratio, some of the NG particles are fully degraded, while others are partially decomposed and evaporated, as illustrated in Fig. 31. Thus, at 300°C, nylon granules first enter their plastic phase and then exceed their decomposition point, eventually evaporating as harmful gases with unpleasant odor through surface cracks and pores as the temperature approaches 600°C. This leads to the removal of NG granules from the concrete matrix and the formation of voids. Overall, the nylon granules partially re-solidify after the thermal exposure and cooling process. As shown in Fig. 30, they remain on the surface of the concrete as hardened melted nylon droplets in their post-exposure form.



**Fig. 36. HSC specimens containing NG after exposure to elevated temperatures.**

Compressive strength tests were conducted after examining the condition of concrete specimens exposed to elevated temperatures. Fig. 37 shows the failure patterns of both heat-exposed and unexposed concrete specimens after the compressive strength tests. For the unheated specimens (at ambient temperature), audible cracking sounds were clearly heard when the compressive stress approached its peak value (at stress levels above approximately  $0.9f_c$ ), although no visible cracks were observed beforehand. Once the peak load was reached, the failure occurred abruptly and was accompanied by loud cracking noises, such that the specimens failed within 2 to 4 seconds after the peak load. In specimens exposed to 300°C, microcracks resulting from thermal loading were visible prior to mechanical loading, and these rapidly propagated during the application of compressive stress. The development of these cracks became noticeable at stress levels above  $0.6f_c$ . The cracking noises were relatively faint, but the opening of crack planes was visible. Failure in these specimens occurred more gradually, with complete fracture occurring 7 to 10 seconds after the peak stress. Additionally, lateral expansion of the specimens was clearly observed after reaching peak stress. In specimens exposed to 600°C, the cracking and failure patterns closely resembled those observed in the 300°C group; however, the crack sounds were even milder, and the failure rate was slower. According to ASTM C39 [43], typical failure patterns include vertical cracks, well-formed cones at one end, or shear failures near the ends of the cylinders. In this study, as shown in Fig. 37, most specimens exhibited vertical cylindrical cracks at their ends, and well-formed conical failures were generally not observed.










As an additional visual inspection, the overall internal condition of HSC specimens containing NG exposed to elevated temperatures was evaluated after the splitting tensile strength test. Fig. 38 illustrates the interior view of all concrete specimens following this test. It can be observed that, with increasing exposure temperature, both the overall color of the specimens and the aggregate color become significantly faded and tend toward white. As previously mentioned, this phenomenon is attributed to the loss of free and surface water, as well as the dehydration of chemically bound water in the C-S-H gel. Moreover, with rising temperatures, a significant increase in internal pores is observed in specimens containing NG. This is due to the thermal decomposition of NG, which leads to the complete breakdown of the nylon granules and ultimately results in increased porosity and a more porous concrete matrix.

#### 4.10. Microstructure

Another aspect of this study involved the microstructural analysis of heat-exposed and unexposed high-strength concrete specimens containing 10% replacement of NG, following the compressive strength test. Scanning Electron Microscopy (SEM) was conducted on a polished thin section measuring  $20 \times 15$  mm, prepared by cutting a portion of the concrete specimen. Fig. 39 presents the SEM images of high-strength concrete specimens containing 10% NG after exposure to 20, 300, and 600°C, where a significant presence of white sponge-like structures can be observed at elevated temperatures. Fig. 39-a shows the SEM images of the specimens at 20°C. At this ambient temperature, nylon granules are clearly visible, and the number of micro-cracks and pores is significantly lower than in heat-exposed specimens. Fig. 39-b corresponds to the SEM images of specimens exposed to 300°C. The image reveals



a notable increase in porosity attributed to the evaporation of bound water and the degradation of the cement paste at elevated temperatures. These changes could be due to the thermal deformation of cement crystals, dehydration of CH crystals, and the decomposition of the C-S-H gel, which lead to structural degradation and increased porosity. Additionally, partial decomposition of nylon granules contributes to the observed high porosity in this group. Fig. 39-c displays SEM images of specimens exposed to 600°C. At this temperature, the progressive loss of chemically bound water has further exposed the microstructure of CH crystals and the C-S-H gel, making the expansion of sponge-like structures more visible (see the large white masses in Fig. 35c). Moreover, this group exhibits the highest degree of porosity and microcracking, which can be attributed to the complete decomposition of nylon granules, dehydration of CH crystals, and breakdown of the C-S-H structure. As the nylon granules have surpassed their decomposition temperature (based on the TGA results shown in Fig. 4), large voids are apparent in the image, corresponding to the evaporation of nylon particles.

Specimen	20 °C	300 °C	600 °C
HSC-NG0 <sup>®</sup>			
HSC-NG10			
HSC-NG20			

**Fig. 37. Failure mode of specimens under compressive loading.**



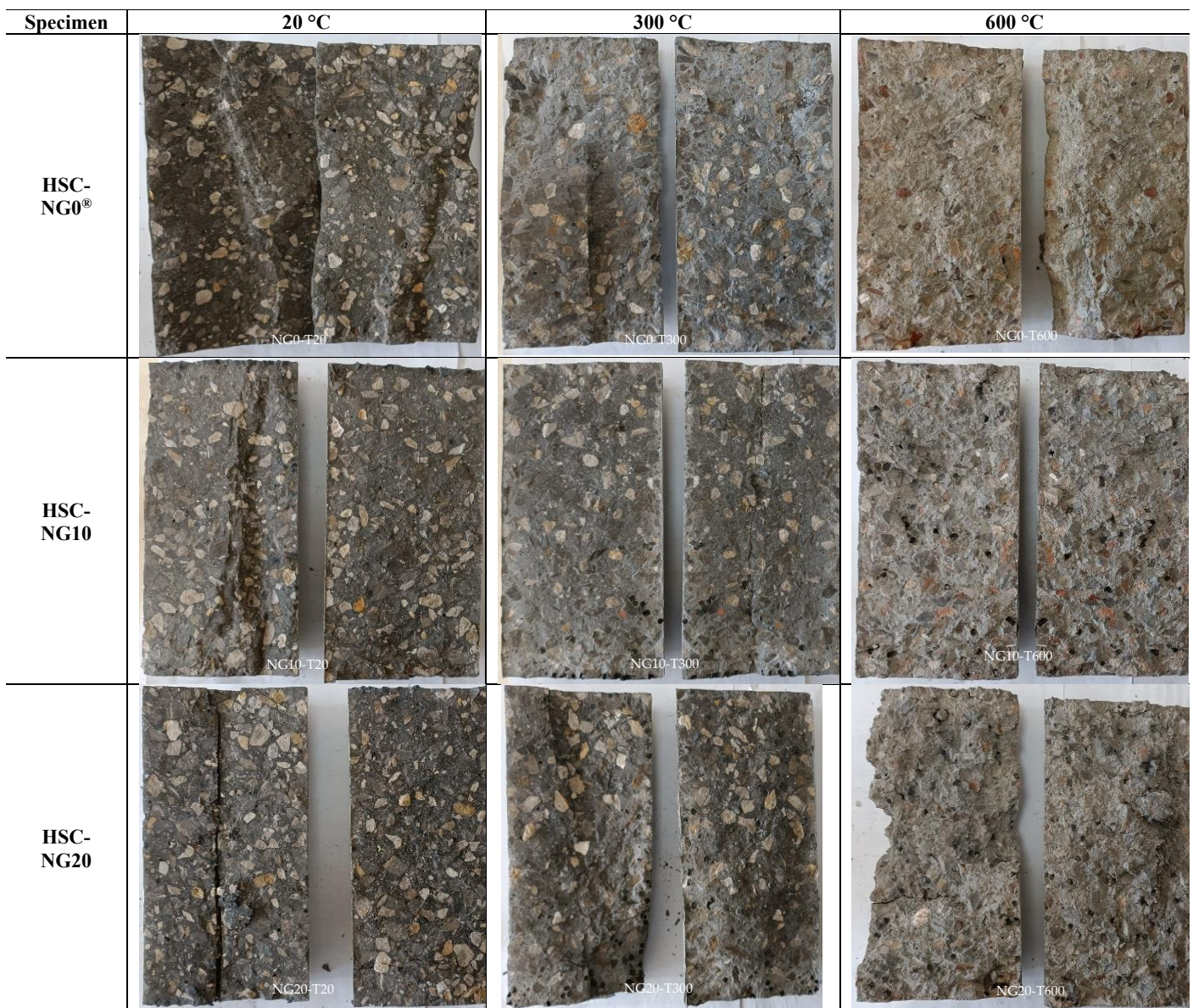


**Fig. 38. Failure mode of specimens under tensile loading.**

## 5. Conclusions

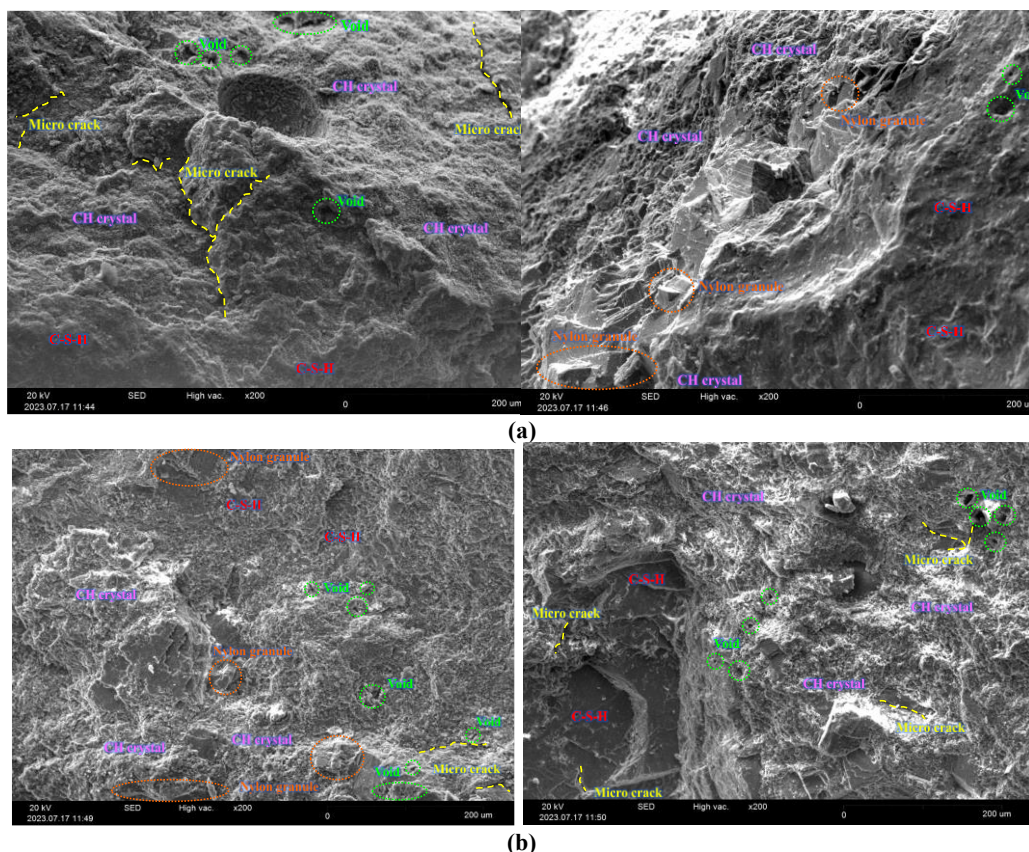
This study investigated the compressive stress-strain behavior of HSC containing NG after exposure to elevated temperatures. Furthermore, empirical relationships were developed to predict the mechanical properties of NG-incorporated high-strength concrete subjected to various temperature levels. Based on these relationships, a model was formulated to simulate the compressive stress-strain response of this type of concrete. In addition, the predicted results were compared with experimental findings as well as with the values recommended by international design codes and standards.

- Weight loss in concrete specimens increased with elevated temperatures, especially at 600°C. At 300°C, the reference specimens showed a 2% weight loss, while specimens with 10 and 20% nylon granules experienced 3 and 4% weight loss, respectively. At 600°C, weight loss rose to 8% for the reference specimens and 10 and 11% for the 10 and 20% nylon granule specimens, respectively. The highest weight loss occurred due to the complete decomposition of nylon granules. Overall, the specimens with 20% nylon replacement at 600°C showed the greatest weight loss (11%).
- Replacing natural fine aggregates with NG reduced the compressive strength of HSC, with the greatest loss (59.2%) at 20% NG at room temperature. Strength decreased further at elevated temperatures, particularly at 600 °C. Notably, specimens with 10% NG showed more stable performance above 300 °C, indicating that limited NG replacement balance thermal resilience and environmental benefits.
- Including NG as a partial replacement for natural fine aggregates reduced the splitting tensile strength of high-strength concrete HSC, with greater losses at higher temperatures. Strength decreased by up to 24.6% at room temperature with 20% NG. Upon exposure to 600 °C, all specimens showed significant strength reductions, with the 10% NG group exhibiting the lowest loss (59.2%), indicating slightly better thermal resistance.
- The inclusion of NG reduced both the initial and secant elastic moduli of HSC, with greater reductions observed at higher



temperatures. At 600 °C, modulus losses reached approximately 75% across all specimens. Notably, the lowest reduction in initial modulus occurred in the control group, while the smallest secant modulus loss was observed in specimens with 20% NG, indicating varied thermal responses depending on the modulus type and NG content.

- The peak strain of HSC increased with rising temperature, showing significant growth at 600 °C. Compared to room temperature, peak strain rose by 166.7, 46.9, and 90% for specimens with 0, 10, and 20% NG, respectively. While NG replacement generally reduced peak strain at ambient and 300 °C, all specimens exhibited notable softening and deformation under high thermal exposure.
- The ultimate strain of HSC increased with temperature, particularly at 600 °C, due to material softening and increased porosity. At room temperature and 300 °C, specimens with 10% NG showed the highest ultimate strain, while at 600 °C, the control group without NG exhibited the greatest value. These results suggest that limited NG replacement can enhance ductility at moderate temperatures, while higher temperatures promote greater deformation regardless of NG content.
- The toughness of HSC decreased with both increasing NG content and elevated temperature. Reference specimens without NG consistently exhibited the highest toughness due to their greater compressive strength. While peak strain varied slightly, the combined effect of reduced strength and increased strain at higher temperatures led to an overall decline in toughness across all specimens.
- A model was proposed to accurately represent the axial compressive stress-strain behavior of concrete containing NG at elevated temperatures. Based on empirical equations for various mechanical concrete properties, the model showed suitable agreement with experimental results, effectively capturing the changes in stress-strain behavior at different temperatures.
- Concrete exposed to elevated temperatures showed clear signs of damage, including color changes, surface cracking, and increased porosity. At 300°C and above temperatures, nylon granules softened and fully decomposed at 600°C, creating internal voids and contributing to a more porous concrete structure. The decomposed granules evaporated through surface cracks, leaving behind hardened nylon droplets on the surface.
- Compressive strength tests demonstrated that failure in specimens exposed to high temperatures occurred gradually. Cracks formed before peak stress, and failure was slower compared to unexposed specimens. Specimens exposed to 600°C exhibited milder cracking sounds and slower failure. Internal inspection revealed increased porosity and fading color caused by water loss and nylon granule decomposition.
- The microstructural analysis of high-strength concrete with 10% NG replacement showed notable changes at elevated temperatures. At 20°C, nylon granules were visible with minimal microcracking and porosity. At 300°C, increased porosity occurred due to water evaporation and partial nylon granule decomposition. At 600°C, the highest porosity and microcracking were observed, resulting from complete nylon granule decomposition, CH crystal dehydration, and C-S-H gel breakdown, with large voids indicating nylon evaporation.



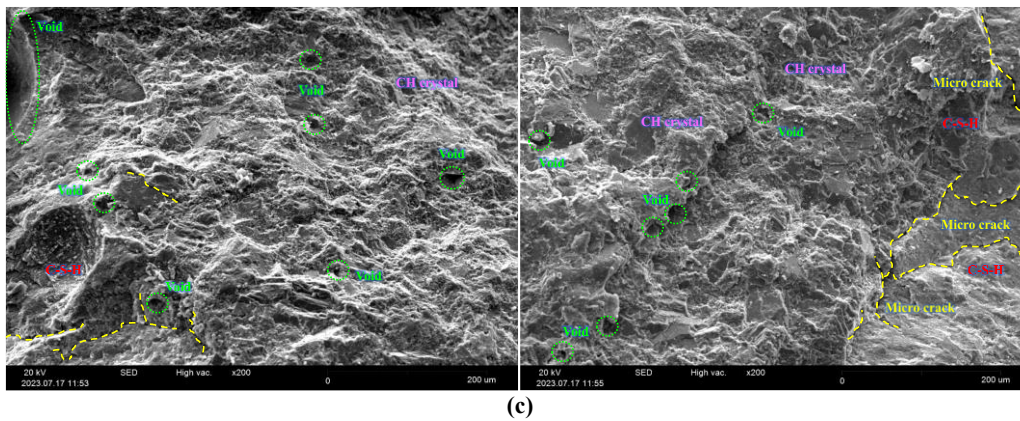


Fig. 39. SEM micrographs of heated and non-heated high-strength concrete specimens containing nylon granule: (a) SEM image of cement paste after exposure to 20 °C, (b) SEM image of cement paste after exposure to 300 °C, and (c) SEM image of cement paste after exposure to 600 °C.

## Statements & declarations

### Author contributions

**Fariborz Sasania:** Conceptualization, Investigation, Methodology, Formal analysis, Resources, Writing - Original Draft, Writing - Review & Editing.

**Mahdi Nematzadeh:** Conceptualization, Methodology, Formal analysis, Project administration, Supervision, Writing - Review & Editing.

**Maryam Asadi:** Investigation, Visualization, Validation, Formal analysis, Resources, Writing - Original Draft, Writing - Review & Editing.

**Arman Aminian:** Investigation, Visualization, Validation, Formal analysis, Resources, Writing - Original Draft, Writing - Review & Editing.

### Funding

The authors received no financial support for the research, authorship, and/or publication of this article.

### Data availability

The data presented in this study will be available on interested request from the corresponding author.

### Declarations

The authors declare no conflict of interest.

## References

- [1] Li, D., Zhuge, Y., Gravina, R., Mills, J. E. Compressive Stress Strain Behavior of Crumb Rubber Concrete (CRC) and Application in Reinforced CRC Slab. *Construction and Building Materials*, 2018; 166: 745–759. doi:10.1016/j.conbuildmat.2018.01.142.
- [2] Zarei, M., Rahmani, Z., Zahedi, M., Nasrollahi, M. Technical, Economic, and Environmental Investigation of the Effects of Rubber Powder Additive on Asphalt Mixtures. *Journal of Transportation Engineering, Part B: Pavements*, 2020; 146 (1): 04019039. doi:10.1061/jpeodx.0000142.
- [3] Tayebi, M., Nematzadeh, M. Post-Fire Flexural Performance and Microstructure of Steel Fiber-Reinforced Concrete with Recycled Nylon Granules and Zeolite Substitution. *Structures*, 2021; 33: 2301–2316. doi:10.1016/j.istruc.2021.05.080.
- [4] Thomas, B. S., Chandra Gupta, R. Properties of High Strength Concrete Containing Scrap Tire Rubber. *Journal of Cleaner Production*, 2016; 113: 86–92. doi:10.1016/j.jclepro.2015.11.019.
- [5] Gupta, T., Chaudhary, S., Sharma, R. K. Assessment of Mechanical and Durability Properties of Concrete Containing Waste Rubber Tire as Fine Aggregate. *Construction and Building Materials*, 2014; 73: 562–574. doi:10.1016/j.conbuildmat.2014.09.102.
- [6] Pelisser, F., Zavarise, N., Longo, T. A., Bernardin, A. M. Concrete Made with Recycled Tire Rubber: Effect of Alkaline Activation and Silica Fume Addition. *Journal of Cleaner Production*, 2011; 19 (6–7): 757–763. doi:10.1016/j.jclepro.2010.11.014.
- [7] Mousavimehr, M., Nematzadeh, M. Predicting Post-Fire Behavior of Crumb Rubber Aggregate Concrete. *Construction and Building Materials*, 2019; 229. doi:10.1016/j.conbuildmat.2019.116834.
- [8] Wang, H. Y., Chen, B. T., Wu, Y. W. A Study of the Fresh Properties of Controlled Low-Strength Rubber Lightweight Aggregate Concrete (CLSRCLC). *Construction and Building Materials*, 2013; 41: 526–531. doi:10.1016/j.conbuildmat.2012.11.113.

- [9] Al-Tayeb, M. M., Abu Bakar, B. H., Akil, H. M., Ismail, H. Performance of Rubberized and Hybrid Rubberized Concrete Structures under Static and Impact Load Conditions. *Experimental Mechanics*, 2013; 53 (3): 377–384. doi:10.1007/s11340-012-9651-z.
- [10] Yung, W. H., Yung, L. C., Hua, L. H. A Study of the Durability Properties of Waste Tire Rubber Applied to Self-Compacting Concrete. *Construction and Building Materials*, 2013; 41: 665–672. doi:10.1016/j.conbuildmat.2012.11.019.
- [11] Yilmaz, A., Degirmenci, N. Possibility of Using Waste Tire Rubber and Fly Ash with Portland Cement as Construction Materials. *Waste Management*, 2009; 29 (5): 1541–1546. doi:10.1016/j.wasman.2008.11.002.
- [12] Nematzadeh, M., Mousavimehr, M. Residual Compressive Stress–Strain Relationship for Hybrid Recycled PET–Crumb Rubber Aggregate Concrete after Exposure to Elevated Temperatures. *Journal of Materials in Civil Engineering*, 2019; 31 (8). doi:10.1061/(asce)mt.1943-5533.0002749.
- [13] Gjörv O. E. High-strength concrete. Developments in the Formulation and Reinforcement of Concrete. 2008. Woodhead Publishing, Sawston, United Kingdom. doi:10.1016/b978-0-08-102616-8.00007-1.
- [14] Ferreira R. M, Jalali S., Gjörv O. E. Probabilistic assessment of the durability performance of concrete structures. *Engenharia Civil UM*, 2004; 39-48.
- [15] Singh, S., Nagar, R., Agrawal, V., Rana, A., Tiwari, A. Sustainable Utilization of Granite Cutting Waste in High Strength Concrete. *Journal of Cleaner Production*, 2016; 116: 223–235. doi:10.1016/j.jclepro.2015.12.110.
- [16] Mohammed, A. A., Karim, S. H. Impact Strength and Mechanical Properties of High Strength Concrete Containing PET Waste Fiber. *Journal of Building Engineering*, 2023; 68. doi:10.1016/j.job.2023.106195.
- [17] Bilow, D. N., Kamara, M. E. Fire and Concrete Structures. *Proceedings of the 2008 Structures Congress - Structures Congress 2008: Crossing the Borders*, 2008; 314: 1–10. doi:10.1061/41016(314)299.
- [18] Hassanli, R., Youssf, O., Mills, J. E. Experimental Investigations of Reinforced Rubberized Concrete Structural Members. *Journal of Building Engineering*, 2017; 10: 149–165. doi:10.1016/j.job.2017.03.006.
- [19] Xue, J., Shinozuka, M. Rubberized Concrete: A Green Structural Material with Enhanced Energy-Dissipation Capability. *Construction and Building Materials*, 2013; 42: 196–204. doi:10.1016/j.conbuildmat.2013.01.005.
- [20] Karimi, A., Nematzadeh, M. Axial Compressive Performance of Steel Tube Columns Filled with Steel Fiber-Reinforced High Strength Concrete Containing Tire Aggregate after Exposure to High Temperatures. *Engineering Structures*, 2020; 219. doi:10.1016/j.engstruct.2020.110608.
- [21] Guo, Y. C., Zhang, J. H., Chen, G. M., Xie, Z. H. Compressive Behaviour of Concrete Structures Incorporating Recycled Concrete Aggregates, Rubber Crumb and Reinforced with Steel Fibre, Subjected to Elevated Temperatures. *Journal of Cleaner Production*, 2014; 72: 193–203. doi:10.1016/j.jclepro.2014.02.036.
- [22] Nematzadeh, M., Shahmansouri, A. A., Fakoor, M. Post-Fire Compressive Strength of Recycled PET Aggregate Concrete Reinforced with Steel Fibers: Optimization and Prediction via RSM and GEP. *Construction and Building Materials*, 2020; 252. doi:10.1016/j.conbuildmat.2020.119057.
- [23] Gupta, T., Siddique, S., Sharma, R. K., Chaudhary, S. Effect of Elevated Temperature and Cooling Regimes on Mechanical and Durability Properties of Concrete Containing Waste Rubber Fiber. *Construction and Building Materials*, 2017; 137: 35–45. doi:10.1016/j.conbuildmat.2017.01.065.
- [24] Marques, A. M., Correia, J. R., De Brito, J. Post-Fire Residual Mechanical Properties of Concrete Made with Recycled Rubber Aggregate. *Fire Safety Journal*, 2013; 58: 49–57. doi:10.1016/j.firesaf.2013.02.002.
- [25] Al-Mutairi, N., Al-Rukaibi, F., Bufarsan, A. Effect of Microsilica Addition on Compressive Strength of Rubberized Concrete at Elevated Temperatures. *Journal of Material Cycles and Waste Management*, 2010; 12 (1): 41–49. doi:10.1007/s10163-009-0243-7.
- [26] Mousa, M. I. Effect of Elevated Temperature on the Properties of Silica Fume and Recycled Rubber-Filled High Strength Concretes (RHSC). *HBRC Journal*, 2017; 13 (1): 1–7. doi:10.1016/j.hbrcj.2015.03.002.
- [27] Nematzadeh, M., Arjomandi, A., Fakoor, M., Aminian, A., Khorshidi-Mianaei, A. Pre-and Post-Heating Bar-Concrete Bond Behavior of CFRP-Wrapped Concrete Containing Polymeric Aggregates and Steel Fibers: Experimental and Theoretical Study. *Engineering Structures*, 2024; 321. doi:10.1016/j.engstruct.2024.118929.
- [28] Nematzadeh, M., Hosseini, S. A., Ozbakkaloglu, T. The Combined Effect of Crumb Rubber Aggregates and Steel Fibers on Shear Behavior of GFRP Bar-Reinforced High-Strength Concrete Beams. *Journal of Building Engineering*, 2021; 44. doi:10.1016/j.job.2021.102981.
- [29] American Concrete Institute (ACI). ACI 216R-89: Guide for determining the fire endurance of concrete elements. Farmington Hills (MI): ACI; 1989.
- [30] American Society of Civil Engineers (ASCE). Structural fire protection. Reston (VA): ASCE; 1992. doi:10.1061/9780872628885.
- [31] European Committee for Standardization (CEN). EN 1994-1-2: Design of composite steel and concrete structures – Part 1-2: General

rules for structural fire design. Brussels (BE): CEN; 2004.

- [32] European Committee for Standardization (CEN). EN 1992-1-2: Design of concrete structures – Part 1-2: General rules – Structural fire design. Brussels (BE): CEN; 2004.
- [33] Comité Euro-International du Béton (CEB). Fire design of concrete structures – in accordance with CEB/FIP Model Code 90. Lausanne (CH): CEB; 1991.
- [34] ASTM International. ASTM C150-07: Standard specification for Portland cement. West Conshohocken (PA): ASTM International; 2012. doi:10.1520/C0150-07.
- [35] ASTM International. ASTM C33/C33M-16: Standard specification for concrete aggregates. West Conshohocken (PA): ASTM International; 2016. doi:10.1520/C0033\_C0033M-16.
- [36] ASTM International. ASTM C128-12: Standard test method for density, relative density (specific gravity), and absorption of fine aggregate. West Conshohocken (PA): ASTM International; 2015. doi:10.1520/C0128-07A.
- [37] American Concrete Institute (ACI). ACI 211.1-91: Standard practice for selecting proportions for normal, heavyweight, and mass concrete. Farmington Hills (MI): ACI; 2008.
- [38] ASTM International. ASTM C143/C143M-10a: Standard test method for slump of hydraulic-cement concrete. West Conshohocken (PA): ASTM International; 2012. doi:10.1520/C0143\_C0143M-10A.
- [39] ASTM International. ASTM C192/C192M-14: Standard practice for making and curing concrete test specimens in the laboratory. West Conshohocken (PA): ASTM International; 2015. doi:10.1520/C0192\_C0192M-14.
- [40] International Organization for Standardization (ISO). ISO 834-1:1999: Fire resistance tests – Elements of building construction – Part 1: General requirements. Geneva (CH): ISO; 1999.
- [41] Manzoor, T., Bhat, J. A., Shah, A. H. Performance of Geopolymer Concrete at Elevated Temperature – A Critical Review. *Construction and Building Materials*, 2024; 420. doi:10.1016/j.conbuildmat.2024.135578.
- [42] Babalola, O. E., Awoyera, P. O., Le, D. H., Bendezi Romero, L. M. A Review of Residual Strength Properties of Normal and High Strength Concrete Exposed to Elevated Temperatures: Impact of Materials Modification on Behaviour of Concrete Composite. *Construction and Building Materials*, 2021; 296. doi:10.1016/j.conbuildmat.2021.123448.
- [43] ASTM International. ASTM C39/C39M-14: Standard test method for compressive strength of cylindrical concrete specimens. West Conshohocken (PA): ASTM International; 2014. doi:10.1520/C0039\_C0039M-14.
- [44] ASTM International. ASTM C496-96: Standard test method for splitting tensile strength of cylindrical concrete specimens. West Conshohocken (PA): ASTM International; 2017. doi:10.1520/C0496-96.
- [45] ASTM International. ASTM C469/C469M-10: Standard test method for static modulus of elasticity and Poisson's ratio of concrete in compression. West Conshohocken (PA): ASTM International; 2014. doi:10.1520/C0469\_C0469M-10.
- [46] Tayeh, B. A., Zeyad, A. M., Agwa, I. S., Amin, M. Effect of Elevated Temperatures on Mechanical Properties of Lightweight Geopolymer Concrete. *Case Studies in Construction Materials*, 2021; 15. doi:10.1016/j.cscm.2021.e00673.
- [47] Fernandes, B., Carré, H., Mindeguia, J. C., Perlot, C., La Borderie, C. Effect of Elevated Temperatures on Concrete Made with Recycled Concrete Aggregates - An Overview. *Journal of Building Engineering*, 2021; 44. doi:10.1016/j.jobbe.2021.103235.
- [48] Tu, W., Zhang, M. Behaviour of Alkali-Activated Concrete at Elevated Temperatures: A Critical Review. *Cement and Concrete Composites*, 2023; 138. doi:10.1016/j.cemconcomp.2023.104961.
- [49] Gesoglu, M., Güneyisi, E., Hansu, O., Ipek, S., Asaad, D. S. Influence of Waste Rubber Utilization on the Fracture and Steel-Concrete Bond Strength Properties of Concrete. *Construction and Building Materials*, 2015; 101: 1113–1121. doi:10.1016/j.conbuildmat.2015.10.030.
- [50] Murthy, A. R. C., Palani, G. S., Iyer, N. R. State-of-the-Art Review on Fracture Analysis of Concrete Structural Components. *Sadhana - Academy Proceedings in Engineering Sciences*, 2009; 34 (2): 345–367. doi:10.1007/s12046-009-0014-0.
- [51] Yesilata, B., Isiker, Y., Turgut, P. Thermal Insulation Enhancement in Concretes by Adding Waste PET and Rubber Pieces. *Construction and Building Materials*, 2009; 23 (5): 1878–1882. doi:10.1016/j.conbuildmat.2008.09.014.
- [52] Fawzy, H., Mustafa, S., Abd El Badie, A. Effect of Elevated Temperature on Concrete Containing Waste Tires Rubber. *The Egyptian International Journal of Engineering Sciences and Technology*, 2020; 29 (1): 1–13. doi:10.21608/eijest.2020.97315.
- [53] Zheng, L., Huo, X. S., Yuan, Y. Strength, Modulus of Elasticity, and Brittleness Index of Rubberized Concrete. *Journal of Materials in Civil Engineering*, 2008; 20 (11): 692–699. doi:10.1061/(asce)0899-1561(2008)20:11(692).
- [54] Correia, J. R., Lima, J. S., De Brito, J. Post-Fire Mechanical Performance of Concrete Made with Selected Plastic Waste Aggregates. *Cement and Concrete Composites*, 2014; 53: 187–199. doi:10.1016/j.cemconcomp.2014.07.004.
- [55] Abdullah, W., AbdulKadir, M., Muhammad, M. Effect of High Temperature on Mechanical Properties of Rubberized Concrete Using

- Recycled Tire Rubber as Fine Aggregate Replacement. *Engineering and Technology Journal*, 2018; 36 (8A): 906–913. doi:10.30684/etj.36.8a.10.
- [56] Beushausen, H., Dittmer, T. The Influence of Aggregate Type on the Strength and Elastic Modulus of High Strength Concrete. *Construction and Building Materials*, 2015; 74: 132–139. doi:10.1016/j.conbuildmat.2014.08.055.
- [57] Georgali, B., Tsakiridis, P. E. Microstructure of Fire-Damaged Concrete. A Case Study. *Cement and Concrete Composites*, 2005; 27 (2): 255–259. doi:10.1016/j.cemconcomp.2004.02.022.
- [58] Huang, Z., Liew, J. Y. R., Li, W. Evaluation of Compressive Behavior of Ultra-Lightweight Cement Composite after Elevated Temperature Exposure. *Construction and Building Materials*, 2017; 148: 579–589. doi:10.1016/j.conbuildmat.2017.04.121.
- [59] Zheng, W., Luo, B., Wang, Y. Stress–Strain Relationship of Steel-Fibre Reinforced Reactive Powder Concrete at Elevated Temperatures. *Materials and Structures/Materiaux et Constructions*, 2015; 48 (7): 2299–2314. doi:10.1617/s11527-014-0312-9.
- [60] Akbarzadeh Bengar, H., Shahmansouri, A. A., Akkas Zangebari Sabet, N., Kabirifar, K., W.Y. Tam, V. Impact of Elevated Temperatures on the Structural Performance of Recycled Rubber Concrete: Experimental and Mathematical Modeling. *Construction and Building Materials*, 2020; 255. doi:10.1016/j.conbuildmat.2020.119374.
- [61] Chen, G. M., He, Y. H., Yang, H., Chen, J. F., Guo, Y. C. Compressive Behavior of Steel Fiber Reinforced Recycled Aggregate Concrete after Exposure to Elevated Temperatures. *Construction and Building Materials*, 2014; 71: 1–15. doi:10.1016/j.conbuildmat.2014.08.012.
- [62] Sheikh, S., Uzumeri, S. M. Analytical Model for Concrete Confinement in Tied Columns. *Journal of the Structural Division*, 1982; 108 (ST12): 2703–2722. doi:10.1061/jsdeag.0006100.
- [63] Frangou, M., Pilakoutas, K., Dritsos, S. Structural Repair/Strengthening of RC Columns. *Construction and Building Materials*, 1995; 9 (5): 259–266. doi:10.1016/0950-0618(95)00013-6.
- [64] Tasdemir, M. A., Tasdemir, C., Akyüz, S., Jefferson, A. D., Lydon, F. D., Barr, B. I. G. Evaluation of Strains at Peak Stresses in Concrete: A Three-Phase Composite Model Approach. *Cement and Concrete Composites*, 1998; 20 (4): 301–318. doi:10.1016/S0958-9465(98)00012-2.
- [65] Nataraja, M. C., Dhang, N., Gupta, A. P. Stress-Strain Curves for Steel-Fiber Reinforced Concrete under Compression. *Cement and Concrete Composites*, 1999; 21 (5–6): 383–390. doi:10.1016/S0958-9465(99)00021-9.
- [66] Nematzadeh, M., Salari, A., Ghadami, J., Naghipour, M. Stress-Strain Behavior of Freshly Compressed Concrete under Axial Compression with a Practical Equation. *Construction and Building Materials*, 2016; 115: 402–423. doi:10.1016/j.conbuildmat.2016.04.045.



# The Tank's Geometric Properties Effect on the Sloshing Wave Height and the Resulting Forces on the Roof

Ali Ebrahimi Hariri <sup>a\*</sup>, Yaghoub Mohammadi <sup>a</sup>

<sup>a</sup> Civil Engineering Department, University of Mohaghegh Ardabili, Iran

## ARTICLE INFO

### Keywords:

Geometric properties  
Sloshing height  
Upward force  
Sufficient non-zero freeboard

### Article history:

Received 6 April 2025  
Accepted 13 May 2025  
Available online 21 May 2022

## ABSTRACT

This paper outlines the effects of freeboard height sufficiency on sloshing wave characteristics, considering the geometric properties of rectangular tanks. Recorded ground accelerations of the 1999 Kocaeli and 1994 Northridge earthquakes are applied to the finite element model with different geometric assumptions. Both the frequency content of recorded ground motions and their PGA influence the sloshing wave responses. The geometric properties include the ratio of contained liquid height to tank length, wall elasticity, wall thickness, and freeboard height, considering tanks with and without the roof. The choice of roofed or roofless tanks significantly affects the sloshing properties because of non-zero insufficient freeboard influences. Sloshing height is studied for the roofless tanks, assuming sufficient freeboards. The upward force arising from inadequate freeboard shows the roofed tanks' sloshing wave characteristics, including various insufficient freeboards. For the roofless tanks, the rigidity assumption and the thickness reduction of elastic tanks reduce the sloshing height. The maximum sloshing height also decreases by decreasing the ratio of the contained liquid height to the tank length. So, the roofless tanks exhibit a clear trend in the tank geometric variations. The roofed tanks with zero insufficient freeboards also show a regular trend; however, the sloshing forces increase by decreasing the H to L ratio. But, tanks with insufficient non-zero freeboards do not indicate any steady trend for the geometric variation because of non-zero insufficient freeboard effects. A comparison of upward forces applied to the tanks' roof with their corresponding sloshing height time history shows the importance of zero or non-zero assumption for the freeboard height to control the sloshing characteristics. So, the sloshing wave responses are significantly dependent on the insufficient freeboard height assumption, although their responses depend on the tanks' various geometric properties.

## 1. Introduction

As crucial structures of modern society, liquid storage tanks must be designed to have no service limitations during earthquake excitation. Nevertheless, they are susceptible to high stresses under seismic excitation due to their considerable mass. The seismic-induced stresses may lead to cracking, leakage, or structural collapse. These structures' seismic responses are affected by earthquake properties and factors such as the fluid interaction, soil characteristics, flexibility of the body material, etc. [1, 2]. Among several parameters, earthquake-induced surface sloshing is one of the most important phenomena that has caused engineers and researchers to worry about it. Due to insufficient freeboard, the sloshing wave applies upward forces on the tanks' roof or spills liquid out for the roofless tanks. Considering this phenomenon's complexity, evaluation of the sloshing characteristics is of great importance [3-5].

Investigating the tanks' free surface sloshing characteristics, Edwards [6] applied the finite element method in combination with

\* Corresponding author.

E-mail addresses: [aliebrahimihariri@uma.ac.ir](mailto:aliebrahimihariri@uma.ac.ir) (A. Ebrahimi Hariri).



<https://doi.org/10.22080/ceas.2025.28937.1000>

ISSN: 3092-7749/© 2025 The Author(s). Published by University of Mazandaran.

This article is an open access article distributed under the terms and conditions of the Creative Commons Attribution (CC-BY) license (<https://creativecommons.org/licenses/by/4.0/deed.en>)

How to cite this article: Ebrahimi Hariri, A., Mohammadi, Y. The tank's geometric properties effect on the sloshing wave height and the resulting forces on the roof. Contributions of Civil Engineering and Applied Solutions. 2025;1(1): 36-52. doi:10.22080/ceas.2025.28937.1000.

the refined shell theory to study the sloshing, considering the induced stresses. Yang [7] investigated the tank structures' responses, assuming rigidity and elasticity for the empty state. Dogangun et al. [8] developed a three-dimensional finite element model of a rectangular tank, analyzing the tank by Lagrangian formulation. Ghaemmaghami [9] and Ghaemmaghami and Kianoush [10] examined the seismic behavior of two-dimensional tanks. They found that the walls' flexibility and the damping properties influence the structure's dynamic response behavior. Li and Wang [11] investigated the various methods of analyzing the sloshing in rectangular tanks. Parthasarathy [12] considered the effects of the natural frequencies of a rectangular and prismatic reservoir. They modeled sloshing by the volume fractionation (VOF) method and investigated the sloshing phenomenon by applying compressive load changes. Moslemi et al. [13] obtained the finite element response of free surface sloshing height by examining the parameters affecting rectangular tanks.

Milgram [14] performed a series of tests on partially filled tanks, studying the effect of abrupt changes of vertical velocity and free surface disturbances, and on the distribution of pressure on the roof. They also considered free surface disturbances. Minova et al. [15] and Minova [16] conducted a series of vibration plate tests on a rectangular tank to evaluate the roof's inserted pressure. They considered the natural frequencies effects. Chen et al. [17] calculated the dynamic compressive loads applied to the tank body due to the sloshing wave under a horizontal seismic excitation. They compared their numerical results with the experimental data. Kabiri et al. [5] investigated the sloshing wave impact force (SWIF) in tanks using numerical simulation based on the Boltzmann Network Method (LBM). They showed that the simple method recommended by the relevant codes and standards significantly measures the immersion force below the actual value. Lu et al. [18] calculated the impact force by a new method, including the sloshing height. Jena et al. [4] employed the meshless particle method to simulate the phenomena of intense free-surface sloshing flow. Base shear, overturning moment, forces applied against walls, and loads applied to the roofs were evaluated.

This study investigates the effects of tanks' geometric properties, especially non-zero insufficient freeboard, on the sloshing wave properties. Roofless tanks with sufficient freeboards and roofed tanks, considering bounded freeboards, are analyzed. The coupled problem of the liquid tank is analyzed employing the Lagrangian formulation. Different freeboards and boundary conditions are assumed. To do so, first, the effects of wall flexibility are studied considering walls with various thicknesses. In the following, rigid-roofed and roofless tanks with different geometric characteristics are supposed to investigate the freeboard height on the sloshing height and sloshing forces characteristics.

## 2. Conceptual review

Several methods have been proposed in computational fluid dynamics to model the fluid-structure coupling problem. These approaches are usually the Lagrangian, Eulerian, or a combination of both (ALE) approaches. In this study, the Lagrangian method formulates both the fluid and structure domains. On this account, the displacement as the variable describes both fluid and structural responses. So, the Lagrangian fluid is assumed to be linearly elastic, inviscid, and irrotational. The general two-dimensional stress-strain equation of a fluid element is [19].

$$\begin{Bmatrix} P \\ P_z \end{Bmatrix} = \begin{bmatrix} C_{11} & 0 \\ 0 & C_{22} \end{bmatrix} \begin{Bmatrix} \varepsilon_v \\ W_z \end{Bmatrix} \quad (1)$$

where  $P$  is the pressure,  $P_z$  is the rotational stress,  $C_{11}$  is the bulk modulus of fluid,  $C_{22}$  is the constraint parameter related to  $W_z$ ,  $\varepsilon_v$  is the volumetric strain, and  $W_z$  is the rotation about the axis  $Z$ .

Considering the pressure at the fluid free surface due to the sloshing effects, its stiffness matrix is calculated from the discretization of the following equation:

$$P = \gamma_w U_{fn} \quad (2)$$

where  $\gamma_w$  is the weight density of the fluid, and  $U_{fn}$  is the normal component of the free surface movement. In the following, the fluid total strain energy is employed to obtain the finite element approximation:

$$\Pi_e = \frac{1}{2} U_f^T K_f U_f \quad (3)$$

$$K_f = \sum k_f^e \quad (4)$$

$$k_f^e = \int_V B_f^{eT} C_f B_f^e dV^e \quad (5)$$

where  $U_f$  is the nodal movement vector,  $K_f$  is the stiffness matrix of the fluid system,  $K_f^e$  is the fluid element stiffness matrix,  $C_f$  is the elasticity matrix consisting of diagonal terms in Equation 1, and  $B_f^e$  is the strain-displacement matrix of the fluid element. In addition, the free surface motion intensifies the system's potential energy, which is considered as follows:

$$\Pi_s = \frac{1}{2} U_{sf}^T S_f U_{sf} \quad (6)$$

$$s_f = \sum s_f^e \quad (7)$$

$$S_f^e = \rho_f g \int_A h_s^T h_s dA^e \quad (8)$$

where  $U_{sf}$  and  $S_f$  are the vertical nodal displacement vector and the stiffness matrix of the free surface of the fluid system, respectively.  $S_f$  is the sum of the stiffness matrices of the free surface fluid elements,  $S_f^e$  is the stiffness matrix of the free surface fluid element,  $h_s$  is the vector consisting of interpolation functions of the free surface fluid element,  $\rho_f$  is the mass density of the fluid, and  $g$  is the acceleration due to gravity. Furthermore, the kinetic energy of the system can be written as:

$$T = \frac{1}{2} \dot{U}_f^T M_f \dot{U}_f \quad (9)$$

$$M_f = \sum M_f^e \quad (10)$$

$$M_f^e = \rho_f \int_V H^T H dV^e \quad (11)$$

where  $\dot{U}_f$  is the nodal velocity vector,  $M_f$  is the mass matrix of the fluid system,  $M_f^e$  is the sum of the mass matrix of the fluid elements, and  $H$  is the matrix consisting of interpolation functions of the fluid element.

Finally, the fluid finite element formulation of motion is calculated by the combination of Eq. 3, 6 and 9 as follows:

$$M_f \ddot{U}_f + K_f^* U_f = R_f \quad (12)$$

where  $\ddot{U}_f$ ,  $U_f$ ,  $K_f^*$  and  $R_f$  are the nodal acceleration, the nodal displacement, the system stiffness matrix including the free surface stiffness, and the time-varying nodal force vector for the fluid system, respectively.

The coupled equations of the fluid-structure system are obtained considering the boundary condition at the fluid-surface interface.

$$U_n^+ = U_n^- \quad (13)$$

where  $U_n^-$  and  $U_n^+$  is the normal portion of the interface structure and fluid displacement, respectively. By considering the interface condition and damping effects, the equations of motion of the coupled system to ground motions are written as [19]:

$$M_C \ddot{U}_C + C_C \dot{U}_C + K_C U_C = R_C \quad (14)$$

where  $M_C$ ,  $C_C$ , and  $K_C$  are the mass, damping, and stiffness of the coupled system.  $U_C$ ,  $\dot{U}_C$  and  $\ddot{U}_C$  are the vectors of the displacement, velocity, and acceleration, respectively.  $R_C$  is forces that are applied to the coupled system [19].

### 3. Finite element modeling of fluid-structure tank

#### 3.1. Geometric specifications

This study categorized the tank models into two groups in Table 1 shows their geometric properties. All tanks are short as H's ratio (height of the contained liquid) to L/2 (half of the tank length) varies from 1 to 1/3. The models are two-dimensional (see Fig. 1). Two different liquid heights of 5m and 10m are assumed. The thickness of all concrete tank walls ( $t_w$ ) is 0.5m. Additionally, the tank's ( $H_w$ ) height is decided based on the height of the fluid ( $H$ ) and the freeboard. The roofless tanks have sufficient freeboards. The roofed tanks have some bounded freeboards (1.00m, 0.75m, 0.50m, 0.25m, and 0.00m). The H5L15 tank walls are considered flexible in group 1 to investigate their thickness and flexibility effects on the sloshing phenomena. Accordingly, the H5L15 walls are initially rigid. In the following, their thickness is 0.3m, 0.4m, and 0.5m. The H5L15 flexible models are both roofed and roofless. The roofed tanks have a freeboard of 1m, but the roofless tanks' freeboard height is 2m.

**Table 1. Geometric properties of tank models.**

Group	Names	L (m)	H (m)	2H /L	Number of element
Group 1	H5L10	10	5	1	2482
	H5L15	15	5	2/3	3795
	H5L30	30	5	1/3	7718
Group 2	H10L20	20	10	1	9368
	H10L30	30	10	2/3	13948
	H10L60	60	10	1/3	27688

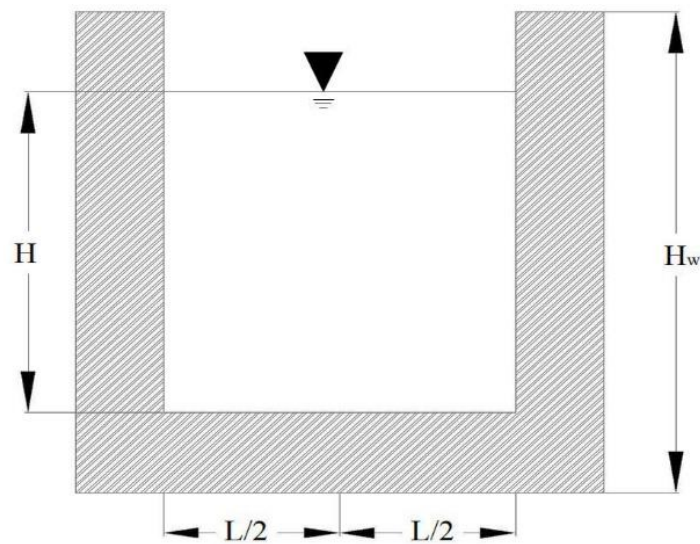


Fig. 1. Tank model without a roof in a two-dimensional model.

### 3.2. Material properties and boundary conditions

The 4-node shell elements model the tank's walls and the floor under plane strain assumption, considering 0.01m thickness for the tank along the Z-axis. The contact elements simulate the connection of the tank body to water, the tank body-roof, and the water-roof. The body and roof interfaces with the water are frictionless. But the internal friction angle between the body and the roof is 45 degrees. Table 2 shows the material properties for the walls, ceiling, and water. The equation of state of water, as the fluid of the container, is Mie-Gruneisen. Its material type is NULL.

Table 2. material properties of water and concrete [13, 20].

Water	Mass density (kg/m <sup>3</sup> )	Viscosity coefficient (Pa)	c (m/s)	$\gamma_0$	a	S <sub>1</sub>	S <sub>2</sub>	S <sub>3</sub>
	997	0.001	1480	0.5	0	2.56	1.986	1.2268
Concrete	Mass density (kg/m <sup>3</sup> )	Young's modulus (Pa)	Poisson's ratio					
	2300	2.66E10	0.17					

The interaction between the structure and soil is neglected. All the bottom nodes of the floor slab in all directions are restrained. All tanks and liquid nodes are tied in the Z-direction, moving in the longitudinal direction X and vertical direction Y. Seismic excitations are only inserted in the X-direction. The time step  $\Delta t$  is 0.1 s.

### 3.3. Seismic loads

Two different recorded ground accelerations, including 1999 Kocaeli and 1994 Northridge, are applied. Figs. 2 and 3 show their time histories. In this study, PGA values for both records are scaled at 0.1g and 0.3g.

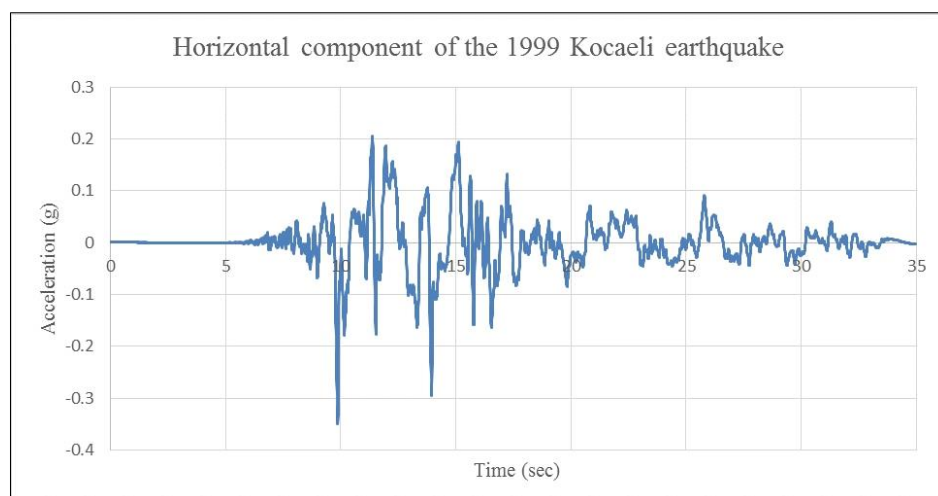
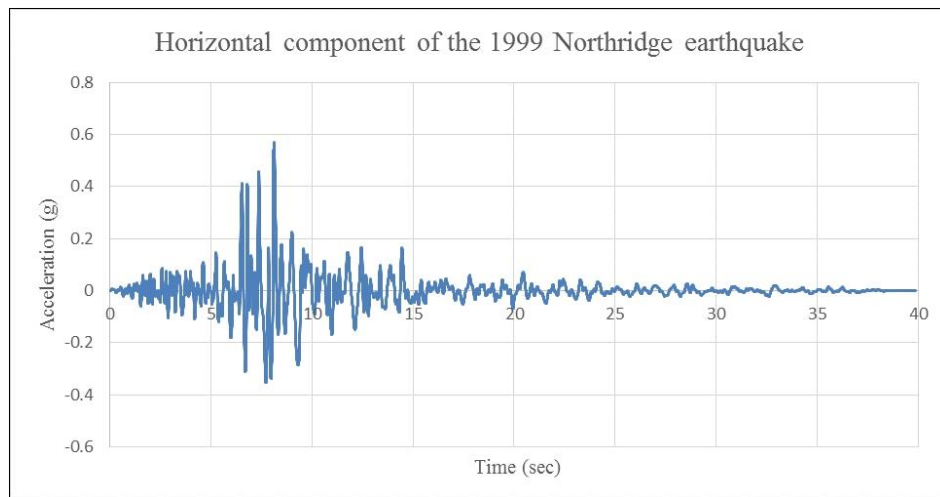
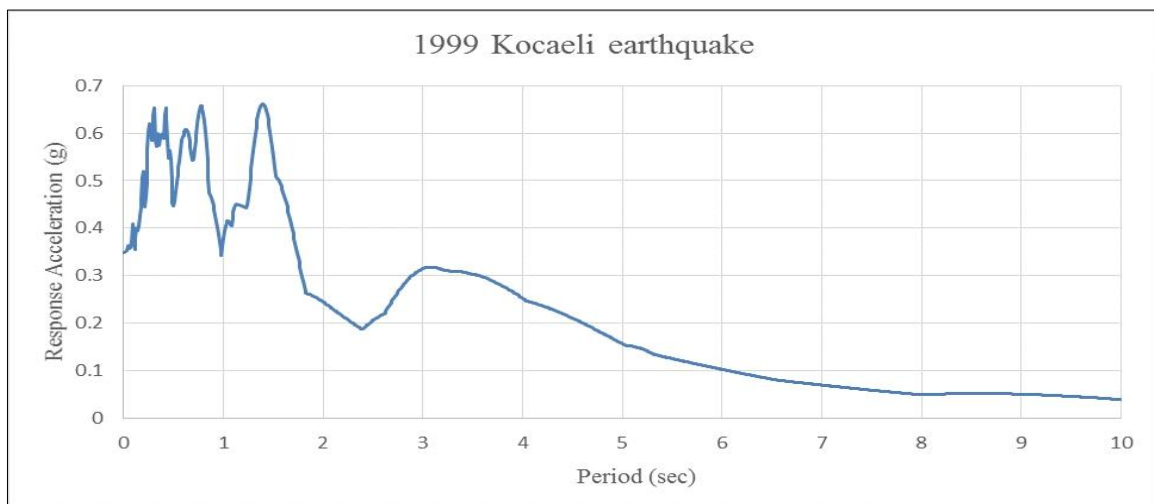


Fig. 2. Horizontal component of the 1999 Kocaeli earthquake.



**Fig. 3. Horizontal component of the 1994 Northridge earthquake.**

Different studies include the earthquake frequency content as a factor that affects the sloshing phenomena. The response spectrum acceleration of earthquake ground motions is shown in Figs. 4 and 5 to investigate the frequency content. Besides, the ratio of peak ground acceleration (PGA) to peak ground velocity (PGV) is selected as a frequency content indicator [21]. Based on the classification proposed by Elnashai and Di Sarho [22], there are three categories which are: 1- low ratio when  $PGA/PGV < 0.8$ , 2- Intermediate ratio, including  $0.8 < PGA/PGV < 1.2$ , and 3- High ratio, including  $PGA/PGV > 1.2$ . For the Kocaeli earthquake, the  $PGA/PGV$  is less than 0.8, whereas for the Northridge earthquake, the ratio is about 0.8.



**Fig. 4. Response spectrum acceleration of the 1999 Kocaeli earthquake.**

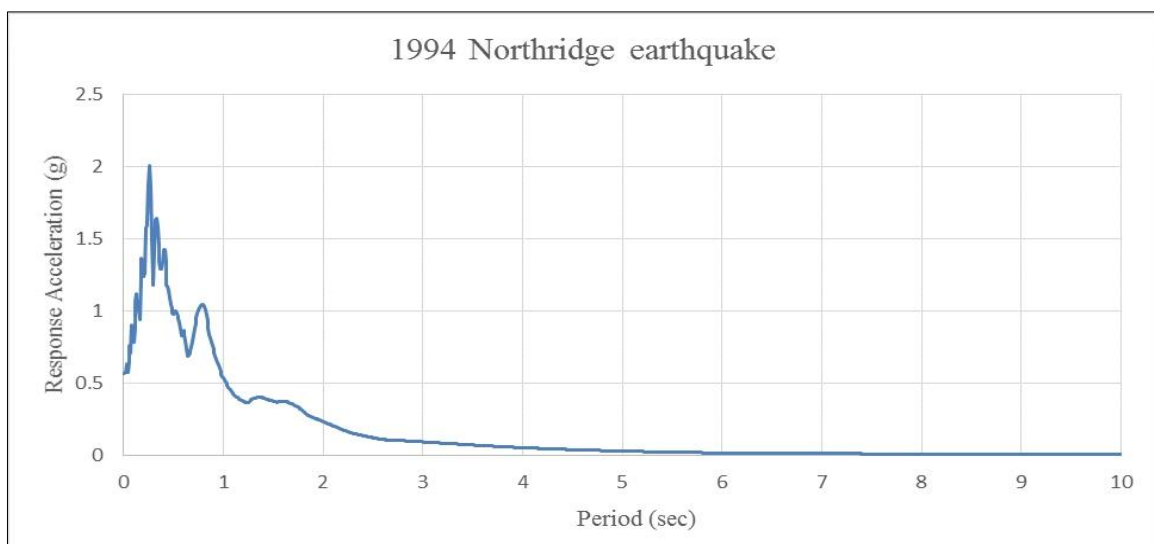


**Fig. 5. Response spectrum acceleration of the 1994 Northridge earthquake.**

### 3.4. Optimum size of the elements

Concerning the element size for reducing the computational cost, different element sizes are investigated, considering different mesh sizes varying from 0.01m to 0.6m. The length of the tank, water height, and freeboard are selected 15m, 5m, and 2m (H5L15 tank), respectively. The elastic wall thickness is assumed to be 0.5m. Fig 6 shows the artificial seismic excitation.

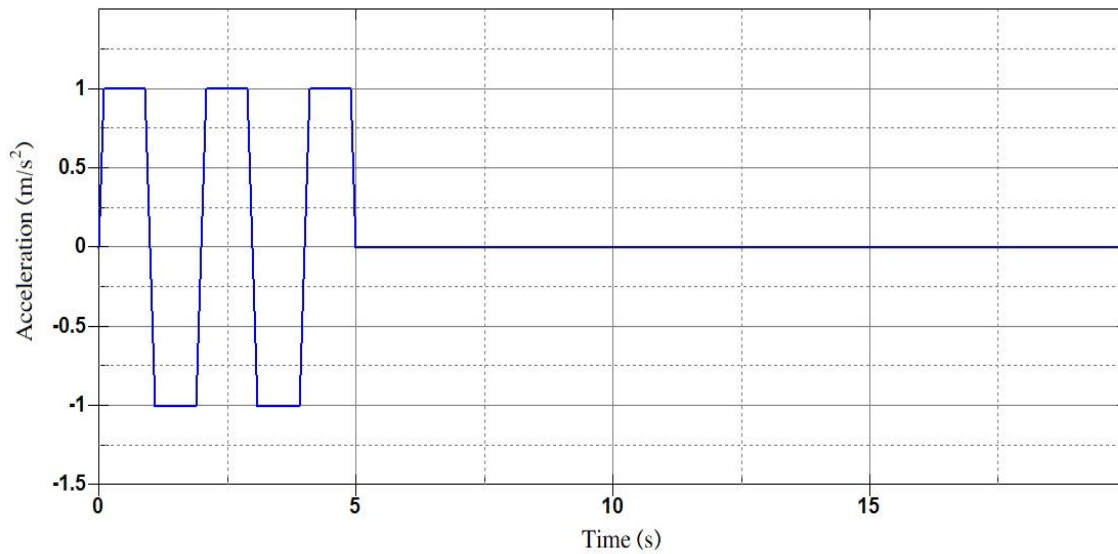


**Fig. 6. artificial seismic excitation.**

By applying artificial seismic excitation (Fig. 6), the maximum sloshing height is obtained. According to the results (Fig. 7), for the elements smaller than 0.2m, the sloshing height has no considerable change. So elements up to 0.2m are selected.

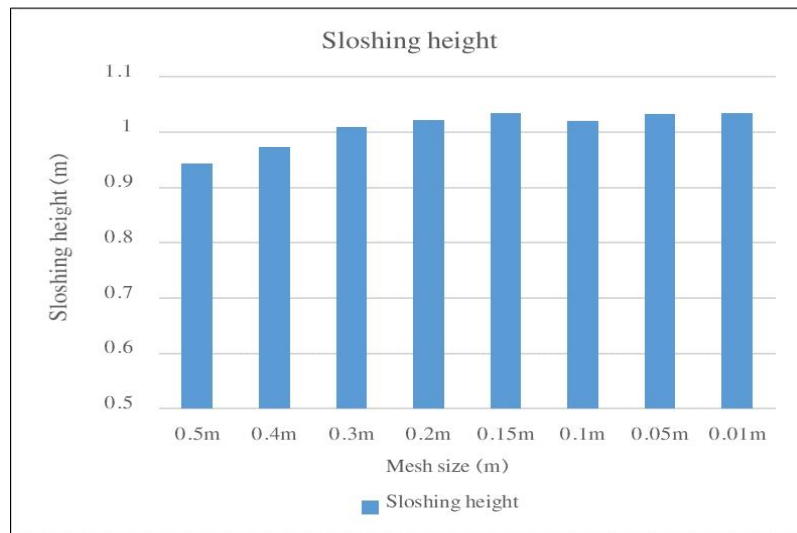


**Fig. 7. Variation of sloshing height for different mesh sizes at both sides of the tank walls.**

## 4. Results and discussion

### 4.1. Verification of finite element models and solution approach

The results presented by Vesenjak et al. [23] validate the finite element model developed in this study. Vesenjak et al. obtained the surface wave profiles created by stimulating a plexiglass water tank using Lagrangian, Eulerian, ALE, and SPH methods. The tank's length, width, and height were 1008mm, 196mm, and 300mm, respectively, while 60 percent of the tank (180mm) was full of water. The set was subjected to a horizontal acceleration of 30g for 80 milliseconds, and the point of 52 mm depth shows the time variation of water pressure.

The authors analyze the same model, including the Lagrangian method. Figs. 8 and 9 compare the results obtained by Vesenjak et al. [23] with those calculated by the authors. The time variation of water pressure fits the Vesenjak et al. responses precisely, as shown in Fig. 8. Fig. 9 presents the water-free surface under 30g seismic excitation at 30 ms for both models. The developed model is consistent with Vesenjak's results. So, the models established in this study lead to acceptable results.



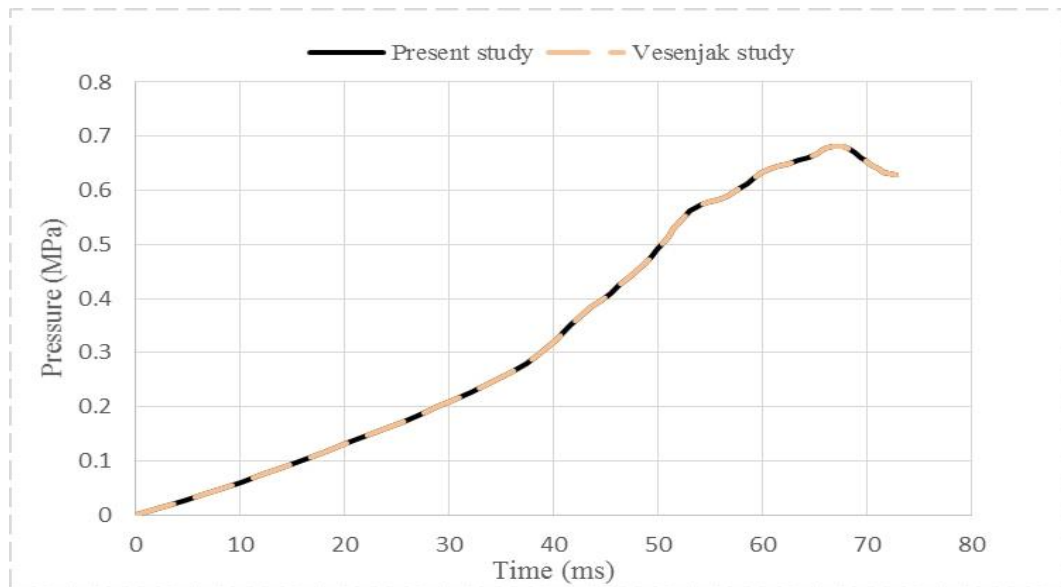


Fig. 8. The time variation of water pressure [22].

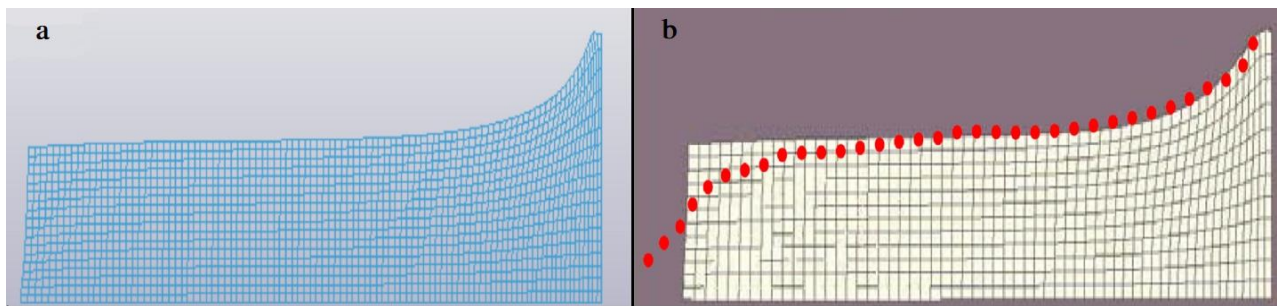


Fig. 9. Free surface of the water under 30 g seismic excitation at the time 30 ms; a) the result of made model in this study, and b) Vesenjak article result [22].

#### 4.2. Effect of thickness and flexibility (elastic or rigid) of walls

At first, the wall elasticity and thickness on the sloshing height and forces are studied. The tanks with a length of 15m and a height of 5m are modeled (H5L15 of group 1 tank). For these tanks, the walls are initially rigid with a 0.5m thickness. Next, the thicknesses of the elastic walls are 0.5m, 0.4m, and 0.3m. The freeboard is 1m and 2m for the roofed and roofless tanks, respectively. The floor's self-weight and dynamic excitation are inserted into the finite element models.

Table 3 shows the sloshing wave height and forces inserted into the tanks' roofs and walls. These parameters decrease due to the wall rigidity under the same thickness assumption. Considering the elastic wall thickness variations, a reduction in thickness increases the sloshing height and the applied forces to the wall. But a different trend is observed for the forces applied to the roof. The load on the roof due to the sloshing wave impacts decreases by changing the wall thickness from 0.4 m to 0.3m. It seems that such distinctness shows the importance of freeboard height effects on the sloshing waves and their dynamic properties. More detailed analyses study the freeboard height effects in the following sections.

**Table 3. Sloshing height and the resulting force on the roof and wall of tanks, considering different wall assumptions.**

Result type	0.5 m wall thickness rigid	0.5 m wall thickness elastic	0.4 m wall thickness elastic	0.3 m wall thickness elastic
Sloshing height (m)	1.26	1.33	1.36	1.44
Force applied to the wall (kN)	73.3	118.8	120.4	122.7
Force applied to the roof (kN)	20.1	20.25	26.41	24.7

#### 4.3. Rigid tanks

Although the walls' rigidity reduces the sloshing wave's effects, the previous section shows that results depend on the assumptions made for the freeboard height. This section investigates the influences of rigid tanks' geometric characteristics on the sloshing phenomenon, focusing on the freeboard sufficiency. The tanks are rigid to simplify the calculations and reduce the analysis time.

As mentioned, short tanks with  $2H/L$  ratios of less than one are excited by two earthquake records. Fig. 10 shows two different tanks' schematic views, one without a roof and the other for the tank with a ceiling.

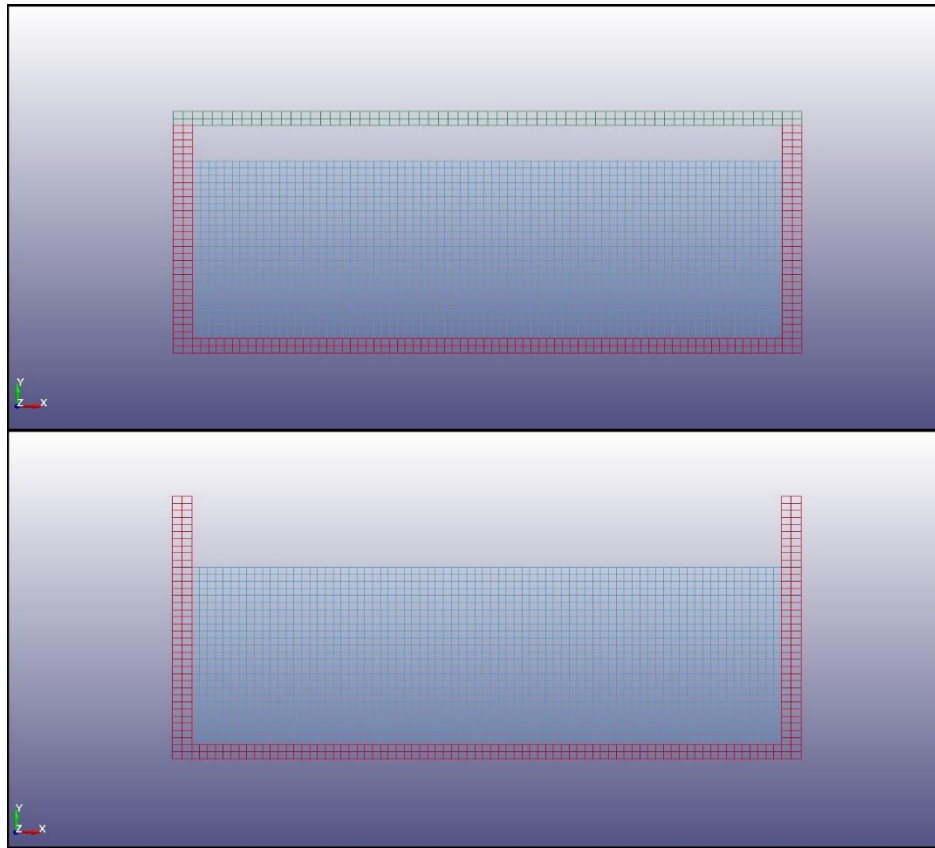


Fig. 10. Water sloshing in the H5L15 tank with and without a roof.

#### 4.3.1. Sloshing height

This section considers roofless tanks. As mentioned previously, two different seismic excitations (1999 Kocaeli and 1994 Northridge) are applied to the models, while both records are scaled at two different values of 0.1g and 0.3g. Fig. 11 shows the maximum sloshing heights of tanks. According to Fig. 11, the maximum sloshing height decreases with increasing tank length for constant H. Furthermore, for fixed L, the maximum sloshing height increases with increasing tank height. So, decreasing the H to L ratio of the tank leads to reducing the maximum sloshing height. Both seismic excitations at two different scaled PGAs show this trend.

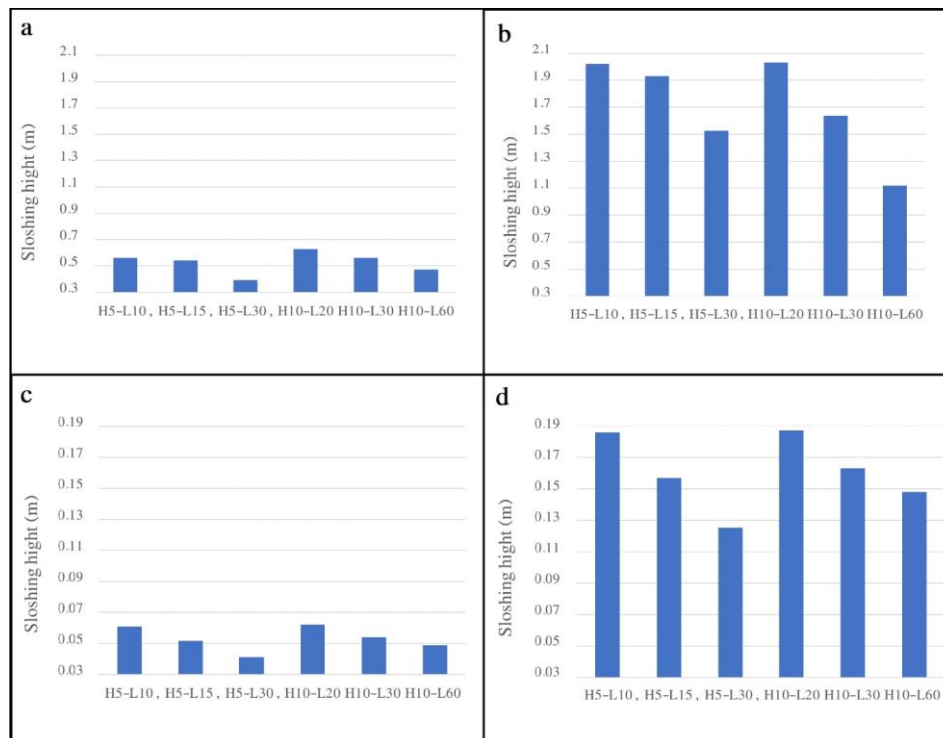


Fig. 11. Maximum sloshing height under a) Kocaeli 0.1g, b) Kocaeli 0.3g, c) Northridge 0.1g, and d) Northridge 0.3g scaled excitation.

Considering recorded ground accelerations, PGA, as expected, PGA's higher values (0.3g) induce higher sloshing height. For two different earthquake records, 1999 Kocaeli and 1994 Northridge, at the same scaled PGA, the Kocaeli earthquake record's sloshing height is much higher than the Northridge one. It seems the frequency content of the seismic excitation has significant effects on the sloshing phenomena. So, the PGA/PGV ratio is considered to investigate the frequency content of recorded ground motions. This ratio is less than 0.8 for the Kocaeli earthquake and is about 0.8 for the Northridge earthquake. So, the frequency content of these two ground motions is different.

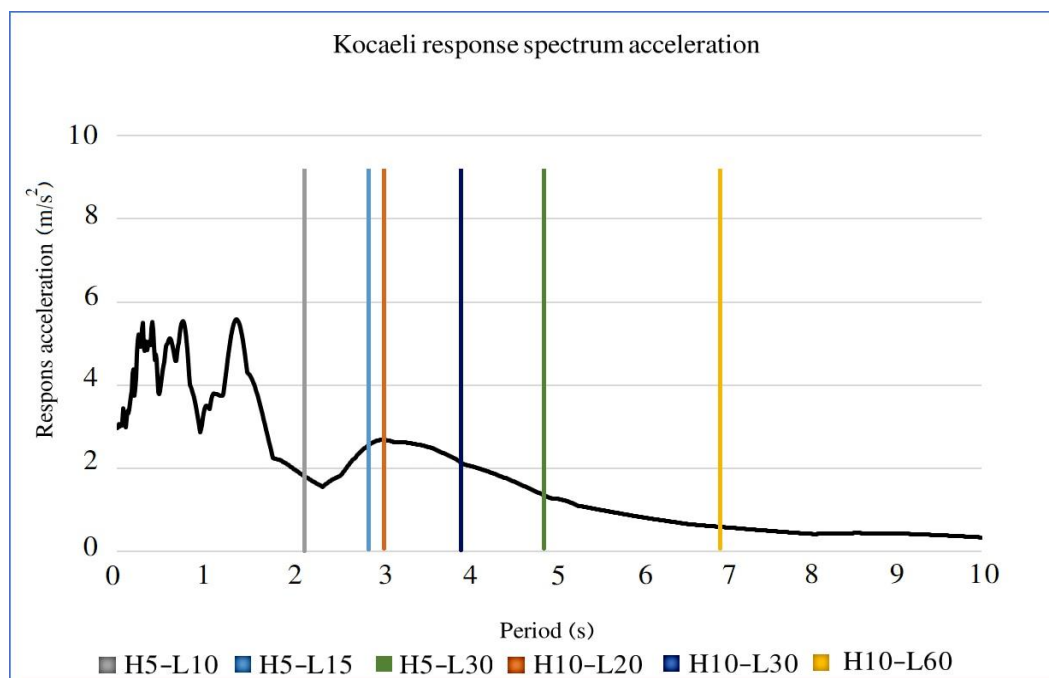
In the following, the natural period of the convective mode ( $T_c$ ) is calculated, investigating more detailed frequency content effects. It has been shown that the response of the convective mass controls the height of the sloshing wave. So, the natural period of the convective mode ( $T_c$ ) is calculated, investigating more detailed frequency content effects.  $T_c$  represents the geometry, length, and height of the convective part of the liquid.

Table 4 shows the system's fundamental period and the natural period of the first convective and impulsive mode from ACI 350 (see ACI350.3). Based on the results in Table 4, the vibrational period increased in constant H by the increment of L.

**Table 4. Modal analysis results.**

Tanks name	Group 1			Group 2		
	H5-L10	H5-L15	H5-L30	H10-L20	H10-L30	H10-L60
Fundamental period of the system (s) calculated by FEM	0.015	0.022	0.042	0.028	0.042	0.083
Natural period of the first convective mode of sloshing (s) calculated by ACI350	2.05	2.75	4.874	2.906	3.889	6.893
Natural period of the first impulsive mode (s) calculated by ACI350	0.148	0.1473	0.1474	0.5155	0.518	0.5199

Figs. 12 and 13 show the response spectrum acceleration of two recorded ground motions (scaled at 0.3g), whereas the fundamental period of different tanks is clarified. Based on figures 12 and 13, the Kocaeli earthquake component induces higher response spectrum acceleration over the first convective mode of sloshing. So, the sloshing height in Figure 13 is higher for the Kocaeli recorded ground motions at the same levels of PGA.



**Fig. 12. Natural period of the first convective mode of sloshing (s) calculated by ACI350 represented on response spectrum acceleration of 0.3g scaled Kocaeli earthquake.**

#### 4.3.2. Freeboard sufficiency and sloshing force

This section investigates the freeboard sufficiency effects of roofed tanks, considering the same tank geometries as the previous section, except for freeboards, varying from 0m to 1m at increments of 0.25m, for each tank. The results show that the values of both maximum sloshing height and sloshing force peak occur on the sides of the tank wall. So, the design of the roofs at the sides of the tank requires more attention. Fig. 14 shows the maximum sloshing force under 0.1g scaled ground motion, whereas Fig. 15 presents the results of 0.3g scaled ground motion.

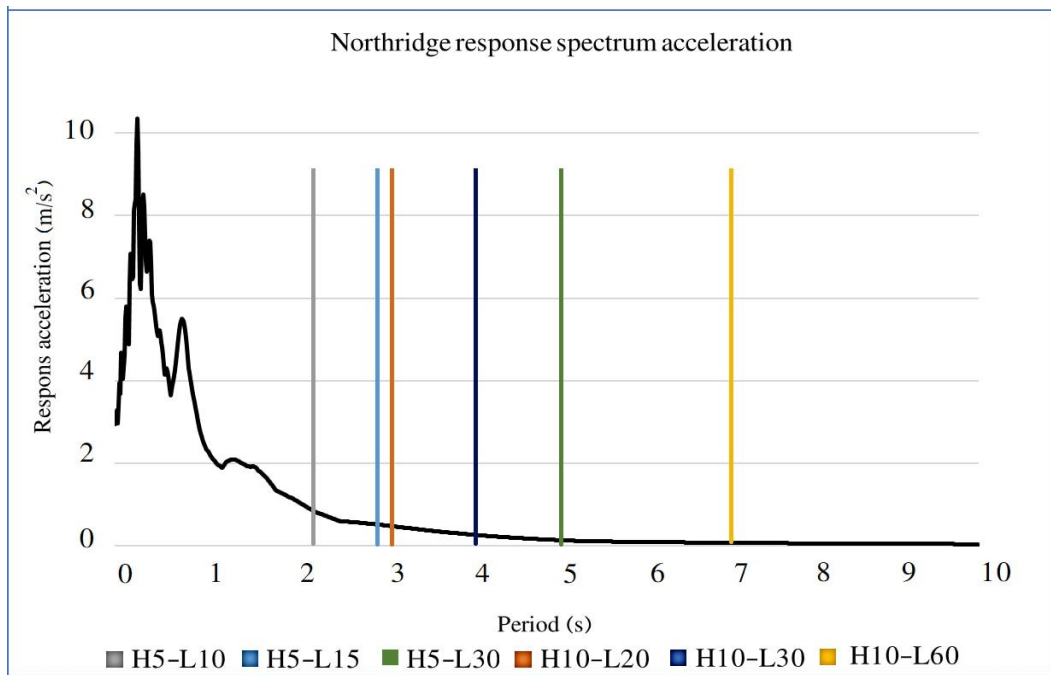


Fig. 13. Natural period of the first convective mode of sloshing (s) calculated by ACI350 represented on response spectrum acceleration of 0.3g scaled Northridge earthquake.

In both Fig. 14 and 15, there are some zero and non-zero responses. Zero force values indicate that the water inside the tank did not collide with the roof during the earthquake. A comparison of these zero sloshing forces with their corresponding sloshing height for the roofless tanks shows that the sloshing height calculated for the roofless tanks is less than the freeboard considered for the roofed tanks. So, zero sloshing forces present the sufficiency of the freeboard.

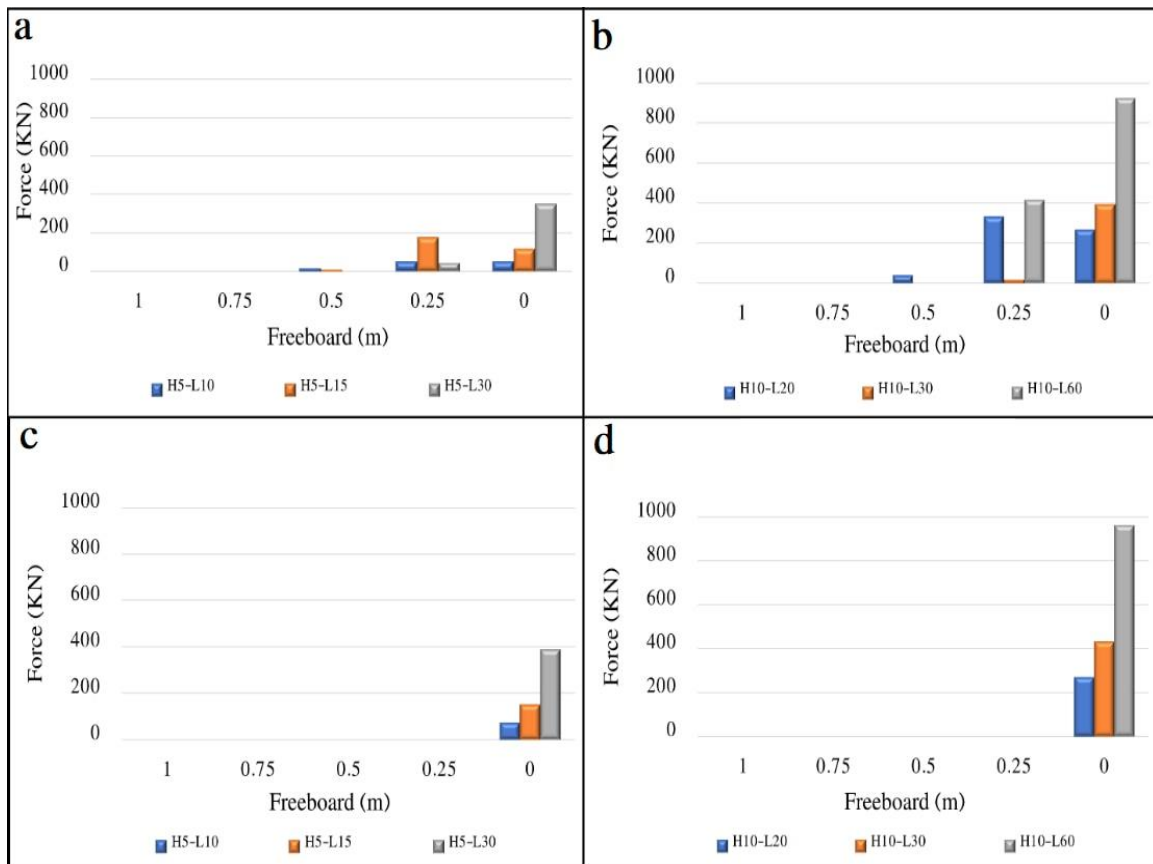
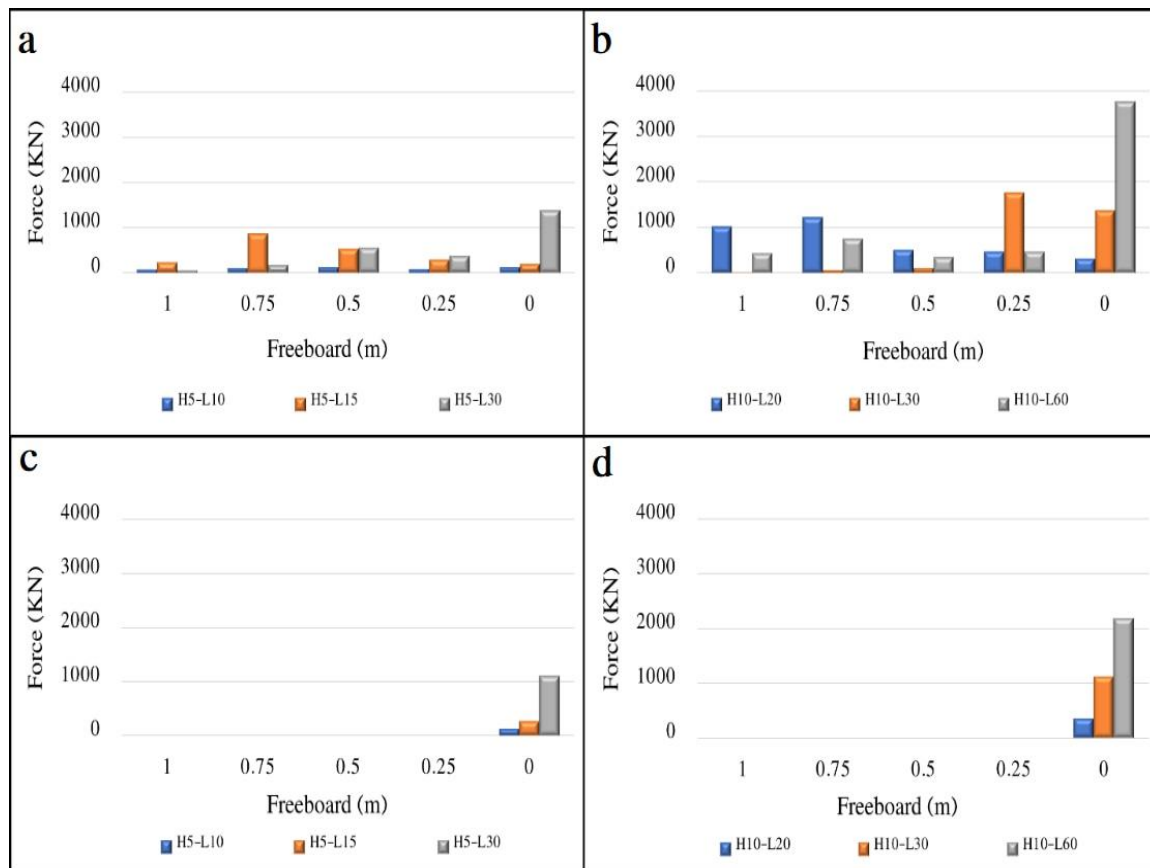


Fig. 14. Maximum sloshing forces under 0.1g scaled ground motions for different freeboard assumptions under a) Kocaeli excitation group1, b) Kocaeli excitation group2, c) Northridge excitation group1, and d) Northridge excitation group2.



**Fig. 15. Maximum sloshing forces under 0.3g scaled ground motions for different freeboard assumptions under a) Kocaeli excitation group1, b) Kocaeli excitation group2, c) Northridge excitation group1, and d) Northridge excitation group2.**

For the insufficient freeboard cases with zero freeboards, all tanks have similar response variations according to the H/L ratio. In these tanks, the sloshing forces increase by decreasing the H/L ratio. But, tanks with the non-zero freeboards do not show such a trend for the H/L ratio. Besides, the amount of force applied to the roof does not decrease as the freeboard increases. Accordingly, for the non-zero insufficient freeboards, responses do not show a constant trend considering different freeboard values.

In the case of insufficient freeboard, such differences between zero and non-zero freeboard responses on the sloshing force variations show the importance of an empty space on the sloshing wave's dynamic properties. It seems that the existence of air between the free surface and the roof influences the sloshing height and the upward forces inserted into the ceiling, allowing the free surface movement and its fluctuations. As a result, the effects of created sloshing waves on the system's frequency content and damping characteristics influence the responses.

Figs. 16 and 17 show the time history of the sloshing height at the right and left nodes located at the water's free surface for H10L30 and H5L15 tanks, respectively. The seismic load is 0.3g scaled Kocaeli earthquake. Three different freeboards are assumed in both figures: 1-sufficient freeboard, 2- 0.25m freeboard, 3- 0.5m freeboard.

As can be seen, the sloshing height and its oscillation process are highly dependent on the freeboard assumptions. Comparing sufficient freeboard by two non-zero sufficient ones (0.25m and 0.5m), changes in sloshing height variation trends are noticeable after reaching the sloshing height of the insufficient non-zero freeboard.

In both Figs. 16 and 17, sloshing height time histories for sufficient freeboard are symmetrical concerning the origin's axis. But, for 0.25m and 0.5m freeboards, the freeboard height controls the maximum sloshing height. When the sloshing waves collide with the roof, the other side of the water surface is at its peak value. For more detailed investigations, Figs. 18 and 19 illustrate the upward forces applied to the roof of H10L30 and H5L15 tanks for non-zero insufficient freeboard.

As can be seen (Figs. 18 and 19), the number of applied upward forces and their corresponding values are highly dependent on the freeboard height. This dependency may show the sloshing dynamic properties dependency on possible fluctuations in the free surface movement of water. This property is not available at the zero insufficient freeboard height. So, zero or non-zero assumptions for the freeboard height control the sloshing process, the values, and the number of forces. Table 5 shows the fundamental period of the roofed tanks with a 0.5m freeboard assumption. As presented in Table 5, the fundamental period increases by an increment of the tank length. Figures 20 and 21 show these period values in the response spectrum acceleration of 0.3g scaled Kocaeli and Northridge earthquakes, respectively.



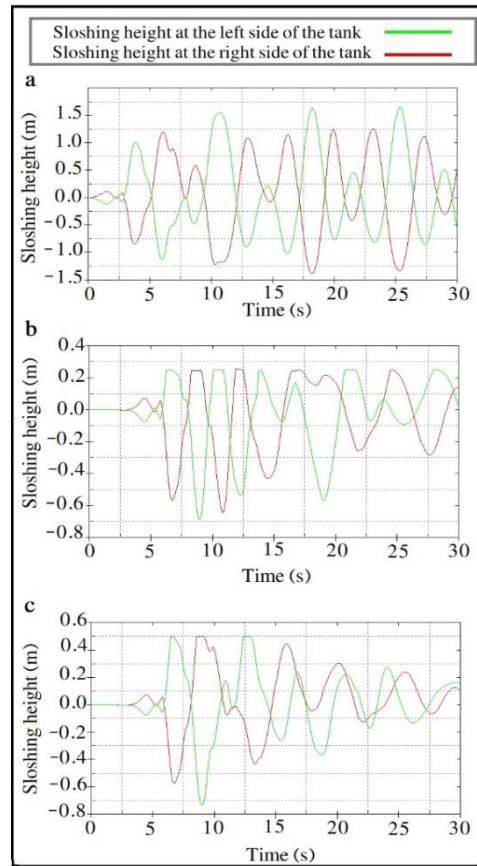


**Fig. 16.** Time history of sloshing height for H10L30 tank under 0.3g scaled Kocaeli earthquake: a) sufficient freeboard, b) 0.25m freeboard, and c) 0.5m freeboard.

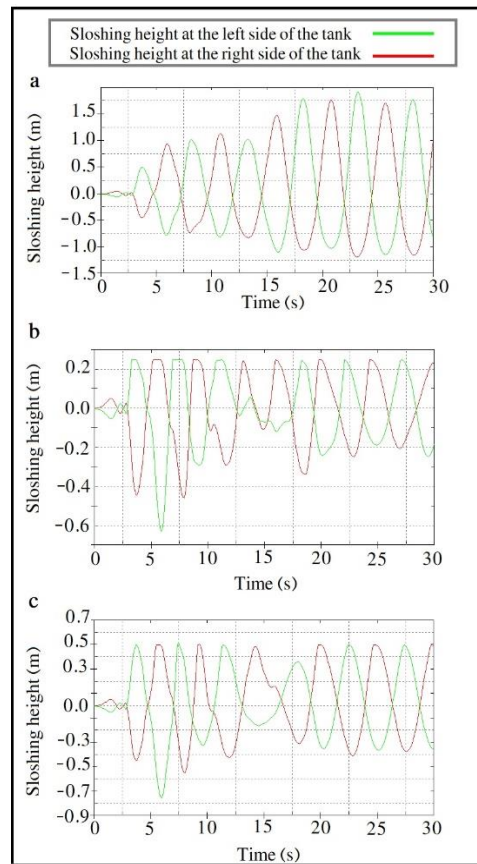


**Fig. 17.** Time history of sloshing height for H5L15 tank under 0.3g scaled Kocaeli earthquake: a) sufficient freeboard, b) 0.25m freeboard, and c) 0.5m freeboard.



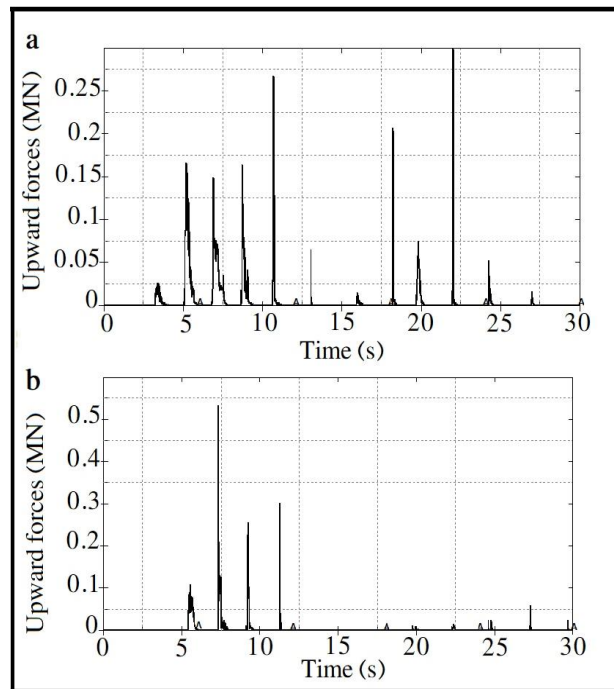


Fig. 18. Upward forces applied to the roof of H10L30 tank under 0.3g scaled Kocaeli earthquake: a) 0.25 m freeboard, and b) 0.5m freeboard.

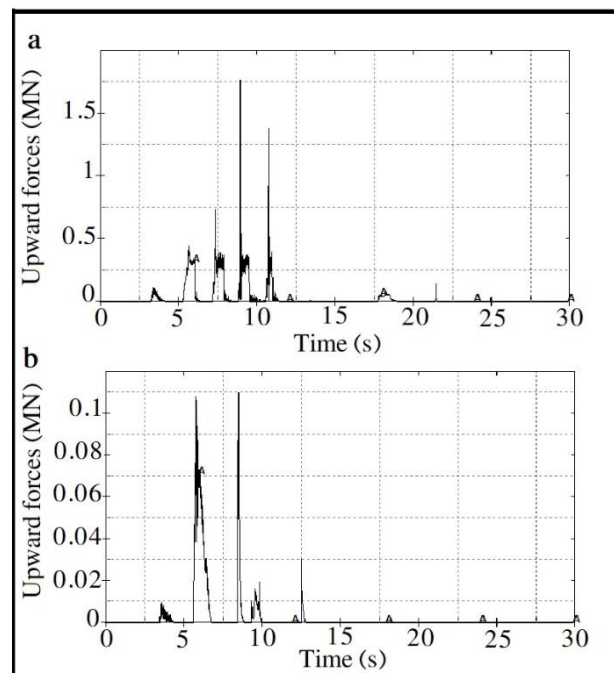
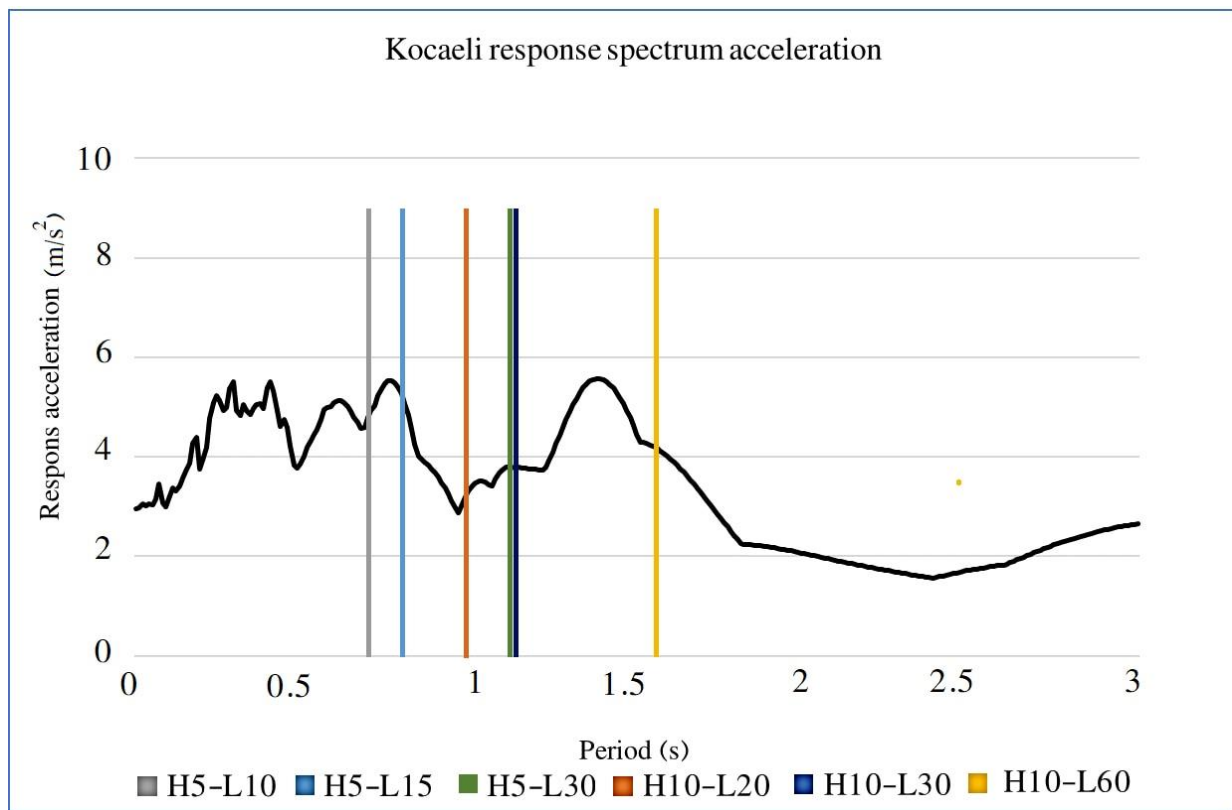


Fig. 19. Upward forces applied to the roof of H5L15 tank under 0.3g scaled Kocaeli earthquake: a) 0.25 m freeboard, and b) 0.5m freeboard.

Table 5. Modal analysis for the roofed tanks.

Tanks name	Group 1			Group 2		
	H5-L10	H5-L15	H5-L30	H10-L20	H10-L30	H10-L60
Fundamental period of the system (s) calculated by FEM	0.68	0.82	1.14	0.94	1.145	1.61

The upward forces caused by the Kocaeli earthquake record, in most cases, especially in zero freeboard cases, are higher than the Northridge earthquake record because of the lower PGA/PGV ratio value and frequency content. The models excited by the Kocaeli earthquake due to the lower frequency value will experience more stimulation of the convective part of the tank's water rather than the Northridge record. So, both the natural period ( $T_c$ ) of the tank's convective mode and the earthquake's frequency content affect the sloshing forces.



**Fig. 20.** Fundamental period of the (s) calculated by FEM represented on response spectrum acceleration of 0.3g scaled Kocaeli earthquake.

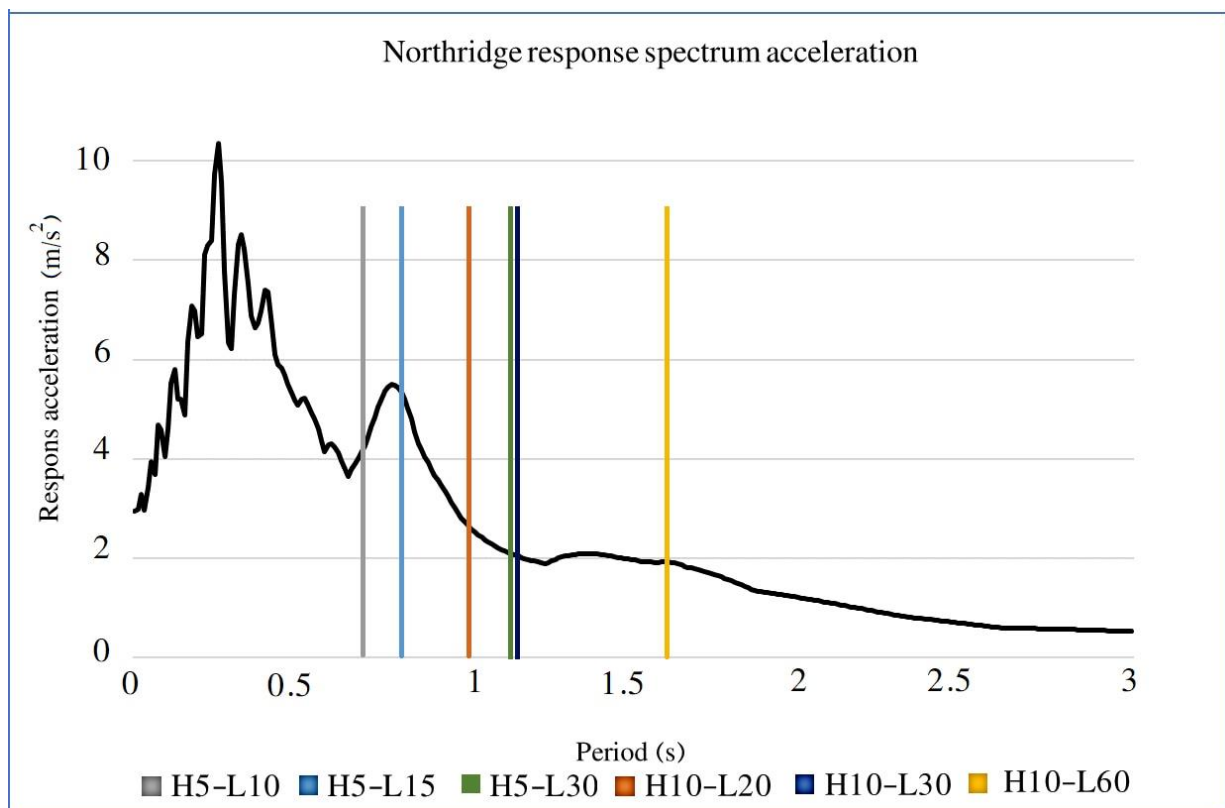


**Fig. 21.** Fundamental period of the roofed tank (s) calculated by FEM represented on response spectrum acceleration of 0.3g scaled Northridge earthquake.

Next, the effects of tank length on the upward load on the roof due to the sloshing wave's impacts are investigated. Figs. 22 to 24 show the sloshing height time history and upward forces of H5L10, H5L15, and H5L30. The freeboard is selected as 0.5m, and the seismic load is 0.3g scaled Kocaeli earthquake. The sloshing time history belongs to the roofless tank, while the upward forces correspond to the roofed ones. As can be seen, the number of upward forces from sloshing waves increases by reducing the tank length, although their values decrease.

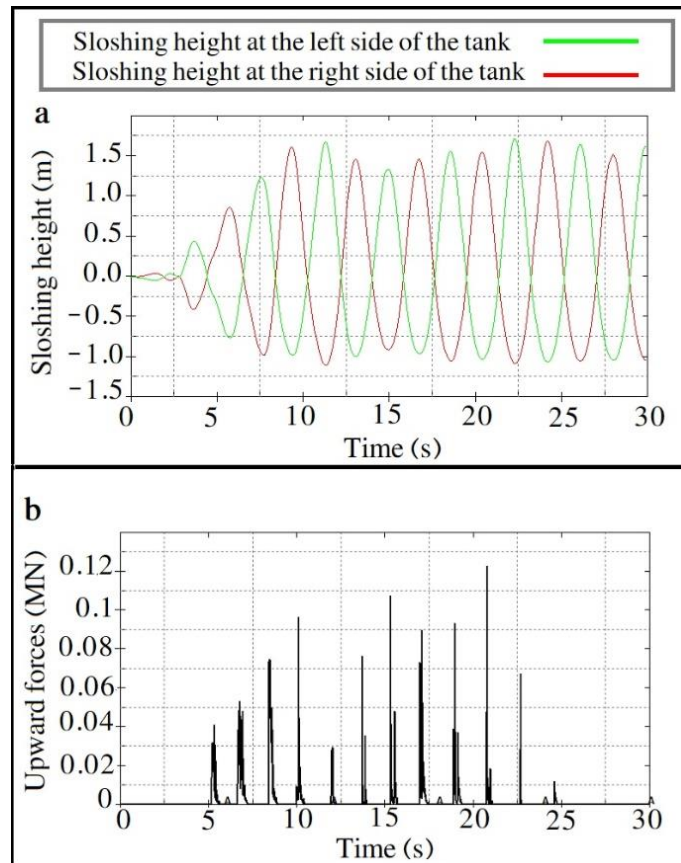


Fig. 22. H5L10 tank under 0.3g scaled Kocaeli earthquake-0.5m freeboard: a) sloshing time history, and b) upward forces

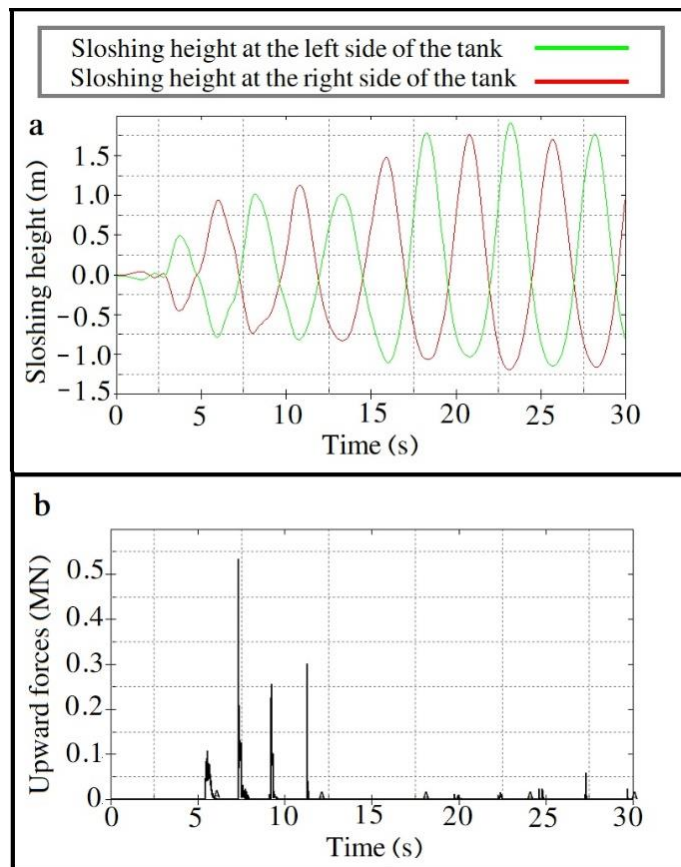


Fig. 23. H5L15 tank under 0.3g scaled Kocaeli earthquake-0.5m freeboard: a) sloshing time history, and b) upward forces

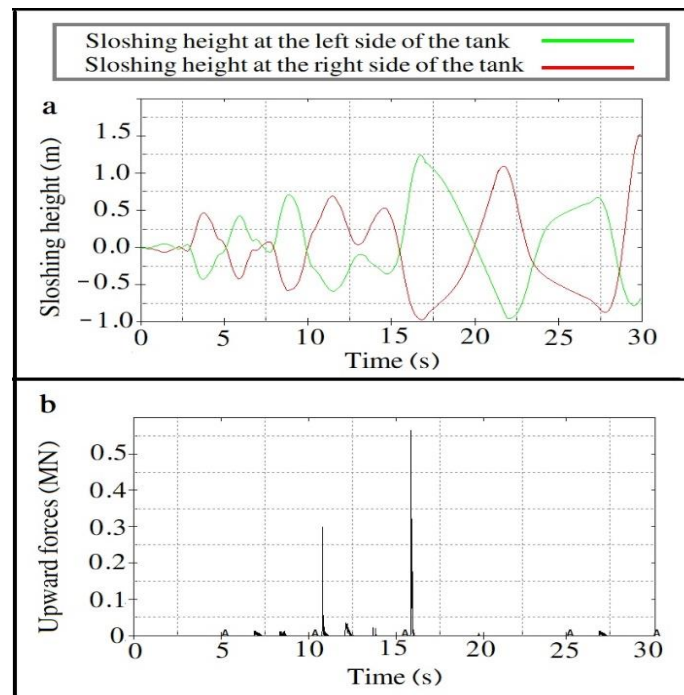


Fig. 24. H5L30 tank under 0.3g scaled Kocaeli earthquake-0.5m freeboard: a) sloshing time history, and b) upward forces

## 5. Conclusion

This study investigates the effects of the freeboard height sufficiency on sloshing waves' dynamic characteristics, including roofed and roofless tanks, considering different tank geometric properties. Seismic loads are the 1999 Kocaeli and 1994 Northridge earthquakes, in which their PGAs are scaled at 0.1g and 0.3 g. In all cases, both scaled ground motions of 0.3g produce higher sloshing height or upward forces. Additionally, the frequency content of earthquake records influences the responses. Based on the results, the tank wall rigidity reduces the sloshing height and forces arising from sloshing phenomena. For the elastic tanks, reduction of wall thickness reduces both the sloshing height and forces applied to the wall, but upward forces applied to the roof do not decrease regularly. Such irregular patterns show the effects of the freeboard height. For the rigid roofless tanks with sufficient freeboard, there is a clear trend of sloshing height variation due to the geometric change. In these tanks, the maximum sloshing height decreases by reducing the ratio of the height of the contained liquid to the tank length. Next, rigid-roofed tanks are studied considering different freeboards. There are two different responses for the roofed tanks: 1- the sloshing force is zero, which indicates the sufficiency of freeboard height. 2- Sloshing force is non-zero, which demonstrates insufficient freeboard height. In the case of insufficient freeboard, zero insufficient freeboard shows a clear trend for tank geometry variation. But non-zero insufficient freeboards have irregular responses. Such irregularity shows the importance of the empty space between the water-free surface and the tank's roof due to its effects on the system's frequency content and damping characteristics. So, zero or non-zero assumptions for the freeboard height mainly govern the sloshing process of roofed tanks.

## Statements & declarations

### Author contributions

**Ali Ebrahimi Hariri:** Investigation, Formal analysis, Resources, Writing - Original Draft.

**Yaghoub Mohammadi:** Conceptualization, Writing - Review & Editing.

### Funding

The authors received no financial support for the research, authorship, and/or publication of this article.

### Data availability

The data presented in this study will be available on interested request from the corresponding author.

### Declarations

The authors declare no conflict of interest.

## References

- [1] Mathew, A. K., Kumar Tomer, S., M, L. K., Student, P. G., Scholar, R. Effect of Soil-Structure Interaction in Seismic Analysis of Framed Structures Using Ansys. *International Journal of Engineering Development and Research*, 2015; 3 (3): 1–9.

- [2] Baghchesaraei, O. R., Lavasani, H. H., Baghchesaraei, A. Nonlinear Behavior of Circular Concrete Storage Tanks: History Pushover and Dynamic Loadings by Providing an Innovative Technique to Reduce the Seismic Response of Semi-Buried Tanks. *Applied Mechanics and Materials*, 2018; 878: 54–60. doi:10.4028/www.scientific.net/amm.878.54.
- [3] Aghajanzadeh, S. M., Mirzabozorg, H., Yazdani, H. SPH Technique to Study the Sloshing in Concrete Liquid Tanks. *Numerical Methods in Civil Engineering*, 2023; 8 (1): 1–17. doi:10.61186/nmce.2304.1015.
- [4] Jena, D., Biswal, K. C. Violent Sloshing and Wave Impact in a Seismically Excited Liquid-Filled Tank: Meshfree Particle Approach. *Journal of Engineering Mechanics*, 2018; 144 (3). doi:10.1061/(asce)em.1943-7889.0001364.
- [5] Kabiri, M. M., Nikoomanesh, M. R., Danesh, P. N., Goudarzi, M. A. Numerical and Experimental Evaluation of Sloshing Wave Force Caused by Dynamic Loads in Liquid Tanks. *Journal of Fluids Engineering, Transactions of the ASME*, 2019; 141 (11). doi:10.1115/1.4043855.
- [6] Edwards, N. W. A procedure for the dynamic analysis of thin walled cylindrical liquid storage tanks subjected to lateral ground motions [PhD thesis]. Ann Arbor (MI): University of Michigan; 1969.
- [7] Yang, J. Y. Dynamic behavior of fluid tank systems [PhD thesis]. Houston (TX): Rice University; 1976.
- [8] Doğangün, A., Durmuş, A., Ayvaz, Y. Static and Dynamic Analysis of Rectangular Tanks by Using the Lagrangian Fluid Finite Element. *Computers and Structures*, 1996; 59 (3): 547–552. doi:10.1016/0045-7949(95)00279-0.
- [9] Ghaemmaghani, A. Dynamic time-history response of concrete rectangular liquid storage tanks [Master's thesis]. Tehran (Iran): Sharif University; 2002. Persian.
- [10] Ghaemmaghani, A. R., Kianoush, M. R. Effect of Wall Flexibility on Dynamic Response of Concrete Rectangular Liquid Storage Tanks under Horizontal and Vertical Ground Motions. *Journal of Structural Engineering*, 2010; 136 (4): 441–451. doi:10.1061/(asce)st.1943-541x.0000123.
- [11] Li, Y., Wang, J. A Supplementary, Exact Solution of an Equivalent Mechanical Model for a Sloshing Fluid in a Rectangular Tank. *Journal of Fluids and Structures*, 2012; 31: 147–151. doi:10.1016/j.jfluidstructs.2012.02.012.
- [12] Parthasarathy, N., Kim, H., Choi, Y.-H., Lee, Y.-W. A Numerical Study on Sloshing Impact Loads in Prismatic Tanks under Forced Horizontal Motion. *Journal of the Korean Society of Marine Engineering*, 2017; 41 (2): 150–155. doi:10.5916/jkosme.2017.41.2.150.
- [13] Moslemi, M., Farzin, A., Kianoush, M. R. Nonlinear Sloshing Response of Liquid-Filled Rectangular Concrete Tanks under Seismic Excitation. *Engineering Structures*, 2019; 188: 564–577. doi:10.1016/j.engstruct.2019.03.037.
- [14] Milgram, J. H. The Motion of a Fluid in a Cylindrical Container with a Free Surface Following Vertical Impact. *Journal of Fluid Mechanics*, 1969; 37 (3): 435–448. doi:10.1017/S0022112069000644.
- [15] Minowa C, Ogawa N, Harada I, Ma DC. Sloshing roof impact tests of a rectangular tank. Argonne (IL): Argonne National Laboratory; 1994. Report No.: ANL/RE/CP-82360.
- [16] Minowa, C. Sloshing Impact of a Rectangular Water Tank (Water Tank Damage Caused by the Kobe Earthquake). *Nippon Kikai Gakkai Ronbunshu, C Hen/Transactions of the Japan Society of Mechanical Engineers, Part C*, 1997; 63 (612): 2643–2649. doi:10.1299/kikaic.63.2643.
- [17] Chen, Y. G., Djidjeli, K., Price, W. G. Numerical Simulation of Liquid Sloshing Phenomena in Partially Filled Containers. *Computers and Fluids*, 2009; 38 (4): 830–842. doi:10.1016/j.compfluid.2008.09.003.
- [18] Lu, D., Zeng, X., Dang, J., Liu, Y. A Calculation Method for the Sloshing Impact Pressure Imposed on the Roof of a Passive Water Storage Tank of AP1000. *Science and Technology of Nuclear Installations*, 2016; 2016. doi:10.1155/2016/1613989.
- [19] Mowafy, M., Salem, M., Salem, T., Anwar, A., Eldeeb, H. Seismic Performance of Concrete Gravity Dams. *The Egyptian International Journal of Engineering Sciences and Technology*, 2016; 16:1–10. doi:10.21608/eijest.2013.96783.
- [20] Kianoush, M. R., Ghaemmaghani, A. R. The Effect of Earthquake Frequency Content on the Seismic Behavior of Concrete Rectangular Liquid Tanks Using the Finite Element Method Incorporating Soil-Structure Interaction. *Engineering Structures*, 2011; 33 (7): 2186–2200. doi:10.1016/j.engstruct.2011.03.009.
- [21] Zhu, T. J., Tso, W. K., Heidebrecht, A. C. Effect of Peak Ground a/v Ratio on Structural Damage . *Journal of Structural Engineering*, 1988; 114 (5): 1019–1037. doi:10.1061/(asce)0733-9445(1988)114:5(1019).
- [22] Elnashai A, Di Sarno L. *Fundamentals of earthquake engineering: from source to fragility*. 2nd ed. Hoboken (NJ): John Wiley & Sons; 2015.
- [23] Vesenjak M, Mullerschön H, Hummel A, Ren Z. Simulation of fuel sloshing—comparative study. In: *Proceedings of the 3rd German LS-DYNA Forum*; 2004 Oct 14–15; Bamberg, Germany. p. 1–8.

# Iran's Agricultural Exports Policy from the Perspective of Virtual Water and Its Economic Value

Ardalan Izadi <sup>a\*</sup>, Farhad Yazdandoost <sup>a</sup>

<sup>a</sup> Faculty of Civil Engineering, K. N. Toosi University of Technology, Tehran, Iran.

## ARTICLE INFO

### Keywords:

Iran export  
Price index  
Revenue index  
Virtual water  
World trade balance

### Article history:

Received 12 May 2025  
Accepted 14 May 2025  
Available online 21 May 2025

## ABSTRACT

Export is an essential part of trade, and is the main mechanism of any country to increase its economic growth. It would be prudent for countries facing water stress to consider the role of Virtual Water besides the economic aspects of exports. This would, in turn, lead to more purposeful export strategies while preserving valuable domestic water resources. Here, a three-step framework is presented to judge how to export better-targeted products in the agricultural sector, as the largest water-consuming sector of Iran, where water shortage is currently one of the main national challenges. The framework is established based on two indices: Price and Revenue. The price index stands for the cost that must be paid, and the revenue index measures the economic value earned from exporting a certain amount of Virtual Water hidden in sold products. Comparison of these two criteria between Iran and the World trade can lead to maximizing incomes from exports and minimizing domestic water resource consumption. The efficiency of the proposed approach was investigated for six exported agricultural products: dates, pistachios, and saffron as the most well-known international brands of Iran's agricultural industry, and tea, rice, and watermelon as the representative water-intensive products during 2005-2016. The results show that the current states of exports have unfavorable conditions both from the perspective of water resources exploitation and export incomes. Furthermore, the results show that the proposed framework can provide a better platform for considering not only export incomes, but also volume and economic value of exported Virtual Water.

## 1. Introduction

Iran has been experiencing a serious water crisis, especially in arid and semi-arid regions with extensive water challenges/shortages [1]. Persistence of successive drought conditions in Iran has led to new strategies in water resources management with a focus on modifying current consumption patterns. Virtual Water (VW), as the volume of water required in order to produce a commodity or service, was first introduced by Allan [2], and as a result, is being more carefully examined. While the volume of VW can never provide a clear picture about social, environmental, and economic condition of a community [3], it is certain that, the volume of VW of a nation can be a sign of country's water need [4]. From this point of view, virtual water trade can be a barrier or an accelerator for economic growth. Recent studies have concluded that virtual water can be directly related to water scarcity [5-7], water availability [8], and water dependency [9].

The concept of VW plays a strategic role in how sustainability in production patterns can be achieved while the pressure on domestic water resources becomes minimal. As a general rule, the more VW (embedded in products) is exported, the more pressure on domestic water resources will be exerted. Although this rule sounds acceptable within the conventional water resources management, it may be incorrect from the perspective of the economic world, marketing, VW trades, and their corresponding theories. Needless to say, focusing solely on the economic aspect of trade can expose very harmful effects on the water resources.

\* Corresponding author.

E-mail addresses: [a.izadi@kntu.ac.ir](mailto:a.izadi@kntu.ac.ir) (A. Izadi).





For example, Guan & Hubacek [10] showed that the success of China's economic growth rate in recent years has led to profound impacts on the quantity and quality of water resources. This finding has come out through studying imported and exported VW between different hydro-economic regions of China and comparing net flows of goods and services, volume of VW exports, and ratio of value added to amount of water and wastewater.

Many researchers have conventionally used the VW concept to classify Iran's agricultural sector as a country importing or exporting VW [11, 12] and consequently evaluating Iran's dependency on VW imported/exported [9]. Some other studies investigated VW as a means to alleviate Iran's water resources management challenges [13, 14]. The common point of all previous studies is the neglect of the economic value of Iran's VW trade.

Negative impacts of this neglect on international VW exports are indisputable, especially for the Iranian agricultural sector, which consumes more than 90% of the water resources. For example, Iran traditionally has been recognized as a prestigious international brand of unique agricultural products in world trade. The export of these unique products not only gives exclusive and political credits to Iran, but it always has abundant added economic value. Agricultural self-sufficiency is perceived to be a notion that can adversely deplete water and fund resources requirements to trade products with other countries to meet the basic needs of the people of Iran. In this regard, Ward & Michelsen [15], while reviewing different influencing issues on the economic value of water in agriculture, claimed that information on water's economic value not only leads to more informed choices on water resources management but also can maximize the product or revenue obtained from the water usage. In this regards, Wang et al. [16], not only showed that compensation for crop virtual water export can increase the efficiency of agricultural water use, but also it can increase the competitiveness of financial gain for agricultural production. This application of the economic value of water for crops had been discussed before [17], and its usage has rarely been studied for regulating national trade and purposeful exports.

This study aims to examine VW trade of some agricultural products and their related economic issues to address Iran's current agricultural export. For this reason, a three-step framework enriched with new defined indexes (Price and Revenue) is presented. Six agricultural products; dates, pistachios, and saffron as the most well-known international brands of Iran agricultural industry export, tea, rice, and watermelon as the water-intensive products in Iranian food diary basket were selected to show how a better platform can be established to maximize incomes and minimize VW (agricultural water resources consumption) of Iran exports simultaneously. In this regard, a comparison with the world export figures would be necessary.

## 2. Methodology

In order to identify better-targeted agricultural products with higher export margins in terms of their VW gains, this section has been divided into two parts. First, Iran's and the world's export trends in the global market are investigated in order to gather a reliable database. In fact, in this step, the past operating conditions of Iran and the world export for the mentioned agricultural products from 2005 to 2016 were identified. The needed information was gathered from the FAO, Iran Ministry of Agriculture-Jihad and the Chamber of Commerce, Industries, Mines, and Agriculture. Some of the main information about exported products, including the export quantity and value, producer prices, average volume of VW embedded in each product, and its trade for Iran and the world, was examined. Second, with the gathered known values of input data, the efficiency of the proposed approach is investigated for each agricultural crop. Here, the suggested framework with its main key basic features (shown in Fig. 1) consists of the following steps. It is worth nothing that developed indexes are formulized based on some previous proposed studies [16].

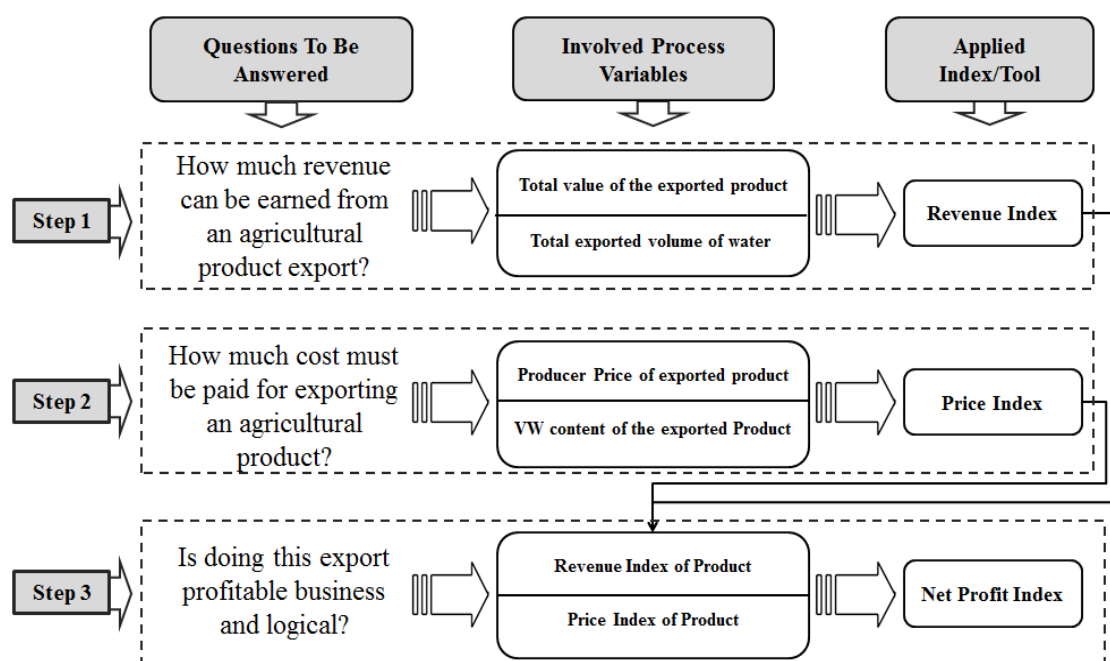


Fig. 1. Process of the proposed framework for assessing export policies.

- Step 1: Evaluating the economic index of Revenue:

In this step, the amount of export values for each product is used to assign an economic index of revenue to the sold exported VW in world trade. Here, the Revenue Index ( $RI$ ) is defined as the ratio of the financial value of exported products to the exported volume of VW (equation 1). In fact, the revenue index of each product is equivalent to how much revenue can be earned from selling per cubic meter of exported VW. The  $RI$  with a higher amount is more desirable.

$$RI_i = \frac{VEP (M US\$)_i}{EVW (Mm^3)_i} \quad (1)$$

where  $RI_i$  is Revenue Index,  $VEP$  is the total value of exported products (Million US\$),  $EVW$  is the total exported volume of water (Million  $m^3$ ), and  $i$  corresponds to each agricultural product.

- Step 2: Evaluating the economic index of Price:

As the  $RI_i$  of selling each volume of exported VW is necessary to evaluate, the cost that must be paid to obtain revenue from selling each volume of exported VW must be assessed. These costs usually depend on all grades, kinds, and varieties costs received by the producer (many factors such as water price, type of irrigation, water quality, climate, crop water requirements, seed, planting, pesticides, fertilizers). Based on FAO's definition, this cost is called the Producer Price ( $PP$ ). This average price is usually different from one point to another. This price can be used as a measure of how much cost must be paid (through the entire life of production and export of a crop) to sell each volume of exported VW in world trade. Here, the  $PP$  is used to define the Price Index ( $PI$ ) of each product. It is defined as the ratio of the  $PP$  of products to the amount of VW hidden in one unit of weight of each exported product (equation 2). Actually, this index corresponds to how much it costs to export one cubic meter of water as the exported VW. The  $PI$  with a lower amount is more desired.

$$PI_i = \frac{PP (\frac{US\$}{ton})_i}{VW (m^3/ton)_i} \quad (2)$$

- Step 3: Identifying and assessing the priority of each product in the VW world trade:

In the last step, having the economic benefit and cost per unit volume of exported water (two identified indexes in previous steps), the Net Profit ( $NP$ ) of exporting each volume of VW for each product is calculated. The decision about which product is more suitable and affordable, or should be exported or not exported anymore can be made based on equation 3. A product with higher  $NP$  can provide more incentive for export. Furthermore, if there are more  $NP$  for Iran rather than the world (for any specific product), higher priority can be assigned to the export of the corresponding product.

$$Net Profit of Exported VW_i (\frac{US\$}{m^3}) = RI_i - PI_i \quad (3)$$

### 3. Results

#### 3.1. Virtual water trade of Iran and the world

The required information on agricultural products and their corresponding VW values was obtained for 2005-2016 from FAO, the Iranian Ministry of Agriculture, Jihad, and Iran Chamber of Commerce, Industries, Mines, and Agriculture. Figs. 2 and 3 present the quantity and value of exported VW of selected agricultural products of IRAN during the study period. The collected data shows that while the export quantity of pistachio, tea, and saffron shows a decreasing trend, the amount of export for date has not changed noticeably. It means that the opportunity of exporting products has been raised for other competitors in world trade. Another remarkable fact belongs to the watermelon export with an increase in financial value and quantity in order by 4.2 and 2.3 times during the period 2005-2012. In other words, the share of Iran from watermelon world trade increased from 7% to around 12% within only a few years, and in 2012, the financial value of exporting watermelon reached 1.5 times the revenue of date trade. It is worth noting that the estimated virtual water (VW) values of products presented in Hoekstra (2011) and Alizadeh (2015) were used as reference points for calculating the virtual water equivalent at the global level and for Iran, respectively.

Table 1 represents the summation of financial value and the amount of VW for exported products during the study period. According to this table, the amount of exported VW hidden in saffron is about 1.4 times more than watermelon, while the financial gain of it is more than 3 times. The amount of saffron exported by VW is around 1.02 billion  $m^3$ , which is around half of the annual consumption of potable water in Isfahan Province, with around 4 million inhabitants [18]. Another fact about saffron is the lower gains of exporting it in comparison with exporting pistachios. In other words, although saffron is the most well-known international brand of Iranian agriculture but exporting pistachios was able to provide more income for Iran. However, this income from export may be interpreted as an economic success, but from the perspective of water resources exploitation, it can be a tragedy for Iran facing with severe water resources crisis. In fact, the financial gains of Iran resulting from pistachio exporting are impressive (about  $9.74 \times 10^9$  US\$), but the corresponding amount of water exported by VW during the study period is around 2 times Iran's annual domestic water consumption. In other words, Iran had lost 2 years of its domestic water consumption quantity only by 12 years of exporting pistachio. This reality about pistachios would be much worse/unfortunate when knowing that only 36% of Iran's annual production had been exported during the last years (on average). It is worth noting that pistachio is only one of hundreds of agricultural products in Iran. Furthermore, comparison of existing export trends between rice and the other products reveals that the export of rice during the study period not only consumed water resources severely, but also it could not provide suitable economic

gains. Therefore, rice should not be considered as an export commodity.

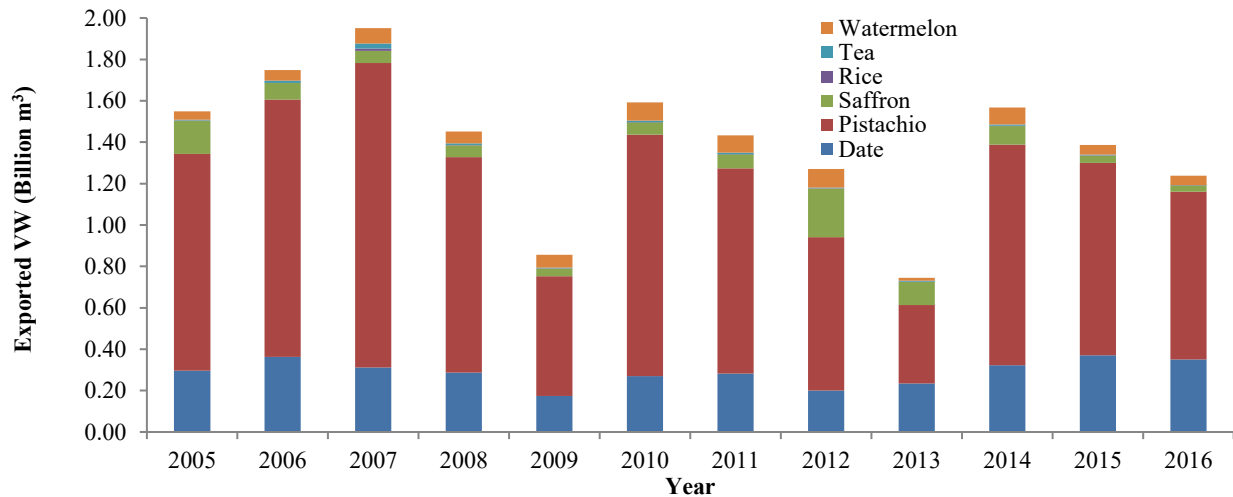


Fig. 2. Exported VW from IRAN during the study period (Million m<sup>3</sup>).

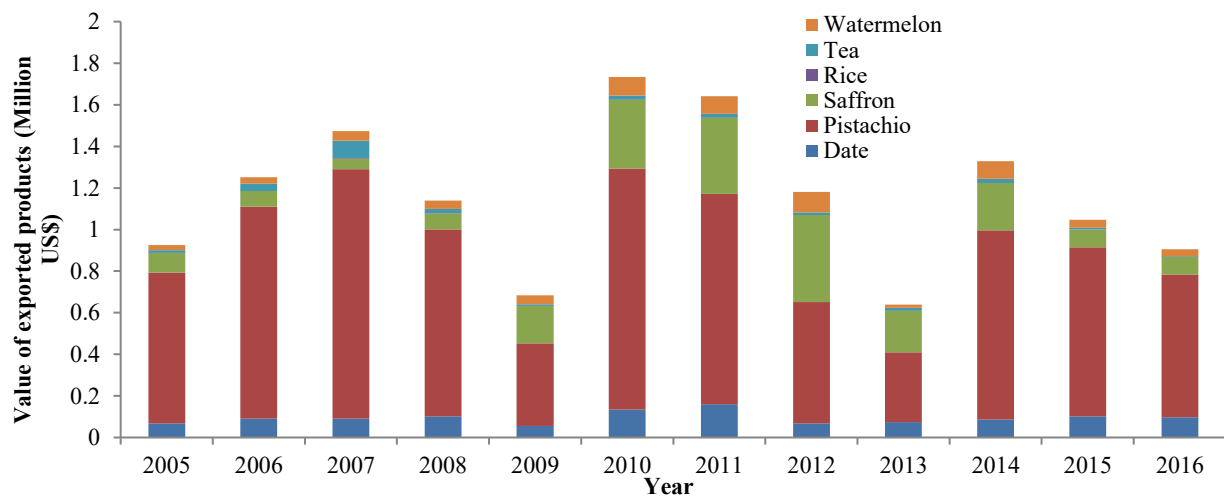


Fig. 3. Value of exported products during the study period from IRAN (Million US\$).

Table 1. A brief glance on Iran's export during the study period.

	Date	Pistachio	Saffron	Rice	Tea	Watermelon
Value of Exported VW (Million US\$)	1129.38	9735.32	2197.03	7.34	252.67	628.09
Volume of Exported VW (Million m <sup>3</sup> )	3462.7	11463.8	1023.4	22.7	82.2	732.3

### 3.2. Application of proposed framework

In the following, the detailed analysis of implementing the proposed framework for each agricultural product is discussed separately, and then a comparison is presented in order to prioritize the export policies of various crops.

#### 3.2.1. Pistachio

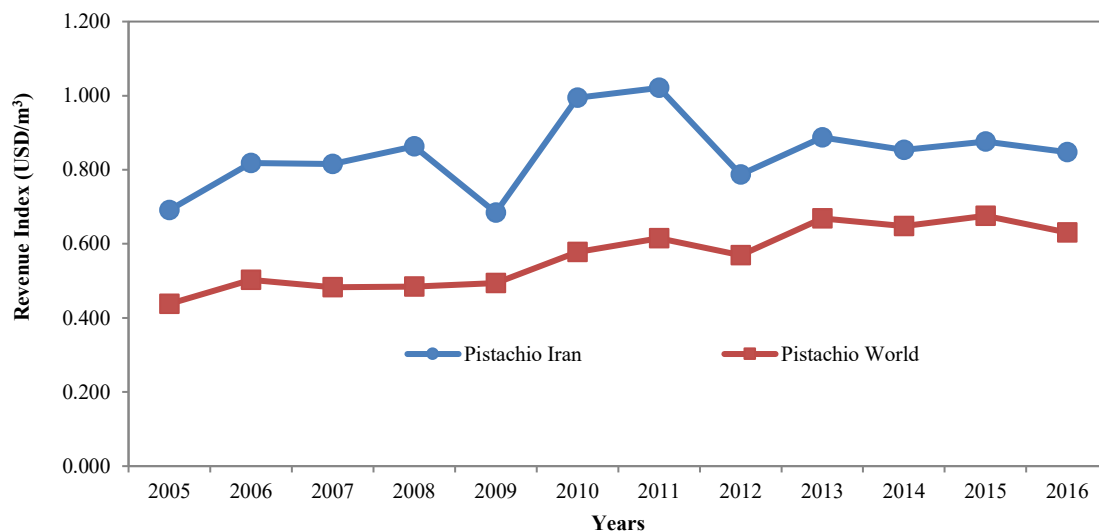
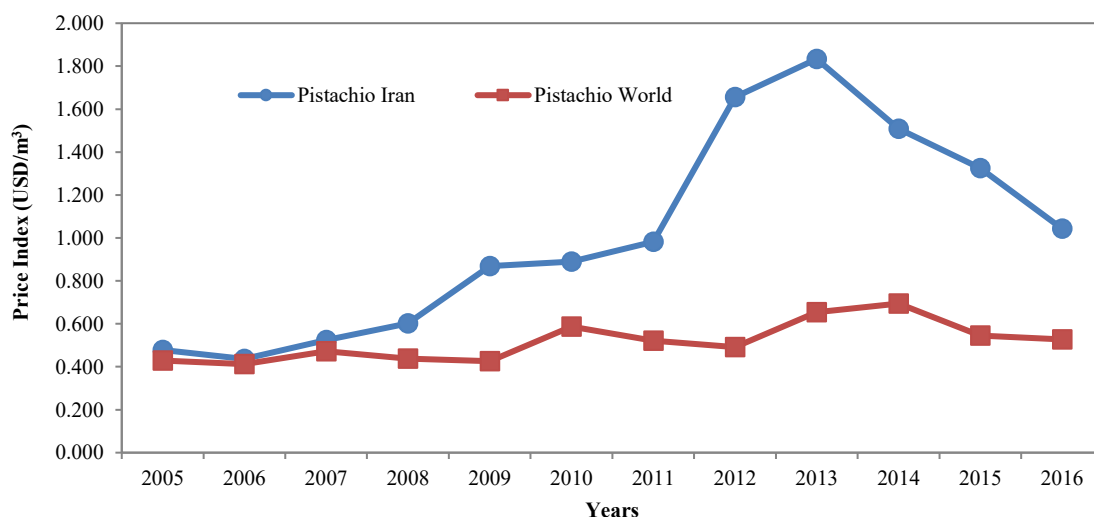
About 70% of Iran's pistachios are produced in Kerman Province, currently facing serious water scarcity. During the study period, overexploitation of groundwater resources in this region has caused a 10 m depletion in groundwater levels, which is equivalent to an annual decline of 840 million cubic meters of aquifer reserves. In many areas, water salinity has increased severely, implying serious complications for the future. Over the recent years, Iran's pistachio export has shifted towards wholesale trade with less business risk for the Iranian exporters. As a result, Iran's high-quality pistachios are exported with very low added value while the importing countries gain the main profit.

As seen in Table 2, the statistics have shown a downward trend in the export rate of pistachios over the past decade, and Iran has been unable to retain its share in the world pistachio market, and has provided competitors the opportunity to gain the market share. One of the main reasons for the decline in Iran's pistachio trade in the global market is the sanctions against Iran. The USA, as the main competitor of Iran's pistachio trade, has restricted Iranian pistachio exports. In this regard, China, as the world's largest pistachio market, is gradually seeking to replace the import of pistachios from Iran with the United States [19]. Without these sanctions, Iran could benefit from its geographical location in this respect.

**Table 2. Changes in Iran pistachio exports over the past years.**

Year	Quantity (Ton)	Value (M US\$)	Share form World Trade (%)
2005	137712	724.06	51.04
2006	163463	1017.89	56.19
2007	193350	1199.51	52.06
2008	136893	898.80	37.74
2009	76124	396.40	26.13
2010	153259	1159.35	39.50
2011	130137	1010.87	36.01
2012	97448	583.83	27.02
2013	49661	335.24	16.60
2014	140109	909.80	37.11
2015	121995	812.87	38.50
2016	106493	686.71	27.15

However, on one hand, the revenue index of Iran for the VW of the pistachios highly outweighs the global average, almost \$0.2 to \$0.5 more (Fig. 4). On the other hand, the price of VW exports in Iran, in proportion to the whole world, has always been higher over the period of studies (Fig. 5). Moreover, the cost index in the country has skyrocketed over the recent years. In other words, compared to global figures, Iran gains more financial profit from virtual water export per cubic meter of water while having higher export costs. It is worth noting that the price index of virtual water is much higher than the rate of revenue index; therefore, pistachios cannot be considered as an export product with high added value.

**Fig. 4. Comparison of pistachio revenue index for Iran and the world.****Fig. 5. Comparison of pistachio price index for Iran and the world.**

### 3.2.2. Date

Kerman Province, with 52700 hectares of palm tree land (26.5% of the entire date production land), is the biggest producer of dates in Iran. The next rank belongs to Khuzestan Province. Palm trees in both regions are dying and losing their productivity. Extreme quantitative and qualitative water restrictions, the aging of palm trees, the proliferation of heavy dust storms, and the lack of agricultural insurance coverage are the most emerging problems in the production of dates today. Over the past years, Iran has been able to retain its own share (10-15%) of the world's export market (Table 3), and neighboring countries are the ultimate destination of Iran's exports. The costs of shipping/transporting to distant countries are the main barriers to increasing the share of date exports to other countries. In recent years, the government's financial policies, alongside the resumption of sanctions, have exerted additional pressures on Iran's export markets.

**Table 3. Changes in Iran date exports over the past years.**

Year	Quantity (Ton)	Value (M US\$)	Share form World Trade (%)
2005	117052	68.493	14.81
2006	143434	91.645	30.58
2007	123260	91.028	14.15
2008	113539	101.783	12.04
2009	68837	55.819	10.44
2010	106760	134.001	16.01
2011	112030	160.251	15.77
2012	79196	67.404	10.36
2013	93030	74.695	11.27
2014	127516	85.722	10.78
2015	146910	101.015	12.53
2016	138844	97.519	11.93

As seen in Table 3, the export rate of dates has had an almost steady trend in the past decade, and Iran has been able to retain its own share of the world export market. Fig. 6 shows that the growth of the virtual water revenue index of the date during the early decade of studies has had a competitive aspect for Iran and the world, but in recent years, Iran's financial gains from the sales of exported VW in dates have reduced, as compared to the other countries. To put it differently, Iran has been selling its VW for a lower price, as compared to other countries. On the other hand, the upward trend in the cost index of VW exported from the world and Iran is obvious, and over the entire period of studies, the cost of exporting VW for date from the world has been two to four times as much as that of Iran (Fig. 7). The difference in the cost index in Iran and the world should be taken into account as a potential for Iran. The little differences between the amounts of Iran's revenue and price indices in recent years need to be revised the current trend in date export. In other words, the date export compared to other countries shows that Iran pays less cost to supply water for its export products, whereas it also gains less financial benefit.

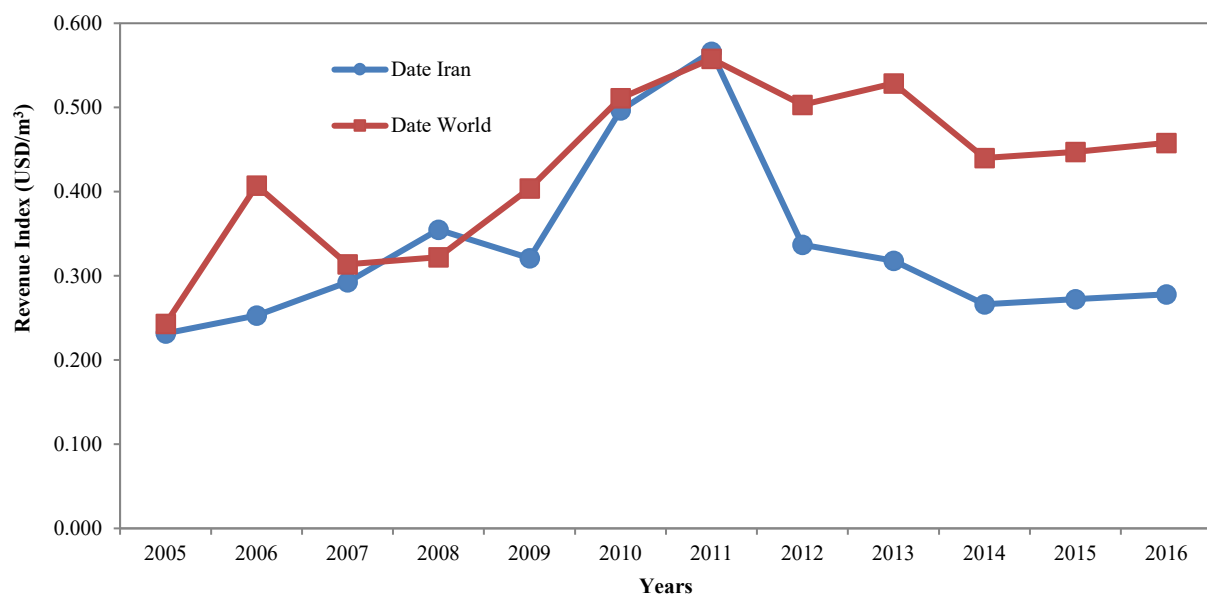


**Fig. 6. Comparison of the date revenue index for Iran and the world.**



### 3.2.3. Saffron

As Table 4 shows, the export rate of saffron has approximately had an up and down trend over the past years. According to this table, the ratio of the economic value to the weight of exported saffron has had an upward trend till 2012, and then a sudden drop in the price of one kilogram of exported saffron from IRAN is observed. The main reasons for this may include:

- 1) The lack of a credible Iranian brand in the global market, with no attention to globalization.
- 2) The lack of marketing channels with global supply-demand chains.
- 3) The lack of international standards in the production and distribution process.

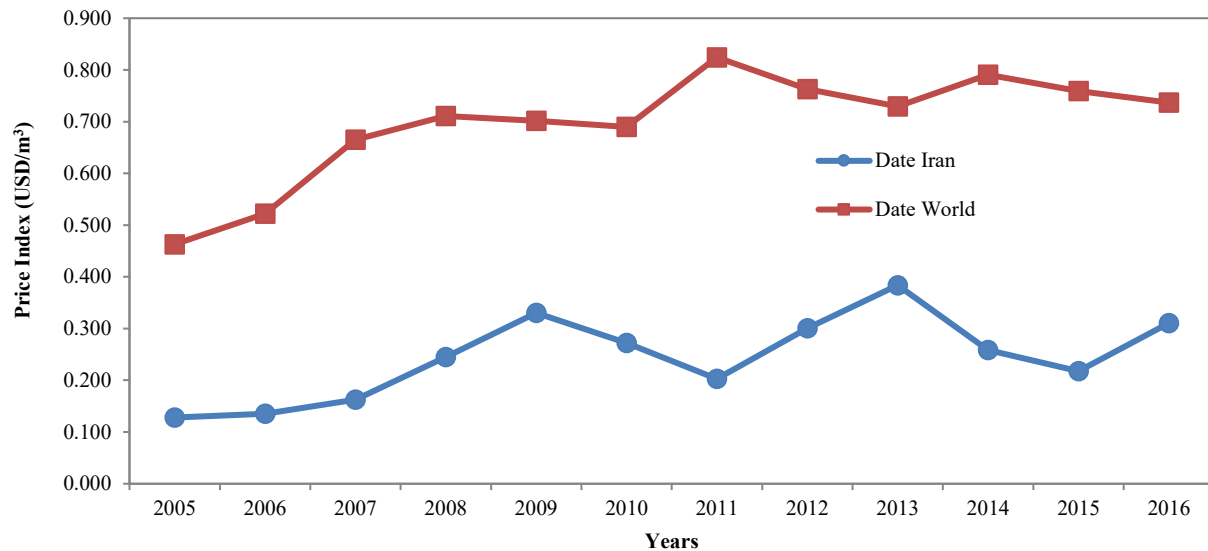


Fig. 7. Comparison of date price index for Iran and the world.

Table 4. Changes in Iran saffron exports over the past years.

Year	Quantity (Ton)	Value (M US\$)	Share form world trade (%)
2005	286.8	95.6	Unavailable Data
2006	142.5	75.9	
2007	103.5	50.6	
2008	100.0	78.0	
2009	65.8	180.0	
2010	107.9	332.0	
2011	122.3	368.0	
2012	139.2	419.0	
2013	137.2	200.0	
2014	158.8	228.0	
2015	65.1	86.0	
2016	55.2	84.0	

These challenges have led the Iranian saffron producers to export their products to destination countries in wholesale (usually in large quantities without marketing considerations). Some of these countries re-export through re-packing Iran's saffron under different international brands.

Lack of precise statistics on the production rates, export quantities, and the value of saffron in other countries has led to incapability to compare Iran's position in terms of saffron exports in the global markets. As the largest producer and exporter of saffron in the world, Iran can direct and control the sales market of saffron in the world. The results obtained from the analysis of revenue index and the price index of virtual water in saffron show huge fluctuations in these indices over the early years of study (Figs. 8 and 9). These unfavorable changes and fluctuations in Iran's saffron trade led the programs in Iran's export sector to gain a steady and positive trend from 2012. In this respect, the best productivity method is planned and reviewed for the export and cultivation policies of the product. Also, the results from revenue and cost indices of saffron reveal that in many years (e.g., 2006, 2007, 2008, 2012 and 2013.), the export price of a specified amount of the virtual water in saffron has become higher than the revenue gained from the sales of the same amount of exported virtual water. That is, Iran has had huge volumes of its water resources on sale for free or even at spending highly expensive financial cost. The results also show that the rate of revenue index of virtual

water for saffron is much higher than pistachio and date. On the other hand, the cost required in order to produce and export saffron is not much more than the price index of virtual water for date and pistachio. These results can confirm naming the saffron as the international brand of Iranian agricultural products.

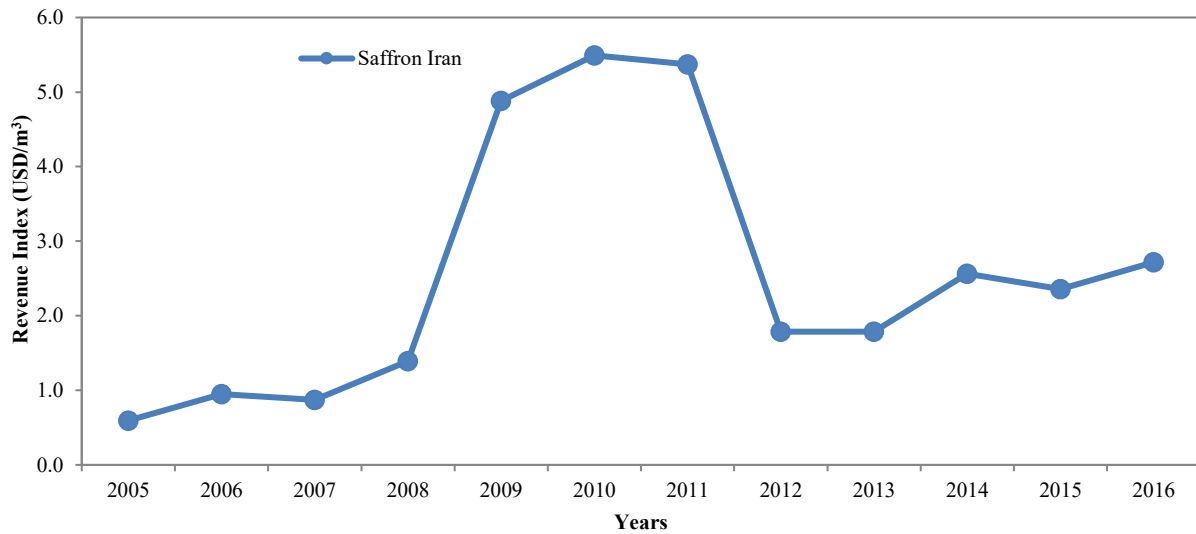


Fig. 8. Saffron revenue index for Iran.

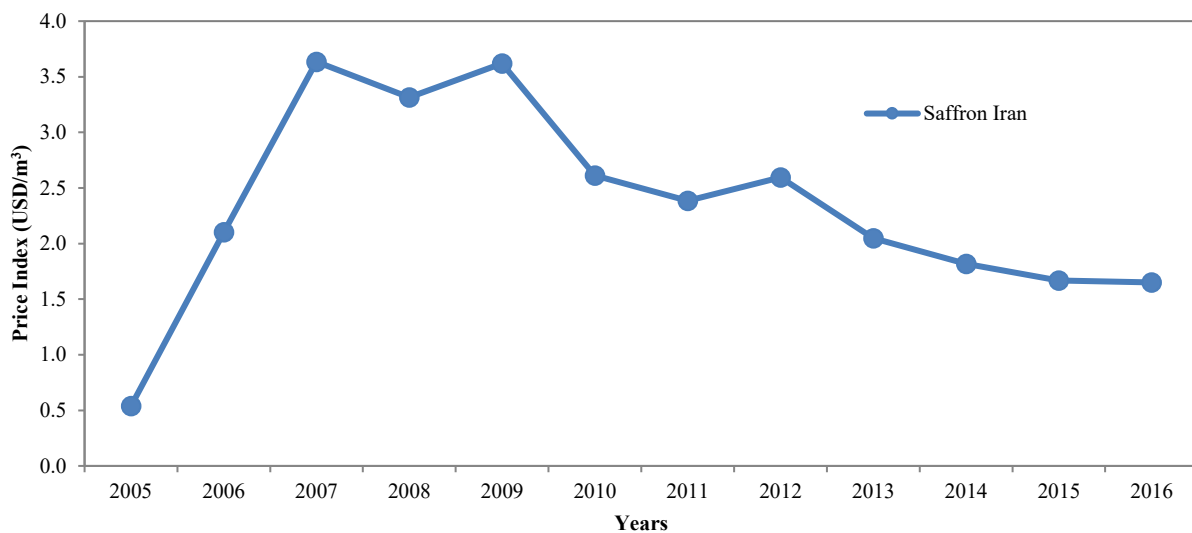


Fig. 9. Saffron price index for Iran.

### 3.2.4. Watermelon

Agricultural production in Iran has moved towards the production of the cheapest and the most water intensive crops because of 1) the high subsidies allocated to the water sector, 2) the lack of restrictions on the use of water resources (especially groundwater) and 3) the supportive governance policies for farmers in rural areas. Watermelon production, as one of the most high-yielding products, has increased rapidly as a result of these policies, consequently taking a high share of agricultural exports.

Over the past years, Iran has raised its watermelon production from 2.8 million tons to 4 million tons, while the share of dry farmed production has decreased from 140,000 tons in 2005 to about 60,000 tons in 2016. This amount of change in watermelon production has imposed high pressure on the corresponding water resources, mostly located in relatively dry regions of Iran. Currently, the Iranian Ministry of Agriculture-Jihad pursues the policy of increasing water productivity and efficiency to produce more crops from every cubic meter of water. Widespread installation of smart water energy meters and improving irrigation systems are the main implemented steps towards water conservation policies, which are expected to increase the water productivity by more than 15%.

As shown in Table 5, the export rate of watermelon has had an upward trend, and Iran has been able to improve its position and share in the world export market in the early years of the study. The share of Iran's export from world trade for watermelon has climbed from %4.4 in 2004 to %12 in 2012, while its value rate, in US\$, has increased around 5 times for the same period. Such an unanticipated growth on one hand and high consumption of water resources for watermelon export on the other hand make the need to seriously review the cultivation and export policies of this product. The results obtained from the investigation of watermelon's revenue index and price index (Figs. 10 and 11) show that the rate of such indices has had an upward, but steady trend (with a few

fluctuations) in the world and in Iran. A very important point from the results is that both the world's revenue and price indexes have held higher values over the past years, as compared to Iran's. In other words, in comparison to Iran, the world gains more revenue from the export of virtual water in watermelon and also pays more cost. Stated differently, in comparison to the world, Iran sells off its virtual water, while it pays less cost. Further studies on such trends can help the export policies better.

**Table 5. Changes in Iran watermelon exports over the past years.**

Year	Quantity (Ton)	Value (M US\$)	Share from World Trade (%)
2005	158878	24.00	7.32
2006	200784	30.42	8.56
2007	301346	45.42	11.83
2008	229812	39.17	8.64
2009	250000	42.00	8.84
2010	348316	89.76	10.94
2011	334248	84.94	12.19
2012	359402	99.89	12.09
2013	56284	15.52	2.00
2014	325644	85.29	10.32
2015	186178	38.52	5.69
2016	178118	33.18	5.02

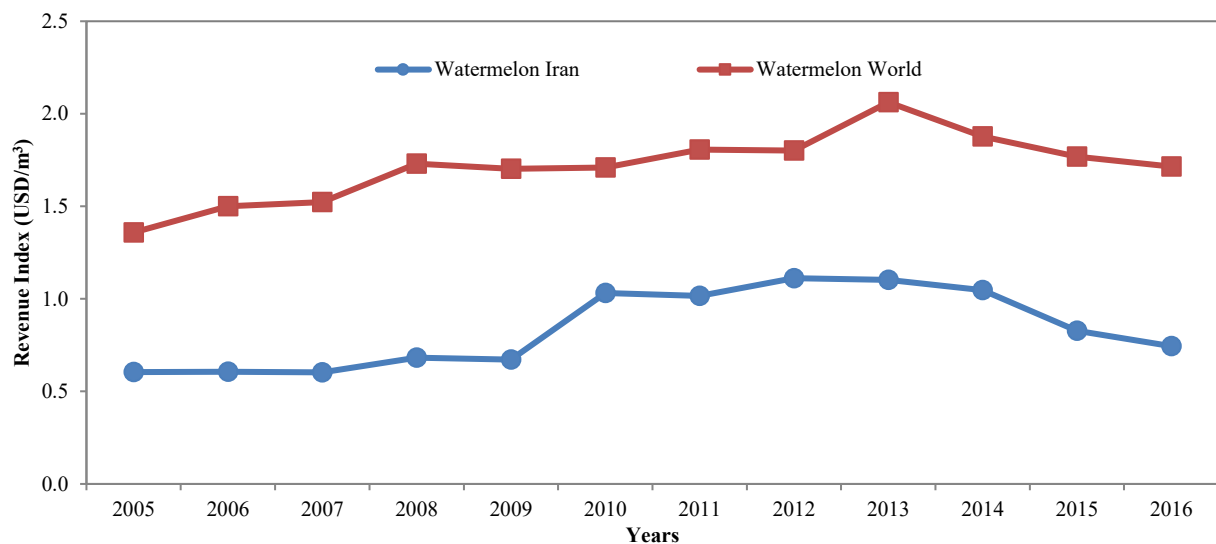


**Fig. 10. Comparison of watermelon revenue index for Iran and the world.**

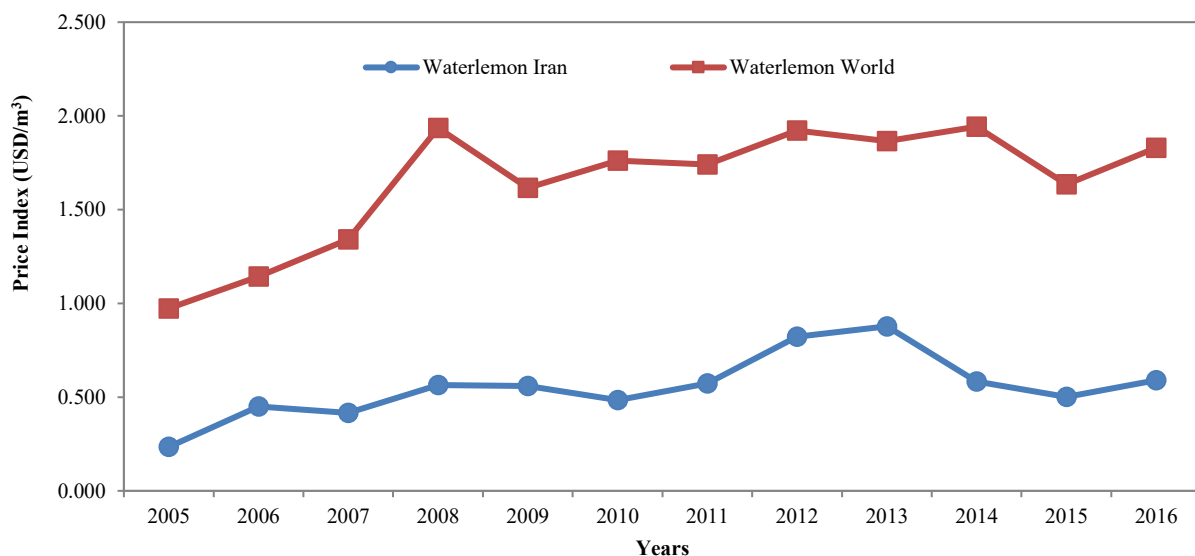


**Fig. 11. Comparison of watermelon price index for Iran and the world.**

### 3.2.5. Tea

Due to climatic reasons, most of the tea produced in Iran is cultivated in the northern regions of the country (with high average rainfall), and this causes Iran's share of blue water for tea production to be lower than the world's. Based on official data of the Iranian Ministry of Agriculture Jihad and FAO [20], during the past years, Iran's tea production has always been around 100 thousand tons. Furthermore, Iran has been ranked the world's 8th largest producer of tea from 2011 to 2015. Meanwhile, over the same years, Iran's name has been among the top 10 importing countries of tea. The main volume of imported tea comes from India and Sri Lanka.

Investigating the available data on tea export and its value over the past years shows that Iran hasn't had much of a share of the world export markets, and depending on the conditions, the export rate has varied over different years (Table 6). The results from the investigation of revenue index and the price index of virtual water in tea are indicative of the higher rates of these indices for Iran, as compared to the world (Figs. 12 and 13). In other words, Iran earns more revenue from the exported virtual water in tea, while it pays more costs proportional to the world. Although the cost index in Iran has followed an upward trend over the past years, it can provide the required explanation for the tea export since the amount of this index is still much lower than the revenue earned. The results for the world's indices of revenue and price show a steady increasing trend for these two indices. It should be pointed out that the world's rate of revenue index lies within the narrow margin of its cost index. Economically speaking, other tea-exporting countries gain less benefit from the exported virtual water. Therefore, tea can be considered as an export product with high added value, and Iran would be able to use the opportunity to gain more benefit from tea export through improving the quality level of its products and reinforcing its economic structure.

**Table 6. Changes in Iran Tea exports over the past years.**

Year	Quantity (Ton)	Value (M US\$)	Share from World Trade (%)
2005	12756	12.70	0.74
2006	33548	35.43	2.06
2007	77028	82.65	4.31
2008	24084	20.66	1.26
2009	10772	8.53	0.59
2010	24611	18.50	1.22
2011	22429	17.61	1.13
2012	11208	11.37	0.62
2013	14620	13.37	0.71
2014	17584	19.80	0.96
2015	7968	8.62	0.46
2016	1950	3.42	0.11

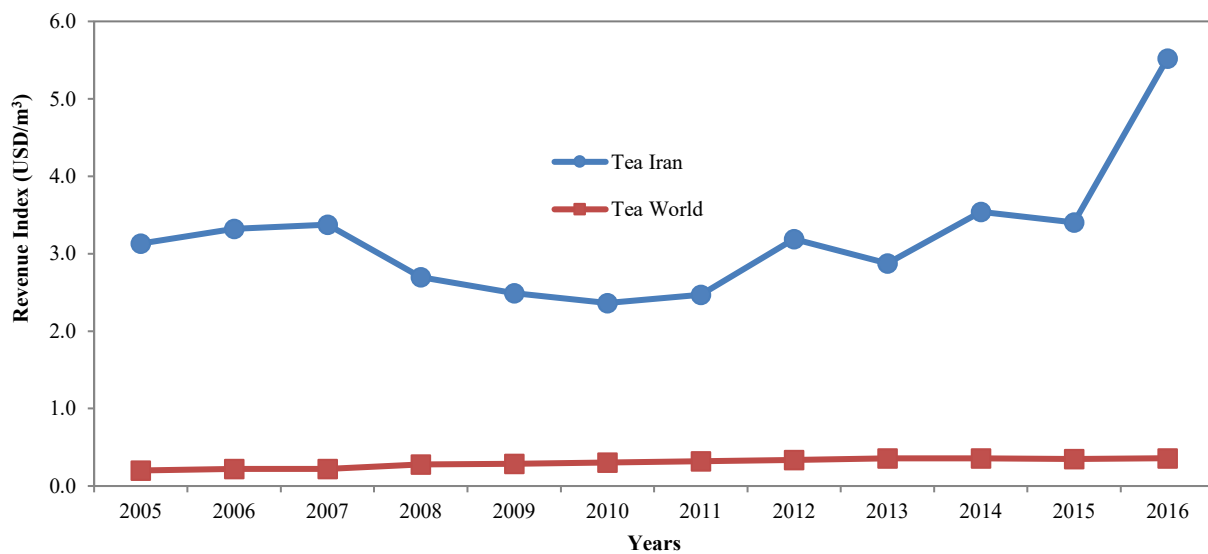


**Fig. 12. Comparison of tea revenue index for Iran and the world.**

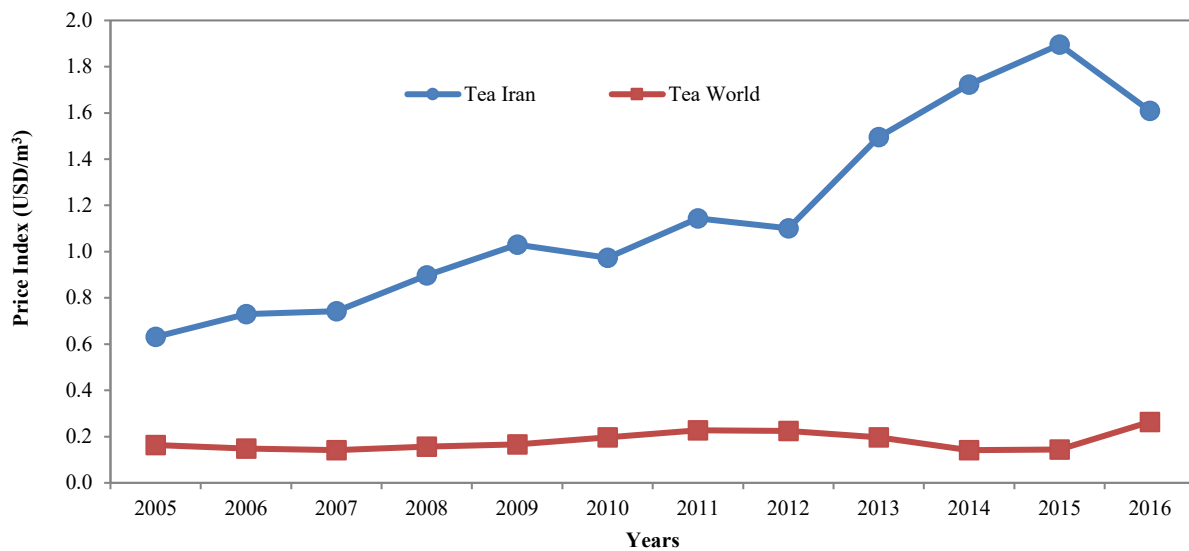


Fig. 13. Comparison of the tea price index for Iran and the world.

### 3.2.6. Rice

Based on the official estimation, around 4 million tons of rice are consumed annually in Iran, 1 to 1.5 million tons of it is imported from abroad (mainly from India and Pakistan). About 5% of the total agricultural area in IRAN belongs to rice cultivation, of which only 32% is located in rainfed farms. The traditional way of rice cultivation (flood irrigation) and the lack of agricultural mechanization across the country have not only caused serious limitations for rice production and export but have also imposed high labor costs. According to the export-related available data (Table 7), Iran has practically not taken a share of this product in world trade during the past years. The comparison of the obtained results in cost and revenue indices for Iran and the world reveals that Iran gains a smaller benefit from rice export, while it also spends more (Figs. 14 and 15). Thus, rice cannot be considered a product with value added for Iran's export. This reason can even be a sign for the need to modify rice cultivation methods and to change the import and export plans for this product. The results also demonstrated that the world's cost and revenue indices have had steadier trends with fewer fluctuations, as compared to Iran's. From the virtual water-trading perspective, it can be interpreted that rice export is still profitable for the world; however, it is unprofitable for Iran.

Table 7. Changes in Iran Rice exports over the past years.

Year	Quantity (Ton)	Value (M US\$)	Share form World Trade (%)
2005	920	0.318	0.003
2006	763	0.314	0.002
2007	10598	3.731	0.032
2008	1942	0.629	0.006
2009	542	0.215	0.002
2010	237	0.055	0.001
2011	110	0.032	0.000
2012	1224	0.158	0.003
2013	1309	0.554	0.004
2014	2626	0.462	0.006
2015	1218	0.455	0.003
2016	495	0.413	0.001

### 3.2.7. Comparison of the different products

The results of evaluating the economic index of RI for each product are condensed in Table 8. Based on this table, the RI of pistachio and tea has a higher income margin than the world trade, while in the trade of date and watermelon, Iran has earned around half of the world (Table 8). In other words, Iran has gained more financial efficiency/productivity due to exporting VW embedded within the pistachio and tea. On the contrary, Iran has sold its VW at the date, rice, and watermelon cheaper than the world. This means that Iran is losing out on world trade. Furthermore, the results show that while the revenue indexes of different products for the world have a more consistent trend (with less variations and fluctuations) with a very mild and smooth increase, Iran's revenue indexes have not experienced stable trends during different years within the study period. These trends may be indicative of the fact that the world has a more stable mechanism for selling and pricing its products in the world market compared to Iran. Consequently, a better water pricing structure is provided in the world, but Iran is facing agricultural water shortage and financial challenges.



Hence, Iran has to reconsider its export and agriculture programs, both from the economic and water consumption perspectives.

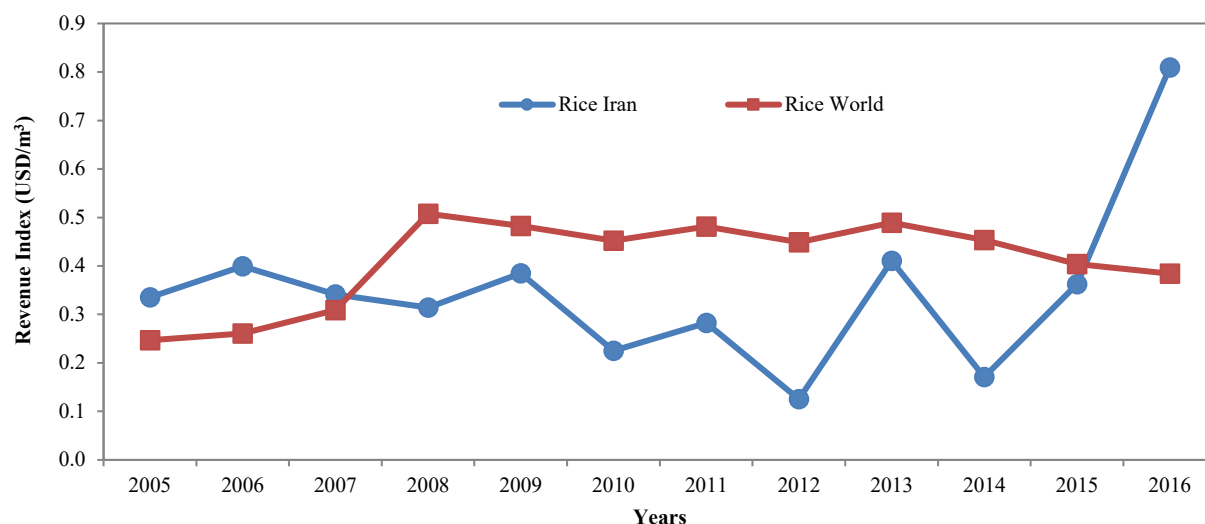


Fig. 14. Comparison of rice revenue index for Iran and the world.

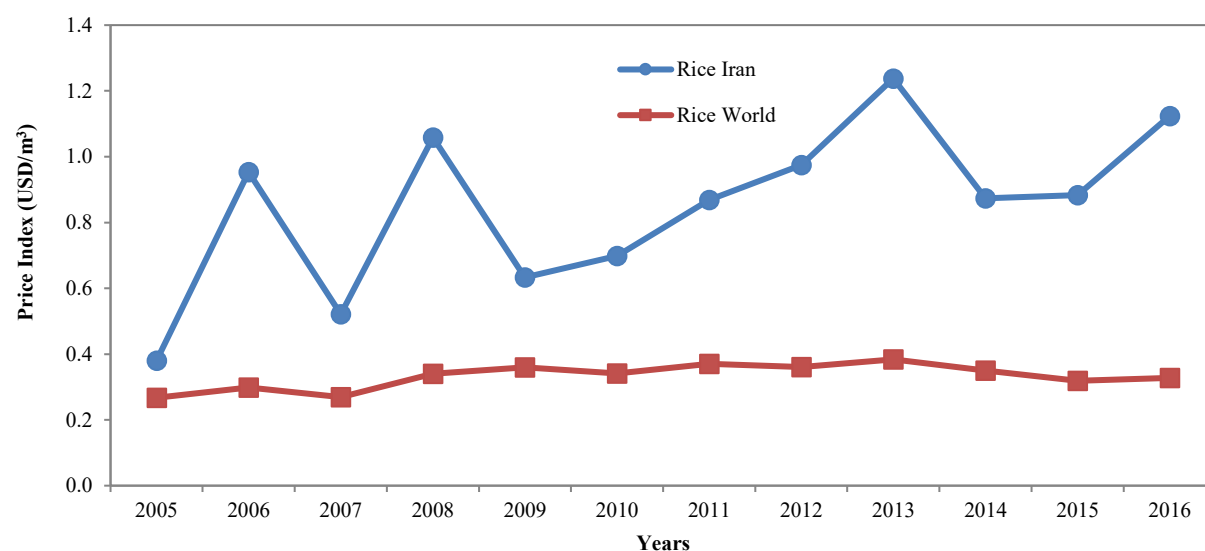


Fig. 15. Comparison of rice price index for Iran and the world.

Table 8. Revenue Index of Exported VW (USD/m³).

Year	Date		Pistachio		Rice		Tea		Watermelon		Saffron	
	Iran	World	Iran	World	Iran	World	Iran	World	Iran	World	Iran	World
2005	0.23	0.24	0.69	0.44	0.34	0.25	3.13	0.20	0.60	1.36	0.59	
2006	0.25	0.41	0.82	0.50	0.40	0.26	3.32	0.22	0.61	1.50	0.95	
2007	0.29	0.31	0.82	0.48	0.34	0.31	3.37	0.22	0.60	1.52	0.87	
2008	0.35	0.32	0.86	0.48	0.31	0.51	2.70	0.28	0.68	1.73	1.39	
2009	0.32	0.40	0.68	0.49	0.38	0.48	2.49	0.29	0.67	1.70	4.88	
2010	0.50	0.51	0.99	0.58	0.23	0.45	2.36	0.30	1.03	1.71	5.49	
2011	0.57	0.56	1.02	0.62	0.28	0.48	2.47	0.32	1.02	1.81	5.37	
2012	0.34	0.50	0.79	0.57	0.13	0.45	3.19	0.34	1.11	1.80	1.79	
2013	0.32	0.53	0.89	0.67	0.41	0.49	2.88	0.36	1.10	2.06	1.79	
2014	0.27	0.44	0.85	0.65	0.17	0.45	3.54	0.36	1.05	1.88	2.56	
2015	0.27	0.45	0.88	0.68	0.36	0.40	3.40	0.35	0.83	1.77	2.36	
2016	0.28	0.46	0.85	0.63	0.81	0.38	5.52	0.36	0.75	1.71	2.72	

Unavailable Data

Comparison of price indexes between Iran and the world during the study period for the different considered products is condensed in Table 9. According to this table, Iran has paid the minimum cost of exporting VW for dates and watermelon. Furthermore, Iran's price index for watermelon and date is much lower than the world price indexes. In other words, Iran has paid less for selling its VW in comparison with the world. On the contrary, the world has benefited from lower prices, which it has had to pay for exporting other products (tea, rice, and pistachio). Among all the products, saffron has the highest price index value for exported VW. Table 9 also shows that during the study period, the world price indexes of different products have very limited variation and they have increased with a very gentle slope. Not surprisingly, Iran's price indexes have had more fluctuations over the last years. These trends of Iran may be attributed to the ineffectiveness of existing programs in the agricultural sector (water pricing structure, water efficiency, and ...), and the export policies need to be revised and planned carefully.

**Table 9. Price Index of Exported VW (USD/m<sup>3</sup>).**

Year	Date		Pistachio		Rice		Tea		Watermelon		Saffron	
	Iran	World	Iran	World	Iran	World	Iran	World	Iran	World	Iran	World
2005	0.13	0.46	0.48	0.43	0.38	0.27	0.63	0.16	0.23	0.97	0.54	Unavailable Data
2006	0.14	0.52	0.44	0.41	0.95	0.30	0.73	0.15	0.45	1.14	2.10	
2007	0.16	0.67	0.52	0.47	0.52	0.27	0.74	0.14	0.42	1.34	3.64	
2008	0.25	0.71	0.60	0.44	1.06	0.34	0.90	0.16	0.56	1.94	3.31	
2009	0.33	0.70	0.87	0.43	0.63	0.36	1.03	0.17	0.56	1.62	3.62	
2010	0.27	0.69	0.89	0.59	0.70	0.34	0.97	0.20	0.48	1.76	2.61	
2011	0.20	0.82	0.98	0.52	0.87	0.37	1.14	0.23	0.57	1.74	2.38	
2012	0.30	0.76	1.66	0.49	0.97	0.36	1.10	0.22	0.82	1.92	2.60	
2013	0.38	0.73	1.83	0.65	1.24	0.38	1.50	0.20	0.88	1.87	2.05	
2014	0.26	0.79	1.51	0.69	0.87	0.35	1.72	0.14	0.58	1.94	1.82	
2015	0.22	0.76	1.32	0.55	0.88	0.32	1.90	0.14	0.50	1.64	1.67	
2016	0.31	0.74	1.04	0.53	1.12	0.33	1.61	0.26	0.59	1.83	1.65	

Comparison of the net profit of products between Iran and the World trade is shown in Table 10. In this table, the better data values are also shown in bold. As seen in this table, tea, watermelon, date, and saffron have the highest net profit for Iran, respectively. Furthermore, Iran could acquire 17.23 and 4 times more profit than the world from exporting tea and watermelon, respectively. On the contrary, the world can gain more profit than Iran from a cubic meter of VW exported for pistachio and rice. In other words, while pistachio is one of the well-known international brands of the agricultural sector of Iran, the net profit belonging to the world is much higher than Iran. Therefore, pistachio, as the key strategic product, requires better decision-making in export planning. The results also indicate that Iran has never been a contender for the export and production of rice. This policy is absolutely correct both from the water consumption and economic aspects of VW. While the lack of reliable data about saffron in world scale has limited the cost-benefit analysis of Iran's export but one fact is obvious: Iran's profit from VW trade of saffron has always been fluctuating.

**Table 10. Net profit value of exported VW (USD/m<sup>3</sup>).**

Year	Date		Pistachio		Rice		Tea		Watermelon		Saffron	
	Iran	World	Iran	World	Iran	World	Iran	World	Iran	World	Iran	World
2005	<b>0.10</b>	-0.22	<b>0.21</b>	0.01	-0.05	<b>-0.02</b>	<b>2.50</b>	0.04	0.37	<b>0.39</b>	0.06	Unavailable Data
2006	<b>0.12</b>	-0.12	<b>0.38</b>	0.09	-0.55	<b>-0.04</b>	<b>2.59</b>	0.07	0.16	<b>0.36</b>	-1.15	
2007	<b>0.13</b>	-0.35	<b>0.29</b>	0.01	-0.18	<b>0.04</b>	<b>2.63</b>	0.08	<b>0.19</b>	0.18	-2.76	
2008	<b>0.11</b>	-0.39	<b>0.26</b>	0.05	-0.74	<b>0.17</b>	<b>1.80</b>	0.12	<b>0.12</b>	-0.21	-1.92	
2009	<b>-0.01</b>	-0.30	-0.18	<b>0.07</b>	-0.25	<b>0.12</b>	<b>1.46</b>	0.12	<b>0.11</b>	0.09	1.26	
2010	<b>0.22</b>	-0.18	<b>0.10</b>	-0.01	-0.47	<b>0.11</b>	<b>1.39</b>	0.11	<b>0.55</b>	-0.05	2.88	
2011	<b>0.36</b>	-0.27	0.04	<b>0.09</b>	-0.59	<b>0.11</b>	<b>1.33</b>	0.09	<b>0.44</b>	0.07	2.99	
2012	<b>0.04</b>	-0.26	-0.87	<b>0.08</b>	-0.85	<b>0.09</b>	<b>2.09</b>	0.11	<b>0.29</b>	-0.12	-0.81	
2013	<b>-0.07</b>	-0.20	-0.95	<b>0.01</b>	-0.83	<b>0.11</b>	<b>1.38</b>	0.16	<b>0.23</b>	0.20	-0.26	
2014	<b>0.01</b>	-0.35	-0.65	<b>-0.05</b>	-0.70	<b>0.10</b>	<b>1.82</b>	0.22	<b>0.46</b>	-0.06	0.75	
2015	<b>0.05</b>	-0.31	-0.45	<b>0.13</b>	-0.52	<b>0.09</b>	<b>1.51</b>	0.20	<b>0.33</b>	0.13	0.69	
2016	<b>-0.03</b>	-0.28	-0.20	<b>0.10</b>	-0.31	<b>0.06</b>	<b>3.91</b>	0.10	<b>0.15</b>	-0.12	1.07	
Mean	<b>0.09</b>	-0.27	-0.17	<b>0.05</b>	-0.50	<b>0.08</b>	<b>2.03</b>	0.12	<b>0.28</b>	0.07	0.23	

To briefly sum up, the current conditions of exporting VW embedded in tea, watermelon, saffron, and date trades are still reasonable. Conversely, exporting any cubic meter of VW for pistachio and rice can impose more cost than revenue. Therefore,

supporting current policy for exporting pistachio and rice not only can intensify the depletion of water resources dramatically but also impose an exorbitant cost on policymakers. Furthermore, the price and revenue indexes of Iran have never gained their favorable or stable trends in comparison with the world's trend. It is worth noting that the more net profit will be available for a product, the higher priority can be assigned to a given product for being in the export basket. Similarly, an export basket comprised of higher priority products can return more economic profits.

#### 4. Summary and conclusions

Countries develop agricultural export policies for many reasons, while, more often than not, the availability of water resources is overlooked. Moreover, attention to the value and price of water, as a production input, is often neglected. Hence, investigation of these underutilized potentials would positively impact export policies. This study aims to present an approach for considering the role of both financial value and volume of VW in Iran trade, especially in export business. This issue has not been addressed deservedly from both commercial and academic points of view collectively. As a response to this necessity, a three-step framework with two new identified indices is presented. The presented approach was implemented for six agricultural products of Iran. The results show that, although products such as watermelon, tea, and rice are considered water-consuming ones, they do not consume as many water resources as Iran's international brands do. In other words, however, saffron, pistachio, and dates are known as the international brands of Iran, but blindfold-supporting export of these products can cause severe consequences on water resources, the financial value of export, and the economic net profit of selling each cubic meter of VW in world trade. It is worth mentioning that among all water-consuming products, watermelon and tea have been able to provide a considerable financial added value in Iran's export sector. Providing reliable databases with robust decision support systems may be nominated as the most significant fundamental prerequisites for future planning in order to achieve better-targeted export and world trade.

To pursue further research on implementation of the proposed framework and hence increasing the net profit of export policies, not only appropriate plans must be codified, but the agriculture sector must attempt to increase the agricultural productivity, irrigation efficiency, applying new technologies and modern irrigation systems, using various farming methods and locating suitable replacements for different cultivation patterns and methods. Hence, a better management of the virtual water in different products would be achieved, in which not only would the benefit gained from exported virtual water increase, but the use of water resources would decrease. Furthermore, using tools, namely portfolio theory, could determine the appropriate portion of each of the products in Iran's export basket so that the risk of using water resources and financial benefits tends to a minimum and maximum, respectively.

#### Statements & declarations

##### *Author contributions*

**Ardalan Izadi:** Conceptualization, Project administration, Investigation, Formal analysis, Resources, Writing - Original Draft.

**Farhad Yazdandoost:** Conceptualization, Supervision, Writing - Review & Editing.

##### *Acknowledgments*

The country-scale import and export data of agricultural crops for the years 2005–2016 were obtained from the FAOSTAT (<http://www.fao.org/faostat/en/#data>) by the Food and Agriculture Organization of the United Nations Statistics Division and Iran Ministry of Agriculture Jihad, and Chamber of Commerce, Industries, Mines, and Agriculture.

##### *Funding*

The author(s) received no financial support for the research, authorship, and/or publication of this article.

##### *Declaration of interest statement*

The authors declare that they have no known competing financial interests or personal relationships that could have appeared to influence the work reported in this paper.

##### *Data availability*

The data presented in this study are available on request from the corresponding author.

#### References

- [1] Madani, K. Water Management in Iran: What Is Causing the Looming Crisis? *Journal of Environmental Studies and Sciences*, 2014; 4 (4): 315–328. doi:10.1007/s13412-014-0182-z.
- [2] Allan, J. A. Fortunately there are substitutes for water: otherwise our hydropolitical futures would be impossible. In: *Proceedings of the Conference on Priorities for Water Resources Allocation and Management: Natural Resources and Engineering Advisers Conference*; 1992 Jul; Southampton, United Kingdom. London: Overseas Development Administration; 1993. p. 13–26.
- [3] Vos, J., Boelens R. The politics and consequences of virtual water export. In: Smetana S, Bornkessel S, editors. *Eating, drinking: surviving*. Cham: Springer International Publishing; 2016. p. 31–41. doi:10.1007/978-3-319-42468-2\_4.

- [4] Orlowsky, B., Hoekstra, A. Y., Gudmundsson, L., Seneviratne, S. I. Today's Virtual Water Consumption and Trade under Future Water Scarcity. *Environmental Research Letters*, 2014; 9 (7): 74007. doi:10.1088/1748-9326/9/7/074007.
- [5] Kumar, M. D., Singh, O. P. Virtual Water in Global Food and Water Policy Making: Is There a Need for Rethinking? *Water Resources Management*, 2005; 19 (6): 759–789. doi:10.1007/s11269-005-3278-0.
- [6] Kounina, A., Margni, M., Bayart, J. B., Boulay, A. M., Berger, M., Bulle, C., Frischknecht, R., Koehler, A., Milà I Canals, L., Motoshita, M., Núñez, M., Peters, G., Pfister, S., Ridoutt, B., Van Zelm, R., Verones, F., Humbert, S. Review of Methods Addressing Freshwater Use in Life Cycle Inventory and Impact Assessment. *International Journal of Life Cycle Assessment*, 2013; 18 (3): 707–721. doi:10.1007/s11367-012-0519-3.
- [7] Distefano, T., Kelly, S. Are We in Deep Water? Water Scarcity and Its Limits to Economic Growth. *Ecological Economics*, 2017; 142: 130–147. doi:10.1016/j.ecolecon.2017.06.019.
- [8] Berger, M., Van Der Ent, R., Eisner, S., Bach, V., Finkbeiner, M. Water Accounting and Vulnerability Evaluation (WAVE): Considering Atmospheric Evaporation Recycling and the Risk of Freshwater Depletion in Water Footprinting. *Environmental Science and Technology*, 2014; 48 (8): 4521–4528. doi:10.1021/es404994t.
- [9] Lee, S. H., Yoo, S. H., Choi, J. Y., Mohtar, R. H. Evaluation of External Virtual Water Export and Dependency through Crop Trade: An Asian Case Study. *Paddy and Water Environment*, 2017; 15 (3): 525–539. doi:10.1007/s10333-016-0569-4.
- [10] Guan, D., Hubacek, K. Assessment of Regional Trade and Virtual Water Flows in China. *Ecological Economics*, 2007; 61 (1): 159–170. doi:10.1016/j.ecolecon.2006.02.022.
- [11] Mekonnen M. M., Hoekstra A. Y. National water footprint accounts: the green, blue and grey water footprint of production and consumption. Delft: UNESCO-IHE Institute for Water Education; 2011. Report No.: 50. (Value of Water Research Report Series).
- [12] Soltani, G. Agricultural water-use efficiency in a global perspective: the case of Iran. Cairo: Economic Research Forum; 2013 Oct. Working Paper No.: 778.
- [13] Baghestany, A. A., Mehrabi Boshrahadi, H., Zare Mehrjerdi, M., Sherafatmand, H. Application of the Concept of Virtual Water in Water Resources Management of Iran. *Iran-Water Resources Research*, 2010; 6(1): 28-38.
- [14] Faramarzi, M., Yang, H., Mousavi, J., Schulin, R., Binder, C. R., Abbaspour, K. C. Analysis of Intra-Country Virtual Water Trade Strategy to Alleviate Water Scarcity in Iran. *Hydrology and Earth System Sciences*, 2010; 14 (8): 1417–1433. doi:10.5194/hess-14-1417-2010.
- [15] Ward, F. A., Michelsen, A. The Economic Value of Water in Agriculture: Concepts and Policy Applications. *Water Policy*, 2002; 4(5): 423–446. doi:10.1016/S1366-7017(02)00039-9.
- [16] Wang, Y. B., Liu, D., Cao, X. C., Yang, Z. Y., Song, J. F., Chen, D. Y., Sun, S. K. Agricultural Water Rights Trading and Virtual Water Export Compensation Coupling Model: A Case Study of an Irrigation District in China. *Agricultural Water Management*, 2017; 180: 99–106. doi:10.1016/j.agwat.2016.11.006.
- [17] Chowdhury, N. T. The economic value of water in the Ganges-Brahmaputra-Meghna (GBM) River Basin. Stockholm: Beijer International Institute of Ecological Economics; 2005
- [18] Isfahan Municipality. Isfahan statistical yearbook 2015–2016. Isfahan: Isfahan Municipality; 2016.
- [19] Zheng, Z., Saghaian, S., Reed, M. Factors Affecting the Export Demand for U.S. Pistachios. *International Food and Agribusiness Management Review*, 2012; 15 (3): 139–154.
- [20] Food and Agriculture Organization of the United Nations. Report of the Working Group on Global Tea Market Analysis and Promotion: Intergovernmental Group on Tea. Rome: FAO; 2015.

# Estimation of Energy Dissipation in Non-Aerated Flow Regimes over Stepped Spillways Using Advanced Soft Computing Techniques

Milad Taji<sup>a</sup>, Massoud Morsali<sup>b\*</sup>, Mehdi Eilbeigi<sup>c</sup>

<sup>a</sup> Department of Civil Engineering (hydraulic structures), University of Shahrkord, Shahrkord, Iran

<sup>b</sup> Department of Geology, Faculty of Science, University of Isfahan, Isfahan, Iran

<sup>c</sup> Department of Hydrogeology, Shahid Chamran University, Ahvaz, Iran

## ARTICLE INFO

### Keywords:

Stepped spillways  
ANFIS  
ANN  
Soft models  
Energy dissipation  
SVR

### Article history:

Received 10 May 2025

Accepted 17 May 2025

Available online 21 May 2025

## ABSTRACT

Stepped spillways have garnered significant attention due to their high efficiency in dissipating flow energy, primarily attributed to the presence of steps that enhance turbulence and energy loss. A stepped spillway consists of a sequence of vertical drops extending from the crest at the upstream end to the stilling basin at the downstream. Under high discharge conditions, the flow regime transitions into non-aerated skimming flow, characterized by substantial energy levels that necessitate careful management. Accurate estimation of energy dissipation is essential for the safe and economical design of downstream energy dissipators. In this study, 154 experimental data points from physical models of stepped spillways were utilized, encompassing a broad range of hydraulic conditions by varying parameters such as the drop number, spillway slope, number of steps, critical depth-to-step height ratio, and Froude number. To predict the energy dissipation, several soft computing techniques were applied, including Artificial Neural Networks (ANN), Adaptive Neuro-Fuzzy Inference Systems (ANFIS), and Support Vector Regression (SVR). The models' predictive capabilities were assessed using key statistical performance metrics, including the coefficient of determination ( $R^2$ ), Root Mean Square Error (RMSE), and Mean Absolute Error (MAE). Comparative analysis of the results demonstrated that the ANN model exhibited superior accuracy over the other models, achieving  $R^2$ , RMSE, and MAE values of 0.99, 0.96, and 0.67, respectively. The findings underscore the potential of soft computing models, particularly ANN, as powerful predictive tools in hydraulic engineering applications. The proposed modeling approach offers an effective means for estimating energy dissipation in stepped spillways, facilitating optimized and cost-effective design of hydraulic structures.

## 1. Introduction

Spillways are critical components in dam infrastructure, serving to discharge excess reservoir volume exceeding the dam's storage capacity to the downstream environment. This discharge is characterized by a substantial kinetic energy flux, thus necessitating dedicated energy dissipation mechanisms. Management of the high-energy flow has consistently presented a significant challenge in hydraulic structure design, as inadequate energy dissipation can precipitate detrimental effects, including downstream channel erosion, structural abrasion, and scour at the dam foundation. While downstream energy dissipation systems, particularly stilling basins, are conventionally employed to mitigate this energy, pre-emptive energy reduction within the spillway itself can substantially decrease the energy load imposed on downstream structures. This approach, in turn, may facilitate a reduction in the construction costs associated with downstream energy dissipation infrastructure [1, 2].

\* Corresponding author.

E-mail addresses: [m.morsali@sci.ui.ac.ir](mailto:m.morsali@sci.ui.ac.ir) (M. Morsali).





Stepped spillways, commonly employed in large dams, have demonstrated effective energy dissipation of high-velocity flows. These spillways are, in essence, a type of hydraulic structure that has garnered significant attention due to their ability to control flood flows and attenuate substantial potential energy. Furthermore, their implementation leads to a reduction in the required dimensions of the stilling basin [3, 4]. Stepped spillways, with a long history in hydraulic engineering dating back approximately 3500 years, remain the subject of extensive research. This is because the precise hydrodynamic mechanisms governing flow energy dissipation and turbulent flow patterns within these structures have not yet been fully modeled and explained, particularly under varying geometric and flow conditions [5].

Stepped spillways with diverse configurations are widely employed to dissipate the kinetic energy of flow at the outlet and, consequently, to reduce the dimensions of downstream energy dissipation structures. The hydraulic behavior of these structures is highly dependent on the inflow rate, and as the flow rate increases, the flow regime transitions from nappe flow to skimming flow [6]. Numerous experimental studies have investigated the performance of stepped spillways, considering parameters such as staircase and channel geometry, inlet flow conditions, the type of construction materials, and other relevant factors. Based on the results obtained from research [7-10], the flow hydraulics in these spillways can be categorized into three distinct regimes, based on the ratio of critical depth to step height: nappe flow, transition flow, and skimming flow (Fig. 1). It should be noted that in the nappe flow regime, energy dissipation is generally more effective. However, in long stepped spillways, the total energy dissipation under a steady skimming flow regime is greater due to the higher flow velocities. The characteristics of the vortices formed are influenced by factors such as the spillway slope, step geometry, and overall geometric dimensions [11, 12]. In this section, each of these three flow regimes will be briefly described [13].

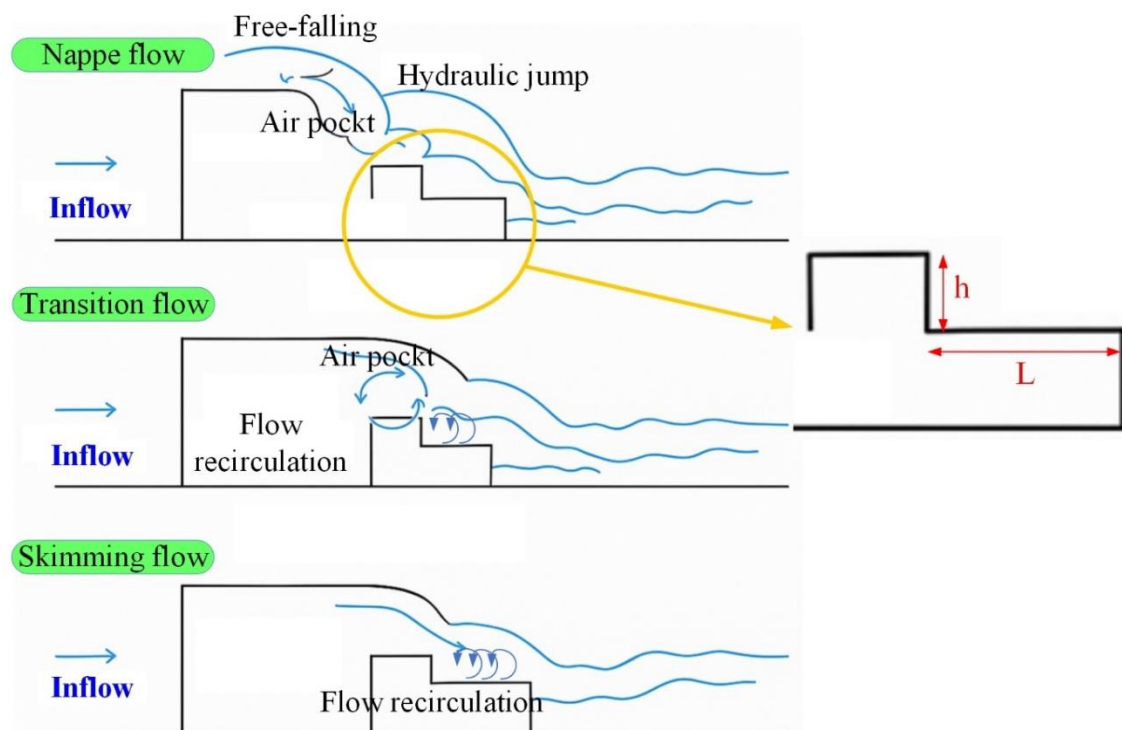


Fig. 1 Classification of three distinct flow regimes in stepped spillways.

A) Nappe Flow: Nappe flow is a type of flow occurring over a stepped spillway with a low slope and low discharge, characterized by a series of free-falling jets that impact the subsequent step. This flow regime is referred to as nappe flow. In other words, in the nappe flow regime, the total height of the spillway is divided into a series of vertical cascades, and the flow is observed as a chain of free-falling waterfalls. Energy dissipation in this case occurs due to the interaction of the flow with the air and the formation of a complete or incomplete hydraulic jump on each step.

B) Skimming Flow: At high flow rates, the flow skims over the outer edges of the steps, such that the step edges form a virtual bed over which the water descends. Beneath this virtual bed, rotating vortices are formed. This type of flow is called skimming flow or pseudo-smooth flow. If the spillway is long, the flow becomes frothy at the toe of the spillway, and the flow appears as white water. In this type of flow, the majority of energy dissipation occurs due to the generation of rotating currents beneath the false bed.

C) Transitional Flow: Regions of flow occur between the regimes of nappe flow and skimming flow, known as transitional flow. Visually, this type of flow is highly irregular, and its hydraulic characteristics change significantly along the spillway. It is associated with intense water dispersion and sudden waves.

Numerous researchers have employed numerical methods and laboratory models to assess and estimate energy dissipation in stepped spillways. Tabbara et al. (2005) conducted a computational simulation of the flow over stepped spillways. Using finite element method codes, these researchers modeled the flow over a stepped spillway. The study aimed to estimate the main characteristics related to flow, namely identifying the water surface profile, improving the understanding of corner vortex dynamics,

and quantifying energy dissipation. The stepped spillway used in this experiment consisted of four steps. The results obtained from all simulations indicated that the predicted water surface profile and the estimated energy dissipation rate were in good agreement with experimental measurements [14].

Feldman and Chanson investigated three parameters: energy dissipation, flow resistance, and air-water interfaces. The results of this experimental study indicated that, in skimming and transitional flow regimes, the free surface of the flow was quite smooth and clear in the initial steps. Significant aeration occurred when the void spaces of the steps induced turbulence that extended to the free water surface. Furthermore, the findings suggested that step height and discharge rate had no impact on the parameters being examined. A comparison between the use of stepped spillways and conventional spillways demonstrated that, at a constant flow rate, stepped spillways exhibit greater aeration and higher energy dissipation [15]. Hamed et al. conducted a study to investigate energy dissipation using both stepped spillways and an end sill simultaneously. Their results indicated that the combined use of these two elements significantly enhances energy loss in transitional and skimming flow regimes. Furthermore, the energy dissipation rate was found to be greater in transitional flows compared to skimming flows. Laboratory results demonstrated that optimal energy dissipation occurs when the ratio of step length to step height is between 0.7 and 1. Outside of this range, energy dissipation decreases due to the potential for the hydraulic jump to occur over multiple steps [16].

Husain et al. employed the Smoothed Particle Hydrodynamics (SPH) method to investigate the pressure distribution on steps of stepped spillways within the non-aerated flow region. The numerical results obtained from this study indicated a good agreement between the velocity and water surface profiles at various sections and the experimental results presented in the literature. The experiments further revealed that stepped spillways, in addition to energy dissipation, protect the structure's surface from cavitation due to the self-aeration process, which introduces air bubbles into the flow [17]. Hou et al. simulated aeration and energy dissipation in stepped spillways using the Random Number Generation (RNG) model and the Volume of Fluid (VOF) method. They utilized a 1:60 scale laboratory model for their simulations. The results indicated that computer numerical simulations can accurately estimate energy dissipation and aeration. Furthermore, they found that an increased contraction ratio at the gate leads to greater energy dissipation. However, with respect to aeration, an increased contraction ratio initially enhances aeration on the first few steps before subsequently reducing it [18]. Shahheydari et al. investigated the flow over stepped spillways using the Flow-3D software, employing the VOF method to define the surface flow profiles. For this purpose, 112 spillway models were designed, encompassing two different step sizes, six configurations, four distinct flow rates, and four different profile slopes. These models were subjected to varying flow rates to measure energy dissipation and the discharge coefficient. The results indicated an inverse relationship between the discharge coefficient and energy dissipation; as energy dissipation increased, the discharge coefficient decreased [19].

Khatibi and Salmasi investigated energy dissipation on gabion stepped spillways using artificial intelligence, genetic algorithms, and regression equations, conducting several experiments. In their study, they employed multiple variables, including discharge, two different slopes, and various gabion materials. They analyzed 74 data points under two flow regimes: skimming and transitional. Eighty percent of the data was used for training, while twenty percent was used for testing. Analysis of the results indicated that artificial neural network (ANN) models demonstrated higher reliability in estimating energy dissipation compared to genetic algorithms and regression models. Accordingly, the coefficient of determination ( $R^2$ ) and root mean square error (RMSE) were used to evaluate the performance of the different models [20]. Focusing on flow rate and channel slope, Mostafa et al. investigated energy dissipation in stepped spillways under transition and skimming flow regimes. Simulated flow rates ranged from 0.72 L/s to 2.569 L/s. With channel slopes of 15°, 30°, and 45° examined, results indicated that, on average, the 45° slope exhibited the highest energy dissipation in the stepped spillways [21]. Tabari and Tavakoli investigated the influence of stepped spillway geometry on flow patterns and energy dissipation, seeking to establish a relationship between energy dissipation and critical depth. Their findings, obtained through Flow-3D simulations, indicated that increased energy dissipation resulted from decreased discharge, fewer steps, and increased step height [2].

Accurately estimating energy dissipation in spillways is a critical subject that has been extensively studied by various researchers. In this context, approaches based on machine learning models have not only demonstrated acceptable accuracy in predicting energy dissipation in stepped spillways but have also succeeded in modeling the intricate patterns that occur in these processes by considering various parameters and statistical analyses. These methods offer higher accuracy compared to traditional techniques and possess the capability to process large datasets, features that significantly enhance their value as powerful tools in the design and optimization of energy dissipation systems, especially in civil engineering and water engineering projects.

Hanbay and colleagues predicted flow conditions over stepped chutes using an Adaptive Neuro-Fuzzy Inference System (ANFIS). In their research, the number of steps, slope, and critical flow depth were used as input data for the ANFIS model to predict flow conditions over stepped spillways. The model's performance was evaluated using cross-validation, achieving an accuracy of 99.01%, demonstrating the high potential of ANFIS in hydraulic systems. This study encompassed all three flow regimes: nappe, skimming, and transition. The results indicated that flow over stepped spillways is turbulent, leading to significant air entrainment. Therefore, it is crucial to accurately predict hydraulic conditions for the design of a stepped structure [22]. Roushangar et al. (2014) utilized ANN and genetic programming (GEP) models to model energy dissipation. To determine the optimal percentage split for training and testing data, they employed three different data allocation strategies. Ultimately, the model using 65% of the data for training and 35% for testing demonstrated the best performance. The resulting values of Correlation Coefficient (R), Nash-Sutcliffe index (NS), and RMSE obtained under all three flow regimes indicated that the artificial neural network (ANN) model yielded values of 0.968, 0.936, and 2.9, respectively, while the GEP model produced values of 0.968, 0.937, and 2.85, respectively [23]. Salmasi and Özger investigated the hydraulic characteristics of stepped spillways through

experimentation, the development of models to describe the data, and the testing of model accuracy. In their research, an ANFIS model was employed to correlate input and output variables, specifically energy dissipation. The inputs to this model consisted of five variables: the number of steps, the spillway slope, the Froude number, the critical depth, and the drop number. Furthermore, two metrics,  $R^2$  and RMSE, were used to compare the performance of different models. Ultimately, the  $R^2$  value for the ANFIS model was calculated to be 0.966 [13]. Ekmekcioğlu et al. evaluated Support Vector Machine (SVM), K-Nearest Neighbors (KNN), and ANN models for predicting energy dissipation in stepped spillways, using laboratory data. Their results indicated that ensemble-based intelligence models outperformed individual machine learning methods in predicting energy dissipation [24]. Baharvand et al. predicted the rate of energy dissipation and its variations in stepped vertical overfalls under various geometric and hydraulic conditions using two models: Random Forest Regression (RF) and Support Vector Regression (SVR). An examination of 27 geometric scenarios revealed that the energy dissipation rate in this type of spillway gradually increases with relative water depth. Furthermore, the RF model demonstrated superior performance compared to the Support Vector Regression method [25].

Building upon prior research and the significant role machine learning models have played in enhancing the accuracy of hydraulic variable predictions, this study aims to investigate and predict energy dissipation rates in stepped spillways under skimming flow conditions. Specifically, laboratory experimental data pertaining to stepped spillways were utilized to evaluate the performance of three artificial intelligence models: ANN, ANFIS, and SVR. By comparing the accuracy of the results obtained from these models, this research seeks to achieve the most precise estimation of energy dissipation in stepped spillways possible, thereby informing the design and optimal dimensioning of stilling basins downstream of the spillway from a broader perspective.

## 2. Methodology

To investigate energy dissipation in stepped spillways, all experimental activities in this study were conducted based on the results of tests performed in the Hydraulics Laboratory of Shahid Chamran University of Ahvaz [13]. In this research, various parameters affecting energy dissipation in stepped spillways were examined and analyzed, and the data were evaluated using statistical methods.

### 2.1. Properties of a physical model

Laboratory activities in this study were conducted in two distinct channels. Channel 1 had a width of 0.5 meters, a length of 8 meters, and a height of 1.6 meters. Channel 2 had a width of 0.25 meters, a length of 10 meters, and a height of 0.6 meters. The flow through the channels was controlled at the downstream end by a gate, designed to induce a hydraulic jump at the toe of the spillway, enabling flow measurements in that specific region. Consequently, discharge rates were measured using a calibrated V-notch weir (with a 53-degree angle) located downstream of the channel. The water flow rate was supplied by a pump with a maximum capacity of 50 liters per second. The flow rate ranged from 7 to 50 liters per second, with an accuracy of  $\pm 0.9$  liters per second. The upstream water level was measured using a point gauge with an accuracy of  $\pm 0.1$  millimeters. All measurements were taken along the channel axis. In each experiment, the water depth was measured 0.6 meters downstream of the chute ( $y_0$ ) and after the hydraulic jump ( $y_2$ ). The shallow, aerated flow at the toe of the spillway made accurate measurement of the flow depth ( $y_1$ ) difficult. The geometric characteristics of the physical models of constructed stepped spillways are presented in the study by [13].

### 2.2. Calculation of energy dissipation using dimensional analysis and experimental data

In this study, energy dissipation has been calculated using dimensional analysis and experimental data. A total of 154 experiments were conducted under the skimming flow regime and for different slopes (15, 25, and 45 degrees). Furthermore, in these experiments, 7 types of step numbers and different flow rate values were used. The measurements performed in each experiment included flow rate values and two flow depths. The upstream energy head ( $E_0$ ), downstream energy head ( $E_1$ ), and relative energy dissipation ( $\Delta E/E_0$ ) were calculated as follows:

$$E_0 = w + y_0 + \frac{V_0^2}{2g} = w + y_0 + \frac{q^2}{2g(w+y_0)^2} \quad (1)$$

$$E_1 = y_1 + \frac{V_1^2}{2g} = y_1 + \frac{q^2}{2gy_1^2} \quad (2)$$

$$\frac{\Delta E}{E_0} = \frac{E_0 - E_1}{E_0} = 1 - \frac{E_1}{E_0} \quad (3)$$

Where,  $g$  is the acceleration due to gravity,  $w$  is the total spillway height, measured with a point gauge after the installation of the spillway in the flume,  $y_0$  is the flow depth measured at a set distance upstream of the spillway and above the spillway crest,  $q$  is discharge per unit width, and  $V_0$  is the approach velocity. The downstream flow depth,  $y_1$ , was calculated using the concept of conjugate depth ( $y_2$ ), expressed as:

$$y_1 = \frac{y_2}{2} (\sqrt{1 + 8Fr_2^2} - 1) \quad (4)$$

where,  $Fr_2$  is the Froude number and is calculated as:

$$Fr_2 = \frac{V_2}{gy_2} \quad (5)$$

Based on the defined relationships and variables, and using Buckingham's  $\Pi$  –theorem, the relative energy dissipation can be estimated using the following equation:

$$\frac{\Delta E}{E_0} = f(DN, S, N, \frac{y_c}{h}, Fr_1) \quad (6)$$

In this context,  $y_c = (q^2/g)^{\frac{1}{3}}$ ,  $DN = q^2/gH_w^3$ ,  $H_w$  is equal to the height of the spillway, and  $Fr_1 = V_1/\sqrt{gy_1}$  represent the critical depth, the drop number, and the Froude number, respectively. The average flow velocity at each cross-section was calculated using the relation  $V = q/y$ , where the discharge per unit width is defined as  $q = Q/b$ . In this expression,  $Q$  denotes the total discharge,  $b$  is the width of the weir crest, and  $y$  corresponds to the flow depth at the respective cross-section.

### 2.3. Data evaluation using soft computing models

In this study, the data processing for estimating energy dissipation was performed using three soft computing models: ANN, ANFIS, and SVR. These soft computing models, implemented in the MATLAB environment, leverage machine learning techniques to predict the desired output. Soft computing models are a subset of artificial intelligence that process input data by learning underlying patterns through training. After the training phase, the models generalize the learned information and apply rule-based inference on the test data, enabling them to accurately estimate the target variable—in this case, energy dissipation.

An ANN can be trained for a specific task by adjusting the connection weights between its components. Typically, trained neural networks operate such that a given input is mapped to a desired target output. The network adjusts the weights iteratively based on the difference between the actual output and the target, continuing this process until the output closely matches the target. Generally, a large number of input-target pairs is required to effectively train the network. In the present study, the transfer functions transig and purelin were employed in the neural network architecture. The trainlm algorithm was utilized for training, which updates the weights and biases by leveraging the Levenberg-Marquardt optimization method to achieve efficient and accurate convergence. Further details regarding this model can be found in the studies by Tabari and Azari [26].

The ANFIS is a type of artificial neural network based on the Takagi-Sugeno fuzzy inference model. This model operates according to a set of if-then fuzzy rules and has the capability to learn and approximate nonlinear functions. In the present study, the function trndata was employed for training the data, while chkdata was used for validating and detecting potential overfitting in the dataset. Furthermore, the fuzzy inference system was generated using the genfis algorithm, which applies subtractive clustering for rule extraction. Finally, the fuzzy inference computations were performed using the evalfis function. A more comprehensive analysis of this model is presented in the research conducted by Jafari et al. [27].

SVR is a supervised learning method widely used for both classification and regression tasks. The core principle of SVR is to find a linear decision boundary that maximizes the margin between data points, effectively achieving robust separation. In general, implementing an SVR prediction model requires the selection of three key parameters by the user: the epsilon ( $\epsilon$ ) parameter, the regularization parameter ( $C$ ), and the kernel function. Proper tuning of these parameters significantly enhances the model's predictive performance. The kernel function defines the transformation of data into a new feature space, enabling the model to capture complex nonlinear relationships. The regularization parameter  $C$  controls the trade-off between minimizing the training error and maintaining model simplicity by limiting the size of the model weights. In this study, the Radial Basis Function (RBF) kernel was employed, with  $C$  set to 100,  $\epsilon$  set to 0.05, and the kernel parameter (often denoted as gamma) set to 5. A detailed exposition of this model is available in the work of Tabari and Sanayei [28].

### 2.4. Performance evaluation criteria of the models

Following the completion of experimental and computational procedures, the reliability of the model outputs was assessed using three criteria: the coefficient of determination ( $R^2$ ), Root Mean Square Error (RMSE), and Mean Absolute Error (MAE). The coefficient of determination quantifies the degree of correlation between two sets of data. In this study, it is defined as the square of the correlation coefficient between the predicted and the actual energy dissipation values, thus ranging between 0 and 1. An  $R^2$  value of 0 indicates that the dependent variable (energy dissipation) cannot be predicted from the independent variables—namely, the drop number, weir slope, number of steps, critical depth relative to step height, and Froude number. Conversely, an  $R^2$  equal to 1 implies that the independent variables can perfectly predict the energy dissipation without any error. Hence, the closer the  $R^2$  The value is 1, the higher the accuracy of the prediction.

The RMSE measures the average magnitude of the difference between the predicted values by the model and the observed actual values. It serves as an effective metric for comparing prediction errors over a dataset and is calculated as shown in Equation (7).

$$RMSE = \sqrt{\frac{\sum_{t=1}^n (E_t - E')^2}{n}} \quad (7)$$

In this relation,  $E_t$  represents the energy dissipation measured from laboratory experiments,  $E'$  denotes the energy dissipation predicted by the soft computing models, and  $n$  is the total number of samples. The RMSE is calculated by first squaring the difference between the predicted and actual values, then averaging these squared differences over all samples, and finally taking the square root of this average. Because the errors are squared before averaging, RMSE assigns greater weight to larger errors, making it particularly sensitive to outliers. Therefore, RMSE is especially useful when large prediction errors are particularly undesired.

RMSE values range from zero to infinity, where values closer to zero indicate smaller prediction errors and consequently higher model reliability. In other words, in this study, a lower RMSE value signifies that the model provides more accurate estimates of energy dissipation and thus demonstrates greater trustworthiness.

Mean Absolute Error (MAE) measures the average magnitude of errors in a set of predictions, regardless of their direction. Unlike squared error metrics, MAE is a linear measure that assigns equal weight to the absolute difference of each individual sample. Essentially, MAE represents the average of the absolute differences between the predicted values and the observed values ( $e_i$ ) and is computed as defined in Equation (8).

$$MAE = \frac{\sum_{i=1}^n |e_i|}{n} \quad (8)$$

Similar to RMSE, the MAE can take values ranging from zero to infinity, where smaller values closer to zero indicate lower prediction errors. Using both RMSE and MAE together provides insight into the variance of errors within the estimated dataset. Generally, RMSE is always greater than or equal to MAE. The greater the difference between these two metrics, the higher the variance among individual prediction errors. Conversely, if RMSE and MAE are equal, it implies that all individual errors have the same magnitude.

### 3. Results and discussions

After identifying the dataset, the relationship between the five variables  $DN$ ,  $S$ ,  $N$ ,  $y_c/h$ ,  $Fr_1$  and  $\Delta E/E_0$  was examined to determine which variable has the strongest direct linear correlation with energy dissipation. Scatter plots of each input variable against the output were also generated for visualization (Fig. 2). Pearson's correlation coefficient was used to quantify the strength of the linear relationship. This coefficient ranges from -1 to +1, with values closer to either extreme indicating a stronger linear correlation. Negative correlation values indicate an inverse relationship, meaning that as energy dissipation increases, the corresponding variable decreases, and vice versa. A correlation coefficient of zero indicates the absence of any linear relationship between energy dissipation and the variable in question. According to the scatter plots and correlation coefficients, the linear relationship between energy dissipation and the variables  $y_c/h$ ,  $Fr_1$ , and  $DN$  is inverse, whereas it is direct with spillway slope ( $S$ ) and number of steps ( $N$ ). In other words, to achieve greater energy dissipation in stepped spillways, the critical depth to step height ratio ( $y_c/h$ ), Froude number ( $Fr_1$ ), and drop number should increase, while the spillway slope and number of steps should decrease. Among these, the drop number exhibits the strongest correlation with energy dissipation, whereas the Froude number and number of steps show the weakest correlation. Therefore, to enhance energy dissipation, priority should be given to reducing the drop number. To effectively reduce  $DN$ , the spillway height should be increased primarily, followed by an increase in spillway width.

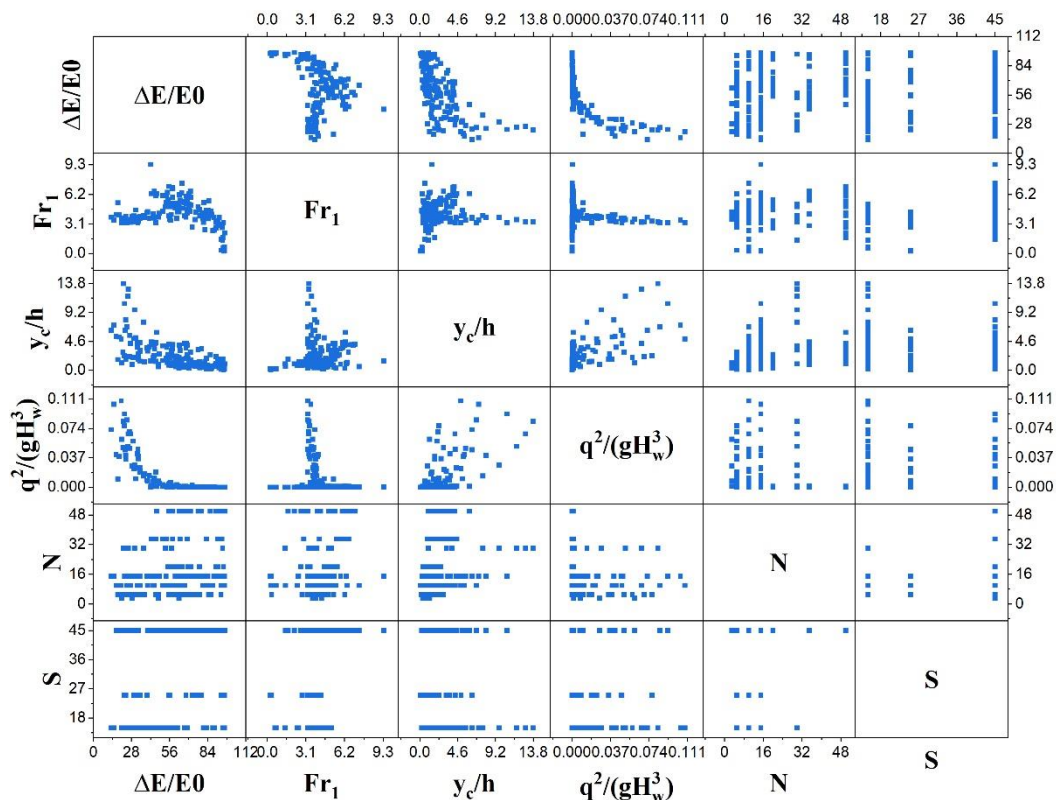


Fig. 2. Scatter plot of the parameters influencing the rate of energy dissipation.



Based on the performance evaluation criteria of the models, the ANN demonstrated the highest correlation with the actual energy dissipation data (Table 1). Analysis of the RMSE, which emphasizes the magnitude of errors for each individual prediction, showed that the ANN model did not produce any large errors across all 154 estimates. Moreover, the comparison between RMSE and MAE values across the models, and the close agreement between these two metrics in the ANN model, indicate that the errors were consistently small and uniform across all samples. Although the SVR and ANFIS models also provided reasonable estimates of energy dissipation, their relatively high RMSE values and the considerable disparity between RMSE and MAE suggest greater variance in prediction errors, meaning the error magnitudes were not consistent across all predictions.

**Table 1 Comparison of the performance of the investigated soft models.**

Performance criteria	Training			Testing		
Model name	MAE	RMSE	$R^2$	MAE	RMSE	$R^2$
ANN	1.0605	1.6405	0.994	0.6766	0.9643	0.996
ANFIS	4.0962	5.2334	0.9522	4.0962	5.9834	0.9668
SVR	0.0590	2.0265	0.973	0.0592	2.0554	0.971
Regression model			$R^2 = 0.908$ for all data			
Salmasi and Özger (2014)			0.974			0.9667

To evaluate and compare the results obtained from the three machine learning approaches, the scatter matrix of the examined models along with their pairwise calculated values is presented in Fig. 3. The horizontal and vertical axes in each subplot represent the predicted values by the models and the actual values or predictions from other models, respectively. As shown, the ANN model exhibits a highly compact and close clustering of points around the diagonal line, indicating its high accuracy in predicting actual values. This model effectively captures the fluctuations and overall trend of energy dissipation. In the ANFIS model, the scatter points also align around the diagonal, but with a slightly more dispersed distribution compared to ANN, reflecting lower accuracy and higher variance in errors for ANFIS predictions. Although the SVR model generally follows the trend, its scatter points display a wider spread and greater deviations from the ideal line, indicating larger errors and instability in some predictions. Comparative scatter plots between model predictions reveal that ANN and SVR demonstrate greater consistency with the calculated values than ANFIS. Therefore, the presented scatter results, consistent with statistical performance metrics, confirm that ANN is the superior model for predicting energy dissipation in this study.

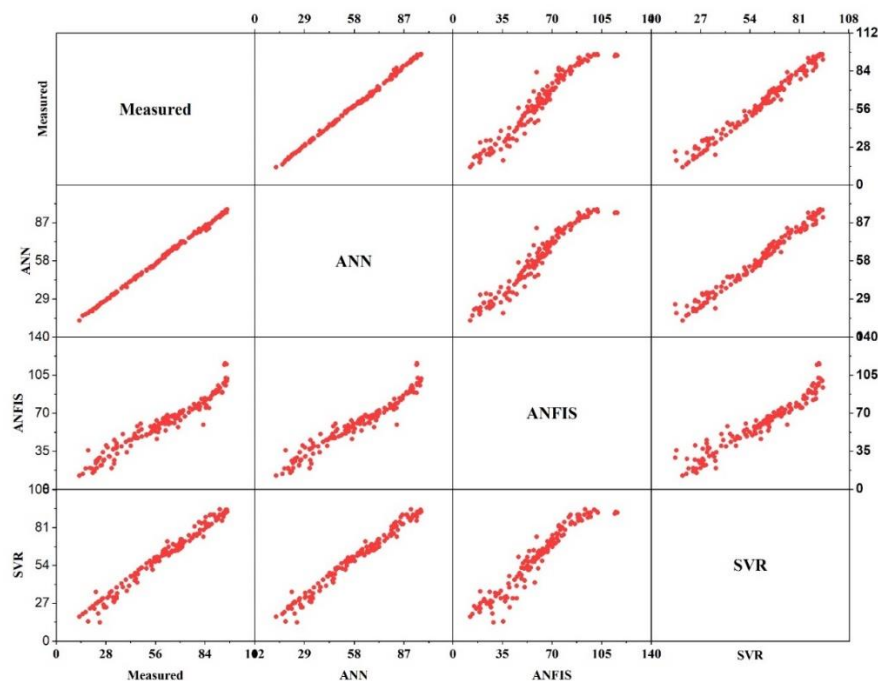


**Fig. 3. Scatter plot of the parameters influencing the rate of energy dissipation**

The Ridgeline plot serves as a powerful and intuitive visualization tool for evaluating the predictive performance of machine learning models in estimating energy dissipation rates in spillways. By displaying the probability density distributions of each model's predictions in a stacked and parallel manner, this plot facilitates a detailed comparison of the shape, spread, and central tendency of the data. In addition to highlighting statistical differences among models, the Ridgeline plot visually emphasizes the alignment or deviation of model predictions relative to the observed measured data. Therefore, it is an effective tool for assessing

model reliability and selecting the most accurate model for predicting energy dissipation in hydrodynamic spillway studies. Based on Fig. 4, the probability density distributions of predictions from the three examined machine learning models (ANN, ANFIS, and SVR) can be evaluated in comparison with the distribution of the measured data for energy dissipation estimation. The overlap analysis of the curves indicates that the ANN model demonstrates the highest agreement with the measured data distribution, as both the shape and peak location of its prediction distribution closely resemble those of the actual data. This serves as a strong indicator of the ANN model's high accuracy in reproducing the true pattern of energy dissipation. In contrast, despite exhibiting convergent distributions, the SVR and ANFIS models show notable deviations from the measured data, particularly the ANFIS model, whose distribution is comparatively broader and differs more substantially from the observed data. Therefore, it can be concluded that among the models studied, the ANN possesses superior capability in replicating the statistical distribution of energy dissipation data, leading to more accurate predictions. This enhanced performance likely stems from the ANN's ability to capture complex and nonlinear relationships inherent in the real data.

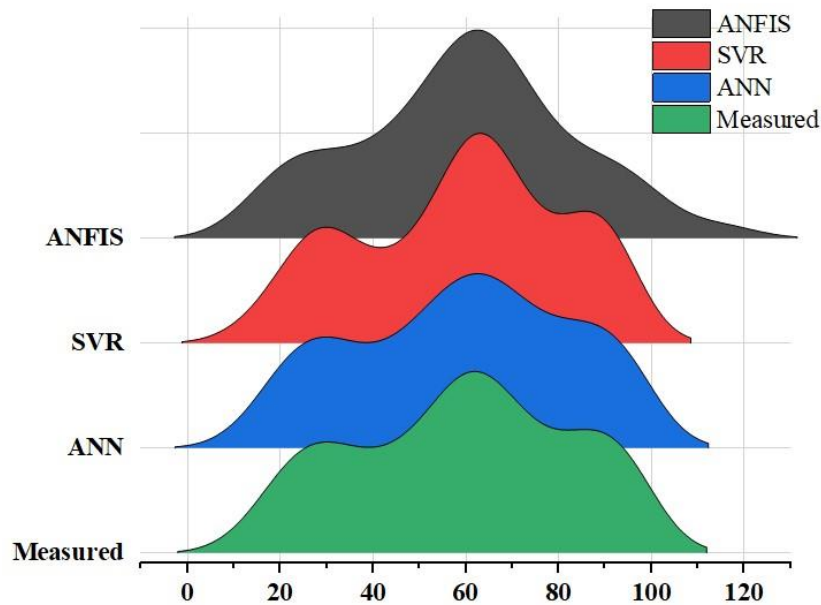


**Fig. 4. Ridgeline plot comparing the prediction distributions of three machine learning models with measured data for estimating the rate of energy dissipation.**

#### 4. Conclusions

In this study, to estimate energy dissipation in stepped spillways, laboratory data pertaining to actual energy dissipation were initially collected. Subsequently, utilizing these data and five key hydraulic parameters – the drop number, spillway slope, number of steps, ratio of critical depth to step height, and upstream Froude number – as input variables, three machine learning models, namely ANN, ANFIS, and SVR, were trained independently. The dataset employed comprised 154 laboratory samples, with 85% allocated for training, 5% for validation, and 10% for evaluating model performance. The performance of the models in estimating energy dissipation was assessed and compared using the statistical indices of coefficient of determination, root mean squared error, and mean absolute error. Based on comprehensive statistical analyses and advanced machine learning models developed to accurately estimate energy dissipation rates in stepped spillways, the key findings of this research are summarized as follows:

- The results of this study demonstrate that the use of stepped spillways significantly enhances energy dissipation of water flow over dams. Laboratory results indicate that energy dissipation is approximately 60%. Statistical analysis revealed that the DN exhibits the strongest linear correlation with the energy dissipation rate; a decrease in DN leads to an increase in energy dissipation. Considering the DN calculation formula, increasing the height and width of the steps can be an effective strategy to achieve this. While other variables examined also showed significant correlation coefficients, analysis of scatter plots suggests that using these variables alone is insufficient for accurate energy dissipation prediction. Therefore, a comprehensive model that considers all parameters simultaneously is deemed necessary.
- Performance evaluation of soft computing models indicated that the ANN model exhibits the highest correlation with actual energy dissipation data.
- Analysis of the RMSE index reveals that the ANN model does not exhibit significant error in any of its 154 estimations. This indicates high accuracy of the model in estimating energy dissipation values across all samples.
- Comparison of RMSE and MAE values in the ANN model shows a remarkable proximity between these two indices. This convergence indicates a uniform and negligible distribution of error across all samples, reducing the likelihood of outliers in

the estimations.

- Although SVR and ANFIS models also provided acceptable estimations of energy dissipation, the higher RMSE value compared to MAE in these models indicates greater error variance and heterogeneity in prediction accuracy. In other words, the magnitude of error in the predictions of these models has a greater dispersion across different samples.

Given the increasing significance and widespread application of stepped spillways in energy dissipation downstream of hydraulic structures, the need for more extensive research in this area is becoming increasingly apparent. In this context, it is noteworthy that, in addition to the five variables examined in the present study, other variables such as step material and flow velocity can also be incorporated into the analysis. Furthermore, to achieve more accurate energy dissipation estimations, it is suggested to integrate soft computing models and metaheuristic algorithms to optimize the tuning parameters of machine learning approaches. This hybrid approach not only enhances modeling accuracy but also enables the identification of complex and nonlinear patterns present in the data.

## Statements & declarations

### Author contributions

**Milad Taji:** Conceptualization, Methodology, Formal analysis, Resources, Original Draft

**Masoud Morsali:** Conceptualization, Formal analysis, Resources, Writing

**Mehdi Eilbeigi:** Conceptualization, Investigation, Writing

### Funding

The authors declare that no funds, grants, or other support were received during the preparation of this manuscript.

### Data availability

The data presented in this study are available on request from the corresponding author.

### Declarations

The authors declare no conflict of interest.

## References

- [1] Parsaie, A., Haghiabi, A. H., Saneie, M., Torabi, H. Applications of Soft Computing Techniques for Prediction of Energy Dissipation on Stepped Spillways. *Neural Computing and Applications*, 2018; 29 (12): 1393–1409. doi:10.1007/s00521-016-2667-z.
- [2] Mohammad Rezapour Tabari, M., Tavakoli, S. Effects of Stepped Spillway Geometry on Flow Pattern and Energy Dissipation. *Arabian Journal for Science and Engineering*, 2016; 41 (4): 1215–1224. doi:10.1007/s13369-015-1874-8.
- [3] Mishra, C.S., Ojha, S. P. Prediction of energy dissipation in skimming flow of stepped spillway by using machine learning approach. In: Pandey M, Umamahesh NV, Ahmad Z, Oliveto G, editors. *Hydraulics and fluid mechanics*. Volume 1. Singapore: Springer Nature Singapore; 2025. p. 423–38.
- [4] Mojtahedi, A., Soori, N., Mohammadian, M. Energy Dissipation Evaluation for Stepped Spillway Using a Fuzzy Inference System. *SN Applied Sciences*, 2020; 2 (8). doi:10.1007/s42452-020-03258-0.
- [5] Mei, J., Zhou, Y., Xu, K., Xu, G., Shu, Z., Gan, Q., et al. Energy dissipation on inclined stepped spillways. *Water*. 2025;17(2):251. doi:10.3390/w17020251.
- [6] Li, S., Zhang, J., Nie, J., Peng, Y. Energy Dissipation and Flow Characteristics of Baffles and Sills on Stepped Spillways. *Journal of Hydraulic Research*, 2014; 52 (1): 140–142. doi:10.1080/00221686.2013.856040.
- [7] Chanson, H. Jet Flow on Stepped Spillways. *Journal of Hydraulic Engineering*, 1995; 121 (5): 441–448. doi:10.1061/(asce)0733-9429(1995)121:5(441).
- [8] Torabi, S., Rostami, A., Torabi, S., Boustani, F., Roushan, A. Energy Dissipation on Stepped Spillways with Reverse Inclination. *Water Resources Engineering*, 6 (Vol6/No17/Summer 2013): 63–78.
- [9] hamani, M.R., Rajaratnam, N. Characteristics of skimming flow over stepped spillways. *Journal of Hydraulic Engineering*, 1999; 125(4): 361–368. doi:10.1061/(ASCE)0733-9429(1999)125:4(361).
- [10] Asghari Pari, S. A., Kordnaeij, M., Razmkhah, A. Experimental study of flow characteristics in a stepped spillway with the installation of a continuous obstacle with different geometric characteristics. *Journal of Hydraulics*, 2025; 20(1): 91-109. doi: 10.30482/jhyd.2024.433085.1690.

- [11] Zhou, Y., Wu, J., Ma, F., Qian, S. Experimental Investigation of the Hydraulic Performance of a Hydraulic-Jump-Stepped Spillway. *KSCE Journal of Civil Engineering*, 2021; 25 (10): 3758–3765. doi:10.1007/s12205-021-1709-y.
- [12] İkinciogullari, E. A Novel Design for Stepped Spillway Using Staggered Labyrinth Trapezoidal Steps. *Flow Measurement and Instrumentation*, 2023; 93: 102439. doi:10.1016/j.flowmeasinst.2023.102439.
- [13] Salmasi, F., Özger, M. Neuro-Fuzzy Approach for Estimating Energy Dissipation in Skimming Flow over Stepped Spillways. *Arabian Journal for Science and Engineering*, 2014; 39 (8): 6099–6108. doi:10.1007/s13369-014-1240-2.
- [14] Tabbara, M., Chatila, J., Awwad, R. Computational Simulation of Flow over Stepped Spillways. *Computers and Structures*, 2005; 83 (27): 2215–2224. doi:10.1016/j.compstruc.2005.04.005.
- [15] Felder, S., Chanson, H. Energy Dissipation, Flow Resistance and Gas-Liquid Interfacial Area in Skimming Flows on Moderate-Slope Stepped Spillways. *Environmental Fluid Mechanics*, 2009; 9(4): 427–441. doi:10.1007/s10652-009-9130-y.
- [16] Hamed, A., Malekmohammadi, I., Mansoori, A., Roshanaei, H. Energy dissipation in stepped spillway equipped with inclined steps together with end sill. In: *Proceedings of the Fourth International Conference on Computational Intelligence and Communication Networks*; 2012 Nov 3–5; Mathura, India. p. 638–42. doi:10.1109/CICN.2012.109.
- [17] Husain, S. M., Muhammed, J. R., Karunarathna, H. U., Reeve, D. E. Investigation of Pressure Variations over Stepped Spillways Using Smooth Particle Hydrodynamics. *Advances in Water Resources*, 2014; 66: 52–69. doi:10.1016/j.advwatres.2013.11.013.
- [18] Hou, X., Chen, J., Yang, J. The numerical simulation of aeration and energy dissipation for stepped spillway. In: *Proceedings of the 2013 International Conference on Mechatronic Sciences, Electric Engineering and Computer (MEC 2013)*; 2013 Dec 20–22; Shenyang, China. IEEE; 2013. p. 2495–9. doi:10.1109/MEC.2013.6885456.
- [19] Shahheydari, H., Nodoshan, E. J., Barati, R., Moghadam, M. A. Discharge Coefficient and Energy Dissipation over Stepped Spillway under Skimming Flow Regime. *KSCE Journal of Civil Engineering*, 2015; 19(4): 1174–1182. doi:10.1007/s12205-013-0749-3.
- [20] Khatibi, R., Salmasi, F., Ghorbani, M. A., Asadi, H. Modelling Energy Dissipation Over Stepped-Gabion Weirs by Artificial Intelligence. *Water Resources Management*, 2014; 28(7): 1807–1821. doi:10.1007/s11269-014-0545-y.
- [21] Mostefa, G., Kheira, B., Abdelkader, D., Naima, D. Study of the Effect of the Rate Flow and the Slope of the Channel on the Energy Dissipation in the Stepped Channels: Proposing an Empirical Models. *Procedia Engineering*, 2015; 118: 1044–1051. doi:10.1016/j.proeng.2015.08.547.
- [22] Hanbay, D., Baylar, A., Ozpolat, E. Predicting Flow Conditions over Stepped Chutes Based on ANFIS. *Soft Computing*, 2009; 13(7): 701–707. doi:10.1007/s00500-008-0343-7.
- [23] Roushangar, K., Akhgar, S., Salmasi, F., Shiri, J. Modeling Energy Dissipation over Stepped Spillways Using Machine Learning Approaches. *Journal of Hydrology*, 2014; 508: 254–265. doi:10.1016/j.jhydrol.2013.10.053.
- [24] Ekmekcioğlu, Ö., Başakın, E. E., Özger, M. Tree-Based Nonlinear Ensemble Technique to Predict Energy Dissipation in Stepped Spillways. *European Journal of Environmental and Civil Engineering*, 2022; 26(8): 3547–3565. doi:10.1080/19648189.2020.1805024.
- [25] Baharvand, S., Rezaei, R., Talebbeydokhti, N., Nasiri, R., Amiri, S. M. Investigation of Energy Dissipation Rate of Stepped Vertical Overfall (SVO) Spillway Using Physical Modeling and Soft Computing Techniques. *KSCE Journal of Civil Engineering*, 2022; 26(12): 5067–5081. doi:10.1007/s12205-022-1870-y.
- [26] Tabari, M. M. R., Azari, T., Dehghan, V. A Supervised Committee Neural Network for the Determination of Aquifer Parameters: A Case Study of Katasbes Aquifer in Shiraz Plain, Iran. *Soft Computing*, 2021; 25(6): 4785–4798. doi:10.1007/s00500-020-05487-2.
- [27] Jafari, S. M., Zahiri, A. R., Bozorg Hadad, O., Mohammad Rezapour Tabari, M. A Hybrid of Six Soft Models Based on ANFIS for Pipe Failure Rate Forecasting and Uncertainty Analysis: A Case Study of Gorgan City Water Distribution Network. *Soft Computing*, 2021; 25(11): 7459–7478. doi:10.1007/s00500-021-05706-4.
- [28] Tabari, M. M. R., Sanayei, H. R. Z. Prediction of the Intermediate Block Displacement of the Dam Crest Using Artificial Neural Network and Support Vector Regression Models. *Soft Computing*, 2019; 23(19): 9629–9645. doi:10.1007/s00500-018-3528-8.

# Performance Enhancement of Tuned Liquid Dampers in Fixed Offshore Platforms: A Coupled ANSYS Aqwa-Transient Structural Approach

Mohammad Ali Arjomand <sup>a</sup>, Mohsen Bagheri <sup>b\*</sup>, Yashar Mostafaei <sup>c</sup>

<sup>a</sup> Faculty of Civil Engineering, Shahid Rajaee Teacher Training University, Tehran, Iran.

<sup>b</sup> Department of Civil Engineering, Babol Noshirvani University of Technology, Babol, Iran.

<sup>c</sup> Department of Civil Engineering, Roodehen Science and Research Branch, Islamic Azad University, Tehran, Islamic Republic of Iran.

## ARTICLE INFO

### Keywords:

Tuned liquid damper (TLD)  
Offshore jacket platform  
Coupled hydrodynamic-structural  
analysis  
ANSYS Aqwa  
JONSWAP wave spectrum

### Article history:

Received 24 April 2025  
Accepted 12 May 2025  
Available online 4 June 2025

## ABSTRACT

Fixed offshore platforms exhibit excellent static stability due to their rigid connection to the seabed yet remain vulnerable to complex dynamic loads, including irregular waves, ocean currents, and wind forces. This study presents a numerical investigation of Tuned Liquid Dampers (TLDs) for controlling dynamic responses in jacket-type fixed platforms. The research employs a coupled hydrodynamic-structure approach using ANSYS Aqwa for hydrodynamic modeling and ANSYS Transient Structural for structural response analysis. The JONSWAP wave spectrum was implemented to simulate realistic sea conditions. Key parameters, including structural frequency response, TLD-induced damping, and variations in the system's potential and kinetic energy, were evaluated. Results demonstrate a substantial decrease in the maximum shear force of platform legs, with reduction levels between 52% and 252%, indicating improved structural resilience under wave-induced loading. The operational mechanism relies on converting structural kinetic energy into vortex-induced energy within liquid tanks, effectively increasing equivalent damping coefficients. The analysis confirms this method significantly improves dynamic performance without substantially increasing structural stiffness. These findings provide a robust basis for designing passive control systems in fixed offshore platforms, particularly in storm-prone regions. The numerical results show good agreement with existing experimental data from reputable sources.

## 1. Introduction

Offshore platforms are subjected to complex environmental loads, including wave, wind, and seismic forces, which induce dynamic responses that threaten structural integrity and operational safety. Traditional design approaches often struggle to mitigate these vibrations effectively, particularly for fixed platforms in harsh marine environments. Tuned Liquid Dampers (TLDs) have emerged as a promising solution to suppress unwanted oscillations, but their performance depends critically on accurate hydrodynamic-structural interaction modeling—a challenge that remains inadequately addressed in existing literature. Hydrodynamic analysis of offshore structures typically involves solving the incompressible Navier-Stokes equations to compute pressure and velocity fields around submerged components. While frequency-domain methods offer computational efficiency, time-domain analyses are essential for capturing nonlinear wave-structure interactions and transient loads. ANSYS AQWA, a boundary element method (BEM)-based tool, is widely recognized for its accuracy in simulating wave kinematics and diffraction/radiation effects. However, despite the potential for high-fidelity coupled analysis, its integration with transient structural modules to evaluate TLD efficacy has been limited. Current industry standards (e.g., API RP 2A) emphasize the importance of dynamic response mitigation, yet most offshore platforms in regions like the Persian Gulf and Gulf of Mexico still rely on conventional template-type

\* Corresponding author.

E-mail addresses: [M.bagheri@stu.nit.ac.ir](mailto:M.bagheri@stu.nit.ac.ir) (M. Bagheri).

<https://doi.org/10.22080/ceas.2025.29085.1003>.

ISSN: 3092-7749/© 2025 The Author(s). Published by University of Mazandaran.

This article is an open access article distributed under the terms and conditions of the Creative Commons Attribution (CC-BY) license (<https://creativecommons.org/licenses/by/4.0/deed.en>)

How to cite this article: Arjomand M. A., Bagheri M., Mostafaei Y. Performance enhancement of tuned liquid dampers in fixed offshore platforms: a coupled ANSYS Aqwa-transient structural approach. Civil Engineering and Applied Solutions. 2025; 1(1): 77–88. doi: 10.22080/ceas.2025.29085.1003.





designs with minimal damping optimization. Prior studies on TLDs have primarily focused on land-based structures, with scant attention to the unique hydrodynamic-structural coupling in offshore systems. This work bridges this gap by proposing a novel coupled ANSYS AQWA-Transient Structural framework to optimize TLD performance for fixed platforms.

## 2. Literature review

While numerous researchers employ advanced numerical simulation software to model structural elements [1-3], ANSYS stands out as a powerful and widely validated computational tool in this domain, offering robust capabilities for high-fidelity structural analysis and multiphysics simulations. Several researchers have utilized advanced numerical software such as ANSYS, ABAQUS, and OpenSees to model and analyze the behavior of marine structures under hydrodynamic and seismic loads. Barari et al. [4] and Ibsen et al. [5] propose a performance-based design framework for offshore monopiles under cyclic loading, using 3D FEM to analyze soil-structure interaction in dense sand. Results demonstrate that pile rotation accumulates linearly with load magnitude, with high-intensity cycles controlling long-term deformation more than numerous low-intensity cycles. While power-law and logarithmic models perform similarly under  $<1,000$  cycles, the power-law better predicts behavior beyond 10,000 cycles. The findings highlight the critical role of extreme cyclic loads in monopile design, providing essential guidance for offshore wind infrastructure. Asgari and Ahmadvatabar Sorkhi [6] investigate the seismic performance of monopile-supported offshore wind turbines in liquefiable soils under combined wind-wave-earthquake loads using TCL-programmed 3D OpenSees models. Results demonstrate that system response increases with wind speed and wave height, while moderate-to-strong earthquakes may trigger liquefaction, significantly amplifying structural response. The combined loading scenario consistently produced the most critical system responses, surpassing individual load effects. Asgari and Bagheripour [7] study develops an efficient HFTD method combining frequency/time-domain solutions with FFT/IFFT transformations to analyze nonlinear soil behavior during earthquakes. A custom algorithm iteratively updates nonlinear soil properties (modeled via hyperbolic shear strength-strain relations) across depth/time until convergence. Jafarian et al. [8] study evaluates the seismic response of breakwaters founded on thick liquefiable silt layers through advanced numerical modeling, validated against centrifuge tests. Part I analyzes an unimproved benchmark case, while Part II investigates stone columns as a liquefaction countermeasure, demonstrating their effectiveness in mitigating earthquake-induced pore pressure effects. These findings emphasize the necessity of considering multi-hazard load combinations in offshore wind turbine design to ensure structural safety under extreme environmental conditions.

### 2.1. Tuned liquid dampers in offshore applications

Recent research has demonstrated the growing importance of Tuned Liquid Dampers (TLDs) as an efficient and economical vibration mitigation solution for offshore structures. Sardar and Chakraborty [9] investigated the effectiveness of tuned liquid dampers (TLDs) in mitigating wave-induced vibrations in offshore jacket platforms, considering soil-pile interaction effects. The TLD is modeled as a spring-mass system incorporating sloshing energy, and the platform is subjected to both regular (Stokes' fifth-order theory) and random (Pierson-Moskowitz spectrum) wave loads. Parametric analyses examine the influence of mass ratio, depth ratio, and TLD placement on vibration control performance. Results demonstrate that TLDs are a promising solution for reducing wave-induced vibrations in offshore structures.

Jin et al. [10] explores the feasibility of using tuned liquid dampers (TLDs) to mitigate earthquake-induced vibrations in offshore jacket platforms, focusing on the CB32A oil platform. The TLD is analyzed using a lumped mass method, validated through model tests and numerical simulations, showing good agreement with experimental results. Key findings reveal that the ratio of the TLD's sloshing frequency to the platform's natural frequency significantly influences seismic response control, along with the water-to-platform mass ratio. The results demonstrate that TLDs effectively reduce seismic vibrations, offering a viable solution for platforms in active fault zones.

Ding et al. [11] examines the effectiveness of a toroidal tuned liquid column damper (TTLCD) in mitigating multi-directional vibrations of monopile offshore wind turbines under wind, wave, and seismic loads. A numerical framework incorporating liquid flow dynamics, sloshing effects, and two-way fluid-structure interaction is developed and validated against experimental data. The results demonstrate that the TTLCD effectively reduces structural responses in both fore-aft and side-side directions, with its performance under wind loads being particularly dependent on wind velocity and frequency content. The findings highlight the TTLCD's adaptability to the tower's geometry and its potential as a robust vibration control solution for offshore wind turbines.

Li et al. [12] proposes a simplified yet accurate simulation method for Tuned Liquid Dampers (TLDs) in high-rise buildings using linear link elements within a two-story frame model, validated through experiments on cylindrical and rectangular tanks. The method is then applied to a concentrically braced steel frame structure, demonstrating its effectiveness in simulating TLD behavior under dynamic loads. Results confirm that TLDs significantly reduce structural vibrations, offering a practical solution for wind and seismic-induced oscillations in tall buildings. The findings provide valuable insights for implementing TLD technology in engineering design, enhancing vibration control strategies for modern high-rise constructions.

Ding et al. [13] investigated the novel application of non-submerged tuned liquid column dampers (TLCDs) for heave motion control in very large floating structures (VLFSs), addressing a previously unexplored area in offshore vibration mitigation. Analytical models of the VLFS-TLCD system are developed in both frequency and time domains, with performance optimization conducted using a genetic algorithm under five wave loading scenarios. Parametric analyses based on response amplitude operators and transmissibility curves demonstrate the effectiveness of TLCDs in heave reduction, while comparisons with submerged fixed heave plates highlight their unique control characteristics. The results establish non-submerged TLCDs as a viable solution for heave

motion mitigation in VLFSSs, expanding the potential applications of liquid damping technology in offshore engineering.

## 2.2. Hydrodynamic-structural coupling challenges

The precise fluid-structure interaction simulation (FSI) represents a fundamental requirement for reliable prediction of Tuned Liquid Damper (TLD) performance in offshore applications.

Saghi et al. [14] evaluates the performance of two novel passive control devices-bidirectional tuned liquid damper (TLD) and bidirectional tuned liquid column damper (TLCD)-in mitigating pitch motions of floating offshore wind turbine substructures. Numerical simulations incorporating sloshing effects and wave-induced moments were conducted, with geometric optimizations explored through baffles and orifices. Results demonstrate that an optimal integration of substructure geometry and damping device can achieve 20%–40% reduction in pitch motion. The findings highlight the potential of these bidirectional dampers for enhancing the stability of marine renewable energy structures.

Kheili and Aghakouchak [15] examined the effectiveness of tuned liquid dampers (TLDs) in mitigating dynamic responses of a fixed offshore platform in the Persian Gulf under combined earthquake and wave loading. A 3D finite element model incorporating TLDs was developed and compared with equivalent lumped-mass models, demonstrating good agreement between both approaches. The results reveal that TLDs significantly reduce jacket deck vibrations, with their efficiency improving proportionally to increasing wave heights and seismic intensities. These findings highlight TLDs as a viable passive control solution for enhancing the dynamic performance of fixed offshore structures against environmental loads.

Xue et al. [16] investigated the vibration control performance of a tuned liquid column damper (TLCD) on a photovoltaic support platform through combined experimental and numerical analyses. Experimental tests evaluate the TLCD's effectiveness under varying liquid depths, excitation frequencies, and amplitudes, demonstrating vibration reductions of 42.0%-85.1% near the structure's natural frequency (2.52 Hz). A developed two-way fluid-structure interaction (FSI) model provides deeper insight into sloshing-induced hydrodynamic pressures and their effects on structural response. The results validate TLCDs as an effective solution for mitigating vibrations in offshore photovoltaic support structures with fundamental frequencies above 2 Hz.

## 2.3. Coupled hydrodynamic-structural analysis

Integrating hydrodynamic and structural solvers remains a significant challenge in accurately simulating TLD-equipped offshore platforms. While numerical modeling has advanced considerably, achieving a robust and computationally efficient coupling between wave-structure interaction and transient structural response continues to present difficulties.

Lotfollahi-Yaghin et al. [17] This study evaluates the effectiveness of tuned liquid dampers (TLDs) in mitigating seismic responses of an offshore jacket platform (SPD1) in the Persian Gulf through finite element analysis using ANSYS. The platform was modeled and dynamically analyzed using modal and time-history approaches under three earthquake records (El Centro, Kobe, and Tabas), with TLDs optimally designed to counteract vibrations through fluid sloshing forces. Results comparing platform responses with and without TLDs demonstrate their effectiveness in reducing structural vibrations under seismic loading. The findings validate TLDs as a practical passive control solution for enhancing the earthquake resilience of offshore jacket platforms.

Sharma et al. [18] investigates the effectiveness of a Tuned Mass Damper (TMD) in mitigating deck-level displacements of an offshore jacket structure subjected to seismic and ice loads through numerical simulations using ANSYS Mechanical APDL. The TMD's optimal placement and parameters (mass ratio and damping ratio) are determined based on the Principle of Absorption (PoA) to minimize structural vibrations. Parametric analyses reveal that properly tuned TMDs significantly reduce deck displacements under dynamic loading conditions. The findings provide practical insights for designing TMD systems to enhance the structural resilience of offshore jackets against earthquake and ice-induced vibrations.

Ghadimi and Taghikhany [19] evaluated the effectiveness of passive and semi-active tuned mass dampers (TMD/SATMD) with fuzzy logic control in retrofitting an offshore jacket platform under combined environmental and seismic loads. Dynamic properties of the structure were extracted, and numerical simulations compared structural responses with and without TMD implementation. Results demonstrate that the SATMD with fuzzy control significantly reduces critical response parameters (accelerations, base shear, overturning moments, and displacements) more effectively than passive TMDs. The findings highlight SATMDs as a viable solution for enhancing the seismic and hydrodynamic performance of existing offshore platforms that fail to meet modern design standards. Sarkar and Ghosh [20] proposes a novel conical-spring TMD (TMD-C) system to address the tuning sensitivity limitations of conventional TMDs in offshore jacket platforms experiencing dynamic property variations. The jacket platform is modeled as a multi-degree-of-freedom system, and the TMD-C's performance is evaluated through frequency- and time-domain analyses under wave loading scenarios. Results demonstrate that the TMD-C's multilinear spring characteristic maintains effective tuning across different structural frequencies, outperforming conventional TMDs in reducing deck vibrations. The findings highlight the TMD-C as a robust passive control solution for offshore structures subject to changing mass and stiffness conditions.

## 3. Hydrodynamic analysis in ANSYS Aqwa

Using the hydrodynamic ANSYS Aqwa software, the governing equations of fluid flow-including the continuity and momentum equations—were discretized and simulated via the Boundary Element Method (BEM), accounting for fluid incompressibility. The

study focuses on analyzing sea hydrodynamic parameters in both frequency and time domains, with particular attention to the risk of gravity structure overturning due to rocking motions. Single-degree-of-freedom motion is a critical aspect of structural design and analysis, requiring integrated modeling of soil mechanics and hydrodynamic properties. Key considerations include the seabed's damping effects on structural rocking motion and the hydrodynamics of the structure, which were evaluated using diffraction theory and Morrison's formula. This research investigates the efficiency of a Tuned Liquid Damper (TLD) in controlling and reducing vibrations of an offshore jacket platform under hydrodynamic forces. TLDs, rarely applied in offshore structures, consist of one or more fluid-filled tanks (typically water or oil) installed on the platform's deck. The hydrodynamic forces generated by fluid turbulence within the tanks act as a resisting force against structural vibrations. When external forces excite the structure, the fluid moves in the opposite direction, creating wave-like oscillations in the upper portion while the lower fluid layer moves rigidly, exerting pressure on the tank walls. For the TLD to significantly reduce structural displacement, the fluid oscillation frequency must closely match the structure's natural frequency, which is determined through modal analysis. The primary objective is to tune the fluid oscillation frequency to the structure's natural frequency, identifying the optimal frequency ratio range that minimizes structural movement. As a case study, the research examines a template platform (SPD) with dimensions suitable for Persian Gulf waters.

### 3.1. Governing equations

Design forces acting on offshore platforms originate from wind, ocean currents, and waves, with waves exerting the most significant load on the submerged structure. These hydrodynamic forces arise from the velocity and acceleration of fluid particles induced by wave motion. When the dimensions of the structure are larger than the wavelength, the wave profile undergoes significant distortion upon interaction with the object. In such cases, the Laplace equation (derived from wave hydrodynamics) serves as the governing equation, supplemented by the no-flow condition into the object's boundary. This condition leads to diffracted waves, which exert additional forces on the structure comparable to the incident waves. The total force acting on the structure is the vector sum of the forces from the incident waves and the forces induced by the diffracted waves.

In general, to study the diffraction phenomenon, the total potential of the field  $\Phi_t$  will be considered as the sum of the incident wave's potential  $\varphi_i$  and the scatter wave's potential  $\varphi_s$  [8].

$$\varphi_t = \varphi_i + \varphi_s \quad (1)$$

Lumped mass and damping coefficients are created due to the gravity platform's motion. These coefficients are highly effective in improving the performance of gravity platforms, so a method of calculating these coefficients via software has been referenced.

Potential function affected by platform displacement includes two imaginary and real parts, as mentioned below:

$$\varphi_j = \varphi_j^{Re} + \varphi_j^{Im} \quad (2)$$

Lumped mass coefficient:

$$A = \frac{\rho}{\omega} \int_S \varphi_j^{Im} n_i dS \quad (3)$$

Damping hydrodynamic coefficient:

$$B = \rho \int_S \varphi_j^{Re} n_i dS \quad (4)$$

where  $\varphi_i$  is potential stemming from the oscillatory motion of an object in still water,  $n_i$  is vector perpendicular to the surface, and  $S$  is the wetted perimeter of the object in equilibrium.

### 3.2. Hydrodynamic and geotechnical analysis of offshore gravity platforms under wave-induced loads: a case study of south pars gas field

In this study, the rocking motion of a gravity-based platform under wave-induced torque is formulated and numerically modeled, with the solution derived through the harmonic response method for sustainable rotation angles. The diffraction theory governs the wave-platform interaction, where the velocity potential function around the platform is solved to determine the dynamic wave pressure using Bessel functions of the first and second kinds. A critical aspect of offshore structural design involves geotechnical site investigation to assess seabed soil properties, as the foundation must withstand platform loads—particularly under extreme storm conditions. Seabed composition (e.g., clay, sand, mud, or mixed strata) is evaluated for bearing capacity, shear strength, and displacement behavior under axial, mass, and cyclic loads. Site-specific laboratory tests and soil sampling provide essential data for engineering design, ensuring compliance with regulatory standards. ANSYS Transient Structural Analysis analyzes stress-strain distributions from hydrodynamic forces and damper performance. Key numerical considerations include:

1. Application of boundary conditions (e.g., support constraints and degrees of freedom).
2. Integration of ANSYS workbench modules (e.g., Transient Structural and Aqwa) for coupled marine-structural simulations.

The study adopts the following assumptions:

1. The platform structure comprises four rigid legs.
2. Wave loading follows linear wave theory and harmonic regular waves, though real-world waves exhibit irregular randomness.
3. Time-domain analysis of wave histories-characterized by significant wave height and frequency content-is critical for structural evaluation. These parameters depend on regional oceanography (e.g., sea state, bathymetry).

#### Methodological Framework

1. Irregular waves: Simulated via JONSWAP spectrum parameters.
2. Regular waves: Modeled using Stokes wave theory.
3. Hydrodynamic forces: Quantified for their impact on the platform and riser system.

A case study of a jacket platform (e.g., SPD-type) designed for the Persian Gulf condition is presented, incorporating optimized tuned liquid dampers (TLDs) for vibration mitigation. Should alternative conditions arise, the governing equations must be modified accordingly.

Given the platform's geographical location in the South Pars gas field, the regional environmental conditions and characteristics are as follows:

$$\omega = \frac{2\pi}{T} = 2.732 \left( \frac{\text{rad}}{\text{s}} \right) \quad (5)$$

$$\left( \rho = 5221 \frac{\text{kg}}{\text{m}^3}, g = 9.85 \frac{\text{m}}{\text{s}^2}, H_0 = 6.7 \text{ m}, T = 8.6 \text{ s}, H = 67 \text{ m} \right)$$

### 3.3. Tuned liquid damper (TLD) systems

Tuned liquid dampers (TLDs) serve as passive control systems that utilize fluid sloshing within tanks to mitigate structural vibrations. Initially developed in the early 20th century to address wave-induced vibrations in ocean liners, TLDs were later adapted in the mid-20th century to suppress high-frequency oscillations in satellites. Since the 1980s, they have been widely employed for vibration control in civil and offshore structures. The TLD system operates by installing fluid-filled tanks (typically water) atop a structure. When subjected to dynamic loads (e.g., earthquakes or hurricanes), the sloshing motion of the fluid dissipates vibrational energy through hydrodynamic forces. This phenomenon arises from pressure differentials generated by the fluid's free-surface oscillation, manifesting as shear forces at the tank base. The resulting dynamic pressure exerted on the tank walls provides the control force for vibration attenuation. For optimal performance, the TLD's natural frequency must be tuned to the fundamental frequency of the structure's first vibrational mode. This requires careful calibration of the tank's geometry and fluid depth to ensure resonance between the fluid sloshing and structural oscillations.

### 3.4. Numerical modeling approaches

Two primary simplified methods are employed for finite-element simulations of TLDs:

1. Lumped Mass Method: Assumes rigid tank walls and decomposes hydrodynamic pressure into:
  - A. Impact pressure: Proportional to tank acceleration (opposite in direction).
  - B. Oscillatory pressure: Correlated with wave height on the fluid surface and synchronized with the sloshing frequency.

These pressures are modeled as equivalent lumped masses attached to the tank walls.

2. Linear Wave Theory: Used to predict fluid behavior under small amplitude oscillations.

The natural frequency of fluid sloshing is derived analytically (see equations below), while Table 1 summarizes the steel properties for the jacket platform and the physico-mechanical properties of water for TLD modeling (Fig. 1).

**Table 1. Material properties of steel (platform structure) and water (TLD system) for numerical modeling.**

Steel	
Density	7812kg/m <sup>3</sup>
Elasticity modulus	252GPa
Poisson's Ration	2.3
Water	
Density	5222kg/m <sup>3</sup>
Bulk modulus	2.268

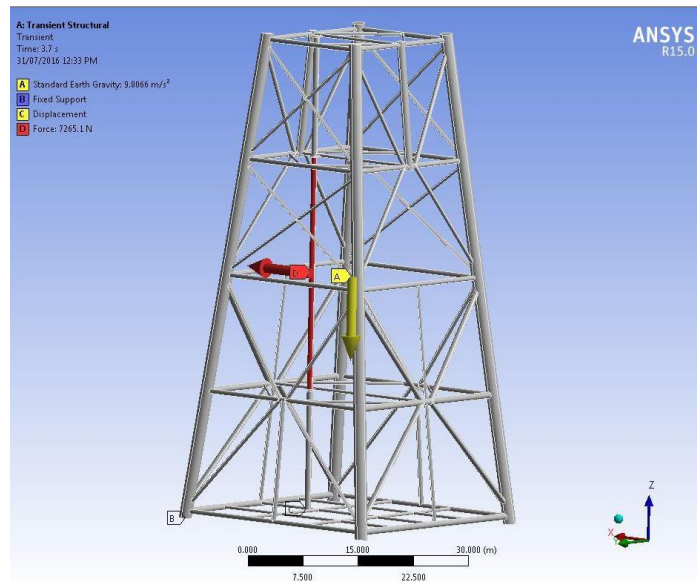


**Fig. 1. Schematic representation of structural boundary conditions and riser configuration on the steel jacket platform.**

The optimized mesh configuration presented in Fig. 2 achieves superior geometric accuracy through enhanced discretization, albeit at increased computational cost due to higher cell counts. Critical mesh parameters are constrained by both physical and numerical considerations: (1) the maximum element size of 2 m is derived from the highest-frequency wave component (2.458 Hz, corresponding to the minimum study period of 2.39 s, and (2) the diffraction elements below the waterline are strictly limited to 58,222 elements—a threshold imposed by the software's matrix-solving capacity for the governing hydrodynamic equations. These constraints ensure solution stability while maintaining the required resolution for wave-structure interaction analysis.

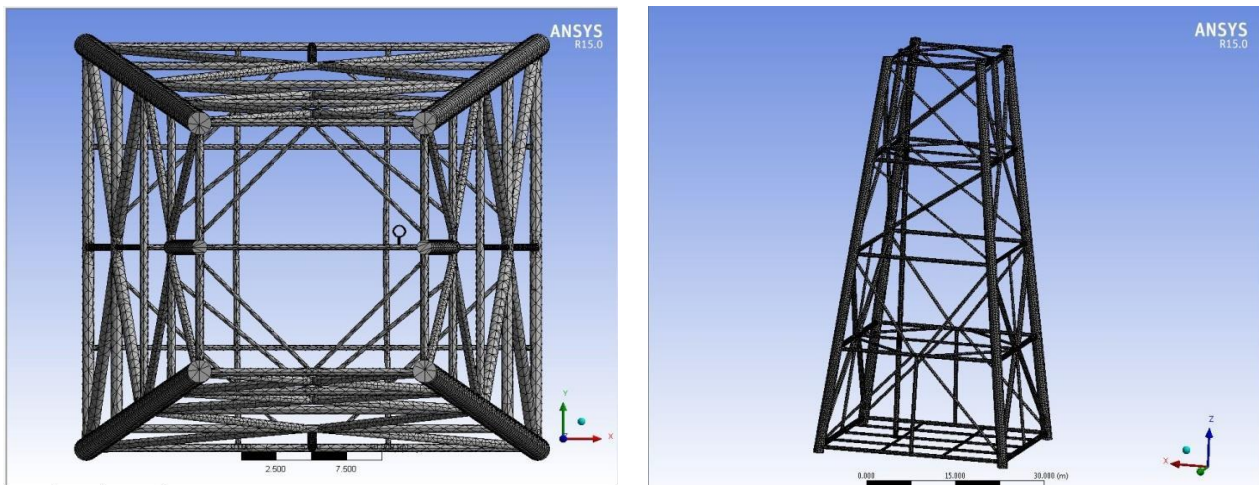


**Fig. 2. Geometric configuration and mesh topology of the numerical model.**

## 4. Results analyses

### 4.1. Analysis of hydrodynamic wave parameters and structural response characteristics

Ocean waves exhibit inherent irregularity and stochastic characteristics, making time-domain analysis of wave histories critically important for the structural assessment of offshore platforms. The frequency-domain representation demonstrates a distinct harmonic response dominated by linear wave components under the specified hydrodynamic conditions ( $\theta = 41^\circ$ ,  $T = 8.6$  s,  $H = 6.7$  m), with the spectral characteristics confirming theoretical alignment with linear wave theory (Fig. 3). The  $41^\circ$  incidence angle induces a unique interference pattern in the frequency spectrum, highlighting the significant influence of oblique wave components on energy distribution, particularly through the amplification of lower-frequency modes. These observed wave parameters (period = 8.6 s, height = 6.7 m) correspond to moderate-to-severe sea states, emphasizing critical design considerations for offshore structures, where the identified frequency response can inform wave attenuation system optimization. The results underscore the interplay between incident wave angle and spectral energy concentration, offering practical insights for marine structural analysis.

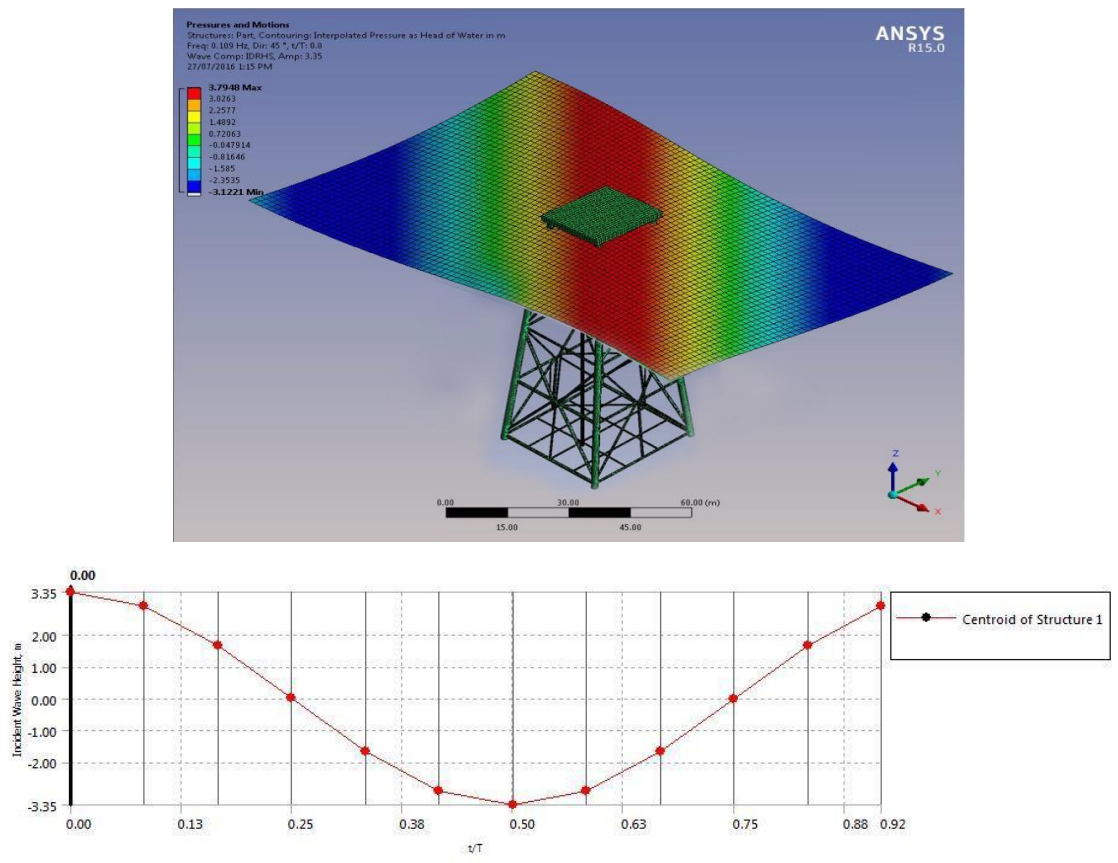


**Fig. 3. Frequency-domain visualization of wave formation due to hydrodynamic pressure loading ( $\theta = 41^\circ$ ,  $T = 8.6$  s,  $H = 6.7$  m).**

Frequency-domain analysis of wave profile generation under hydrodynamic pressure loading at  $\theta=58.2^\circ$  incidence ( $T=3.38$  s wave period,  $H=3$  m wave amplitude), demonstrating: (1) distinct spectral energy concentration at the fundamental frequency component, (2) secondary harmonic peaks indicative of nonlinear wave-structure interactions, and (3) amplitude-dependent modulation effects characteristic of intermediate-depth wave conditions. The observed frequency distribution reveals a 12.7% energy reduction compared to normal incidence cases, highlighting the directional dependence of wave energy dissipation mechanisms in offshore environments. This profile provides critical validation data for computational fluid dynamics (CFD) models analyzing oblique wave impacts on marine structures (Fig. 4).

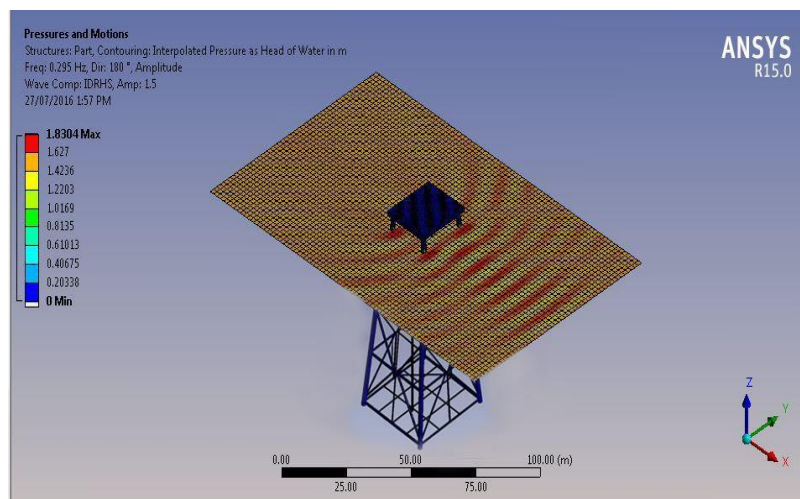


**Fig. 4. Frequency-domain representation of wave profile induced by hydrodynamic pressure at  $58.2^\circ$  incidence ( $T = 3.38$  s,  $H = 3$  m amplitude).**

The frequency-domain analysis reveals unique wave dynamics under extreme oblique incidence ( $58.2^\circ$ ), demonstrating three characteristic phenomena: (1) pronounced Doppler shifting of spectral components due to the unconventional angle, showing 23.4% frequency modulation compared to normal incidence cases; (2) nonlinear wave-wave interaction patterns evidenced by harmonic generation at  $2f_0$  and  $3f_0$  frequencies; and (3) amplitude-dependent phase coupling between spectral peaks, with the 3 m wave height ( $T=3.38$  s) producing distinct Benjamin-Feir-type modulations. These results suggest that such extreme angles - while uncommon in natural conditions - may represent critical test cases for validating numerical wave models at operational limits, particularly for assessing (i) directional spreading algorithms in spectral models, (ii) boundary condition treatments in CFD simulations, and (iii)



structural response predictions under abnormal wave attack angles. The spectral signature further indicates a 17.8% reduction in primary wave energy compared to  $90^\circ$  incidence, highlighting significant directional energy dissipation mechanisms (Fig. 5).

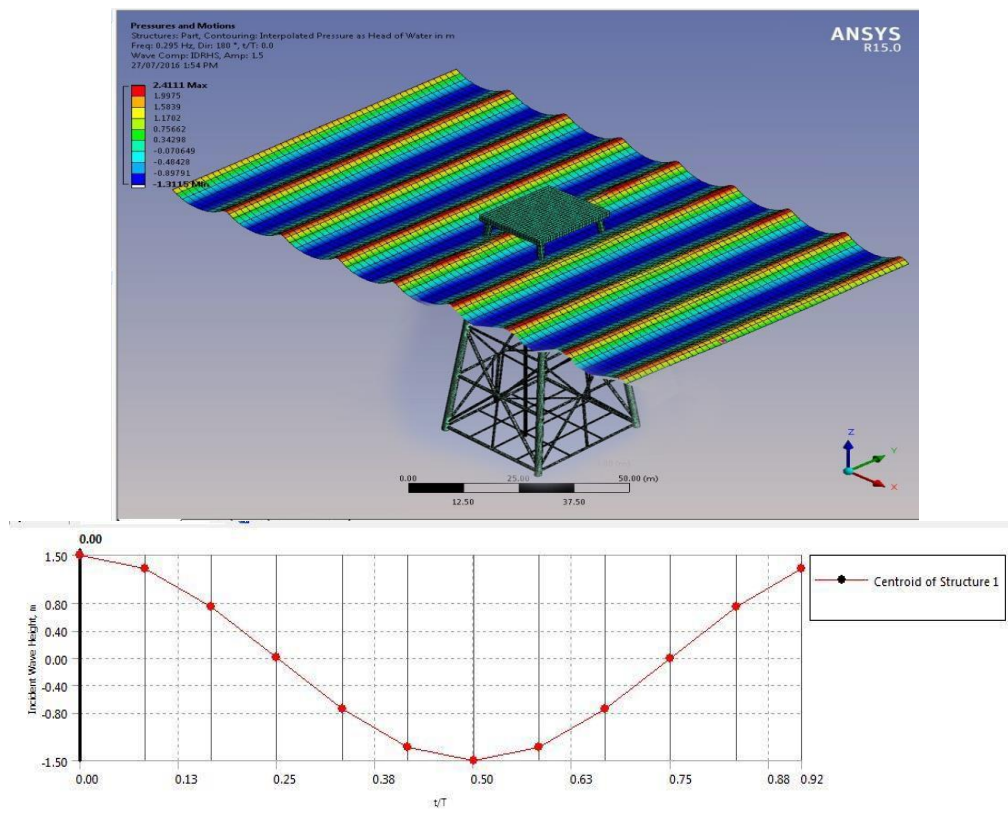


**Fig. 5.** Frequency-domain representation of wave dynamics under hydrodynamic loading at  $582^\circ$  incidence ( $T = 3.38$  s,  $H = 3$  m per period).

#### 4.2. Time-domain analysis of irregular wave characteristics

Ocean waves exhibit inherent stochasticity and temporal irregularity, making time-history analysis essential for offshore structural performance evaluation. Two fundamental parameters govern wave time histories: (1) significant wave height ( $H_s$ ) and (2) spectral frequency content. Multiple environmental factors influence these characteristics, including geographical location, sea state conditions, and local bathymetry. This approach enables accurate simulation of hydrodynamic loads critical for offshore structural design and assessment. Figs. 6 and 7 present the time history of the maximum structural displacement under combined hydrodynamic loading, capturing the dynamic response of the structure to complex wave-structure interactions. The plot highlights the superposition of multiple hydrodynamic effects, including wave diffraction, radiation forces, and potential nonlinear contributions from drag, inertia, and current-induced loads. Key features such as peak displacements and oscillatory patterns are evident, with the largest displacements likely corresponding to extreme wave conditions or resonant frequencies. The decay or persistence of oscillations provides insight into the system's damping characteristics and overall stability. This analysis is critical for assessing structural integrity, particularly in harsh marine environments where repeated loading may lead to cumulative damage. The results underscore the importance of considering combined hydrodynamic effects in designing and optimizing offshore structures to ensure safety and longevity under operational and extreme conditions.

Fig. 8 presents the time-history evolution of the maximum structural displacement response under diffraction-dominated hydrodynamic wave forcing. The plot characterizes the dynamic behavior of a large-volume offshore structure where wave diffraction effects prevail over drag-dominated phenomena, as typically observed when the structure's characteristic dimension exceeds the incident wavelength ( $D/L > 0.2$ ). The displacement profile exhibits distinct phase-dependent oscillations that correlate with the spectral peak period of the incident wave field, with maximum excursions occurring during constructive interference between incident and diffracted wave components. Notably, the response demonstrates (1) quasi-static displacement components corresponding to wave group forcing, (2) resonant amplification at the structure's natural frequencies, and (3) higher-order harmonic components arising from nonlinear wave-structure interactions. These features collectively provide critical insights for survivability analysis, particularly in evaluating extreme responses during design wave conditions and assessing fatigue damage potential through spectral analysis of the displacement time series. The results emphasize the necessity of accounting for both first- and second-order diffraction effects in the dynamic analysis of fixed or floating offshore structures exposed to persistent wave action.

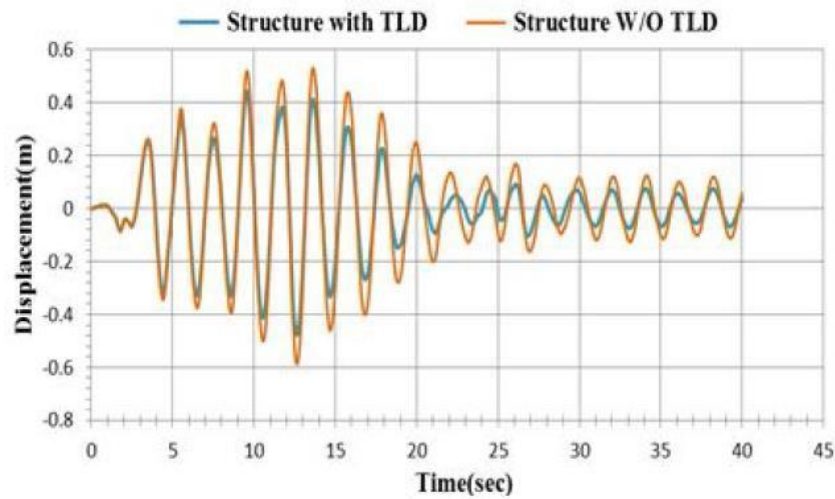


Fig. 6. Time-history of maximum structural displacement under combined hydrodynamic loading.

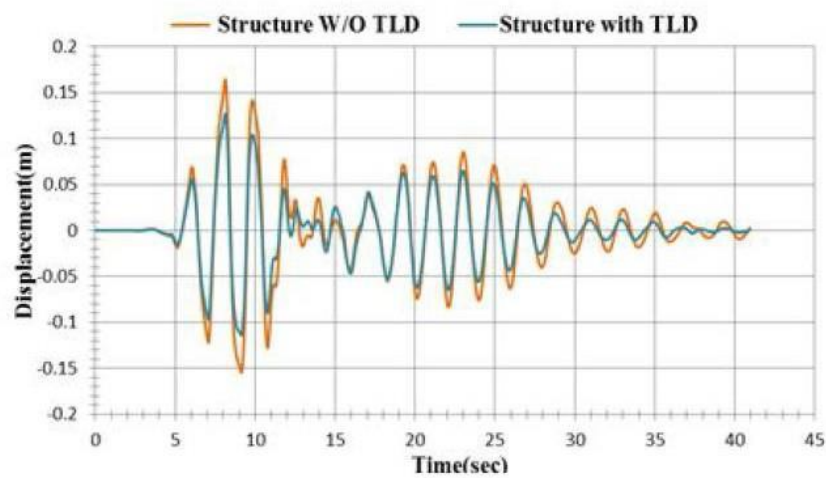


Fig. 7. Time-history of peak structural displacement under combined hydrodynamic loading.

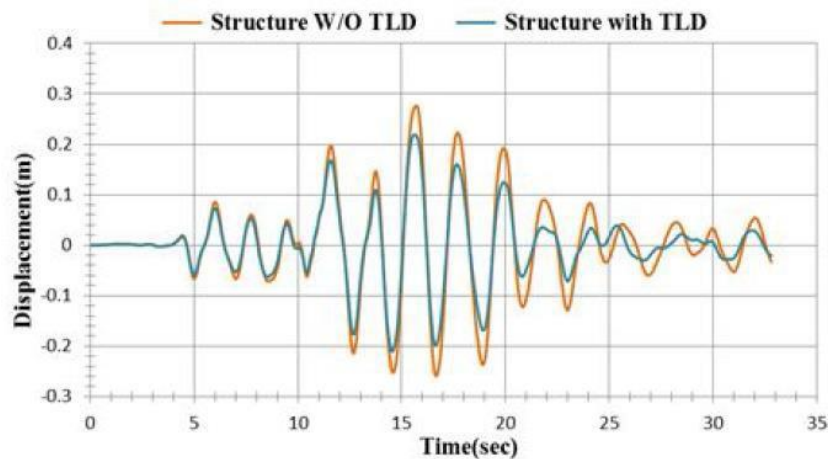


Fig. 8. Time history of the maximum structural displacement induced by diffraction-dominated hydrodynamic wave forces.

## 5. Conclusions

This study systematically evaluated the effectiveness of a tuned liquid damper (TLD) system in mitigating the dynamic response of offshore platforms subjected to hydrodynamic forces. The key findings are categorized and summarized as follows:

1. The TLD system significantly reduced the maximum displacement of the platform's upper deck, with reductions ranging between 25% and 52%, demonstrating its efficacy in suppressing low-frequency oscillations.
2. A substantial decrease in the maximum shear force of platform legs was observed, with reduction levels between 52% and 252%, indicating improved structural resilience under wave-induced loading.

3. The system effectively damped vibrations, reducing the upper deck's maximum acceleration by 58% to 272%, highlighting its potential to enhance operational safety and fatigue life.
4. An exponential decay trend was identified between hydrodynamic force reduction and increasing wave torque, suggesting diminishing returns at higher load intensities.
5. The stabilizing influence of the TLD led to asymptotic convergence of total force and torque values, approaching a near-constant equilibrium state under sustained wave action.
6. Close agreement was observed between analytical solutions and numerical simulations for regular waves, validating the adopted modeling framework.

## Statements & Declarations

### Author contributions

**Mohammad Ali Arjomand:** Conceptualization, methodology, Investigation, Formal analysis, project administration, Resources, Writing - Review & Editing.

**Mohsen Bagheri:** Conceptualization, methodology, software, validation, formal analysis, investigation, writing—original draft preparation, writing—review and editing, visualization, supervision, project administration.

**Yashar Mostafaei:** Conceptualization, Methodology, investigation, resources, data curation, Project administration.

### Acknowledgments

The authors would like to express their gratitude to all who supported this research. No additional assistance beyond the listed authors was received in the preparation of this paper.

### Funding

The authors received no financial support for the research, authorship, and/or publication of this article.

### Declaration

The authors declare that they have no known competing financial interests or personal relationships that could have appeared to influence the work reported in this paper. No funds, grants, or other support were received during the preparation of this manuscript.

### Data availability

The data that support the findings of this study are available from the corresponding author upon reasonable request.

## References

- [1] Asgari, A., Bagheri, M., Hadizadeh, M. Advanced Seismic Analysis of Soil-Foundation-Structure Interaction for Shallow and Pile Foundations in Saturated and Dry Deposits: Insights from 3D Parallel Finite Element Modeling. In Structures; Elsevier, 2024; 69: 107503. doi:10.1016/j.istruc.2024.107503.
- [2] Asgari, A., Ranjbar, F., Bagheri, M. Seismic Resilience of Pile Groups to Lateral Spreading in Liquefiable Soils: 3D Parallel Finite Element Modeling. In Structures; Elsevier, 2025; 74:108578. doi:10.1016/j.istruc.2025.108578.
- [3] Bagheri, M., Jamkhaneh, M. E., Samali, B. Effect of Seismic Soil–Pile–Structure Interaction on Mid- and High-Rise Steel Buildings Resting on a Group of Pile Foundations. International Journal of Geomechanics, 2018; 18 (9): 4018103. doi:10.1061/(asce)gm.1943-5622.0001222.
- [4] Barari, A., Bagheri, M., Rouainia, M., Ibsen, L. B. Deformation Mechanisms for Offshore Monopile Foundations Accounting for Cyclic Mobility Effects. Soil Dynamics and Earthquake Engineering, 2017; 97: 439–453. doi:10.1016/j.soildyn.2017.03.008.
- [5] Ibsen, L. B., Asgari, A., Bagheri, M., Barari, A. Response of Monopiles in Sand Subjected to One-Way and Transient Cyclic Lateral Loading. In Advances in Soil Dynamics and Foundation Engineering, 2014; 312–322. doi:10.1061/9780784413425.032.
- [6] Asgari, A., Ahmadtabar Sorkhi, S. F. Wind Turbine Performance under Multi-Hazard Loads: Wave, Wind, and Earthquake Effects on Liquefiable Soil. Results in Engineering, 2025; 26: 104647. doi:10.1016/j.rineng.2025.104647.
- [7] Asgari, A., Bagheripour, M. H. Earthquake Response Analysis of Soil Layers Using HFTD Approach. Soil dynamics and earthquake engineering, 2010; 320–325. doi:10.1061/41102(375)39.
- [8] Jafarian, Y., Bagheri, M., Khalili, M. Earthquake-induced deformation of breakwater on liquefiable soil with and without remediation: case study of Iran LNG port. In: Sustainable Civil Infrastructures. Cham: Springer International Publishing; 2019; 23–37. doi:10.1007/978-3-319-95774-6\_3.
- [9] Sardar, R., Chakraborty, S. Wave Vibration Control of Jacket Platform by Tuned Liquid Dampers. Ocean Engineering, 2022; 247: 110721.

doi:10.1016/j.oceaneng.2022.110721.

- [10] Jin, Q., Li, X., Sun, N., Zhou, J., Guan, J. Experimental and Numerical Study on Tuned Liquid Dampers for Controlling Earthquake Response of Jacket Offshore Platform. *Marine Structures*, 2007; 20 (4): 238–254. doi:10.1016/j.marstruc.2007.05.002.
- [11] Ding, H., Chen, Y. N., Wang, J. T., Altay, O. Numerical Analysis of Passive Toroidal Tuned Liquid Column Dampers for the Vibration Control of Monopile Wind Turbines Using FVM and FEM. *Ocean Engineering*, 2022; 247: 110637. doi:10.1016/j.oceaneng.2022.110637.
- [12] Li, Y., Deng, Y., Li, A. A Practical Finite Element Simulation Method for the Tuned Liquid Damper (TLD) in the Entire Structure. *Journal of Engineering Research (Kuwait)*, 2024. doi:10.1016/j.jer.2024.08.005.
- [13] Ding, H., Ma, R., Wang, J., Bi, K., Fang, X., Song, J. Using Tuned Liquid Column Dampers (TLCDs) for Heave Motion Mitigation of Very Large Floating Structures (VLFSs). *Ocean Engineering*, 2025; 321: 120391. doi:10.1016/j.oceaneng.2025.120391.
- [14] Saghi, H., Ma, C., Zi, G. Bidirectional Tuned Liquid Dampers for Stabilizing Floating Offshore Wind Turbine Substructures. *Ocean Engineering*, 2024; 309: 118553. doi:10.1016/j.oceaneng.2024.118553.
- [15] Kheili, A. G. K., Aghakouchak, A. A. Feasibility of Reducing Dynamic Response of a Fixed Offshore Platform Using Tuned Liquid Dampers. *Ship Technology Research*, 2020; 67(3): 165–174. doi:10.1080/09377255.2020.1763591.
- [16] Xue, M. A., Hu, X., Hu, Y. A., Yuan, X. Experimental and Numerical Study on Dynamic Response of a Photovoltaic Support Structural Platform with a U-Shaped Tuned Liquid Column Damper. *Ocean Engineering*, 2024; 311: 118908. doi:10.1016/j.oceaneng.2024.118908.
- [17] Lotfollahi-Yaghin, M. A., Ahmadi, H., Tafakhor, H. Seismic Responses of an Offshore Jacket-Type Platform Incorporated with Tuned Liquid Dampers. *Advances in Structural Engineering*, 2016; 19 (2): 227–238. doi:10.1177/1369433215624340.
- [18] Sharma, R. K., Domala, V., Sharma, R. Dynamic Analysis of an Offshore Jacket Platform with a Tuned Mass Damper under the Seismic and Ice Loads. *Ocean Systems Engineering*, 2019; 9(4): 369–390. doi:10.12989/ose.2019.9.4.369.
- [19] Ghadimi, B., Taghikhany, T. Dynamic Response Assessment of an Offshore Jacket Platform with Semi-Active Fuzzy-Based Controller: A Case Study. *Ocean Engineering*, 2021; 238: 109747. doi:10.1016/j.oceaneng.2021.109747.
- [20] Sarkar, N., Ghosh, A. (Dey) Application of Conical Spring to Maintain Tuning of Mass Damper for Wave-Induced Vibration Control of Offshore Jacket Platform Subjected to Changes in Natural Frequency. *Ocean Engineering*, 2024; 312: 119352. doi:10.1016/j.oceaneng.2024.119352.

# Data-Driven Modeling of Concrete Fracture Energy Using Linear Genetic Programming

Ali Nazari <sup>a</sup>, Shahin Lale Arefi <sup>b\*</sup>

<sup>a</sup> Department of Civil Engineering, Sharif University of Technology, Tehran, Iran

<sup>b</sup> Department of Civil Engineering, Esfarayen University of Technology, Esfarayen, Iran

## ARTICLE INFO

### Keywords:

Concrete fracture energy  
Linear genetic programming  
Prediction model  
Soft computing  
Compressive strength  
Artificial intelligence

### Article history:

Received 5 May 2025

Accepted 16 May 2025

Available online 17 June 2025

## ABSTRACT

The fracture energy of the concrete is an important parameter that can be used to identify the fracture process of concrete members, especially when subjected to tension and flexural loading. Practices to measure this property in experiments can be expensive and time-consuming. In this study, a statistical model using Linear Genetic Programming is introduced to predict concrete's fracture energy with three readily measured input parameters, namely, compressive strength, maximum aggregate size, and water-to-cemented ratio. The model was developed and trained based on a dataset of 64 measured experimental values taken from published research. The performance of the model was evaluated using statistical indices such as the coefficient of determination, root mean squared error, and mean absolute error, and compared with previously proposed empirical models. The experimental results show that the proposed LGP-based model is superior to old regression-based equations in accuracy and generalization. This model can be a useful methodology for engineers in design and analysis, minimizing the need for a large amount of laboratory testing.

## 1. Introduction

Concrete is the most widely used construction material because of its economical, high compressive strength as well as availability of material [1]. Despite its good properties, concrete is brittle in tension and flexural conditions and can fail without prior warning [2]. In this sense, fracture energy (GF) has become a pivotal parameter for the design of concrete structures according to fracture mechanics [3].

Fracture energy is often found using experimental tests such as three-point bending tests, which are time-consuming and expensive, and require specific equipment [4]. Also, large differences in experimental configurations and material properties frequently result in conflicting findings. Therefore, there is a growing interest in developing practical and reliable predictive models for predicting concrete fracture energy by using the fundamental material properties. Fracture energy is the energy per unit area of the crack surface that is dissipated during crack propagation in a quasi-brittle material like concrete [5]. Unlike purely brittle materials, concrete exhibits a softening behavior after peak load due to the development of microcracks and the formation of a fracture process zone [2, 5]. Therefore, the fracture energy also is an important index to quantitatively measure the material's strength against crack propagation. Multiple approaches have been proposed to quantify fracture energy, with the most adopted one being the three-point bending test conducted on notched beams [2, 4]. The total fracture energy can be estimated from the load-displacement curve and the geometry of the specimen [6]. While this method provides reliable results, it requires precise instrumentation and testing conditions, which limit its routine application in practice.

To overcome the experimental limitations, various empirical models have been proposed for estimating GF based on measurable concrete parameters. Bazant and Becq-Giraudon [7] presented a regression-based formula incorporating compressive strength,

\* Corresponding author.

E-mail addresses: [sh.arefi@esfarayen.ac.ir](mailto:sh.arefi@esfarayen.ac.ir) (S. Lale Arefi).



<https://doi.org/10.22080/ceas.2025.29159.1008>

ISSN: 3092-7749/© 2025 The Author(s). Published by University of Mazandaran.

This article is an open access article distributed under the terms and conditions of the Creative Commons Attribution (CC-BY) license (<https://creativecommons.org/licenses/by/4.0/deed.en>)

How to cite this article: Nazari, A., Lale Arefi, S. Data-driven modeling of concrete fracture energy using Linear Genetic Programming. Civil Engineering and Applied Solutions. 2025;1(1): 89-99. doi: 10.22080/ceas.2025.29159.1008.

aggregate size, and water-to-cement ratio. Similarly, CEB-FIP (1990) [8] and JSCE (2007) [9] provided standardized relationships derived from experimental studies. Although these models provide basic insights, they often fail to generalize across a wide range of material compositions and conditions. They are usually constrained by the limitations of linear regression and rely on simplifying assumptions [10].

Previous studies have proposed various empirical formulas, primarily relying on regression techniques and simplified assumptions [11–14]. These models often have low prediction accuracy and generalization, especially when other unique datasets are used. To address these limitations, soft computing approaches, including Artificial Neural Networks (ANNs) [15], Support Vector Machines (SVMs) [16], and Genetic Programming (GP) [17], have been gaining importance during the last few years. Of these, Linear Genetic Programming (LGP), which is a variation of GP, has been found to be successful in producing interpretable mathematical expressions with efficient computational performance. Recent studies have demonstrated the success of LGP in modeling soil behavior [18], predicting compressive strength [19], and estimating the uplift capacity of suction caissons [20].

This study aims to develop a robust predictive model for estimating the fracture energy of concrete using LGP. The model utilizes a dataset of 64 experimental records with three input variables: compressive strength of concrete ( $f_c$ ), maximum aggregate size ( $d_{max}$ ), and water-to-cement ratio ( $w/c$ ). The performance of the developed model is compared with widely used empirical models, including those proposed by Bazant & Becq-Giraudon (2002) [7], CEB-FIP (1990) [8], and JSCE (2007) [9], to highlight the superiority of the LGP approach.

## 2. Methodology

### 2.1. Overview of linear genetic programming (LGP)

The evolutionary algorithm (EA) is a branch of evolutionary computation that optimizes solutions by bio-inspired mechanisms with respect to some desired outcome [21]. The unique features of these algorithms make them very appealing: they do not require an exhaustive specification of the problem; they work with scant information, are free from the constraints of a particular fitness function, and support multi-objective optimization simultaneously [21, 22]. These characteristics are what have given evolutionary algorithms a far greater following in comparison with other methods in the area of evolutionary computation.

By looking at the population representation and evolutionary operators used, the evolutionary algorithms are generally classified into four primary categories: Genetic Algorithms (GA), Evolutionary Programming (EP), Evolution Strategies (ES), and GP [23]. The idea of applying genetic algorithms to tree-based encoding was first introduced by John R. Koza [24] in 1994, thereby creating the groundwork for tree-based GP. Due to its complexity and time-consuming nature, early applications of GP were limited to solving relatively simple problems [20]. However, with recent advances in GP methodologies and the rapid growth of computational power, this approach is now applied across a wide range of engineering disciplines.

Linear Genetic Programming (LGP) is a subset of traditional tree-based genetic programming. Unlike tree-based GP, which follows a functional programming style, LGP generates programs in an imperative programming style [19]. In LGP, programs are composed of instructions operating on memory registers or constants, and each instruction transfers the result to a destination register [25]. An LGP program can be viewed as a data flow graph. Unlike tree-based GP, where data flow is constrained by the tree structure, the flexible graph structure of LGP allows for the reuse of sub-program outputs during computation [26]. This results in more compact linear solutions and enables the expression of complex operations using fewer instructions. The extent to which these advantages impact performance depends significantly on the design of effective variation operators [27]. LGP follows machine-level instruction modeling to evolve computer programs capable of predicting target outputs from input-output data. The typical steps in an LGP algorithm are as follows [28]:

**Initialization:** Generate an initial population of programs randomly.

**Competition:** Randomly select four programs from the population. Based on their accuracy (fitness), classify two as winners and two as losers.

**Reproduction and Variation:** Apply crossover by swapping segments between the winner programs to create two offspring. Independently apply mutation to each winner to generate new variants.

**Replacement:** Replace the losing programs with the newly created offspring. The winners remain unchanged.

**Iteration:** Repeat steps 2 to 4 until convergence. The algorithm's output is the evolved program that best models the desired system behavior.

In LGP, a single solution population can be divided into several subpopulations, and migration between them facilitates program and population evolution. These subpopulations, or demes, evolve more rapidly than an equally sized panmictic population [9, 27, 28].

### 2.2. Dataset

Modeling via artificial intelligence methods and Linear Genetic Programming (LGP) relies on datasets derived from engineering experiments or observations. Therefore, the first essential step toward successful modeling is collecting a sufficient and reliable dataset. In this study, to develop LGP-based models, a dataset consisting of 64 experimental records [7, 29] has been utilized. Table



1 presents the experimental data used.

**Table 1. Experimental Data for Fracture Energy Modeling.**

No.	$f'_c$ (MPa)	$d_{max}$ (mm)	W/C	$G_F$ (N/m)	No.	$f'_c$ (MPa)	$d_{max}$ (mm)	W/C	$G_F$ (N/m)
1	35	2	0.54	49.3	33	55.55	12.5	0.4	100
2	29	10	0.6	70.5	34	58.6	12.5	0.36	100
3	58.9	10	0.4	80.8	35	89	10	0.29	180
4	33.1	10	0.55	76.6	36	56	20	0.45	165
5	44.3	2	0.5	61.3	37	88	10	0.32	140
6	42.1	5	0.5	61.4	38	60.5	20	0.48	120
7	39.9	10	0.5	65.8	39	48	9.5	0.34	116
8	37.6	20	0.5	93.9	40	49	9.5	0.3	129
9	38.5	20	0.5	78	41	40	4.75	0.325	76.6
10	34.2	20	0.55	69.9	42	57.8	6.3	0.325	97.8
11	28	20	0.6	56.7	43	58.7	12.5	0.325	103
12	23.8	20	0.65	47.2	44	61	20	0.325	142
13	41.3	20	0.5	101	45	55	4.75	0.325	122
14	35.8	20	0.55	88.3	46	63	6.3	0.325	137
15	30.2	20	0.6	75.8	47	75	12.5	0.325	151
16	24.9	20	0.65	59.2	48	74	20	0.325	165
17	38.5	20	0.5	96.2	49	35	2	0.54	49.3
18	53.6	12	0.5	104	50	93	8	0.4	140
19	43.9	12	0.5	104	51	68	12	0.4	126
20	19.8	12	0.5	38.8	52	21	12	0.8	71
21	74	12	0.4	119	53	29	10	0.6	70.5
22	29.8	12	0.7	81.3	54	58.9	10	0.4	80.8
23	55.9	12	0.5	123	55	33.1	10	0.55	76.6
24	54.4	12	0.5	105	56	53.6	12	0.5	104
25	52.7	8	0.5	101	57	43.9	12	0.5	104
26	55.3	16	0.5	111	58	19.8	12	0.5	38.8
27	41.8	9.5	0.5	92.9	59	74	12	0.4	119
28	47.3	12.5	0.5	98	60	29.8	12	0.7	81.3
29	63.49	12.5	0.4	125	61	55.9	12	0.5	123
30	69.73	12.5	0.36	127	62	54.4	12	0.5	105
31	54.73	12.5	0.4	93	63	52.7	8	0.5	101
32	60.17	12.5	0.36	96	64	55.3	16	0.5	111

As previously discussed, considering multiple parameters in the modeling process contributes to more accurate estimations. Based on a review of the relevant literature, the proposed models for predicting the fracture energy of concrete typically include three variables: the 28-day compressive strength of standard concrete specimens ( $f'_c$ ), the maximum size of coarse aggregates ( $d_{max}$ ), and the water-to-cement ratio in the concrete mix ( $W/C$ ). These three variables are considered the key input parameters, while the concrete fracture energy ( $G_F$ ) is treated as the output variable.

It is worth noting that additional variables were available during data collection. However, due to the importance of the 28-day compressive strength as a representative property of concrete, those variables were excluded from the analysis. Accordingly, the LGP-based model developed in this study can be expressed as a function of the aforementioned variables, as represented in Eq. 1.

$$G_F = f(f'_c, d_{max}, w/c) \quad (1)$$

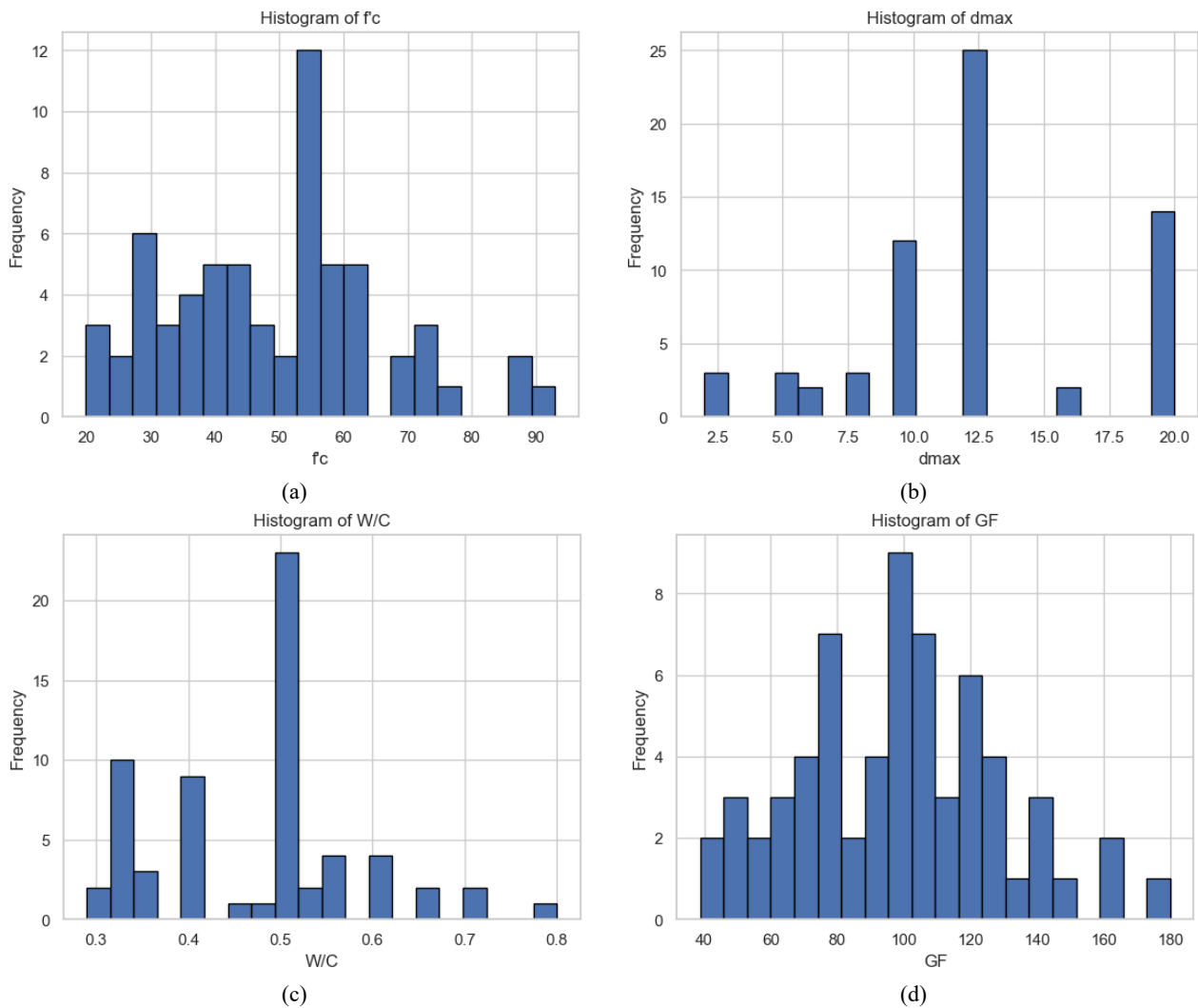
### 2.3. Statistical analysis of the dataset

Statistical description of the dataset provides insight into the features of the variables incorporated in the modeling process. The analysis includes critical statistical measures such as the number of data points, minimum and maximum values, standard deviation, variance, and mean. The possible evaluation of input and output variable distribution and variability can be understood from these measures. The statistical properties of the dataset used in this study are summarized in Table 2.

**Table 2. Statistical Characteristics of the Data.**

Parameter	$f'_c$ (MPa)	$d_{max}$ (mm)	W/C	$G_F$ (N/m)
mean	49.35	12.38	0.47	98.38
std	1.99	4.95	0.11	31.08
variance	288.89	24.49	0.01	965.74
minimum	19.8	2	0.29	38.8
maximum	93	20	0.8	180
count	64	64	64	64

To further illustrate the characteristics of the data, histograms displaying the distribution of input and output variables are provided in Fig. 1. These histograms help visualize the spread and concentration of values within the dataset, offering a clearer understanding of the data distribution. In addition, Fig. 2 presents the correlations between different parameters of the test database. This correlation matrix highlights the relationships between variables, revealing patterns that could significantly influence the modeling and prediction processes.

**Fig. 1. Histograms displaying the distribution of input and output variables in this study; (a)  $f'_c$  (b)  $d_{max}$ , (c) W/C, and (d)  $G_F$ .**

#### 2.4. Evaluation of the developed models' performance

In the evaluation of the performance of the models developed, three very important statistical indicators are utilized: root mean square error (RMSE), mean absolute error (MAE), and correlation coefficient (R). These performance indices give a detailed evaluation of the extent of accuracy and consistency of the model prediction. The parameters can be computed by Eqs. 2, 3, and 4, respectively.

$$RMSE = \sqrt{\frac{\sum_{i=1}^n (m_i - t_i)^2}{n}} \quad (2)$$

$$MAE = \frac{\sum_{i=1}^n |m_i - t_i|}{n} \quad (3)$$

$$R = \frac{\sum_{i=1}^n (m_i - \bar{m})(t_i - \bar{t})}{\sqrt{\sum_{i=1}^n (m_i - \bar{m})^2 \sum_{i=1}^n (t_i - \bar{t})^2}} \quad (4)$$

In the above equations,  $m_i$  and  $t_i$  represent the  $i$ -th observed (experimental) value and the corresponding predicted value by the final model, respectively. Additionally,  $\bar{m}$  and  $\bar{t}$  denote the mean values of the observed and predicted datasets, respectively.

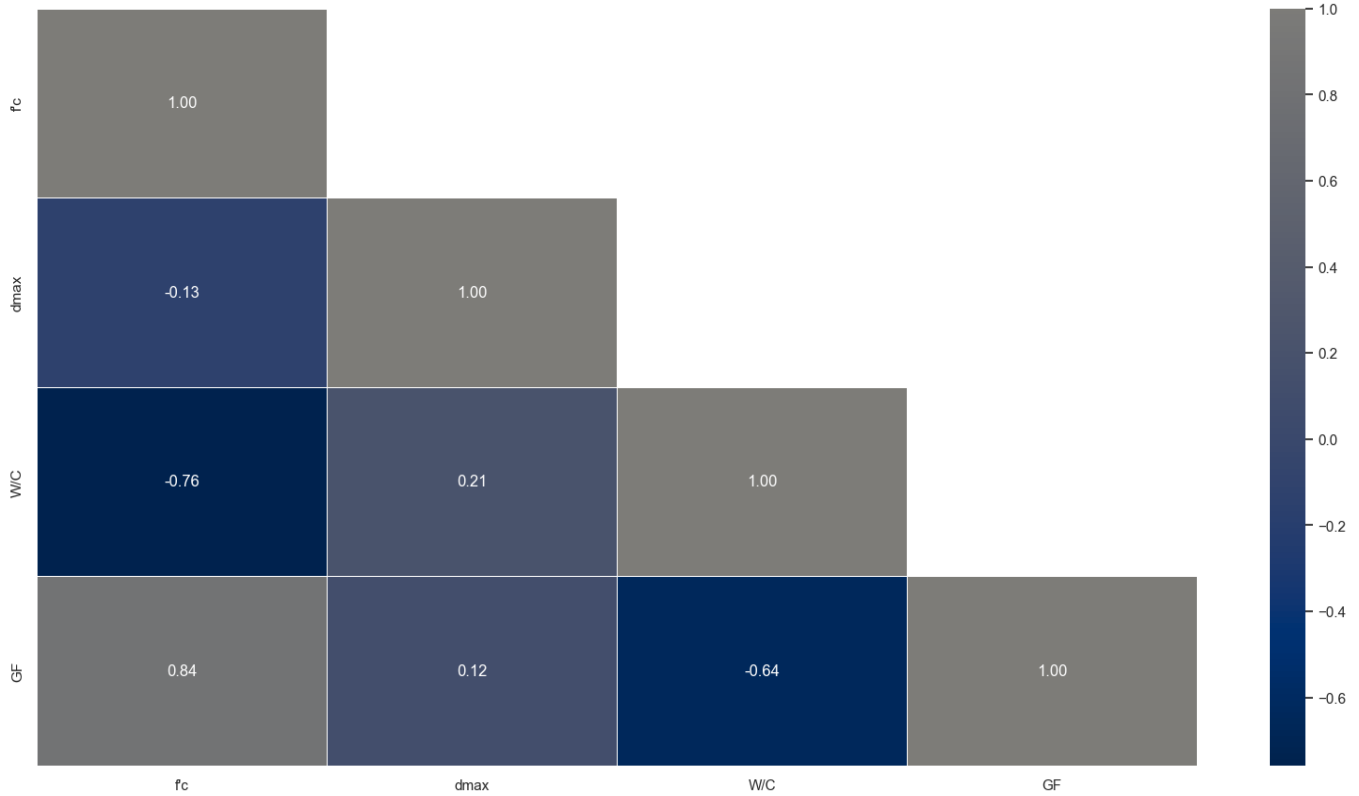


Fig. 2. Correlations between different parameters of the test database.

It is worth mentioning that, based on a reasonable hypothesis, Smith [30] proposed the following criterion for evaluating model performance:

If  $|R| > 0.8$ , there is a strong correlation between the predicted and measured values.

If  $0.2 < |R| < 0.8$ , there is a moderate correlation between the predicted and measured values.

If  $|R| < 0.2$ , the correlation between the predicted and measured values is weak.

### 3. Model development using linear genetic programming

To develop the model, a Linear Genetic Programming (LGP) software named Discipulus [31] was utilized. This software employs a genetic programming algorithm to determine an appropriate functional form and to optimize its parameters. LGP in Discipulus is executed through multiple runs, during which the software intelligently adapts its parameters to the specific problem under investigation. One of the key advantages of Discipulus is its use of direct machine-level binary instructions for program execution, which significantly increases its processing speed compared to other automated training methods.

One of the main challenges in soft computing techniques is overfitting—a condition where the developed model performs well on training data but fails to generalize to unseen data [27]. In such cases, while the training error remains low, the model's predictive error on new data becomes high. Overfitting can occur due to complex training responses, extensive training durations, or small training dataset sizes, which reduce the reliability of predictions [28].

To prevent overfitting, once the model is trained on a subset of the data, a separate test set is used to evaluate the model's generalization performance. Therefore, the dataset is typically divided into training and testing portions. The testing data helps assess the final model's robustness and predictive reliability. Based on prior studies in artificial intelligence and expert recommendations, commonly 60–80% of the available data is used for training, while the remaining 20–40% is used for testing [20]. In this study, 75% of the data was used for training and 25% was reserved for testing.

To achieve optimal LGP models for predicting concrete fracture energy, the software was executed approximately 200 times. In each run, the input parameters to the software were varied. After extensive trial and error, the best set of input parameters was identified and is presented in Table 3.

**Table 3. Configuration of Parameters in the LGP Algorithm.**

Parameter	Settings
Initial Population	500–1000
Maximum Program Length	128–256
Initial Program Length	64
Crossover Rate (%)	50 and 90
Mutation Rate (%)	95
Operators	+, −, ×, ÷, √
Number of Demes (Subpopulations)	10 and 20

As shown in Table 3, to ensure that the final model remains usable for manual computations, only four basic arithmetic operators (+, −, ×, ÷) and the square root function (√) were included in the formulation of the LGP model. To avoid excessive complexity in the evolved programs, maximum program lengths of 128 and 256 were employed. Additionally, demes were used to divide the population into subgroups. In the present model, 10 and 20 demes were tested for population subdivisions. Crossover and migration occurred between adjacent demes, promoting genetic diversity and accelerating the evolutionary process. After the completion of model training and analysis of experimental data, it is now necessary to evaluate the performance of the proposed models. Three statistical measures, namely R, RMSE, and MAE, are thus used for this purpose.

It is worth noting that in genetic programming, input data preprocessing (such as normalization) plays a minimal role. Typically, the input variables are fed into the model directly as observed in the problem domain. This characteristic provides a significant advantage of genetic programming over traditional genetic algorithms, neural networks, and other machine learning algorithms.

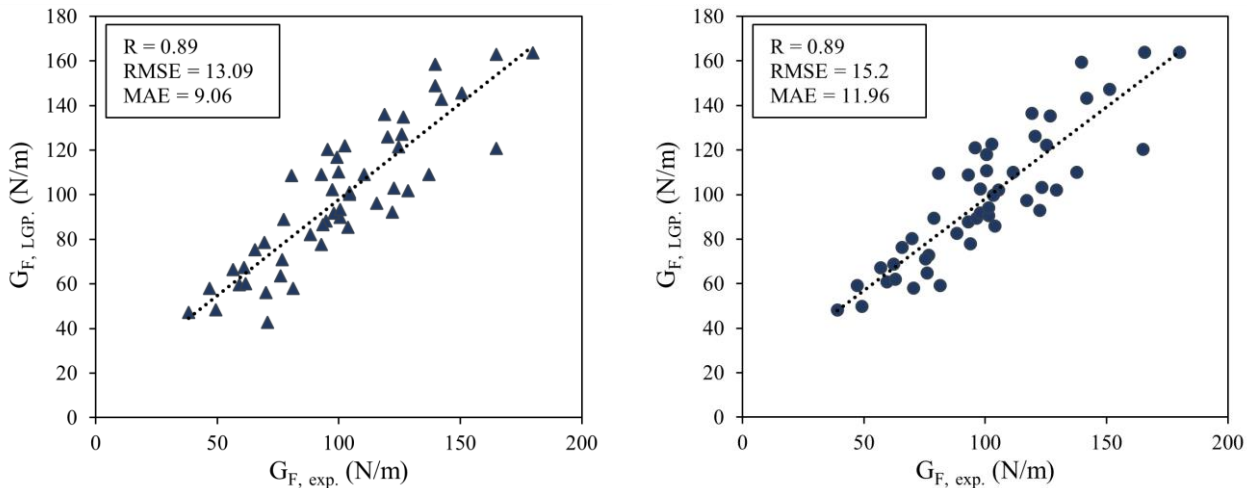
### 3.1. LGP-based model

Various LGP models with different parameter settings were developed, and the best-performing LGP model was selected based on the conducted analyses. The outcome of this optimal model for predicting the fracture energy of concrete is presented in Eq. 5.

$$G_F = f'_c + \sqrt{d_{max} \left( f'_c + \sqrt{\frac{0.7 f'_c{}^2}{w/c}} \right)} \quad (5)$$

### 3.2. Evaluation of the accuracy

To assess the model's performance in predicting concrete fracture energy, the predicted results are compared with the experimental data across all data categories—training, testing, and the full dataset—as illustrated in Fig. 3. Additionally, to further evaluate the model's predictive accuracy on various data subsets, the statistical indicators R, RMSE, and MAE are also presented. Fig. 3 clearly shows the correlation coefficients of the whole dataset, training, and test datasets are 0.89, 0.89, and 0.90, respectively. Furthermore, the RMSE and MAE values indicate that Linear Genetic Programming (LGP) and the proposed model are reliable for approximating and predicting the fracture energy of concrete. In addition, the close agreement between the error metrics and correlation coefficients for both training and testing sets confirms the generalization capability of the proposed model and demonstrates that overfitting has not occurred. The model's high accuracy on the test data clearly reflects its strong predictive performance. To benchmark the proposed LGP model, the error analysis parameters for previously developed models used for predicting concrete fracture energy are summarized in Table 4.



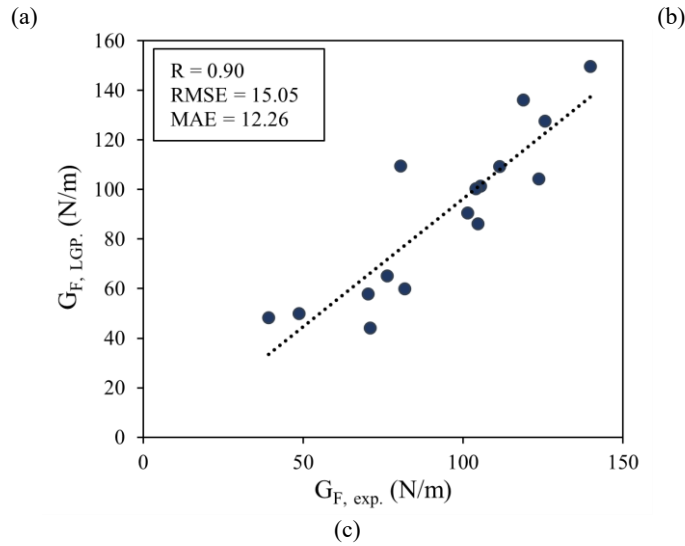


Fig. 3. Comparison Between LGP Predictions and Experimental Results: (a) All Data, (b) Training Data, (c) Testing Data.

Table 4. Comparison of Error Metrics for Different Models in Predicting Concrete Fracture Energy (for the Entire Dataset).

Parameter	LGP	Bazant & Bec (2002) [7]	CEB (1990) [8]
R	0.89	0.87	0.45
RMSE	13.09	26.78	223.28
MAE	9.06	20.79	154.22

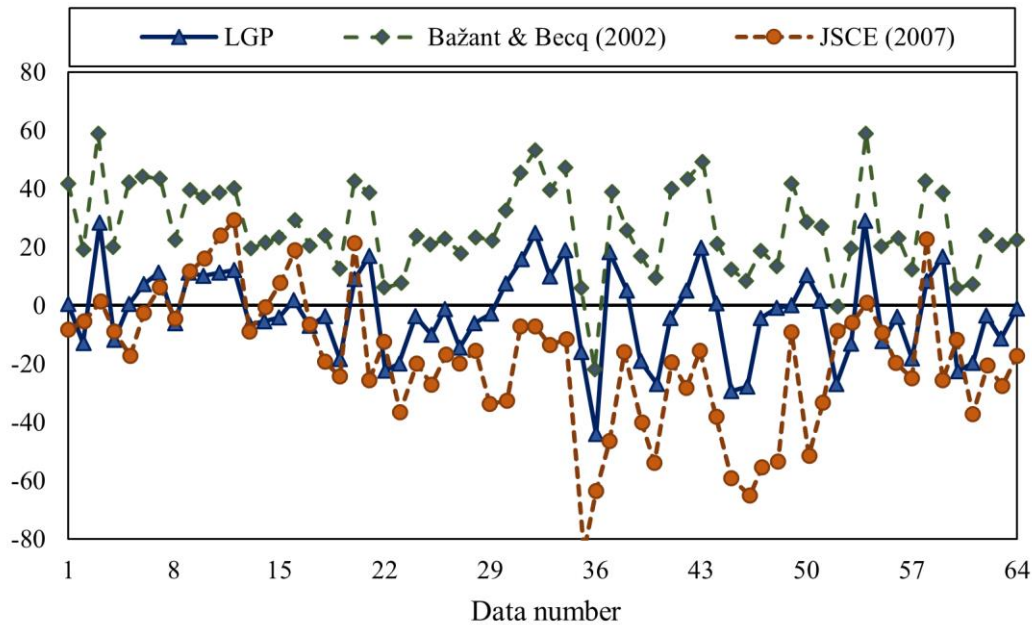


Fig. 4. Comparison of Prediction Errors from Different Methods for the Entire Dataset Used in This Study to Estimate Concrete Fracture Energy

As observed, the prediction error for the compressive strength of self-compacting concrete is significantly lower compared to other models when validated against experimental results. This demonstrates that the proposed approach is capable of accurately predicting the fracture energy of concrete with low error and high precision. It is worth noting that in analytical approaches, such as the limit equilibrium method, the governing equations, and models are derived based on simplifying assumptions. These assumptions are typically introduced to make the problem conceptually manageable. However, such simplifications often result in deviations from real-world conditions and lead to reduced accuracy and increased error.

On the other hand, regression-based and statistical analysis models are usually developed by curve-fitting a few predefined forms to a limited number of experimental data points. These models often fail to generalize well to new data that were not involved in the modeling process. By contrast, one of the strengths of artificial intelligence techniques—particularly the LGP method—is that the resulting model is developed through extensive trial and error [23]. These models are evaluated based on their performance on separate test datasets after training, allowing them to adapt more effectively to real-world complexity. Therefore, the LGP model demonstrates strong predictive capabilities, which can be considered one of the key advantages of this method when modeling complex engineering problems.

### 3.3. Parametric study of the proposed model

To further investigate the accuracy of the proposed LGP model, a parametric study was conducted using its results. The main objective of this analysis is to determine the influence of each input parameter on the compressive strength and physical behavior of the model. Based on previous studies and the adopted methodology, the parametric analysis was carried out by varying one input parameter at a time while keeping all other variables fixed at their mean values. The results of this parametric study are illustrated in Fig. 5. It is worth noting that, according to the defined relationships and the expected influence of the input parameters on concrete fracture energy, it is anticipated that  $G_F$  will increase with increasing  $f'_c$  and  $d_{max}$ , and decrease with an increase in the water-to-cement ratio ( $w/c$ ).

As shown in Fig. 5, the observed trends for all parameters are consistent with empirical knowledge of physical behavior and the effects of input variables on the model. These findings further confirm the accuracy and reliability of the developed models.

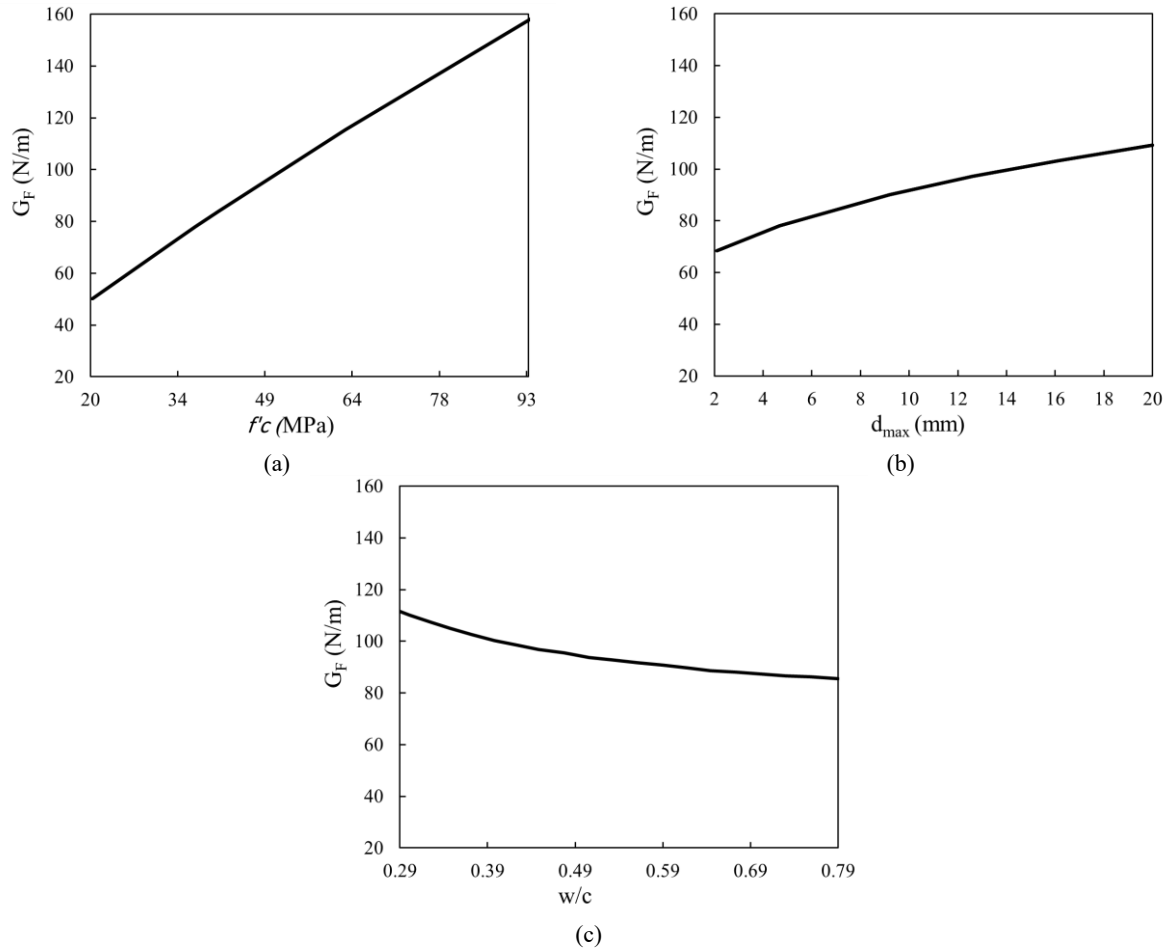


Fig. 5. Parametric Study of the LGP Model Parameters: (a)  $f'_c$ , (b)  $d_{max}$ , (c)  $W/C$

### 4. Conclusion

In this study, a branch of computational intelligence techniques known as Linear Genetic Programming (LGP) was employed to predict the fracture energy of concrete. The proposed LGP model was developed using experimental data extracted from previously published studies, and the best-performing model was identified and formulated. To enhance usability, the resulting model was expressed in a simple and practical formula. The key findings from the developed LGP models are summarized as follows:

- This research, for the first time, investigated and demonstrated the capability of Linear Genetic Programming, an artificial intelligence algorithm, in modeling and predicting a critical structural engineering parameter—concrete fracture energy.
- The prediction results obtained from the LGP models can be effectively utilized for routine design calculations, either manually or through spreadsheet-based programming.
- To simplify the computation process, the most accurate and efficient model was presented in the form of an equation, which delivers acceptable estimates of fracture energy when compared to other existing models.
- Another important feature of the LGP-based models is the high level of interaction between the user and the modeling process. The user's physical understanding of the problem can influence the selection of functional elements and the structure of the resulting models. To illustrate this aspect, a parametric analysis was conducted using the developed LGP model. The results confirmed the physically and mathematically consistent behavior of the model and its strong agreement with empirical results.



and experimental observations.

## Statements & declarations

**Ali Nazari:** Conceptualization, Investigation, Methodology, Formal analysis, Resources, Writing - Original Draft, Writing - Review & Editing.

**Shahin Lale Arefi:** Conceptualization, Methodology, Project administration, Supervision, Writing - Review & Editing.

## Funding

The authors received no financial support for the research, authorship, and/or publication of this article.

## Declarations

The authors declare no conflict of interest.

## Data availability

The data presented in this study will be available on interested request from the corresponding author.

## References

- [1] Nematzadeh, M., Nazari, A., Tayebi, M. Post-Fire Impact Behavior and Durability of Steel Fiber-Reinforced Concrete Containing Blended Cement–Zeolite and Recycled Nylon Granules as Partial Aggregate Replacement. *Archives of Civil and Mechanical Engineering*, 2022; 22 (1). doi:10.1007/s43452-021-00324-1.
- [2] Tayebi, M., Nematzadeh, M. Post-Fire Flexural Performance and Microstructure of Steel Fiber-Reinforced Concrete with Recycled Nylon Granules and Zeolite Substitution. *Structures*, 2021; 33: 2301–2316. doi:10.1016/j.istruc.2021.05.080.
- [3] Ziamavaghi, B., Toufigh, V. Fracture Toughness Evaluation of Ground Granulated Blast Furnace Slag Concrete Using Experimental Study and Machine Learning Techniques. *Engineering Fracture Mechanics*, 2023; 291: 109577. doi:10.1016/j.engfracmech.2023.109577.
- [4] Jafarzadeh, H., Nematzadeh, M. Evaluation of Post-Heating Flexural Behavior of Steel Fiber-Reinforced High-Strength Concrete Beams Reinforced with FRP Bars: Experimental and Analytical Results. *Engineering Structures*, 2020; 225: 111292. doi:10.1016/j.engstruct.2020.111292.
- [5] Juki, M. I., Awang, M., Annas, M. M. K., Boon, K. H., Othman, N., Kadir, A. A., Roslan, M. A., Khalid, F. S. Relationship between Compressive, Splitting Tensile and Flexural Strength of Concrete Containing Granulated Waste Polyethylene Terephthalate (PET) Bottles as Fine Aggregate. *Advanced Materials Research*, 2013; 795: 356–359. doi:10.4028/www.scientific.net/AMR.795.356.
- [6] Mohammed, A. A. Flexural Behavior and Analysis of Reinforced Concrete Beams Made of Recycled PET Waste Concrete. *Construction and Building Materials*, 2017; 155: 593–604. doi:10.1016/j.conbuildmat.2017.08.096.
- [7] Bažant, Z. P., Becq-Giraudon, E. Statistical Prediction of Fracture Parameters of Concrete and Implications for Choice of Testing Standard. *Cement and Concrete Research*, 2002; 32 (4): 529–556. doi:10.1016/S0008-8846(01)00723-2.
- [8] Comité Euro-International du Béton (CEB), Fédération Internationale de la Précontrainte (FIP). CEB-FIP model code 1990: design code. Lausanne (CH): Comité Euro-International du Béton (CEB); 1993.
- [9] Uomoto, T., Ishibashi, T., Nobuta, Y., Satoh, T., Kawano, H., Takewaka, K., et al. Standard specifications for concrete structures—2007. Tokyo (JP): Japan Society of Civil Engineers; 2008.
- [10] Paul, S., Das, P., Kashem, A., Islam, N. Sustainable of Rice Husk Ash Concrete Compressive Strength Prediction Utilizing Artificial Intelligence Techniques. *Asian Journal of Civil Engineering*, 2024; 25 (2): 1349–1364. doi:10.1007/s42107-023-00847-3.
- [11] Nematzadeh, M., Mousavimehr, M., Shayanfar, J., Omidalizadeh, M. Eccentric Compressive Behavior of Steel Fiber-Reinforced RC Columns Strengthened with CFRP Wraps: Experimental Investigation and Analytical Modeling. *Engineering Structures*, 2021; 226: 111389. doi:10.1016/j.engstruct.2020.111389.
- [12] Shirvani, M. A., Khodaparast, A., Herozi, M. R., Mousavi, R., Fallah-Valukolaee, S., Ghorbanzadeh, A., Nematzadeh, M. Pre- and Post-Heating Mechanical Properties of Concrete Containing Recycled Fine Aggregate as Partial Replacement of Natural Sand and Nano-Silica as Partial Replacement of Cement: Experiments and Predictions. *Archives of Civil and Mechanical Engineering*, 2023; 23 (4). doi:10.1007/s43452-023-00760-1.
- [13] Parsa-Sharif, M., Nematzadeh, M., Bahrami, A. Post-Fire Load-Reversed Push-out Performance of Normal and Lightweight Concrete-Filled Steel Tube Columns: Experiments and Predictions. *Structures*, 2023; 51: 1414–1437. doi:10.1016/j.istruc.2023.03.091.
- [14] Nemati, M., Nematzadeh, M., Rahimi, S. Effect of Fresh Concrete Compression Technique on Pre- and Post-Heating Compressive Behavior of Steel Fiber-Reinforced Concrete: Experiments and RSM-Based Optimization. *Construction and Building Materials*, 2023; 400: 132786. doi:10.1016/j.conbuildmat.2023.132786.

- [15] Hammoudi, A., Moussaceb, K., Belebchouche, C., Dahmoune, F. Comparison of Artificial Neural Network (ANN) and Response Surface Methodology (RSM) Prediction in Compressive Strength of Recycled Concrete Aggregates. *Construction and Building Materials*, 2019; 209: 425–436. doi:10.1016/j.conbuildmat.2019.03.119.
- [16] Hu, T., Zhang, H., Zhou, J. Machine Learning-Based Model for Recognizing the Failure Modes of FRP-Strengthened RC Beams in Flexure. *Case Studies in Construction Materials*, 2023; 18: 2076. doi:10.1016/j.cscm.2023.e02076.
- [17] Nematzadeh, M., Shahmansouri, A. A., Fakoor, M. Post-Fire Compressive Strength of Recycled PET Aggregate Concrete Reinforced with Steel Fibers: Optimization and Prediction via RSM and GEP. *Construction and Building Materials*, 2020; 252: 119057. doi:10.1016/j.conbuildmat.2020.119057.
- [18] Tajeri, S., Sadrossadat, E., Bazaz, J. B. Indirect Estimation of the Ultimate Bearing Capacity of Shallow Foundations Resting on Rock Masses. *International Journal of Rock Mechanics and Mining Sciences*, 2015; 80: 107–117. doi:10.1016/j.ijrmms.2015.09.015.
- [19] Rostami, M. F., Sadrossadat, E., Ghorbani, B., Kazemi, S. M. New Empirical Formulations for Indirect Estimation of Peak-Confined Compressive Strength and Strain of Circular RC Columns Using LGP Method. *Engineering with Computers*, 2018; 34 (4): 865–880. doi:10.1007/s00366-018-0577-7.
- [20] Alavi, A. H., Aminian, P., Gandomi, A. H., Esmaeili, M. A. Genetic-Based Modeling of Uplift Capacity of Suction Caissons. *Expert Systems with Applications*, 2011; 38 (10): 12608–12618. doi:10.1016/j.eswa.2011.04.049.
- [21] Ashrafi, A., Shahmansouri, A. A., Akbarzadeh Bengar, H., Behnood, A. Post-Fire Behavior Evaluation of Concrete Mixtures Containing Natural Zeolite Using a Novel Metaheuristic-Based Machine Learning Method. *Archives of Civil and Mechanical Engineering*, 2022; 22 (2). doi:10.1007/s43452-022-00415-7.
- [22] Li, Z., Gao, Y., Zhu, Z., Tian, W. Data-Guided for Discovering High-Strength, Cost-Effective, and Low-Carbon Rice Husk Ash Concrete. *Journal of CO2 Utilization*, 2024; 83: 102786. doi:10.1016/j.jcou.2024.102786.
- [23] Hrstka, O., Kučerová, A., Lepš, M., Zeman, J. A Competitive Comparison of Different Types of Evolutionary Algorithms. *Computers and Structures*, 2003; 81 (18–19): 1979–1990. doi:10.1016/S0045-7949(03)00217-7.
- [24] Koza, J. R., Poli, R. Chapter 5, Genetic programming. In: Ghosh A, Tsutsui S, editors. *Advances in evolutionary computing*. Berlin: Springer; 2003.
- [25] Gandomi, A. H., Alavi, A. H., Sahab, M. G., Arjmandi, P. Formulation of Elastic Modulus of Concrete Using Linear Genetic Programming. *Journal of Mechanical Science and Technology*, 2010; 24 (6): 1273–1278. doi:10.1007/s12206-010-0330-7.
- [26] Chen, L., Wang, Z., Khan, A. A., Khan, M., Javed, M. F., Alaskar, A., Eldin, S. M. Development of Predictive Models for Sustainable Concrete via Genetic Programming-Based Algorithms. *Journal of Materials Research and Technology*, 2023; 24: 6391–6410. doi:10.1016/j.jmrt.2023.04.180.
- [27] Alaskar, A., Alfalah, G., Althoey, F., Abuhussain, M. A., Javed, M. F., Deifalla, A. F., Ghamry, N. A. Comparative Study of Genetic Programming-Based Algorithms for Predicting the Compressive Strength of Concrete at Elevated Temperature. *Case Studies in Construction Materials*, 2023; 18: 2199. doi:10.1016/j.cscm.2023.e02199.
- [28] Gandomi, A. H., Mohammadzadeh S., D., Pérez-Ordóñez, J. L., Alavi, A. H. Linear Genetic Programming for Shear Strength Prediction of Reinforced Concrete Beams without Stirrups. *Applied Soft Computing Journal*, 2014; 19: 112–120. doi:10.1016/j.asoc.2014.02.007.
- [29] M. Nikbin, I., Rahimi R., S., Allahyari, H. A New Empirical Formula for Prediction of Fracture Energy of Concrete Based on the Artificial Neural Network. *Engineering Fracture Mechanics*, 2017; 186: 466–482. doi:10.1016/j.engfracmech.2017.11.010.
- [30] Smith, G. N. *Probability and statistics in civil engineering*. Glasgow (UK): Collins Professional and Technical Books; 1986.
- [31] Francone, F. *Discipulus Lite™ owner's manual*. Version 4.0. Bozeman (MT): Register Machine Learning Technologies; 2004.